Flow Pattern Analysis for Magnetic Resonance Velocity Imaging

Yin Heung Pauline Ng

A thesis submitted in partial fulfilment of the requirements
for the degree of Doctor of Philosophy
of the University of London

Department of Computing
Imperial College London

February 2005

Abstract

Blood flow in the heart is highly complex. Although blood flow patterns have been investigated by both computational modelling and invasive/non-invasive imaging techniques, their evolution and intrinsic connection with cardiovascular disease has yet to be explored. Magnetic resonance (MR) velocity imaging provides a comprehensive distribution of multi-directional in vivo flow distribution so that detailed quantitative analysis of flow patterns is now possible. However, direct visualisation or quantification of vector fields is of little clinical use, especially for inter-subject or serial comparison of changes in flow patterns due to the progression of the disease or in response to therapeutic measures. In order to achieve a comprehensive and integrated description of flow in health and disease, it is necessary to characterise and model both normal and abnormal flows and their effects.

To accommodate the diversity of flow patterns in relation to morphological and functional changes, we have described in this thesis an approach of detecting salient topological features prior to analytical assessment of dynamical indices of the flow patterns. To improve the accuracy of quantitative analysis of the evolution of topological flow features, it is essential to restore the original flow fields so that critical points associated with salient flow features can be more reliably detected. We propose a novel framework for the restoration, abstraction, extraction and tracking of flow features such that their dynamic indices can be accurately tracked and quantified. The restoration method is formulated as a constrained optimisation problem to remove the effects of noise and to improve the consistency of the MR velocity data. A computational scheme is derived from the First Order Lagrangian Method for solving the optimisation problem. After restoration, flow abstraction is applied to partition the entire flow field into clusters, each of which is represented by a local linear expansion of its velocity components. This process not only greatly reduces the amount of data required to encode the velocity distribution but also permits an analytical representation of the flow field from which critical points associated with salient flow features can be accurately extracted. After the critical points are extracted, phase portrait theory can be applied to separate them into attracting/repelling focuses, attracting/repelling nodes, planar vortex, or saddle.

In this thesis, we have focused on vortical flow features formed in diastole. To track the movement of the vortices within a cardiac cycle, a tracking algorithm based on relaxation labelling is employed. The constraints and parameters used in the tracking algorithm are designed using the characteristics of the vortices. The proposed framework is validated with both simulated and in vivo data acquired from patients with sequential MR examination following myocardial infarction.

The main contribution of the thesis is in the new vector field restoration and flow feature abstraction method proposed. They allow the accurate tracking and quantification of dynamic indices associated with salient features so that inter- and intra-subject comparisons can be more easily made. This provides further insight into the evolution of blood flow patterns and permits the establishment of links between blood flow patterns and localised genesis and progression of cardiovascular disease.

Acknowledgments

First and foremost, I would like to thank my supervisor Professor Guang-Zhong Yang for his guidance, encouragement and support. His enthusiasm and vision in medical imaging research has greatly inspired me throughout the course of this PhD

I am most grateful to Dr Sharmeen Masood, who has been a constant source of support and constructive discussion. Her help in proofreading and preparing the figures in this thesis is appreciated. I would also like to thank Professor David Firmin and Dr Raad Mohiaddin for their help in MR velocity data acquisition and Mr Bernardo Carmo for his effort in validating the proposed methods in 3D. I am also grateful to Dr Quan Long for providing the CFD simulated data for validation.

I would like to thank my friends and family who have offered me endless support and encouragement during my studies. Special thanks go to my sister, Yin-Nam, and brother-in-law, Stephen, for offering me tremendous support especially towards the end of my studies.

This work is supported by the Croucher Foundation Scholarship. I am grateful to the Croucher Foundation for funding my studies and Dr Wayne Luk and Miss Elaine Sit for helping to resolve various issues during the tenure of the scholarship.

Table Of Contents

List of Figures

Chapter 1

Introduction

Cardiovascular disease (CVD) is the biggest killer in the UK and the developed world. It caused around 238,000 deaths in the UK in 2002 according to the statistics published by the British Heart Foundation [1]. This represents 39% of all deaths, compared to 26% from all kinds of cancers and 13% from respiratory diseases. About half of the deaths from cardiovascular disease are from coronary artery disease (CAD), one of the main forms of cardiovascular disease. Coronary artery disease, sometimes called coronary heart disease, by itself is the most common cause of death in the UK accounting for around 117,000 deaths per year; and nearly all deaths from coronary artery disease are caused by myocardial infarction (MI), commonly known as heart attack. Extensive effort has therefore been directed towards the prevention, diagnosis and treatment of coronary artery disease.

The culprit of coronary artery disease is atherosclerosis, which is a progressive disease that typically begins in childhood and continues to progress as people grow old. If not treated promptly, it could lead to myocardial infarction, strokes and aneurysms. In patients who have survived myocardial infarction, the function and morphology of the heart may continue to change in the weeks and months following myocardial infarction. This process involves continuous morphological changes and is known as myocardial remodelling,

during which an expansion in the infarcted region and a dilation of the ventricle may be observed. This progressive change in the morphology of the diseased ventricle may be accompanied by deteriorated cardiac function and cause altered ventricular flow patterns. Significant difference has been observed in normal subjects and patients with dilated ventricle.

For the diagnosis and treatment of cardiovascular disease, cardiac imaging techniques have become an important clinical tool. They allow clinicians to gain a better understanding of the cardiac morphology and function. Current cardiac imaging techniques include Computed Tomography (CT), ultrasound, Magnetic Resonance Imaging (MRI), Positron Emission Tomography (PET) and Single Photon Emission Computed Tomography (SPECT). Cardiovascular Magnetic Resonance (CMR) is one of the most popular techniques in cardiovascular medicine because of its non-invasive and non-destructive nature. Early applications of CMR are mainly concerned with obtaining anatomical images of the heart. In recent years, CMR has been widely used in the assessment of cardiac function and the quantitative measurement of in vivo blood flow.

One of the key developments of MR in the last 20 years is MR velocity imaging. It provides a comprehensive distribution of multi-directional in vivo flow distribution so that detailed quantitative analysis of the flow patterns is now possible. In existing studies, a number of flow indices are derived from the velocity data and the overall flow patterns in the cardiac chambers are also studied extensively. However, direct visualisation or quantification of the vector fields is of limited clinical use, especially for inter-subject or serial comparisons of changes in flow patterns due to the progression of the disease or in response to therapeutic measures. To this end, it is necessary to characterise and model both normal and abnormal flows and their effects in order to achieve a comprehensive and integrated description of flow in health and disease.

To accommodate the diversity of flow patterns in relation to morphological and functional changes, we propose in this thesis the approach of detecting salient topological features prior to analytical assessment of dynamical indices of the flow patterns. We start in Chapter 2 with an introduction to the basic anatomy of the heart and its associated blood flow dynamics. It also describes major cardiac imaging techniques with particular emphasis on their suitability for flow field quantification. This is followed by a comprehensive review

of MR flow imaging techniques in Chapter 3. MR flow imaging is a non-invasive and versatile technique which is capable of providing detailed quantitative flow measurement. Time-of-flight and phase flow imaging methods are the two main flow measurement methods, of which phase contrast imaging method is the most widely used. The underlying principle of the technique is to introduce a flow related phase shift that is proportional to the velocity. In this Chapter, we will also outline different rapid imaging strategies and describe common errors in phase contrast velocity imaging methods. The key clinical applications of MR velocity imaging and the significance of certain haemodynamic factors related to atherosclerosis are described in Chapter 4. Since the reference data used for algorithm validation is derived from Computational Fluid Dynamics (CFD), we will also provide in this Chapter the basic principles of CFD and the key numerical steps involved. The current trend towards subject-specific blood flow simulation through the combination of medical imaging and computational flow modelling techniques is also discussed.

Chapters 5 to 7 form the main contribution of the PhD work reported in this thesis. In these chapters, we describe a novel framework for the restoration, abstraction, extraction and tracking of flow features such that their dynamic indices can be accurately tracked and quantified. To improve the accuracy of quantitative analysis of the evolution of topological flow features, it is essential to restore the original flow fields so that critical points associated with salient flow features can be more reliably detected. In Chapter 5, the restoration method is formulated as a constrained optimisation problem to remove the effects of noise and to improve the consistency of the MR velocity data. A computational scheme is derived from the First Order Lagrangian Method for solving the optimisation problem. Chapter 6 presents a flow abstraction algorithm that is designed to reduce the amount of data required to encode the velocity distribution while serving as an analytical representation of the flow field from which critical points associated with salient flow features can be accurately extracted. By using the proposed flow abstraction algorithm, the entire flow field is partitioned into clusters, each of which is represented by a local linear expansion of its velocity components. With this representation, critical point can then be easily extracted. After the critical points are extracted, phase portrait theory can be applied to separate them into attracting/repelling focuses, attracting/repelling nodes, planar vortex, or saddle. In Chapter 7, an algorithm based on relaxation labelling technique is developed for tracking the movement of vortical flow features formed in the left ventricle during diastole. The constraints and parameters used in the tracking algorithm are based on the

characteristics of the vortices, and the proposed framework is validated with both CFD simulated and in vivo data acquired from patients with sequential MR examination following myocardial infarction.

The main contribution of the thesis is in the new vector field restoration and flow feature abstraction methods proposed. They allow the accurate tracking and quantification of dynamic indices associated with salient features so that inter- and intra-subject comparisons can be more easily made. This provides further insight into the evolution of blood flow patterns and permits the establishment of links between blood flow patterns and localised genesis and progression of cardiovascular disease.

Most part of this thesis are published in peer-reviewed journals and conference proceedings, which include:

- Ng YHP and Yang GZ, Vector-valued image restoration with application to magnetic resonance velocity imaging. Journal of WSCG, 2003. 11(2): p. 338-45.
- Ng YHP, Sherwin S and Yang GZ. Vector field restoration for MR phase contrast velocity mapping. In Proc. 11th ISMRM Scientific Meeting. 2003. Toronto, Canada. p. 2548.
- Ng YHP, Carmo BS and Yang GZ. Flow field abstraction and vortex detection for MR velocity mapping. In Proc. 6th International Conference on Medical Image Computing and Computer Assisted Intervention (MICCAI). 2003. Montreal, Canada: Springer-Verlag. p. 424-31.
- Ng YHP, Carmo BS, Prugel-Bennett A and Yang GZ. A First-Order Lagrangian-based variational approach for 3D flow vector field restoration. In Proc. Computer Assisted Radiology and Surgery. 2003. London, UK: Elsevier. p. 1185-90.
- Carmo BS, Ng YHP, Prugel-Bennett A, and Yang GZ. A data clustering and streamline reduction method for 3D MR flow vector field simulation. In Proc. 7th International Conference on Medical Image Computing and Computer Assisted Intervention (MICCAI). 2004. Rennes, France: Springer-Verlag. p. 451-8.

Chapter 2

Cardiovascular Anatomy, Function and Imaging Techniques

2.1 Basic Cardiovascular Anatomy

The cardiovascular system consists of the heart and a closed network of blood vessels including arteries, veins and capillaries. The heart is the most important organ in the body and is responsible for pumping blood to the lungs through the pulmonary circulation and to the rest of the body through the systemic circulation. This is accomplished by systematic contraction and relaxation of the cardiac muscle in the myocardium.

2.1.1 Anatomy of the Heart

The heart consists of four chambers, the upper chambers are the left and right atria and the lower chambers are the left and right ventricles [2]. The two atria are thin-walled chambers that receive blood from the veins. The left and right ventricles are thick-walled chambers that are responsible for pumping blood to other parts of the body. The heart comprises of

three layers surrounding the inner chambers, epicardium (outer layer), myocardium (middle layer), and endocardium (inner layer). The heart is further enclosed in a fourth protective layer known as the pericardium. The epicardium, also called the visceral pericardium, is composed of a simple squamous epithelium, fibroelastic connective tissue, within which nerves and coronary blood vessels are embedded. The myocardium is the contractile layer made of specialised striated cardiac muscle fibres. The endocardium lines the lumen of the heart and is composed of simple squamous epithelium and a thin layer of loose connective tissue.

Studies into the structure of the heart at the muscle level can provide insight into how the heart functions. The muscle structure of the heart can be obtained by dissection. It is found that the heart is a helically wound structure with a clear difference between the structures at the base and the apex. At the base (the uppermost part of the heart), the muscle fibres run in anti-clockwise direction from the epicardium to the endocardium when viewed from below, whereas at the apex, the muscle fibres pass in clockwise direction. Studies have revealed that the heart is made up by a muscle band with helical winding that forms different chambers [3]. It is known that the right ventricular wall is much thinner than that of the left ventricle. This is due to the fact that the left ventricular wall is made up of two windings of the muscle band whereas the right ventricular wall is made up of one winding only. It can be perceived that the ventricular myocardium consists of a single muscle band twisted on itself like a rope extending from the origin of the pulmonary artery to the root of the aorta that define the left and right ventricles through two turns in a helical fashion [4]. Although this theory of macroscopic muscle structure provides an easy way of understanding cardiac anatomy, it does not always explain the complexity of the muscle fibre architecture. This has lead to the development of several different theories describing the myofibre architecture [5][6].

The blood vessels of the body, on the other hand, are functionally divided into three distinctive circuits: pulmonary circuit, systemic circuit and coronary circuit. The right ventricle is responsible for pumping de-oxygenated blood through the pulmonary circuit, which circulates blood through the lungs where it is oxygenated. The left ventricle is the largest chamber that does the majority of the work by pumping blood through the coronary circuit to the heart itself, and the systemic circuit to the rest of the body.

The basic anatomical structure of the heart can be illustrated in Figure 2.1. At the exit of each chamber there is a valve to ensure that there is no backwards flow once the blood leaves the chamber. The valves between the atria and ventricles are the atrioventricular valves or cuspid valves, while those at the bases of the large vessels leaving the ventricles are the semilunar valves. The right atrioventricular valve is the tricuspid valve, whereas the left atrioventricular valve is the bicuspid, or mitral, valve. Finally, the valve between the right ventricle and pulmonary trunk is the pulmonary semilunar valve, and the valve between the left ventricle and the aorta is the aortic semilunar valve.

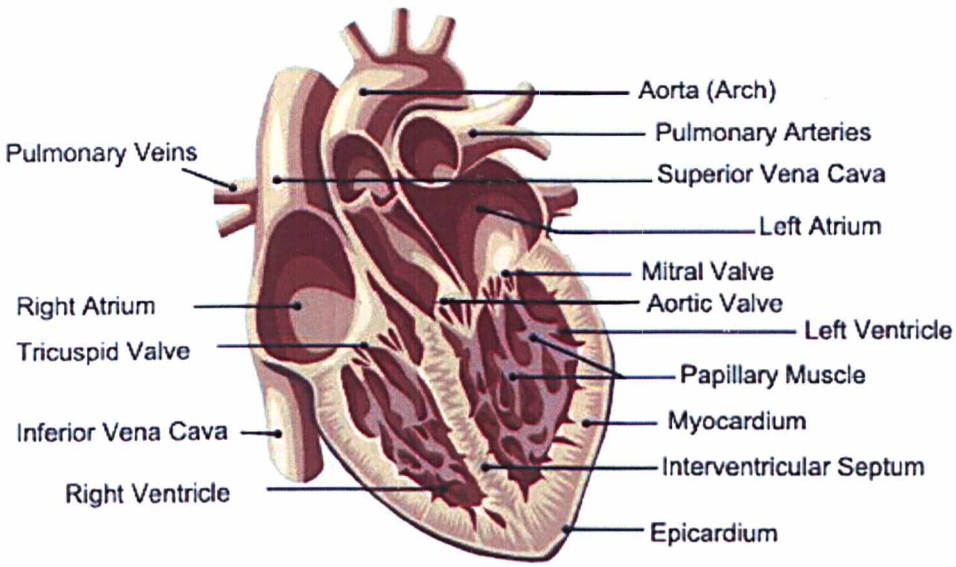

Figure 2.1 The basic anatomy of the heart. The right hand side consists of the right atrium and right ventricle, connected via the tricuspid valve. Oxygen-depleted blood from the rest of the body flows into the right atrium through the pulmonary veins, passing through the tricuspid valve into the right ventricle from where it is pumped out through the pulmonary arteries into the lungs. Once reoxygenated in the lungs, the blood returns to the left atrium via the pulmonary veins. It is then pumped through the mitral valve into the left ventricle. The left ventricle subsequently pumps out the blood to the rest of the body via the aorta.

2.1.2 The Conduction System

The synchronised contraction and relaxation of the heart is coordinated through the electrical conduction system of the heart. The system is made of two nodes, the sinoatrial (SA) node and the atrioventricular (AV) node, and a series of conduction fibres or bundles (pathways), as shown in Figure 2.2. The SA node, referred to as the pacemaker of the heart, is a section of nodal tissue that is located in the upper wall of the right atrium and it rhythmically initiates impulses 70 to 80 times per minute without neural stimulation. A normal heartbeat begins with an electrical impulse from the SA node. The impulse spreads throughout the atria, causing them to contract; then it moves through the AV node into the conduction fibres (Purkinje fibres) that are located in the ventricles themselves. As the impulse travels down the fibres, the ventricles contract and the cycle then repeats itself.

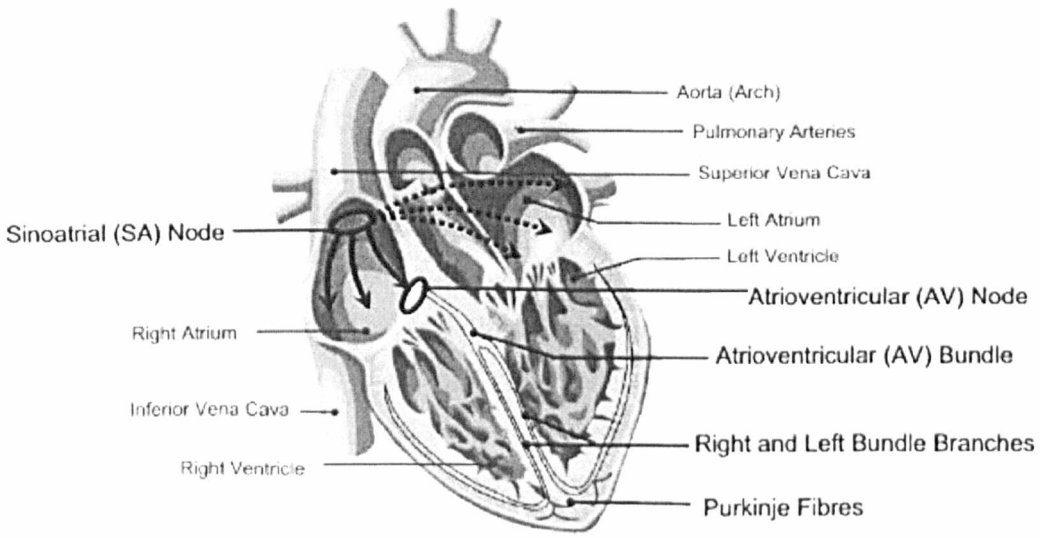

Figure 2.2 The conduction system of the heart. The impulse is initiated at the sinoatrial (SA) node causing atrial contraction. It travels to the atrioventricular (AV) node and subsequently through the atrioventricular (AV) bundle to both ventricles initiating ventricular contraction.

2.1.3 The Cardiac Cycle

The cardiac cycle is a sequence of events that occurs during one heartbeat and is initiated at the sinoatrial node [7]. It can be divided into two basic phases: diastole and systole. Diastole is the phase at which the ventricles relax whereas systole represents the period when the ventricles are contracting. The cardiac cycle can be characterised by the electrocardiogram (ECG) as shown in the bottom half of Figure 2.3. An ECG measures the electrical activity of the heart and the cardiac cycle can be further divided into smaller segments, each depicting activity in a particular area of the heart. To help explaining the events in a cardiac cycle, the characteristic pressure curves of the left ventricle, atrium and the aorta are also illustrated in Figure 2.3.

The first phase of the cardiac cycle is atrial systole. It is initiated by atrial depolarisation which appears as the P wave in the ECG diagram. During this phase, blood leaves the atria and enters the ventricles. Following atrial systole comes ventricular systole, which is triggered by ventricular depolarisation (the QRS complex). During this phase, the pressure in the ventricle rises while the ventricular volume remains unchanged as both the tricuspid and mitral valves remain closed. This phase is therefore referred to as the isovolumetric contraction. Between the QRS complex and the T wave, the pressure in the ventricles continues to rise and causes the aortic and pulmonary valves to open and the blood is ejected to the aorta and pulmonary artery. The last wave in the cardiac cycle, the T wave, represents ventricular repolarization, which causes ventricular pressure to fall and the ejection rate gradually falls. This is followed by ventricular diastole, during which the aortic and pulmonary valves close and ventricular filling begins at the point when ventricular pressure falls below atrial pressure. When the ventricles are completely relaxed, the cardiac cycle is completed. Atrial repolarization is not distinguishable in an ECG diagram because it occurs during ventricular depolarisation and the wave of atrial repolarization is relatively small in amplitude, as it is masked by the much larger ventricular-generated QRS complex.

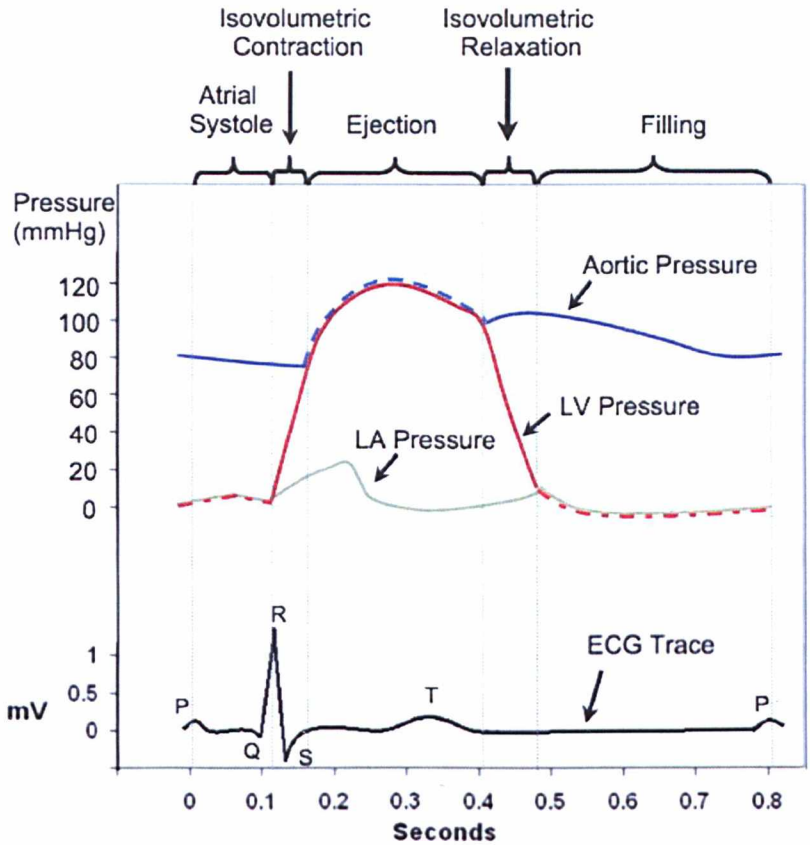

Figure 2.3 Typical cardiac pressure curves of the left ventricle (red), atrium (brown) and the aorta (blue), and electrocardiogram (ECG) (black) of a cardiac cycle. The P-wave in the ECG trace marks the start of the cardiac cycle. The main phases in a cardiac cycle are: atrial systole, ventricular systole (consists of the isovolumetric contraction and ejection phases) and ventricular diastole (consists of the isorelaxation and filling phases).

In terms of muscle motion, it is clear that the ventricles dilate at diastole, resulting in a drop in pressure which in turn leads to LV filling, this is followed by contraction of the ventricles at systole to increase the inter-ventricular pressure which forces the blood into arteries. In addition to contraction-dilation, lengthening and shortening of the ventricle in the longitudinal direction have been observed and these motions explain why the base of the heart moves down towards the apex. By observing the movement of the beating heart using MRI or echocardiography, it is found that the apex remains relatively motionless whereas the base of the heart moves up and down towards the apex. This is a rather strange phenomenon considering that the apex is free hanging and unattached whereas the base is

fixed and attached to the pulmonary artery, aorta and atria. Another observed motion is the torsion of the heart, the motion of which could not be accurately measured until recent advances in imaging [3]. This torsion involves the base twisting in one direction while the apex twists in the opposite direction. Both the up and down movement of the base and the torsion of the heart can be explained by the four basic motions of the heart which include the narrowing of the base, the shortening in the longitudinal direction, followed by lengthening in the longitudinal direction and finally widening of the base.

2.1.4 Blood Flow Dynamics

From a functional level, the heart acts like two pumps, one on the left and the other on the right, working in synchrony. On the right side of the heart, blood from the body enters the right atrium from the superior vena cava (SVC) and the inferior vena cava (IVC) and then passes through the tricuspid valve to the right ventricle. It is then pumped through the pulmonary valve into the pulmonary artery and then to the lungs. The blood is re-oxygenated in the lungs and then it passes through the pulmonary veins to the left atrium. When the left atrium is full, the blood is injected into the left ventricle through the mitral valve. Finally, the left ventricle pumps the blood through the aortic valve to all parts of the body. A sequence of schematic diagrams showing the principal flow path is shown in Figure 2.4.

In a recent study on the redirection of flow through the heart [8], it was observed that asymmetries and curvatures of the looped heart have significant dynamic advantages. It was shown that the atrial filling patterns appear to be asymmetric, thereby allowing the momentum of the inflow stream to be redirected towards the atrio-ventricular valves. Whereas at the ventricular level, the flow stream changes direction in such a way that recoil of the ventricle away from ejected blood enhances ventriculo-atrial coupling. Based on these observations, it was suggested that the heart is able to redirect blood through the cardiac chambers with minimal dissipation of energy, which can dynamically enhance reciprocation of atrial and ventricular function during exercise. The efficiency of the heart involves coupled interactions between contractility, elasticity and changes in momentum of all heart chambers. This interpretation was expected to provide further insight in clinical cases where the relations between forms, flow, mobility and timing of the heart was affected.

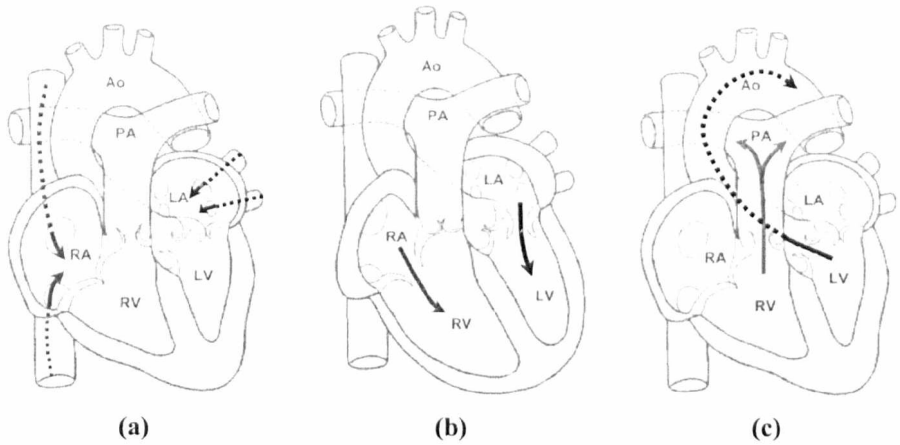

Figure 2.4 Schematic diagrams showing the principal flow path through the heart chambers. (a) During systolic inflow, re-oxygenated blood enters the left atrium (LA) from the pulmonary veins, while oxygen depleted blood enters the right atrium (RA) from the superior and inferior vena cava. (b) During diastole, blood is injected into the ventricles from the atria, through the tricuspid (right side) and mitral (left side) valves. (c) During systolic outflow, the ventricles eject blood, via the pulmonary and aortic valves, through the pulmonary artery (PA) and the aorta (Ao) into the lungs and the systemic circulation respectively.

Over the years, blood flow patterns of the heart, particularly the left ventricle, have been extensively investigated by both medical imaging [9, 10] and computational techniques [11, 12]. Nevertheless, the interaction between flow patterns and cardiovascular structure and the link between disturbed flow patterns and cardiovascular disorders have yet to be fully explored [13, 14]. Vortical flow pattern in the left ventricle during diastole is one of the most intriguing features that has been studied over the years [15, 16]. It has been suggested that its existence might have a beneficial effect in assisting the closure of the mitral valve. Previous study has shown that in a normal ventricle, two vortices, namely the anterior and posterior vortex, are formed during early diastole [16]. The posterior vortex, formed behind the posterior mitral valve leaflet, is more constricted and only lasts for a shorter period of time compared to the anterior vortex, which is formed near the anterior mitral valve leaflet. It has been observed that in patients with a dilated ventricle, early diastolic inflow through the mitral valve is directed towards the posterior free wall instead of the apex as in the normal ventricle. Apart from the deviation in inflow direction, the evolution of the anterior

and posterior vortices is significantly different from that observed in normal ventricles. The cause of this difference in the flow patterns, however, has yet to be established.

2.1.5 The Coronary Circulation

In order to maintain the mechanical function of the heart, normal coronary circulation is critical. The coronary tree consists of blood vessels that supply blood to, and remove blood from, the myocardium. The locations of the major coronary arteries and the coronary sinus are depicted in Figure 2.5. The main coronary arteries include the left main coronary artery (LM), right coronary artery (RCA), left anterior descending artery (LAD), left circumflex artery (LCX) and posterior descending artery (PDA). The LM and RCA originate at the base of the ascending aorta just above the aortic valve, ensuring that the myocardium receives richly oxygenated blood at a high pressure. The LM, which branches into the LAD and LCX, supplies the inter-ventricular septum, the left atrium and both ventricles. The RCA, from which the PDA branches off, mainly supplies the right atrium, right ventricle and variable parts of the inter-ventricular septum. Occlusions of one or more of the major coronary arteries could lead to myocardial ischaemia and consequently infarction. Further details on the causes and consequences of coronary heart diseases are described in Section 2.2.

From a cellular level, the myocardium carries a dense capillary network so that each cardiac myocyte has several capillaries running parallel to the muscle fibre. The high capillary-to-fibre density ensures short diffusion distances to maximize oxygen transport into the cells and removal of metabolic waste products from the cells. Most of the deoxygenated blood is returned to the right atrium through the coronary sinus, whereas a very small amount is drained through numerous microscopic veins that open directly into the heart chambers.

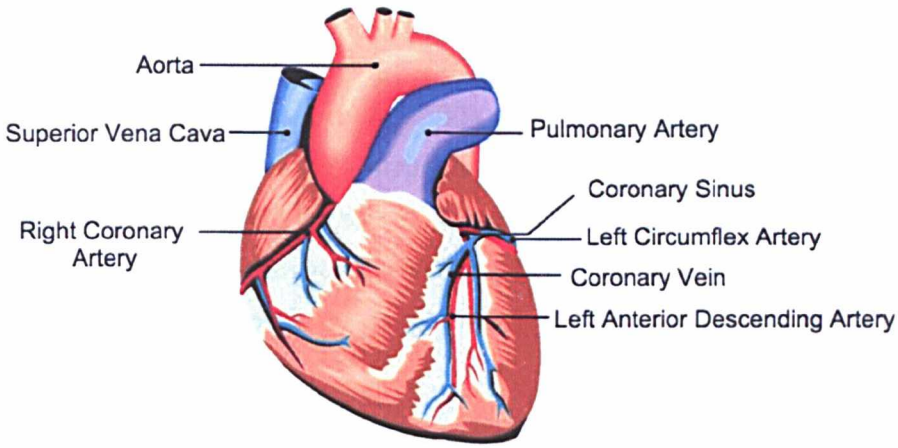

Figure 2.5 Anatomical locations of the major coronary arteries and the coronary sinus. The main coronary arteries are the right coronary artery (RCA), the left circumflex artery (LCX) and the left anterior descending (LAD). The RCA supplies the right side of the heart while the LCX and LDA supply the left side and the apex.

2.2 Coronary Artery Disease

Diseases of the heart and circulatory system (cardiovascular diseases or CVD), are the leading cause of death in the UK, accounting for about 238,000 deaths in 2002 alone [1]. The main forms of CVD are coronary artery disease (CAD) and stroke. About half of all deaths from CVD are from CAD. Coronary artery disease is caused by the blockage of one or more coronary arteries. The two main forms of CAD are myocardial infarction (MI), commonly known as heart attack, and angina. Almost all deaths by CAD are caused by myocardial infarction. Since myocardial infarction could be fatal, it is important to study its causes and consequences for the prevention, diagnosis and prognosis of the disease.

2.2.1 Perfusion

The heart is a highly oxidative organ that has a high demand for oxygen [17]. The oxygen consumption of the heart is about 8 ml/min/100g at rest and can go up to 70 ml/min/100g during heavy exercise. The oxygen supply to the myocardium is determined by two factors: coronary blood flow and the oxygen content of the blood. In general, the oxygen content of arterial blood changes relatively little. Therefore, the primary determinant of oxygen supply is coronary blood flow.

There is a unique relationship between myocardial oxygen consumption, coronary blood flow (CBF), and the extraction of oxygen from the blood (arterial-venous oxygen difference, AO_2 -VO_2). This relationship can be explained using the Fick Principle:

$$Myocardial\ Oxygen\ Consumption = CBF \times (AO_2 - VO_2) \tag{2.1}$$

Note that in this equation, $CBF \times AO_2$ is the oxygen supply to the heart.

At rest, myocardial oxygen extraction is nearly maximal, implying that coronary flow rate has to increase during exercise to keep up with the increased oxygen consumption. The amount of blood flow to the myocardium is regulated through the constriction and dilation of the coronary arteries by local regulatory mechanisms.

When blood flow to the myocardium is restricted (ischaemia), the oxygen supply/demand ratio is reduced, resulting in hypoxia. Hypoxia and ischaemia stimulate vasodilatation to allow increased coronary flow rates. In ischaemic regions due to stenosis or occlusion of epicardial arteries, collateral circulation may arise to increase blood supply. Collateral blood flow may be an important mechanism in limiting infarct size in the heart.

2.2.2 Atherosclerosis

The culprit of CAD is atherosclerosis, which is a progressive disease that typically begins in childhood and continues throughout life. During the process, deposits of fatty

substances, cholesterol, cellular waste products, calcium and other substances build up in the inner lining of the artery and subsequently become atherosclerotic plaques. This disease usually affects large and medium-sized arteries such as the coronary arteries. As plaques develop, they may gradually become large enough to start narrowing the artery and thereby reducing the blood flow through the artery. More damage may result when the plaque ruptures, exposing the blood to elements within the plaque that stimulate blood clot formation. This clotting process may be controlled by the body, which contains substances to dissolve clots, but may also lead to complete blockage of the artery. When a coronary artery is blocked acutely, it leads to inadequate blood supply to the myocardium causing ischaemia, resulting in an immediate loss of contractility in the affected region. When the artery is blocked for more than a few minutes, cell death starts to occur and it could lead to irreversible damage to the heart.

2.2.3 Myocardial Ischaemia

Ischaemic heart disease is currently responsible for about 14% of all deaths. Therefore, diagnosing myocardial ischaemia prior to heart attack is important. Ischaemia occurs when there is an imbalance between myocardial oxygen supply and demand [18]. It is usually brought by the disruption of the supply of blood and oxygen to the myocardium because of narrowing or obstruction of one or more of the coronary arteries.

When the imbalance is caused by an increase of myocardial oxygen demand by exercise, an excessive increase in heart rate, or emotion, it is referred to as demand ischaemia. Demand ischaemia is responsible for most incidents of chronic stable angina. On the other hand, when the imbalance is caused by a reduction of oxygen supply, it is referred to as "supply ischaemia". Supply ischaemia is frequently caused by increased coronary vascular tone or by platelet aggregates or thrombi, and is responsible for myocardial infarction and most cases of unstable angina. In many circumstances, ischaemia results from both an increase in oxygen demand and a reduction in supply.

Myocardial ischaemia can lead to myocardial stunning, hibernation and necrosis. Myocardial stunning refers to a condition when there is prolonged myocardial dysfunction with a gradual return of contractile activity. Stunning may occur following exercise-

induced ischaemia and coronary spasm. It affects both systolic and diastolic function and can occur in globally as well as the regionally ischaemic heart.

2.2.4 Myocardial Contractility

Contractility is associated with the heart's inotropic state, *i.e.* its contractile state. It is defined as the inherent capacity of the myocardium to contract independently of changes in the preload or afterload. Increased contractility means increased rate of contraction for reaching a greater peak force. Factors that could increase contractility include exercise, adrenergic stimulators, digitalis and other inotropic agents.

Contractility is usually measured using generalised quantities such as stroke volume, cardiac output and ejection fraction. Contractility is an important regulator of myocardial oxygen uptake because of the close link between myocardial oxygen uptake and the work done by the heart. Increases in the heart rate, preload or afterload will cause an increase in oxygen demand. The relationships between cardiac output, blood pressure and work done are given below:

$$\begin{aligned} \textit{Cardiac output} &= \textit{stroke volume} \times \textit{heart rate} \\ \textit{Work done} &= \textit{systolic blood pressure} \times \textit{cardiac output} \end{aligned} \tag{2.2}$$

In order to get a better understanding of contractility, it is necessary to understand what preload and afterload are. Preload is the load present before contraction starts at end-diastole. This value reflects the venous filling pressure that fills the atrium and consequently the left ventricle. If preload increases, the left ventricle becomes distended and stroke volume rises according to Starling's Law. At the same time, the heart rate also rises because the arterial mechanoreceptors are stimulated, thus causing an increase in the discharge rate of the sino-atrial node. These two effects contribute to an increase in cardiac output, which is the product of heart rate and stroke volume.

A direct measure of preload is the wall stress at end-diastole, which can be calculated using Laplace's Law given below:

$$\textit{Wall stress} = (\textit{pressure} \times \textit{radius}) \ / \ (2 \times \textit{wall thickness}) \qquad (2.3)$$

However, measurement of wall stress in vivo is difficult as simple measurements of LV radius ignore the complex anatomy of the left ventricle. From this equation, we can see that an increase in ventricular radius or pressure will results in an increase in wall stress, which in turn leads to increased myocardial oxygen uptake.

The afterload is the systolic load on the left ventricle after it starts to contract. Clinically, the arterial blood pressure is commonly used to represent the afterload. In a normal heart, the left ventricle is capable of overcoming any physiologically acute increase in afterload. However, chronically increased afterload caused by sustained arterial hypertension or significant stenosis will lead to LV hypertrophy.

The relationship between preload and afterload can be explained by using the Frank-Starling curve, which illustrates the link between preload and afterload. The Frank-Starling curve indicates that an increased LV volume (indicator of preload) leads to increased contractility, which in turn leads to an increase in systolic blood pressure and hence afterload. The Frank-Starling curve is obtained by combining Starling's Law, which states that stroke volume is directly related to end-diastolic volume, *i.e.* preload, and Frank's theory published in 1895, which states that the greater the initial LV volume, the more rapid the rate of rise, the greater the peak pressure and the faster the rate of relaxation.

2.2.5 Myocardial Infarction

Myocardial infarction (MI), commonly known as heart attack, is the term used for cell death due to a lack of oxygen supply to the myocardium [19]. The most common cause of myocardial infarction is atherosclerotic narrowing of the coronary arteries leading to inadequate blood flow and oxygen supply to the tissue. As mentioned above, the

immediate precursor to myocardial infarction is the rupture of an atherosclerotic plaque leading to the formation of thrombus over the plaque and hence, resulting in rapid occlusion of the coronary vessel.

Myocardial infarction can be fatal, if not treated promptly. The amount of myocardial injury varies with the severity of initial coronary occlusion. Although reperfusion therapy has proven to improve survival significantly, permanent or temporary decrease in LV regional function might result. On the other hand, injury may also occur in the conduction system and resulting in interventricular or atrioventricular heart block. Patients who have heart block will need temporary or permanent pacing.

Reperfusion therapy for acute myocardial infarction involves restoration of blood flow through an occluded coronary artery. Early reperfusion after myocardial infarction has been proven to preserve left ventricular function and improve survival. However, a significant number of patients have persistent occlusion of the infarct-related artery (IRA) late (days to weeks) after myocardial infarction because of ineligibility for thrombolytic therapy, failure of reperfusion, or reocclusion. Several observations have demonstrated an association between late (2-42 days) patency of the IRA and improved clinical outcome [20].

After reperfusion therapy, the injured myocardial territory can be divided into three regions according to the extent of myocardial ischaemia experienced during coronary occlusion. At the extreme periphery of the injured territory, myocardial cells may be protected from ischaemia due to prompt opening of the collateral vessels. In the region closer to the core of injury, myocardial tissues salvaged by reperfusion can be found. This portion of myocardium may exhibit decreased regional function such as myocardial stunning or varying degrees of cellular injury. At the very core of the infarcted region, profound ischaemia during coronary occlusion and reperfusion may result in collapse and occlusion of the microvasculature. This region of microvascular obstruction with impaired blood flow is termed as the no-reflow or low-reflow territory. The presence of microvascular obstruction predicts unfavourable post-infarction prognosis in patients who have sustained acute myocardial infarction. It was reported that LV remodelling is directly related to the magnitude of microvascular obstruction. However, it is not yet known how microvascular obstruction induces greater ventricular remodelling.

2.2.6 Ventricular Remodelling Following Myocardial Infarction

During recovery of myocardial infarction, changes in the topography of both the infarcted and non-infarcted regions of the ventricle may occur. These changes in left ventricular size, shape, and thickness are collectively referred to as left ventricular remodelling (LV remodelling) [21]. In general, LV remodelling represents an adaptive mechanism including LV enlargement, hypertrophy and distortion of regional and global geometry [22]. This remodelling process can greatly affect the function of the ventricle and the prognosis for survival. It is believed that limiting ventricular remodelling will improve ventricular function and the long-term outcome of patients who suffer from acute myocardial infarction. The two most marked changes in the remodelling process are infarct expansion in the infarcted region and ventricular dilation of the noninfarcted region.

2.2.7 Myocardial Remodelling

Myocardial remodelling refers to a consequence of structural and functional changes accompanied by molecular changes. It can be caused by ischaemic or non-ischaemic heart disease. The major form of myocardial remodelling associated with ischaemic heart disease occurs as a consequence of myocardial infarction.

In heart failure, there is a compensatory increase in blood volume that serves to increase ventricular preload and thereby enhance stroke volume by the Frank-Starling mechanism. The heart chambers then dilate to make room for this greater blood volume. This expansion can initially restore some of the heart's pumping strength because the more the muscle is stretched, the more forcefully it can contract. A dilated heart, in the long term, could lead to adverse effects such as reduced contractile function.

Dilated cardiomyopathy (DCM) is a form of myocardial remodelling associated with non-ischaemic heart disease. It is characterised by cardiac enlargement and systolic contractile dysfunction of one or both ventricles. In most cases of DCM, the exact cause remains unclear. It is likely that this condition represents a final common pathway that is the end result of myocardial damage produced by a variety of cytotoxic, metabolic, immunological, familial, and infectious mechanisms. For instance, myocardial damages caused by

excessive alcohol consumption, viral infection and pregnancy could present the same symptoms as those of DCM.

2.2.7.1 Infarct Expansion

In the early period after myocardial infarction, regional dilation of infarcted segments, also called infarct expansion, is observed. This process appears to be caused by a combination of slippage between muscle bundles, disruption of normal myocardial cells and tissue loss within the necrotic zone, and these lead to thinning and dilation of the necrotic zone. This process is best recognised by echocardiography as a lengthening of the noncontractile region. It has been observed to occur clinically as early as 3 days after infarction and may progress over days or weeks independent of additional myocardial necrosis or infarct extension. The degree of infarct expansion appears to be related to the pre-infarction wall thickness; it has also been reported that infarct size, infarct location, preload, afterload, and contractile pull from noninfarcted segments all impact on the degree of infarct expansion. Infarct expansion is associated with increased mortality and may be important in the development of late aneurysm formation. Infarction expansion seems to be more common in patients experiencing transmural infarctions involving the anterior-apical surface than other regions of the left ventricle. The anterior-apical region is particularly vulnerable to infarct expansion because it is the thinnest and has the most curvature.

2.2.7.2 Ventricular Dilation

Although infarct expansion plays an important role in the ventricular remodelling that occurs early following myocardial infarction, remodelling is also caused by dilatation of the viable portion of the ventricle, commencing immediately after acute myocardial infarction. This global dilation of the noninfarcted zone may be viewed as a compensatory mechanism that maintains the stroke volume in the face of a large infarction. However, ventricular dilatation is also associated with nonuniform repolarization of the myocardium that predisposes the patient to life-threatening ventricular arrhythmias [23].

In a study by McKay and colleagues [24], it was observed that the degree of dilation observed in noninfarcted regions was correlated to the size of the initial infarct and was not due to higher left ventricular filling pressures. Subsequent studies demonstrated that the late increase in heart size after anterior myocardial infarction is due to elongation of the noninfarcted segment, and not due to further infarct expansion. Although an increase in cavity size tends to restore stroke volume, a precarious balance can be exceeded in which increased cavity volume with insufficient compensatory hypertrophy results in loading conditions promoting further enlargement and dysfunction.

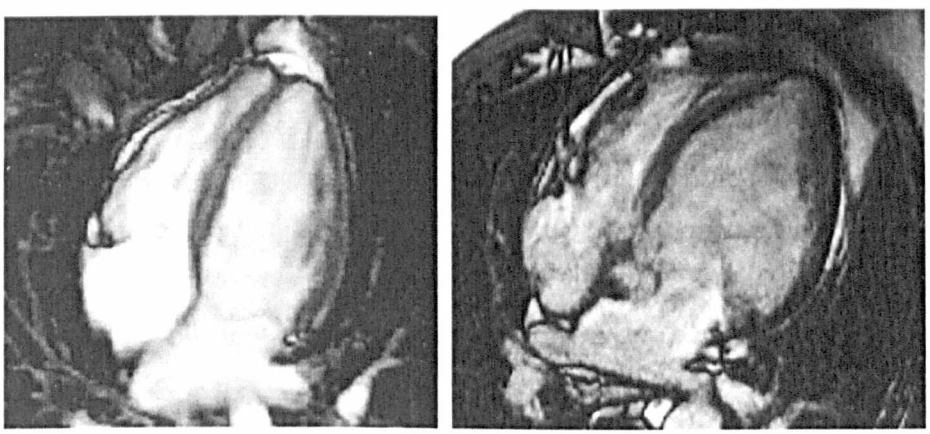

(a) (b)

Figure 2.6 A four-chamber view of the heart acquired using CMR in (a) a normal subject and (b) in a patient with a dilated LV due to ischaemic heart disease. The difference in LV volume and shape can be clearly seen.

2.3 Cardiac Imaging Techniques

2.3.1 X-Ray Imaging

Conventional X-ray imaging is based on the absorption of X-rays photons as they pass through different tissues of the body [25]. The amount of photons that pass through the patient depends on the x-ray attenuating properties of the tissues. A radiographic image is

created by the interaction of x-ray photons with a photon detector. The final image is therefore a 2 dimensional projection of the 3 dimensional distributions of the x-ray attenuating properties of all the tissues in the traversed paths. The contrast of the final image can be enhanced by increasing the amount of x-ray transmission. However, increasing the contrast also implies higher radiation dose to the patient, it is therefore important to get a balance between the amount of radiation and the image contrast. The primary limitation of X-ray imaging is that it can only produce planar images without depth information. Another important limitation is the exposure of the patient to harmful radiation.

Conventional X-ray imaging has been widely used in orthopaedics, dentistry and angiography whereas its application in cardiology is rather limited. In a typical chest X-ray image, which is the posteroanterior projection of the heart, the heart and other mediastinal structures appear as a featureless, opaque silhouette. Blood, myocardium, pericardium, coronary arteries and great vessels, valves, and mediastinal fat cannot be separated because they have similar radiographic attenuation characteristics, so that there is little or no contrast available to differentiate these structures. Although the four chambers are indistinguishable, the cardiac borders are clearly outlined and can be used for initial evaluation of the patient because any deviation from the normal configuration may suggest anomalies or functional disease.

Apart from the posteroanterior projection, other types of projections are also employed in clinical examinations. The lateral projection is used in the assessment of the left ventricular and atrial sizes, the right anterior oblique projection is used in examining the enlargement of right ventricular outflow tract and major pulmonary arteries and the left anterior oblique projection is useful for demonstrating dilation of the ascending aorta.

2.3.1.1 X-Ray Angiography

X-ray angiography is performed to image and diagnose diseases of the blood vessels of the body, including the brain and heart. Traditionally, angiography was used to diagnose pathology of these vessels such as stenosis. In cardiac examination, X-ray angiography is generally performed in conjunction with cardiac catheterisation, during which a catheter is

inserted and threaded to the target artery or the heart chambers. With this method, the oxygen concentration can be measured across the valves and septa of the heart so that pressures within each chamber of the heart and across the valves can be measured. In angiographic examination, the catheter is also used to inject contrast agents into the blood vessel. After the injection of contrast agents, a rapid sequence of X-ray images is taken to generate angiograms in real time.

X-ray angiography has been used in a range of clinical examinations. Coronary angiography is frequently performed to detect occlusion and identify thrombosis in the coronary arteries. During the procedure, physicians may also measure the coronary arterial pressure by attaching a transducer to the catheter. When applied to the thoracic aortic region, it allows the evaluation of aortic valve disease, thoracic aortic aneurysms and aortic dissection. Apart from imaging the arteries, X-ray angiography can also be used to image the ventricles. Left ventricular angiography is generally employed to evaluate acquired heart diseases such as ischaemia, valvular disease and cardiomyopathies, while right ventricular angiography is used for assessing right ventricular and tricuspid valve function.

2.3.2 Computed Tomography (CT)

Computed Tomography (CT), also known as Computerised Axial Tomography (CAT), is a computerised imaging technique that generates cross-sectional images of the body by combining several X-ray images. The basic principles of obtaining the cross-sectional images are the same as conventional X-Ray imaging, which is based on the absorption of x-rays photons as they passing through different tissues. In a CT scan, the X-ray beam interrogates only a certain part of the body that lies inside and parallel to the imaging plane. By combining the results from several X-rays, the depth information can be deduced and used to reconstruct the final image.

In practice, there are three main categories of CT systems: conventional CT, spiral (or helical) CT and electron beam CT (EBCT). CT scanning of the heart usually requires modification of the standard CT techniques. For the evaluation of thoracic aortic disease, pericardial disease, paracardiac and intracardiac tumours, and patency of coronary arterial bypass grafts, exposure times of less than 2 seconds are usually adequate. With Spiral CT

scanners, the exposure time can be further reduced with no interscan delay between images at sequential anatomical levels. This can produce images of the entire heart within a single breath-hold.

2.3.2.1 Electron Beam CT (EBCT)

In conventional CT and helical CT, the acquisition time is relatively long when compared to the cardiac cycle, hence their practicality in cardiac imaging has been limited. For many years, EBCT has been the only CT modality with sufficient temporal resolution to image the fast-beating heart [26]. Instead of using a mechanically rotating X-ray tube, EBCT scanner uses a focused electron beam that is successively swept across four cadmium tungsten target arcs at the speed of light. Each of the four targets generates a fan beam of photons that pass from beneath the patient to a bank of photon detectors arranged in a semicircle above the patient. With EBCT, a complete cardiac imaging can be completed in 50 ms without the need for ECG gating. Figure 2.7 illustrates an example EBCT images acquired at the level of aortic valve, also depicting some of the coronary arteries captured within the image.

The EBCT can be operated in three different modes: the cine mode, the triggered mode and the volume mode. The cine mode is used to assess global and regional myocardial function. The scans are obtained at an exposure time of 50 ms and at a rate of 17 scans per second. The triggered mode, used for flow analysis, employs a series of 20 to 40 successive scans in which each 50ms exposure is triggered at a specific phase of the cardiac cycle of successive heart beats or every other heart beat. From such a series of scans, time-density curves can be constructed for specific regions of interest in the cardiac chamber or myocardium, providing an estimate of transit time, perfusion, or blood flow. The volume mode provides eight scans by the use of all four target arcs in an imaging period of approximately 200 ms. These eight transverse scans can sometimes encompass the entire left ventricle and thereby provide an estimate of left ventricular volume and mass. Usually 10 to 12 tomographic levels are needed to cover the entire heart.

Because multiple images can be acquired at different levels, EBCT permits the acquisition of images at end-diastole and end-systole. Real-time sequential imaging is accomplished

within a single heartbeat at multiple levels, and these images can then be displayed in a close-loop cine format. EBCT has been widely used for calcium scoring as it can accurately identify calcium deposition in the coronary tree non-invasively. Coronary calcium is believed to be linked with coronary atherosclerosis but its reproducible use in clinical environment requires further investigation [27, 28]. The main advantage of CT is its high temporal and spatial resolution, whereas the primary limitation of CT is the exposure of patients to harmful radiation as prolonged exposure to radiation can induce a fatal malignancy in tissues [29].

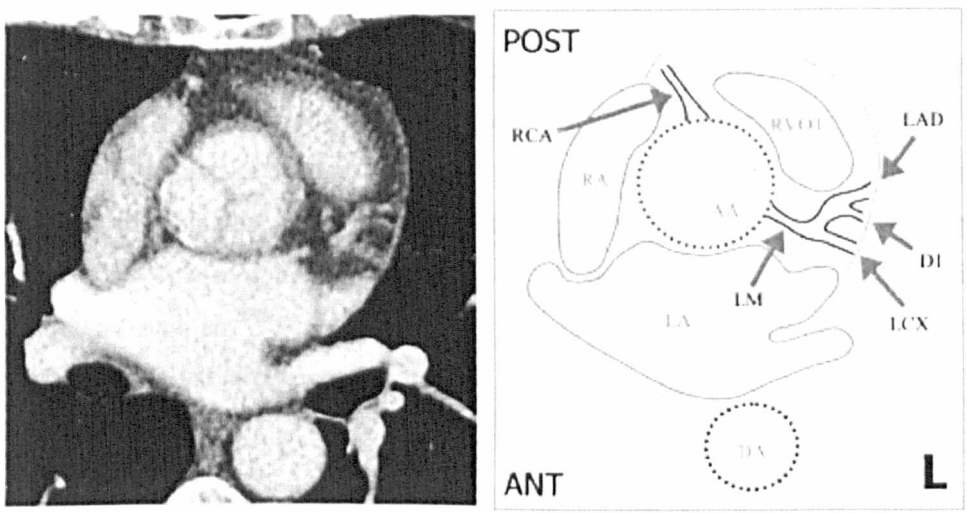

(a) (b)

Figure 2.7 The anatomical configuration of the major coronaries depicted by CT (a) and its corresponding schematic diagram (b) showing different anatomical landmarks within the region including ascending aorta (AA), proximal right coronary artery (RCA), left main (LM), left anterior descending artery (LAD) with first diagonal (D1) and left circumflex artery (LCX). In this figure, RA, RVOT, LA, and DA represent right atrium, right ventricular outflow track, left atrium and descending aorta, respectively. [Image courtesy P Horkaew and GZ Yang, Imperial College London, UK]

2.3.3 Nuclear Cardiology

In general nuclear medicine, planar imaging is the normal method of image acquisition. However, projectional imaging suffers from the disadvantage that it is difficult to separate the activity from overlapping structures [30]. The acquisition of multiple projections can ease this problem. This advantage, together with the great improvements in the performance of imaging hardware and reconstruction software, has lead to the widespread use of emission tomography in nuclear medicine.

2.3.3.1 Tracers & Emission Computed Tomography (ECT)

The idea of injecting a tracer into the blood stream and detecting its transit and distribution through the heart is well established. Tracers have been utilised in the quantitative measurements of blood flow for over a century. The earliest indicators are mainly non-radioactive matters such as dyes or hypertonic saline. The choice of tracers varies with the regions being imaged, the pathology and the scanner used for detecting the tracer. In relation to blood flow measurement using emission computed tomography (ECT), single-photon emitters such as ^{99m}Tc, ^{123}I, ^{201}Tl, and ^{111}In and positron-emitting isotope such as 11C, 13N, 15O, and 18F are frequently used.

Emission computed tomography (ECT) is the main imaging technique used in nuclear medicine. Unlike other imaging modalities such as magnetic resonance imaging (MRI), or X-ray, an ECT image gives a picture of organ function, but not strict anatomy [29]. This is because an ECT image depends on the detection of radionuclide (radioactive atoms) distribution inside the patient. These radionuclides are administered into the specific part of the body by using specific radiopharmaceuticals. A radiopharmaceutical is a protein or an organic molecule that has a radionuclide attached to it. Different radiopharmaceutical will be absorbed by different tissue in the organ.

In radionuclide cardiac imaging, the radionuclides are either extracted by the myocardium or remain in the cardiac blood pool. Several components are required to acquire gamma rays and to produce an image. These include a scintillation device such as the sodium iodide (NaI) crystal, which absorbs the gamma rays and generates photons that are converted to an electrical signal by photomultiplier tubes. The electrical signal is then

amplified and accelerated such that the energy of the gamma ray initially absorbed by the crystal is directly proportional to the height of the generated electrical pulse. Different radionuclides emit at different energies. This allows discrimination between photons from the target and scatter.

The main advantages of positron imaging are the ability to label and thus image biologically active compounds and drugs. A major advantage of the method is the ability to derive absolute quantitative measurements with the appropriate kinetic model [31]. However, by using this technique, the achievable spatial and temporal resolution is limited. In addition, it does not allow quantitative measurement of the dynamics of blood flow, such as velocity and strain, thus, limiting the general practicality of the technique.

There are two main categories of ECT: single photon emission computed tomography (SPECT) and positron emission tomography (PET). In SPECT imaging, conventional single-photon emitters such as ^{99m}Tc, ^{123}I, ^{201}Tl, and ^{111}In have several limitations. These isotopes decay with the emission of a single photon travelling in a random direction. The percentage of photons reaching the detector depends upon scatter attenuation and the distance between the photon source and detector. These factors result in a loss of relevant physiological information, which precludes accurate quantification of volumes and blood flow. In contrast, positron-emitting isotopes overcome these limitations, therefore making PET imaging more suitable for quantitative blood flow measurement [32].

2.3.3.2 Single Photon Emission Computed Tomography (SPECT)

Over the past several years SPECT acquisition has been predominantly used in cardiovascular nuclear medicine imaging. With SPECT, a series of planar images is obtained over a 180-degree arc around the patient's thorax. Transaxial images are recreated using a technique called filtered backprojection. These transaxial images are reconstructed into short axis and horizontal and vertical long axis orientations relative to the anatomical axis of the heart. The overall result is an improvement in anatomical resolution and contrast. Alternatively, SPECT imaging requires more attention to detail with regard to the parameters set for acquisition and more stringent quality control measures.

Recently, gamma cameras with multiple detector heads have been developed. These systems have improved electronics and count sensitivities, which improve image resolution and decrease SPECT imaging time. The optimal detector configuration is two camera crystal heads separated by 90 degrees. Because two camera heads are used simultaneously, the full 180-degree orbit may be required, with only a 90-degree motion resulting in half the acquisition time. Optimal 360-degree acquisition may be performed with triple head systems, in which each head is separated by 120-degrees. The increased count sensitivity of these detectors allows high-resolution collimation and improved image quality and quantification.

A significant limitation of traditional single-photon imaging is inhomogeneous attenuation of radiation by soft tissue. Attenuation artefacts are most commonly located in the anterior wall owing to breast or chest wall attenuation or in the inferior wall due to diaphragmatic attenuation. Attenuation correction systems currently are under clinical investigation. Another problem with SPECT imaging is patient motion. Motion correction software has been developed but as yet is not widely used clinically. Finally, scatter photons are a major source of degraded image quality. Scatter correction signifies a major improvement of radionuclide image quality.

The main application of SPECT in cardiology is myocardial perfusion imaging. The regional distribution of myocardial perfusion can be visualised using radiopharmaceuticals that accumulate proportional to regional myocardial blood flow. The most important clinical application of myocardial perfusion imaging is in conjunction with stress testing for the evaluation of ischaemic heart disease. Another main application of SPECT is myocardial infarct imaging.

2.3.3.3 Positron Emission Tomography (PET)

Positron emission tomography (PET), long viewed as primarily a research imaging modality, is currently becoming a clinically important technique [33, 34]. The uniqueness of PET imaging lies in its ability to image and quantify metabolic processes, receptor occupancy, and perfusion.

PET imaging begins with the injection of a metabolically active tracer-a biological molecule that carries with it a positron-emitting isotope (for example, 11C, 13N, 15O, or 18F). Within minutes, the isotope accumulates in an area of the body for which the molecule has an affinity. Positron-emitting radionuclides are characterised by excess protons. This unstable structure results in the conversion of an excess proton to a neutron, which in the process, a positron (antielectron) is emitted. The positron travels a few millimetres in tissue and when it encounters an electron, annihilation ensues. This results in the release of a pair of photon with characteristic energy of 511 keV. These two photon gamma rays travel away from each other in near opposite direction. Using detectors that are paired and aligned, the photon pairs emitted from the positron annihilation can be detected by coincidence counting.

PET imaging utilizes 1200 to 1500 small stationary crystal/detectors arranged in a circle, allowing photons to be detected in coincidence. This principle allows the correction of body attenuation by using electronically, not structurally, collimated data. These factors result in better count statistics and the ability to quantify various metabolic processes. With the present technology, up to 21 simultaneous tomographic slices may be obtained, allowing reconstruction along cardiac planes similar to those displayed in cardiac SPECT imaging.

The major clinical applications of PET have been in cancer detection of the brain, breast, heart, lung and colorectal tumours. In cardiology, PET studies are recommended for the identification of myocardial viability in patients with established coronary artery disease and regional or global left ventricular dysfunction. It is also frequently used for non-invasive diagnosis of coronary artery disease. Other readily available imaging alternatives have limited PET application for these indications. These include conventional perfusion imaging, reinjection thallium imaging, and the development of new classes of ^{99m}Tc-perfusion agents. Although ^{201}Tl and PET both have high accuracies for predicting recovery of regional and global left ventricular dysfunction after revisualisation, PET has a higher positive and negative predictive accuracy for improvement in left ventricular function and is considered the gold standard for detection of viability.

2.3.4 Echocardiography

The basic principles of ultrasound imaging rely on the fact that ultrasonic waves are reflected, in the form of echoes, when they encounter a change in density in their path and these reflected echoes can be measured and used to produce an image [29]. In ultrasonic imaging, a transducer generates bursts of ultrasonic waves that are sent into the body. In a homogenous medium, the ultrasonic waves travel in a straight line without a change of direction, whereas at an interface of two media with different acoustical impedance, the waves reflect and refract in a similar fashion to light. The degree of reflection and refraction depends on the difference in acoustical impedance at the interface. Although acoustical impedance is the product of the density of the object and the velocity of sound through that object, for all practical purposes one can consider the acoustical impedance to be a function of density. The reflected waves are detected by the transducer which then sends the echo signals to the amplifiers and the signal processing unit for image reconstruction.

Echocardiography (cardiac ultrasound) is a valuable non-invasive tool for imaging the heart and surrounding structures. Three types of echocardiography are commonly used clinically: M-mode, two-dimensional (2-D B-mode), and Doppler. The M-mode echocardiogram provides a one-dimensional view (depth only) into the heart. 2D echocardiography is a relatively complicated technique. To produce a continuous cross-section image, a B-mode echocardiograph is systematically traced across a sector field at a sufficiently high rate. This approach allows a plane of tissue (both depth and width) to be imaged, thus the orientation and anatomic relationships between various structures are easier to appreciate than that with M-mode images. On the other hand, Doppler echocardiography can be used to measure blood flow velocity, thus allowing the evaluation of blood flow patterns, direction, and velocity profile. This technique has become an important tool in blood flow measurement [35-37]. Figure 2.8 illustrates an example of 3D echocardiographic images showing the parasternal long axis and apical short axis views of the mitral valve of a normal subject.

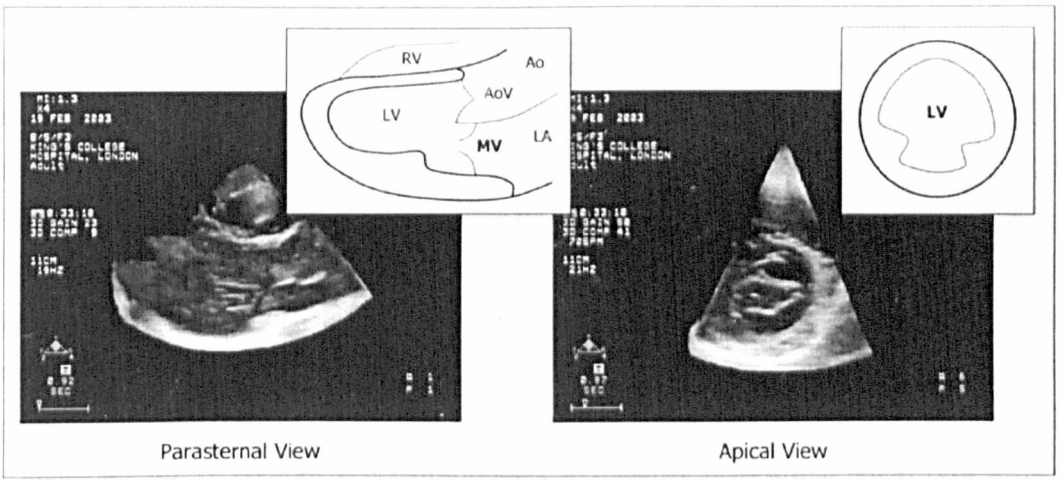

Figure 2.8 An example of 3D echocardiographic images showing the parasternal long axis and apical short axis views of the mitral valve of a normal subject. The images were acquired with a SONOS 7500 scanner, Phillips Medical Systems. [Image courtesy P Horkaew and GZ Yang, Imperial College London, UK]

The advantages of echocardiography are numerous. The examination is painless and it is less costly than other sophisticated imaging techniques. In addition, the required equipment is portable making it the choice of bedside imaging modality. However, some technical difficulties exist that require expertise on the part of the examiner and interpreter of the images. The main problem is posed by the poor transmission of ultrasound through bony structures or air-containing lungs. The examiner must therefore try to avoid these structures. In Doppler echocardiography, in particular, the image quality relies heavily on the skill of the examiner as the direction of incident wave must be carefully aligned in order to obtain accurate measurement.

2.3.4.1 Contrast Echocardiography

Contrast echocardiography is a technique where a contrast agent containing microbubbles is rapidly injected into a peripheral vein or selectively into the heart. This technique makes use of the characteristic that ultrasound is extremely sensitive to intravascular bubbles. The microbubbles move with the blood stream and generate a cloud of tiny echoes on the echocardiogram. Contrast echocardiography is a very sensitive technique for detecting right-to-left shunts. The contrast agents that have been used include the patient's blood, saline, indocyanine green dye, agitated or sonicated angiographic contrast agents, and sonicated albumen. In all cases the contrast effect originates from suspended microbubbles in the fluid. The potential clinical uses for contrast echocardiography are numerous which includes the use of contrast echocardiography to quantify myocardial blood flow through the destruction of microbubbles administered with a constant rate venous infusion, as shown in Figure 2.9 [38].

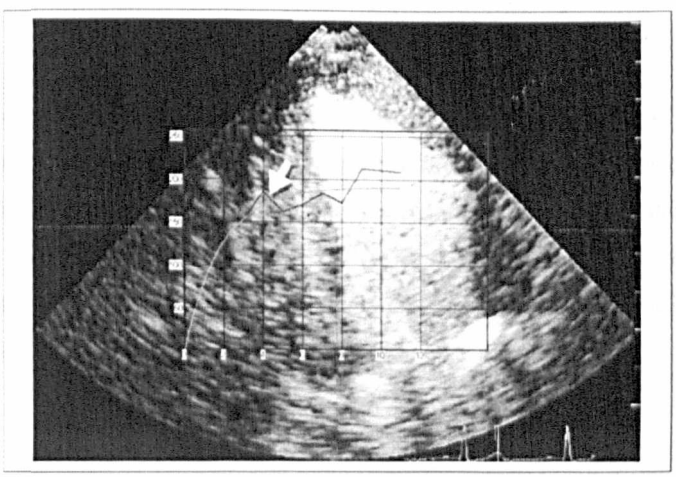

Figure 2.9 An example of perfusion echocardiography showing the uptake of the microbubble contrast agent into the myocardium. The curves superimposed show the recovery of the signal at the septum [Image courtesy of GZ Yang, Department Of Computing, Imperial College London, UK].

2.3.4.2 Doppler Effect & Doppler Echocardiography

Doppler effect is the variation in the frequency of the wave due to relative motion between the observer and the source of the wave [32]. The observed frequency increases if the source is moving towards the observer and vice versa. Based on this property, one can apply the Doppler effect in ultrasonic imaging to detect movement of scattered substances, usually red blood cells, by the analysis of the change in frequency of the returning echoes and hence obtain information of the blood flow velocity. This technique is referred to as Doppler echocardiography. In general, the transducers that emit and receive ultrasound waves are kept stationary whereas the reflector is moving.

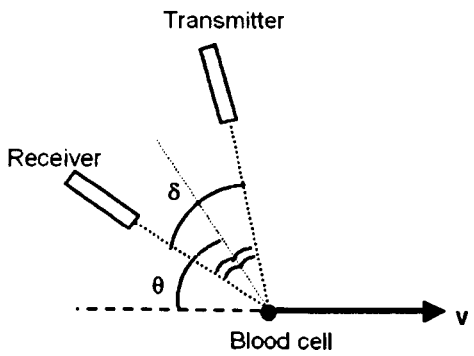

Figure 2.10 Principle of Doppler ultrasound imaging. Sound waves emitted from the transmitting transducer hit the moving reflector, the blood cell, at an angle. The frequency of the reflected beam is recorded by the receiving transducer and the Doppler equations can be used to calculate the velocity of the blood cell. v is the reflector's velocity, θ is the angle between the bisector of the transmitter and receiver beams and the direction of the movement, and δ is the angle between the transmitted and received waves.

The relationship between the shift in frequency and the velocity of the moving observer can be written as follow:

$$f_d = \frac{-2vf_0 \cos\theta \cos(\delta/2)}{c} \tag{2.4}$$

where v is the reflector's velocity, f_0 is the transmitted frequency, c is the speed of ultrasound, θ is the angle between the bisector of the transmitter and receiver beams and the direction of the movement, and δ is the angle between the transmitter and receiver beams as illustrated in Figure 2.10. Thus, if the movement of the reflector is away from the transducer, *i.e.*, positive, the shift in frequency is negative, *i.e.*, it becomes lower. The angle between transducer and receiver is usually small enough to reduce the expression to:

$$f_d = \frac{-2vf_0 \cos\theta}{c} \tag{2.5}$$

It should be noted that if $\theta = 90°$, there is no Doppler shift. So to measure the velocity of the reflector accurately, which in the case of blood is the red blood cell, the transducer should be in line with the blood vessel of interest and/or the angle between the vessel and the transducer should be known.

Two types of Doppler echocardiography are used clinically: pulsed wave and continuous wave, each has its advantage over the other. Pulsed wave systems use the same transducer to send and receive short bursts of ultrasound waves whereas continuous wave systems use separate emitters and receivers so that ultrasound waves can be simultaneously and continuously sent and received. Using pulsed wave systems, blood flow velocity, direction and spectral characteristics from a specified sample in the heart or blood vessel can be calculated. This is not feasible in a continuous wave system because sampling of blood flow velocity and direction occurs along the ultrasound beam, not in a specified area. Nevertheless, the advantage of a continuous wave system is that the maximum measurable velocity is not limited, unlike that in a pulsed wave system because the pulse repetition frequency is limited.

In clinical practice, pulsed wave Doppler technique is usually combined with 2D echocardiography to incorporate anatomical information with flow information to generate colour-coded flow images as shown in Figure 2.11. This combined technique, referred to as Colour Doppler flow imaging, facilitates the examination of flow patterns in the cardiac chambers and the major arteries. For instance, velocity gradient and turbulent flow can be highlighted and therefore, more easily spotted [39]. Clinical applications of Colour Doppler flow imaging are not limited to the examinations of blood flow patterns, potential applications in oncological imaging and gynaecological imaging have also been reported. In oncological imaging, it has found to be valuable in investigating breast lesions, prostrate cancer, ovarian cancer and detecting metastases [40, 41]. In gynaecological imaging, this technique is employed to examine the uterine and ovarian blood flow [42].

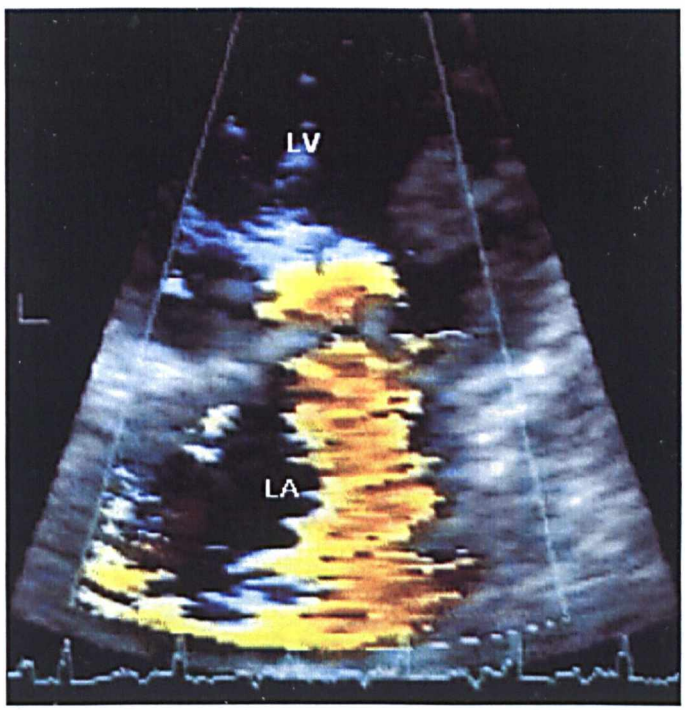

Figure 2.11 Colour Doppler image of a patient with mitral valve regurgitation. LV is the left ventricle and LA is the left atrium. The blue is blood flowing into the LV while the orange is the regurgitant flow back into the LA. [Image courtesy Dr P Nihoyannopolous, Department of Clinical Cardiology, Hammersmith Hospital, Imperial College London, UK]

2.3.5 Cardiovascular Magnetic Resonance (CMR)

Magnetic resonance (MR) is a rapidly developing diagnostic imaging modality in medicine. It is non-invasive and it offers a multitude of tissues parameter measures that are controlled by the user. The principles of magnetic resonance were first discovered by Block and Purcell in 1946, and the use of MR for diagnostic imaging was first suggested in 1973 by Lauterbur. Since then, extensive development of magnetic resonance imaging (MRI) has been achieved in the clinical world.

Traditionally, cardiovascular magnetic resonance (CMR) is used mainly for studying cardiac anatomy. In recent years, it has been more widely used to assess cardiac function. CMR can be used to obtain images of the heart in any plane. To effectively evaluate a specific structure or function of the heart, the imaging plane has to be carefully chosen to suit the purpose [43]. The basic imaging planes can be grouped into: 1) planes oriented with respect to the heart, such as horizontal and vertical long axis and short axis, and 2) planes oriented with respect to major axes of the body, such as transaxial, sagittal, and coronal planes. Cardiac oriented planes, as shown in Figure 2.12, are essential for evaluation of cardiac chamber size and function. Whereas imaging planes oriented with respect to the principal axes of the body are useful in the evaluation of the aorta, pericardium and anterior right ventricular wall.

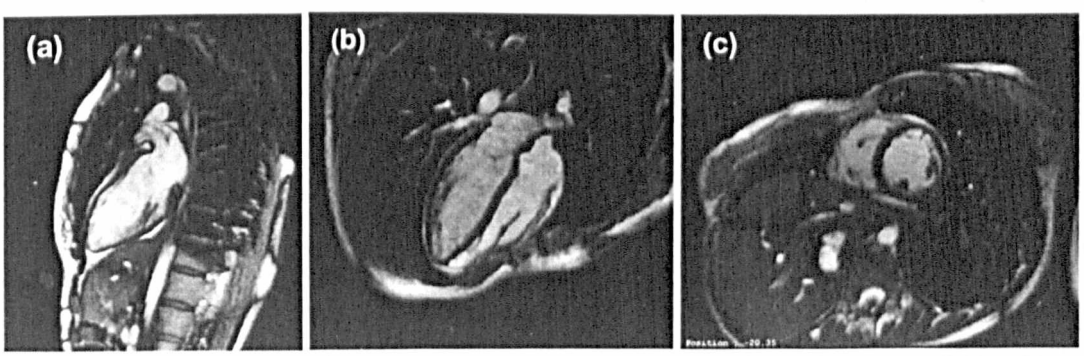

Figure 2.12 Cardiac oriented imaging planes. (a) VLA: vertical long axis view. (b) HLA: horizontal long axis view. (c) SA: short axis view.

2.3.5.1 Basic Principles

In clinical MRI, the MR signal originates from the hydrogen nuclei H^+ that exist in water and fat in human body [44]. Because of the high concentration of hydrogen atom in the human body, even a weak magnetic resonance signal can be detected and used to create an image. MR active nuclei are characterised by their tendencies to align their axis of rotation to an applied magnetic field [45]. The physical property responsible for this alignment is a coupling between the magnetic moment of the charged, spinning nucleus and the applied magnetic field.

When these nuclei are subjected to an external magnetic field B_0 (Z-direction), the spins align with this magnetic field and precess at the Larmor frequency ω_0 defined by the Larmor equation:

$$\omega_0 = \gamma \cdot B_0 \tag{2.6}$$

where γ is the gyromagnetic ratio which is a constant value that depends on the charge and mass of the nucleus. In this state, the spins are precessing out-of-phase in the transverse plane, resulting in zero transverse magnetisation. To make the spins to precess in a coherent manner, a weak magnetic field oscillating at the Larmor frequency is applied perpendicular to the main magnetic field. In practice, this is achieved by generating a polarised radio-frequency (RF) excitation, usually referred to as the RF pulse, by placing a circular coil in the transverse plane. When the RF pulse is turned off, the spins begin to precess out of phase and go back to their equilibrium position and emit radio signals which can be detected and processed to generate images.

To create an MR image, we need to localise the MR signal and acquire the spatial information at the same time. This can be achieved by applying orthogonal gradient fields in the x, y and z direction and reconstructing by fast Fourier transformation (FFT). Gradient fields are achieved by additional coils in the MR scanner, which generate these spatially varying magnetic fields. Details on the physics of MR and explanations on MR image formation can be found in [25, 29, 44, 45].

A number of common artefacts related to CMR are known to cause complication in interpretation of the images. These artefacts relate primarily to the basic features of CMR, they are: cardiac and respiratory motion artefacts, metal artefact and chemical shift artefact. Cardiac and respiratory artefacts result from the relatively long acquisition time of CMR. These problems are inevitable but should be recognised and minimised if possible. Metal artefact appears when pieces of metal are present on or in the body during the scan because metal can alter the local magnetic field, leading to distortion and local signal loss. Chemical shift artefact occurs because the hydrogen nuclei in fat see a slightly different magnetic field than hydrogen nuclei in water. This leads to signal cancellation at interfaces of water and fatty tissues.

2.3.5.2 Assessment of Cardiac Function

The evaluation of cardiovascular disease is critically dependent on the assessment of cardiac function. CMR provides highly accurate and reproducible assessments of global and regional cardiac function and is being recognised as the gold standard for the non-invasive evaluation of cardiac function [46].

The assessment of global ventricular function of the left ventricle is based on measuring changes in end-diastolic and end-systolic (ES) volumes. Accurate measurement of ventricular volumes can be obtained using Simpson's rule. A stack of contiguous images encompassing the entire left ventricle is acquired and the ventricular volume can be calculated by summing the endocardial areas multiplied by the distance between the centres of each slices [47]. Other global function can also be measured directly or indirectly with CMR. Stroke volume can be readily calculated by subtracting the end-systolic volume from the end-diastolic volume. Cardiac output can be easily computed by multiplying the stroke volume by the heart rate. The mass of the left ventricular wall can be estimated by measuring the volume of the myocardium and multiplying it by the specific gravity of myocardium. Assessment of valvular function, on the other hand, involves evaluation of morphology, motion, competence and effects on ventricular function. The use of CMR in this aspect is limited due to high spatial resolution required to evaluate valve morphology.

2.3.5.3 Evaluation of the Effect of Myocardial Infarction

Reperfusion therapy after myocardial infarction can preserve left ventricular function and survival. However, it is difficult to determine if and when optimal reperfusion has occurred [48]. In addition, the assessment of the extent and transmurality of myocardial injury, and the detection of unresolved reversible components are also important to determine the risk of remodelling. Recent developments in CMR have enabled improved assessment of different types of myocardial injury caused by coronary occlusion. Combining CMR imaging techniques with contrast enhancement by paramagnetic agents facilitates the reliable measurement of infarct size both in experiment models and in patients [49]. In a CMR image, the reperfused infarcted myocardium is characteristically seen as an enhanced region on late imaging [50]. The accuracy of infarct size measurements by CMR has been confirmed in a number of studies that compare CMR with the histopathological gold standard of TTC method [51] and nuclear methods [52]. Following reperfusion therapy, the infarct core may experience the no-reflow phenomenon due to microvascular obstruction. This process can be assessed using contrast-enhanced CMR techniques, in which microvascular obstruction is visualised as a dark area within the infarcted area [53].

The ability to assess myocardial viability following acute reperfused myocardial infarction is also clinically important. A recent CMR technique combines 3D tagged imaging technique with dobutamine to quantify myocardial 3D deformation and strain. This approach was found to be accurate and precise and may be a more sensitive method for characterising viability [54]. Another technique is contrast enhanced CMR, in which the regions that exhibit delayed contrast hyperenhancement are identical to regions of irreversible injury whereas regions that do not hyperenhance are viable [51].

The ventricular remodelling processes subsequent to myocardial infarction are also well studied with CMR techniques. With the ability to obtain volumetric images covering the entire left ventricle, CMR is particularly suited for monitoring the changes in LV mass and volume during the remodelling process. The CMR measurement of LV mass after myocardial infarction has been validated with that obtained at autopsy [55]. CMR is also used to analyse wall thickening and myocardial motion of the left ventricle.

2.3.5.4 Blood Flow Velocity Measurement using MRI

An important feature of MR is its sensitivity to motion, and this feature allows the measurements of velocity and vessel flow without the constraints of Doppler methods. The use of magnetic resonance image (MRI) for measuring blood flow was first suggested by Singer in 1978 [56]. Since then, a number of methods have been developed for blood flow measurement. These methods generally fall into two main categories: time-of-flight methods and phase shift methods. The basic principles of both methods are briefly described in the following chapter. The main goals of applying MR techniques in imaging flow are twofold; the first goal is to acquire quantitative flow measurements. The second aim is to understand the flow pattern because this appearance gives important information for the diagnosis of a particular disorder.

Time-of-flight methods involve the labelling of a specified portion of flowing fluid and detecting its motion after a fixed period of time [57]. There are two categories of time-of-flight techniques. The first one is known as flow enhancement methods or wash-in/wash-out methods; it relies on the saturation or partial saturation of material in a selected slice being replaced by fully magnetised high-signal spins due to flow. The second one involves tagging a selected volume of blood and then imaging the motion of the tagged blood.

Phase shift methods are the most widely used techniques for quantifying blood flow. The underlying principle of phase shift methods is to cause flowing material to attain a phase shift that is related to its motion. In general, it is achieved by using a bipolar gradient pulse that consists of a positive magnetic gradient followed by an equal but opposite negative gradient in the direction of the flow. While the positive gradient is applied, both the flowing material and the stationary material will attain a certain frequency shift. When the gradient is turned off, the phases of both materials are equal. When the negative gradient is applied, the two materials are separated and therefore experience different magnetic field strengths and will respond differently. The stationary material takes up an equal but opposite frequency shift and returns its original phase, whereas the flowing material takes up an additional frequency shift depending on the distance it has moved and therefore attains a final phase shift dependent on this distance and hence its velocity. The two main approaches of using the phase shift to produce flow image are phase contrast velocity

mapping methods and Fourier flow imaging methods. Details of these two methods are discussed in the next chapter.

MR velocity imaging technique can be applied to examine a range of clinical conditions. It has been used to study blood flow in all the major blood vessels such as the thoracic aorta, pulmonary arteries and veins [58, 59]. The approach for measuring aortic flow is relatively straightforward. A set of velocity map images in which the grey scale indicates the velocity of motion in each voxel is obtained. Velocity is measured at each voxel across the vessel, integrated over the cross-sectional area of the vessel and then integrated over the cardiac cycle. Pulmonary artery flow can be measured using the same technique for measuring aortic flow. This is particularly valuable for patients with left-to-right intra-cardiac shunting. CMR provides the first method for the non-invasive measurement of absolute coronary artery flow. This method is similar to the phase contrast method used in the aorta. Although resting coronary flow is of interest, it does not always reflect minor stenosis. Thus, coronary flow under conditions of stress is also measured so that one can determine if flow increases normally.

MR velocity images can also be used to assess valvular disease such as mitral regurgitation by analysing regurgitant flow depicted by MR velocity mapping [60-62]. Another important clinical application is the assessment of flow patterns in the cardiac chambers, in particular, the left ventricle [15, 16]. It has been shown that the flow patterns exhibit significant differences in normal and dilated ventricles.

Apart from deriving flow patterns or velocity profile directly from the measured flow velocity, studies have shown that it is feasible to assess vessel compliance by estimating the pressure from the blood flow velocity. One technique calculates pressure by considering the vessel compliance and the flow pulse waveform [63, 64]. Another technique uses the Navier-Stokes equations to compute the flow pressure fields from the acquired velocity fields [65, 66].

The major advantage of using MR for blood flow measurement is that the measurement process does not interfere with the flow. Moreover, it is non-invasive and flexible, allowing images to be taken in any selected plane. More importantly, the ability to acquire 3D flow images is unique to MR, making it an unparalleled clinical tool for acquiring detailed flow data. The main drawback of the MR technique, however, is that the equipment is expensive and requires dedicated space in hospital. Also, the acquisition time is relatively long compared to other techniques, and in some acquisition procedures patients are required to hold their breath to reduce artefacts caused by respiratory motion. This drawback, which maybe particularly unbearable for patients, can be overcome by applying retrospective gating techniques, by using respiratory gating and by using rapid MR imaging techniques such as echo planar imaging (EPI) and spiral imaging. These rapid imaging techniques are important clinical tools and they will be discussed in further detail in the next chapter.

2.4 Conclusions

The heart is a vital organ in the human body. The four main chambers, the left and right atria and the left and right ventricles, work together to pump blood round the body through the systemic and pulmonary circuits. The heart itself receives blood supply through the coronary circulation. Coronary artery disease is the main culprit of heart diseases, which is caused by atherosclerosis that leads to narrowing or obstruction of one or more coronary arteries. As the blood supply reduces, myocardial ischaemia may occur. Myocardial infarction can follow when an artery becomes completely blocked. Myocardial infarction can lead to permanent damage to the myocardium and the conduction system. If not treated promptly, it could be fatal. Previous research has shown that following myocardial infarction, the left ventricle could undergo a remodelling process that involves morphological changes of the left ventricle. This ventricular remodelling process may further affect cardiac function. Myocardial remodelling can also be associated with non-ischaemic heart disease such as dilated cardiomyopathy and heart failure. In general, the remodelling process involves topological changes characterised by the dilation of one or both ventricles as well as functional changes such as reduced contractility.

With the recent advances in medical imaging, a wide variety of cardiac imaging modalities are available for assessing cardiac function and monitoring the progress of disease. They include X-ray, electron beam computer tomography (EBCT), positron emission tomography (PET), single photon emission computer tomography (SPECT), ultrasound imaging and magnetic resonance imaging. X-ray radiography has very limited use in cardiac study, apart from delineating the cardiac boundary. X-ray angiography is an invasive technique which carries a certain risk of patient mortality and morbidity, but the resolution details it can depict still surpasses any of the competing techniques. Clinically, SPECT is one of the most widely used techniques for myocardial perfusion imaging but its role is being increasingly challenged by CMR. The main advantage of PET is its quantification ability in measuring the concentration of injected tracers in the blood stream, thereby enabling the calculation of blood flow in volume/time/mass.

CMR is a versatile technique with extensive routine clinical applications. It can be used to assess both the morphology and the global and regional ventricular functions. CMR has proven to be an accurate and effective technique in the assessment of heterogeneity of myocardial infarction. It has been readily used to measure infarct size and detect microvascular obstruction, both of which are important in identifying the prognosis of patients. CMR also supports techniques for accessing myocardial viability and is particularly well suited for monitoring the remodelling process subsequent to myocardial infarction.

An important feature of MR is its sensitivity to motion, and this feature allows the measurements of velocity and blood flow without the constraints of alternative methods such as Doppler Ultrasound. With MR velocity imaging, flow velocity can be measured with high spatial and temporal resolution in any imaging plane without affecting the blood flow itself. In addition, MR flow imaging has the unique advantage of acquiring 3D flow data, making it ideal for collecting detailed in-vivo blood flow data. A further advantage is that detailed and accurate anatomical data is available using MR, which allows the investigation of variations in functional indices in relation to morphological changes in disease. The unique features of MR velocity imaging have enabled in-depth analysis of blood flow dynamics. MR velocity imaging has been applied in many clinical applications, ranging from flow patterns analysis to the assessment of vessel compliance. In particular, it facilitates a comprehensive study of flow patterns in the ventricle, thus permitting the

establishment of the link between the topological changes of the ventricles and the blood flow patterns. In the next chapter, we will discuss the basic principles of MR flow imaging and its recent technical advances.

Chapter 3

MR Flow Imaging

3.1 Introduction

The potential of using nuclear magnetic resonance (NMR) to measure blood flow has been discussed for many years. As early as 1959, Singer studied NMR relaxation time due to flow and suggested that NMR could be used as a non-invasive tool to measure in vivo blood flow [67]. Early methods of using NMR for measuring blood flow velocity, however, were of little practical value because of unknown accuracy. In 1978, the idea of mapping blood flow measurements onto MR images was first proposed [56]. Since then, extensive research has been conducted and MR velocity imaging now plays an important role in providing in-vivo blood flow information in both clinical and research settings.

3.2 Methods of MR Flow Imaging

3.2.1 Time-of-Flight Methods

There are two categories of time-of-flight techniques: washin/washout methods and tagged time-of-flight methods. Washin/washout methods are also known as flow enhancement methods. In essence, these methods rely on the saturation or partial saturation of material in a selected slice being replaced by fully magnetised high-signal spins due to flow. The principle of this method is illustrated in Figure 3.1. The second one involves tagging a selected volume of blood and then imaging the motion of the tagged blood. The main advantage of the time-of-flight method is that only one image is required whereas the phase velocity method usually requires a separate reference image for removing the reference phase shift.

3.2.1.1 Washin/washout method

Depending on the flow velocity, slice thickness, slice profile and sequence repeat time, flow through the imaging plane during a pulse sequence replaces some or all of the material in the selected slice. This principle underlies two categories of washin/washout methods: 1) by preceding each phase-encoding step with a slice selective saturation band perpendicular to the flow and a washin delay, and 2) by using fast repetition gradient-echo sequences which saturate stationary spins.

Singer and Crooks [68] adopted the first method with a spin-echo sequence to image blood flow in the brain. This method, however, has a major drawback as the highest velocity that can be measured is limited by signal loss caused by intra-voxel flow dephasing [69]. The second method involves the use of shorter gradient-echo time in fast low flip angle short (FLASH) sequences and it reduces flow dephasing enough for imaging the wash-in enhancement of aortic blood flow. With this method, the fast gradient-echo sequence was repeated in a cine mode by exciting the same plane across the aorta. By using a high flip angle so that the signal was proportional to the fresh washin, the method was calibrated to give the intensity of fresh washin obtained at the end of each cine.

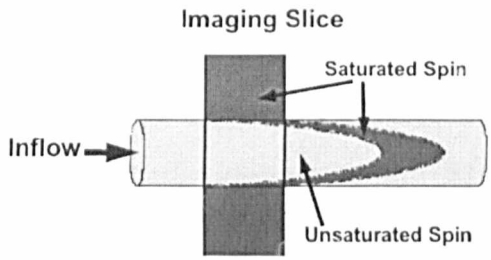

Figure 3.1 A schematic illustration of the washin/washout method. The unsaturated spin due to inflow gives more signal than the surrounding stationary spin in the imaging slice.

3.2.1.2 Tagged Time-of-Flight Approach

The first tagged time-of-flight approach was proposed by Feinberg, Crooks and Hownninger in 1984 [70]. Their method tracked the excited blood flowing in the slice selection direction. This was achieved by a dual spin-echo sequence in which the two 180° slices were offset but remain parallel to the 90° slice. The first 180° slice was displaced by one-third of the distance displaced by the second 180° slice. With this approach, the first echo image gives a good anatomical image whereas the second echo image gives high signal from the through plane flow that moves from the 90° slice to the second 180° slice in the time between the two RF pulses. Methods for visualising flow movement in one single image have also been described in a number of publications [57, 71]. These methods track in-plane flow, by applying frequency encoding in the same axis as slice selection, so that the movement of the tagged spins along this axis could be imaged and measured directly.

Another time-of-flight approach is to saturate a band of tissue and then follow the progress of this dark band in the orthogonal planes [72]. This is achieved by applying a 90° saturation pulse in a sharp-edged slice across the vessel before each phase-encoding step of a conventional gradient-echo sequence. A single saturation pulse is followed by a cine gradient-echo sequence with cardiac gating and the images obtained show motion of the saturated bolus down the vessel and hence, enable velocity waveforms to be obtained simply be measuring its position. The major drawback of this approach is signal loss due to T1 recovery and the spread-out of spins with different velocities. In addition, it is difficult to achieve high sensitivity for low velocities. Because of these limitations, tagging

methods have not been widely used in flow imaging but have been more successful in tracking myocardial motion.

3.2.2 Phase Flow Imaging Methods

Phase effects due to motion of excited spins along a magnetic field gradient were first observed by Singer in 1978 [56]. The first work on phase encoded velocity imaging was published by Moran in 1983 [73], which suggested the use of a bipolar velocity phase-encoding pulse with zero area to measure velocity. Soon after this theory was published, Bryant *et al* [74] described a method for measuring blood flow based on this theory in 1984. Since then, several methods for measuring blood flow were proposed.

Currently, the two principal approaches of using the phase shift to produce flow image are phase contrast velocity mapping methods and Fourier flow imaging methods. Phase contrast velocity mapping methods involve mapping the phase of the signal directly to measure flow, whereas Fourier flow imaging methods involve the use of a velocity phase encoding gradient to produce images with velocity information in one dimension. The underlying principles of both methods, however, are the same, *i.e.*, to cause the flowing material to attain a phase shift that is related to its motion. To illustrate this principle, a schematic diagram showing the phase shift due to the application of a bipolar gradient pulse to flowing material surrounded by stationary material is given in Figure 3.2. As mentioned in Chapter 2, the bipolar gradient pulse consists of a positive magnetic gradient followed by an equal but opposite negative gradient in the direction of the flow. While the positive gradient is applied, both the flowing material and the stationary material will attain a certain frequency shift. When the gradient is turned off, the phases of both materials are equal. When the negative gradient is applied, the two materials, now separated and therefore experiencing different magnetic strength, will respond differently. The stationary material takes up an equal but opposite frequency shift and returns to the original phase whereas the flowing material takes up an additional frequency shift depending on the distance it has moved. Therefore, the velocity can be determined by measuring the phase shift.

From the basic physics principle, the relationship between the phase of the signal and the flow velocity is given by:

$$\phi = \gamma \Delta A_g v \tag{3.1}$$

where ϕ is the phase of the signal, γ is the gyromagnetic ratio of H^+, Δ is the time between the centres of the two gradient pulses, A_g is the area of one gradient pulse and v is the velocity of the flowing material. Since γ, Δ and A_g are all constants for a particular imaging sequence the velocity can be calculated if the phase shift is known.

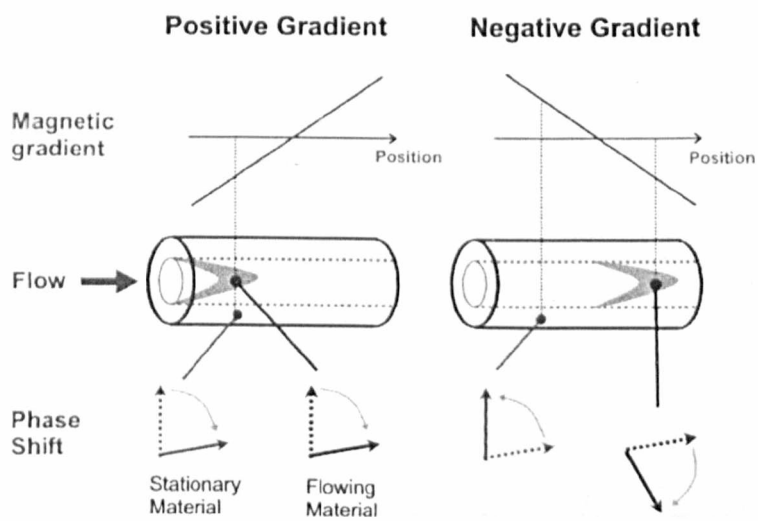

Figure 3.2 The principles of phase velocity encoding for a fluid flowing down a tube surrounded by stationary material using a bipolar gradient pulse. The bipolar gradient pulse consists of a positive and an equal but negative gradient. The positive gradient causes the same phase shift in both stationary and flowing material. Subsequently, the negative gradient causes the phase shift of the stationary material to return to zero. However, the flowing material acquires a phase shift related to its position and hence is directly proportional to its velocity

3.2.2.1 Phase Contrast Velocity Mapping

Early phase contrast velocity mapping methods were based on spin-echo sequences [74, 75], which are not ideal because of the signal loss problem due to shear and other more complex flows. It is also difficult to repeat the sequence rapidly because of the 180° pulse applied. These problems were reduced by the use of gradient-echo sequences. More importantly, this method is made more useful clinically by the introduction of velocity compensated gradient waveforms [76].

With phase contrast velocity mapping, two images are acquired with different gradient waveforms in the direction of desired flow measurement. The difference in the waveforms is calculated to produce a velocity-related phase shift between the two images, and a phase reconstruction is produced for each of the images. In order to remove phase variations that are not related to flow, the resultant images are then subtracted pixel by pixel to produce the final velocity map. Figure 3.3 illustrates a typical sequence diagram for a phase contrast GRE sequence.

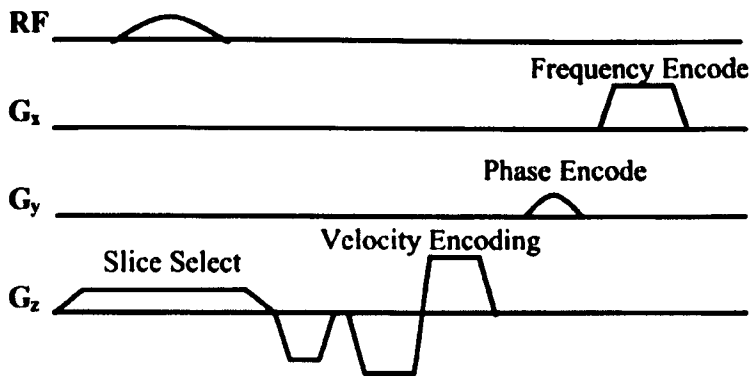

Figure 3.3 A schematic sequence diagram of through-plane velocity encoding sequence. The bipolar gradient pulse is played in the slice-select/through-plane direction. In practice, it can be played on the different axes to enable velocity mapping in all three directions.

In practice, velocity mapping can be accomplished in two ways, either two opposing bipolar gradients are used, or one reference scan without a bipolar gradient and a velocity encoded scan with a bipolar gradient. The first method requires six separate acquisitions to acquire three directions of velocity encoding. On the other hand, with the second method, only four scans would be required as the same reference scan can be used for all three directions. The advantages in using two opposing bipolar gradients is that the velocity sensitivity range is doubled and phase errors due to concomitant gradients are cancelled out during phase subtraction. If only one bipolar gradient is used, the scan time is much shorter but phase errors can become much more pronounced, especially at higher velocity sensitivities. Figure 3.4 shows example velocity maps in three orthogonal directions acquired with the phase contrast velocity mapping technique.

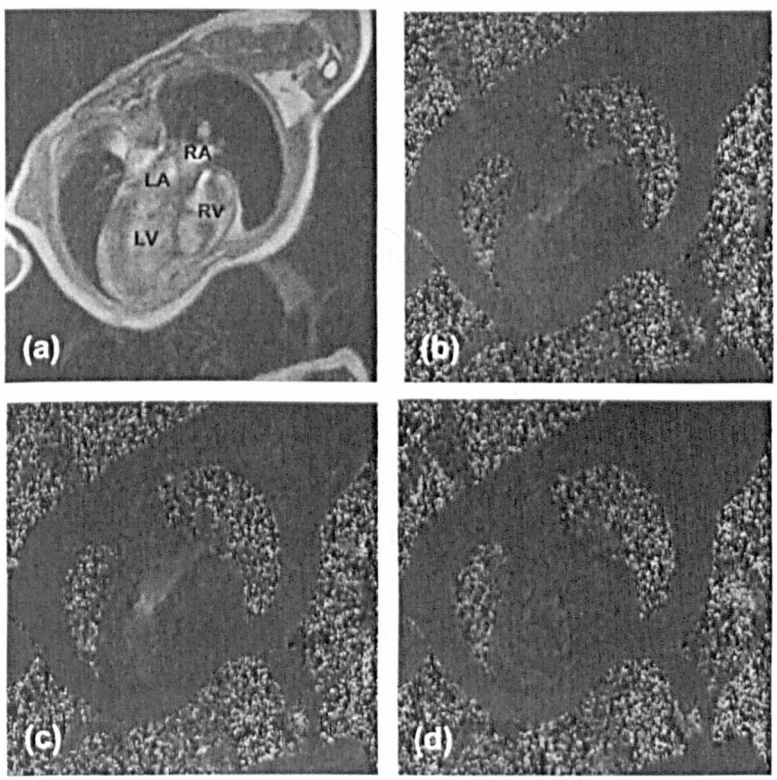

Figure 3.4 (a) An MR image showing the anatomy of four cardiac chambers (horizontal long axis view) of the heart. LV: left ventricle, LA: left atrium, RV: right ventricle, RA: right atrium. (b-d) The corresponding MR velocity maps represent the velocity along the x, y & z directions, respectively. The grey level in each velocity image is proportional to the velocity value and mid-grey represents zero velocity.

3.2.2.2 Fourier Velocity Imaging

Fourier velocity imaging methods encode flow velocity to generate an image with spatial information in one dimension and velocity information in another. This is achieved by replacing the spatial phase encoding gradient with a bipolar velocity phase encoding gradient that is stepped through a range of defined amplitudes [77]. In a typical Fourier velocity image, stationary materials are positioned in the centre whereas higher velocity materials are positioned towards the edge. In Fourier velocity images, each voxel contains information on all the velocity distribution and therefore partial volume effect is naturally avoided. On the other hand, in phase contrast velocity mapping, each voxel contains the average signal, which can be obtained much more rapidly when compared to that of Fourier velocity images. Because of the relatively long acquisition time, Fourier velocity imaging is more preferable when the range of velocity within a voxel is large, for example when assessing wall shear stress in large arteries.

3.3 Rapid Phase Flow Imaging Methods

With the advances in scanning hardware, it is now possible to acquire low-resolution images in a few hundred milliseconds or a high-resolution image in a single breath-hold by repeating a phase contrast velocity sequence rapidly. However, if the acquisition period per cardiac cycle is too long, the accuracy of the measurements and the temporal resolution for measuring pulsatile flows can be limited. On the other hand, if high spatial resolution is required, the cardiac motion of structures such as the coronary arteries can cause significant errors in the flow measurement. To this end, rapid flow imaging techniques and more efficient k-space coverage methods are being developed [45]. For phase contrast velocity mapping, the higher imaging speed was either accomplished by imaging only one spatial dimension or by combining a phase mapping approach with imaging methods such as single shot echo-planar and spiral imaging. In general, compromises in temporal or spatial resolution and signal-to-noise ratio have to be made but these methods have generally been shown to be accurate.

3.3.1 Sequences Leading to Rapid Phase Flow Imaging

3.3.1.1 FLASH phase velocity mapping

The simplest approach to rapid imaging is to reduce the time between RF pulses in a gradient-echo sequence with the shortest possible RF pulse and gradient-echo time. This sequence is known as the Fast Low flip Angle SHot imaging (FLASH) [78], the single shot version of this sequence can acquire an image containing 128 by 64 3mm to 4mm pixels in 300ms. FLASH imaging does not generally require special enhancement of the gradient system performance. Artefacts may occur if transverse magnetisation from previous RF excitations combine coherently, which can be difficult to predict in a long series of RF pulses. These artefacts can generally be avoided by using a low RF flip angle and extra gradient dephase pulses or a transmitter RF phase-shifting scheme. Variations of the basic idea of rapid RF pulse repetition by reusing the transverse magnetisation rather than discarding it are also widely used but these methods do not apply to flow imaging because of the accumulation of flow-related phase errors in the transverse magnetisation. One drawback of the FLASH method is that it cannot be combined with localised RF excitation approaches, which will be discussed later, for reducing imaging times.

When applied to cardiac imaging, flow and respiratory artefacts are reduced with the FLASH method but the contrast between blood and myocardium varies depending on fresh inflow and flow dephasing effects. In general, snapshot FLASH is not rapid enough and it does not generate sufficient resolution for accurate imaging of the moving ventricles. Therefore, a segmented version of FLASH [79] is used to obtain multiple phase-encode steps per cardiac cycle and to improve the resolution. The segmented FLASH technique can produce an image of 256 by 128 pixels with 1mm resolution. The k-space coverage of the sequence is designed so that changing signal amplitude or phase during each of the segments causes a gradual slope across the raw data in the phase-encoding direction. The amplitude of each signal during a segment tends to change with the decreasing longitudinal magnetisation, and an incrementing flip angle sequence is often employed to increase the flip angle during each segment in an effort to obtain the same or largest possible transverse magnetisation after each RF pulse [80].

Snapshot FLASH imaging has been used for phase velocity mapping [81] and in an iterative real-time mode with a colour velocity display superimposed upon an anatomical image. The segmented FLASH approach with segmented acquisitions as short as 50ms has been widely used in coronary artery velocity mapping due to its robustness [82]. However, it has been demonstrated that a maximum acquisition window of 35ms is allowed for avoiding cardiac motion related blurring. A long acquisition window results in both an underestimation of the peak velocity in pulsatile flow and a temporal broadening of the systolic velocity peak, hence causing overestimation of the total flow per cardiac cycle by segmented FLASH compared to conventional cine gradient-echo phase velocity mapping.

3.3.1.2 Echo-planar imaging (EPI)

Echo-planar imaging is a rapid gradient echo technique, in which an entire set of phase steps is acquired during one acquisition TR. This is accomplished by rapidly reversing the readout gradient. In single shot EPI, all of the raw data is obtained after a single RF pulse [83]. A single shot EPI sequence diagram is depicted in Figure 3.5. Early EPI work used a constant phase-encode gradient to cover a zigzag k-space path. The sequence is repeated with a reversed readout gradient and the final image is reconstructed by merging the echoes from parallel sections of the paths in the two data sets. Another technique called the Blipped Echo-Planar Technique (BEST) [84] uses a "blipped" phase-encode gradient to enable image reconstruction from a single readout by reversing the alternate echoes. However, this method suffers from a type of sampling artefact, known as the Nyquist, or N/2 ghost. This is because in EPI, adjacent lines in k-space are sampled under opposite readout gradients. If there is any misalignment in sampling, or differences in positive and negative gradients, then there is an alternate line modulation in k-space, which leads to a 'ghosting' of the image. Both of these early methods acquire only one half of the phase-encoding axis of the k-space and depend heavily on the main field uniformity for the validity of the assumed k-space conjugate symmetry. An improved method called Modulus BEST imaging (MBEST) [85] can be used to obtain a 2D-FFT image in a single shot. This is achieved by preceding the EPI acquisition with a k_y offset so that the k-space path returns through the centre. However, this method results in reduced SNR, increased T2* contrast and lower image resolution.

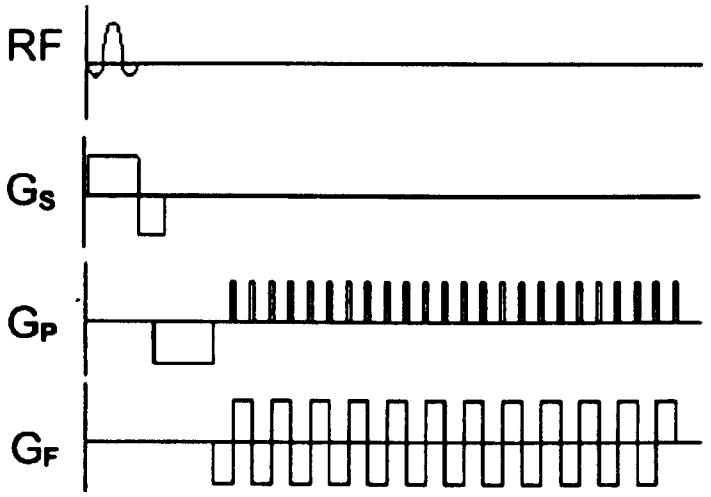

Figure 3.5 Schematic sequence diagram of an Echo Planar Imaging (EPI) sequence.

In general, single shot EPI is not suitable for cardiac imaging because myocardial T2* is so short at ~30ms, which can result in poor SNR and image distortions. However, this can be overcome by collecting only a few phase encoding steps per RF pulse excitation and repeat the process until the complete image is created. This process is called the segmented EPI technique and it has been widely used to perform rapid volumetric imaging of the heart and real-time imaging of cardiac contraction. In general, flow artefacts in EPI other than signal loss are ignored. There are various ways of segmenting the k-space. In Fast Fourier Imaging [86], an oscillating gradient was applied to the phase-encoding axis during conventional gradient-echo readout to collect multiple k-space lines after each RF pulse. In Mosaic EPI, the quadrants of k-space are collected in four readouts or in two readouts followed by conjugate synthesis.

3.3.1.3 Interleaved EPI (IEPI)

A more successful method is known as interleaved EPI (IEPI) [87]. A series of EPI trajectories across k-space is combined into one image. Figure 3.6 illustrates a conventional k-space trajectory and that of a two-shot interleaved EPI. For interleaved EPI, asymmetric phase encoding with zero filling is frequently used instead of a conjugate symmetry approach. The benefits of interleaved EPI include a larger coverage of k-space and a higher resolution image can be acquired because the duration of sampling after each RF pulse is usually shorter than that for single-shot EPI. However, one main drawback of interleaved EPI is that the Nyquist ghosting would be magnified depending on the number of shots. This is because the lines in the k-space are now grouped into blocks making the steps longer. To compensate for this, a sliding readout delay is applied before each interleaved readout. This slight delay is increased with the k_y offset so that the steps are replaced by a smooth curve [88].

In cardiac imaging with IEPI, changes in image orientation and offset are more difficult, except along the slice axis. An offset in the phase encoding direction may be achieved by post-processing of images, or by a frequency offset during acquisition. Offsetting along the readout direction requires a frequency offset which changes sign with the polarity of the readout waveform. For oblique EPI, problems can occur if the readout gradient is shared between two gradient axes with differing time delays. Small timing differences between the gradient axes were shown to cause artefact that coincides with Nyquist ghosting which is not eliminated by perfect alignment of echoes in the phase-encoding direction [89]. Although this ghosting effect can be removed by interactive adjustment of alternate phase-encode blips, this adjustment in addition to the echo alignment along k_x makes oblique operation of EPI quite delicate. A more robust solution is to build correction circuits into each gradient axis to equalise the delay times [89].

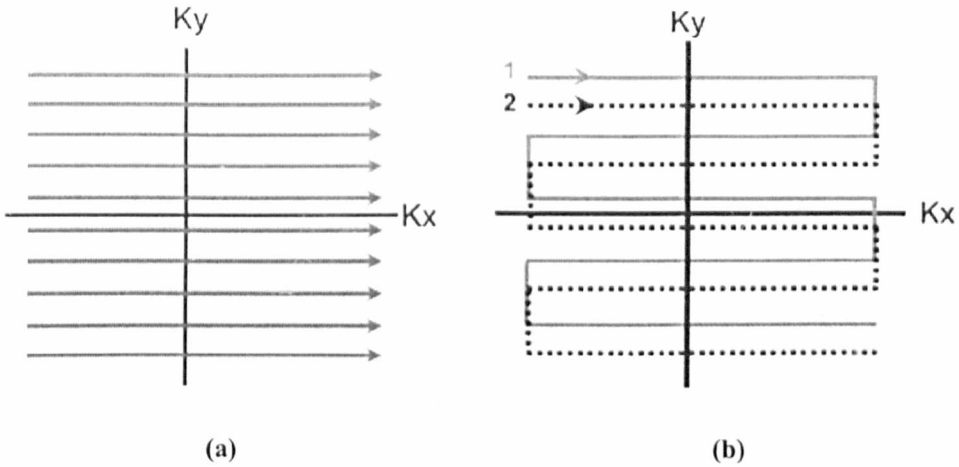

Figure 3.6 (a) A conventional k-space trajectory. (b) A 2-shot interleaved EPI k-space trajectory.

3.3.1.4 Spiral Imaging

The limitation in implementing fast imaging sequences such as EPI is switching the gradients at the fast rates required. Spiral imaging is similar to EPI but is slightly easier to implement. It involves acquiring the k-space in a spiral path starting from the centre [90], and this requires sinusoidal gradients with increasing amplitude with time for both phase-encode and readout directions. Figure 3.7 illustrates the sequence diagram and the k-space trajectory of spiral imaging. It has been shown that the highest priority in determining the rate of traversal of the k-space is to reduce phase errors by acquiring the data as quickly as possible.

To obtain an image with higher resolution but is less sensitive to off-resonance phase errors, several short readouts may be combined. In this case, all the readouts start from the centre of k-space and each of them are rotated $2\pi/N$ radians from the previous one. By the effective averaging of central k-space in projection reconstruction imaging [91] and in interleaved spiral imaging [92], flow variability and other types of inter-shot variability can be greatly reduced.

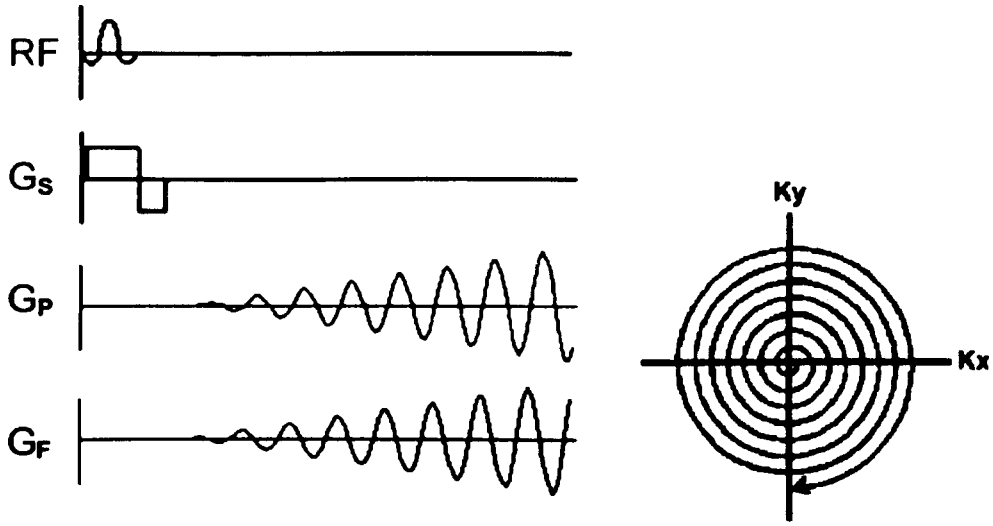

Figure 3.7 Spiral imaging sequence diagram and the corresponding k-space path.

3.3.2 Real time Acquisition and velocity Evaluation (RACE)

RACE is a one-dimensional rapid acquisition method which can be used to measure flow perpendicular to the imaging slice [93]. The technique can be repeated rapidly throughout the cardiac cycle in order to give near real time flow information. The main problem with this type of approach is that data are acquired from a projection through the patient, which means that any signal overlapping with the flow signal will be combined and introduce errors to the flow measurement. To avoid this problem, several methods such as spatial presaturation, applying a gradient to suppress stationery tissue, have been suggested for localizing the signals.

3.3.3 2D Selective Radio Frequency Excitation

Instead of the conventional way of exciting a slice using a 1D RF pulse, it is possible to excite a cylinder of any cross-sectional shape with a 2D selective RF pulse. Typically, a cylinder with small cross-sectional area is selected to reduce scanning time. This technique has been combined with EPI to acquire real-time flow measurements in the aorta [94].

Based on the 2D selective RF excitation scheme, a 3D zonal echo-planar imaging technique has been developed for MR coronary angiography [95].

3.4 Errors in Phase Velocity Mapping

3.4.1 Cardiac and Respiratory Motion Artefacts

In Cardiovascular MR (CMR), the acquisition time is often relatively long compared to physiological processes and therefore, cardiac and respiratory motion artefacts can become a potential problem. Respiratory and/or cardiac or peripheral gating techniques have been developed to reduce these problems.

3.4.1.1 Cardiac Motion Artefacts and ECG Gating

CMR techniques, except for single shot echo-planar imaging or other real time imaging approaches, require cardiac gating to avoid ghosting caused by cardiac motion. Problems with gating can result in ghosting and other noise that degrades the quality of the images. In general, efforts are focused in obtaining the best ECG possible before scanning in order to minimize cardiac motion artefacts and save time. Surprisingly good quality images can be obtained in patients with atrial fibrillation, which may be related to the relatively consistent length of systole relative to changes in heart rate. On the contrary, ventricular bigeminy often results in poor images in that every other beat is activated differently, hence resulting in combining data from two different activation patterns. Many CMR systems provide arrhythmia rejection in an attempt to reduce these effects but at a cost of prolonged scanning time.

ECG gating involves the division of MR data acquisition over multiple cardiac cycles, using the R wave of the ECG as a synchronizing signal. A schematic illustration is given in Figure 3.8. Different segment of the k-space are acquired in successive cardiac cycles at the same delay following an R wave, and hence, at the same stage of the cardiac cycle. This allows the full signal to be pieced together from segments short enough to prevent

blurring. In general, imaging time is defined by two parameters: the acquisition window within each cardiac cycle and the total number of cardiac cycles. The duration of the acquisition window determines the degree of blurring from cardiac motion.

Although prospective ECG gating is preferable, in some patients, R wave detection can be relatively limited. More sophisticated algorithms such as vector ECG or peripheral pulse gating can resolve this problem. Reports have suggested that the vector ECG method is relatively robust, even in myopathic hearts. On the other hand, peripheral pulse gating has a considerable delay between the R wave and the peripheral pulsation, and therefore is more suitable for diastolic imaging.

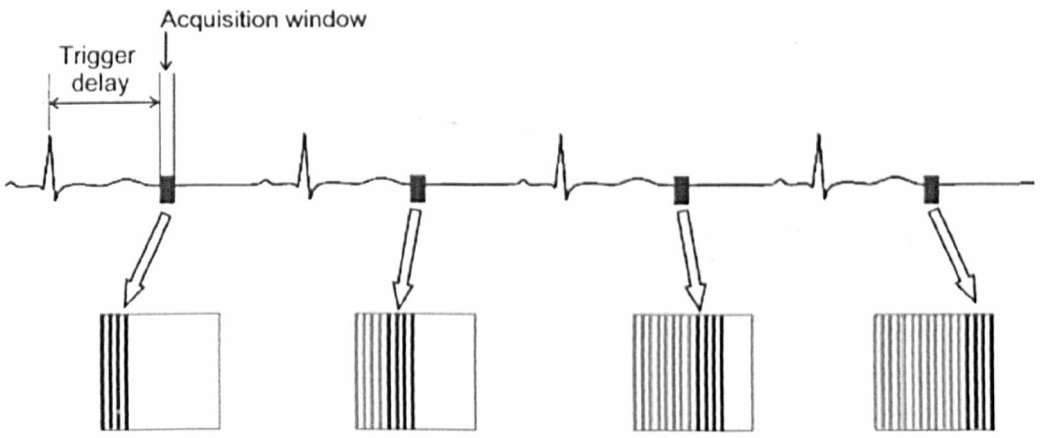

Figure 3.8 A schematic illustration of the principle of Electrocardiogram (ECG) gating. Data acquisition occurs during the acquisition window at a fixed trigger delay following the R wave. Different segments of the data matrix are acquired during 4 cardiac cycles and are pieced together.

3.4.1.2 Respiratory Motion Artefacts

Respiration is associated with significant motion of the heart. Motion in the craniocaudal direction is in the order of a centimetre in normal individuals. This motion can result in significant image degradation with ghosting and blurring, particularly in those with inconsistent respiratory patterns. Strategies to address this problem include breath hold imaging [96], presaturation of the high-intensity signal from fat in the chest wall and the use of respiratory gating. Respiratory gating has been demonstrated to improve image quality substantially and is particularly useful in coronary imaging without breath-hold and patients with heart failure. Like other gating methods, respiratory gating will result in prolonged imaging time.

The ordering of k-space lines in segmented acquisitions may have an influence on relaxation effects and image artefacts. Artefacts may occur when segments acquired in different cardiac cycles do not line up due to arrhythmias or respiratory motion. The most straightforward approach to compensating for respiratory motion is by having the patient hold their breath during image acquisition. In cooperative patients, breath-holding yields high-quality images. However, patients, especially those with cardiac and/or respiratory disease, may not be able to hold their breath for the prolonged imaging times associated with high-resolution scans. Furthermore, breath-holding does not eliminate all diaphragmatic motion, and residue diaphragmatic drift may be sufficient to cause image artefacts.

Another approach to respiratory motion compensation involves monitoring of the respiratory motion itself. Respiratory bellows gating has been used in a number of applications. This method is accomplished by placing an air-filled bellows between the chest wall and a rigid support structure of a circumferential belt. When the chest wall expands, it compresses the bellows and expands the circumferential belt; thereby producing a pressure tracing that can be used for timing of CMR acquisitions. Respiratory bellows gating is combined with ECG triggering, and only cardiac cycles that occur in the same general region of the respiratory motion tracing are used for data acquisition.

More accurate monitoring of respiratory motion can be achieved by using navigator echo techniques. "Navigator echoes" refer to targeted CMR scans that serve to identify the

position of some clearly visible anatomical structure whose relation to the heart is known and can therefore be used to predict cardiac position for a subsequent full scan. Commonly used navigator positions include the right hemidiaphragm and the left ventricular free wall. This technique has been combined with interleaved spiral velocity mapping technique to generate high quality cine coronary artery flow images [97]. Figure 3.9 illustrates the diastolic and systolic frames of the right coronary artery acquired with a conventional breath-hold FLASH sequence and a free-breathing spiral sequence using navigator echo techniques. It can be seen that in the images acquired with the breath-hold FLASH sequence, the arteries are visualised with poor contrast and particularly during systole when through plane enhancement is low (as indicated by the arrow).

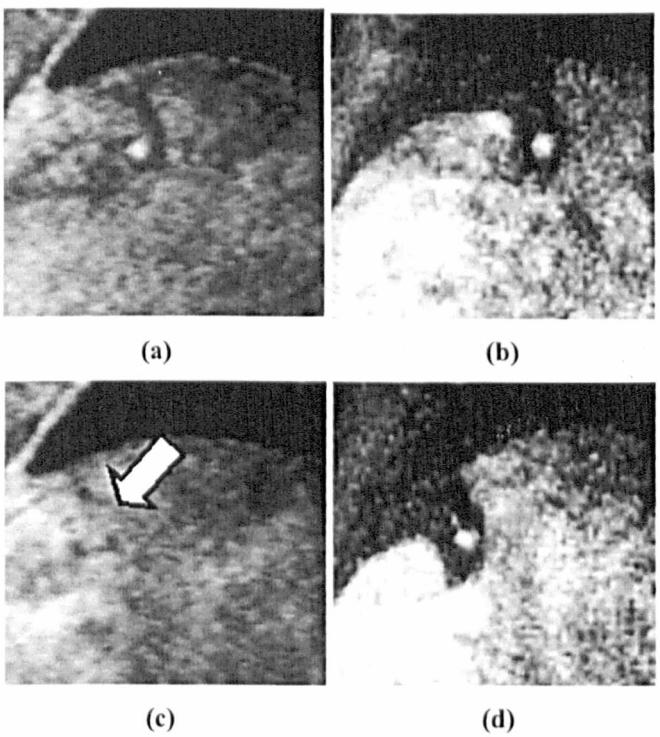

Figure 3.9 Diastolic (a, b) and systolic (c, d) frames from a right coronary artery study. Images (a, c) are acquired with a conventional breath-hold FLASH sequence, whereas (b, d) are acquired with a free-breathing spiral sequence using navigator echo techniques. In images (a, c), the arteries are visualised with poor contrast with the breath-hold FLASH sequence, particularly during systole when through plane enhancement is low (as indicated by the arrow). [Image courtesy of Dr. Jenny Keegan, Cardiovascular Magnetic Resonance Unit, Royal Brompton Hospital, UK]

3.4.2 Phase Wrap/ Aliasing

Phase contrast velocity mapping is by far the most popular method in flow imaging. The accuracy of this method is highly dependant on factors such as the flow pulsatility, the velocity, and the size and tortuosity of the vessel. One simple method to improve the overall accuracy is to carefully adjust the velocity sensitivity of the sequence in such a way that the velocity-related phase shift is close to 2π for maximum expected velocity. This can be explained by looking at the derivation of velocity-to-noise ratio (VNR). VNR is defined as the *velocity phase shift* divided by the *phase noise level*. The phase noise level σ has been shown to be inversely proportional to the signal-to-noise ratio (SNR), *i.e.* $\sigma = 1/SNR$ [98]. Since phase velocity mapping is achieved by subtracting two phase images, the noise level is therefore $\sqrt{2} \cdot \sigma = \sqrt{2}/SNR$, and the VNR is then

$$VNR = \left(\frac{v}{v_\pi}\pi\right) \Big/ \left(\frac{\sqrt{2}}{SNR}\right) = \frac{\pi}{\sqrt{2}} \cdot \left(\frac{v}{v_\pi}\right) \cdot SNR \tag{3.2}$$

where v is the instantaneous velocity and v_π is the encoded velocity that corresponds to a phase shift of π. The velocity-to-noise ratio can be maximised by setting v_π close to the maximum expected v. This approach was further extended by Buonocore by varying v_π during the cardiac cycle by considering the fact that the arterial flow velocity is high in systole but low in diastole [99]. The major drawback of this technique is that phase wraparound is more likely to occur.

The problem of phase wrap or aliasing occurs when the velocity of flow being imaged is outside the pre-defined velocity range. The velocity phase sensitivity of the final velocity map is normally set such that the expected phase shifts are between $+\pi$ and $-\pi$. Any phase shift due to a larger range of velocities will cause ambiguity since a phase shift of $x + \pi$ that corresponds to a larger out-of-range velocity is indistinguishable from a phase shift of x that corresponds to a smaller velocity. The simplest way to avoid this problem is to reduce the velocity sensitivity. Alternatively, for phase contrast velocity mapping, this problem can be corrected for by the phase unwrapping algorithm suggested by Yang et al [100]. Figure 3.10 illustrates a sequence of velocity images with phase warping in the descending aorta and the outflow tract of the right ventricle and the corrected results.

Another solution is to combine phase velocity mapping and Fourier velocity mapping with a small number of velocity phase encoding steps [101]. The final phase velocity map is calculated from the best fit through the Fourier velocity-encoded result. However, this method has a potential problem of signal loss due to phase dispersion and ghosting artefacts due to the high velocity sensitivity.

3.4.3 Errors due to Phase Shifts

Errors may be introduced into the velocity field from background phase shifts. The two main causes of background phase shifts are eddy currents that occur when the gradients are switched rapidly and concomitant magnetic fields. Eddy currents are caused by imperfections in the active shielding of the magnet and gradient fields. In general, they are difficult to predict as they vary from frame to frame in a non-steady state cine and hence can only be corrected by using software which corrects background phase errors for each frame of a cine.

On the other hand, concomitant magnetic fields with non-linear spatial dependence are introduced whenever a linear gradient is switched on [102]. A sample phase image with phase shift error caused by concomitant magnetic fields is illustrated in Figure 3.11. These undesirable magnetic fields could become significant and cause artefacts in velocity images when the gradient is increased to improve velocity sensitivity, in which case the background phase shifts should be calculated and corrected to reduce error.

The occurrence of concomitant magnetic fields is a consequence of the Maxell's equations for the divergence and curl of the magnetic field [102]. The relationship between the concomitant term and the main magnetic field B_0, applied gradients G_x, G_y and G_z is illustrated in Figure 3.12. It can be seen that when there are non-zero components in the x or y directions (B_x and B_y), the length of the magnetic field vector to be greater than the sum of $B_0 + G \cdot r$ (where $G \cdot r = G_x x + G_y y + G_z z$) by an amount B_C.

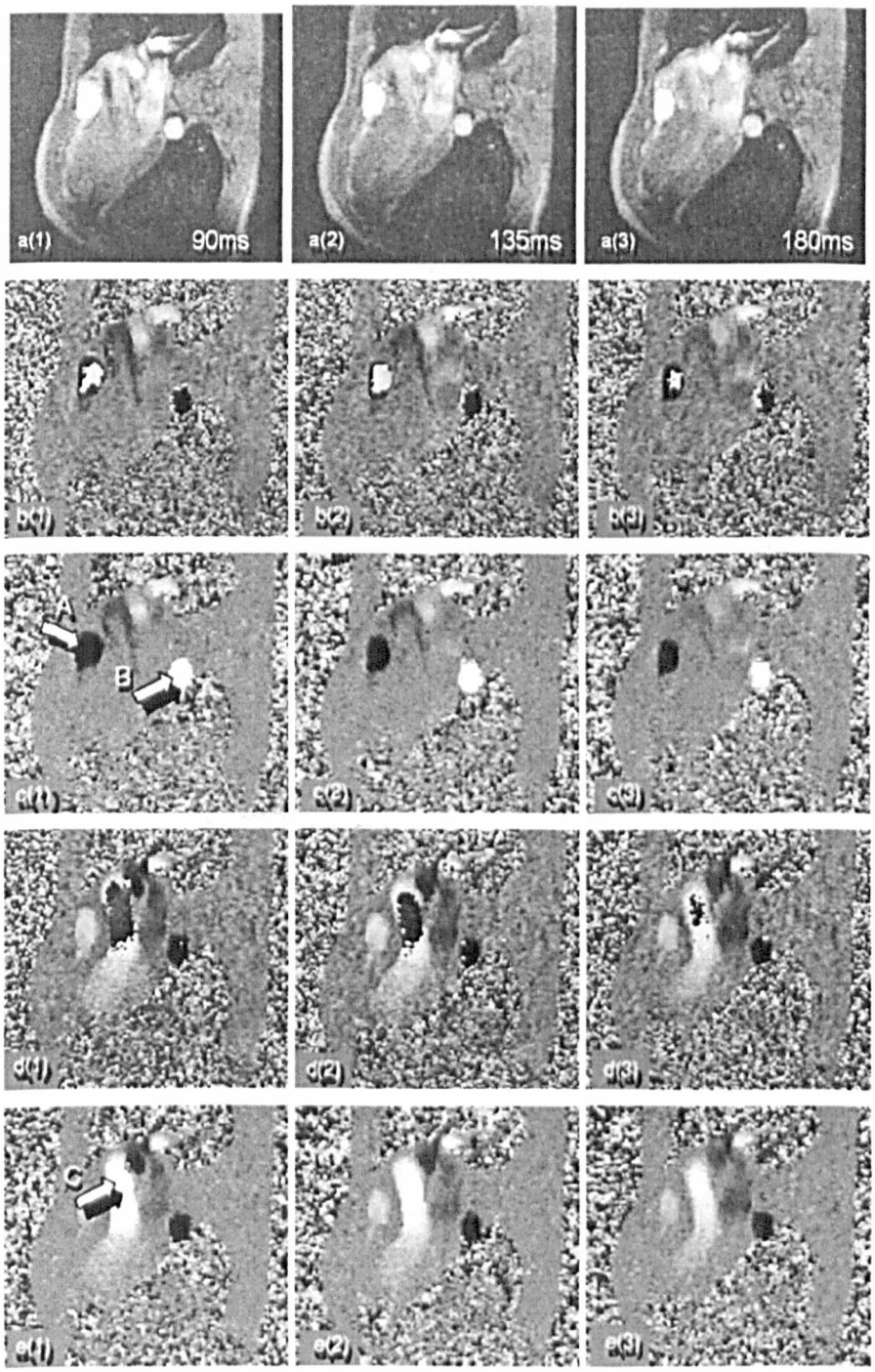

Figure 3.10 Phase unwrapping for dynamic range extension for phase contrast velocity mapping. Images (b,c,d,e) show the flow images with and without the phase unwrapping in the descending aorta and the outflow tract of the right ventricle. (a) shows the corresponding anatomical MR magnitude images.[Image courtesy G. Yang *et al.*, *"Dynamic range extension of cine velocity measurements using motion-registered spatiotemporal phase unwrapping," J Mag Res Imag, vol. 6, pp. 495-502, 1996*]

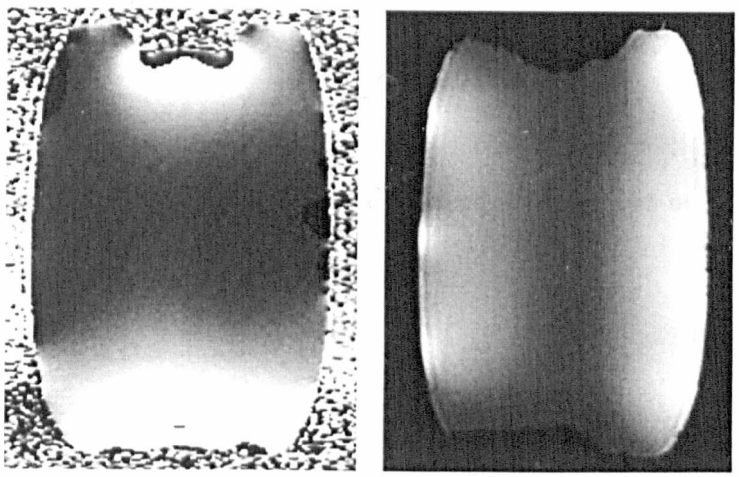

(a) (b)

Figure 3.11 The phase (a) and magnitude (b) images of a phantom acquired with a FLASH velocity encoding sequence. The phase image shows a phase shift error caused by the concomitant magnetic fields.

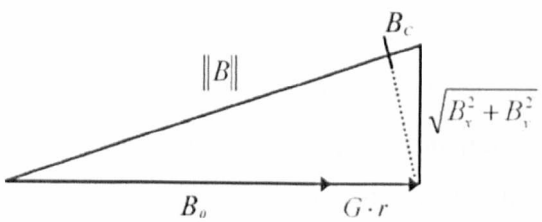

Figure 3.12 Relationship of the concomitant gradient term B_c, and the x- and y-component of the gradient field, G_x and G_y. The concomitant gradient increases with B_x and B_y.

The concomitant fields can be accurately calculated from the Maxwell's equations; the lowest order form is as follows:

$$B_C(x,y,z,t) = \frac{1}{2B_0}\left(G_x^2 z^2 + G_y^2 z^2 + G_z^2 \frac{x^2+y^2}{4} - G_x G_z xz - G_y G_z yz\right) \tag{3.3}$$

Because B_c is non-negative, it is more intuitive to express it in the non-negative form:

$$B_C(x,y,z,t) = \frac{1}{2B_0}\left\{\left(G_x z - \frac{G_z x}{2}\right)^2 + \left(G_y z - \frac{G_z y}{2}\right)^2\right\} \tag{3.4}$$

The accumulated phase shift due to the concomitant field is:

$$\phi_C = \gamma \int B_C(x,y,z)dt \tag{3.5}$$

Subsequently, the resulting phase error in the subtracted phase contrast image will simply be the difference between the reference and velocity encoded scans:

$$\Delta\phi_C = \phi_{C,venc}(x,y,z) - \phi_{C,ref}(x,y,z) \tag{3.6}$$

Several methods for reducing these phase errors have been developed over the years. These methods tackle the problem by employing special pulse sequence design or by correcting the phase error directly in the subtracted images or in the raw data. The simplest way of dealing with these phase errors is to employ two opposing bipolar gradients in the reference and velocity encoded scans. In such a way, the phase due to the concomitant magnetic fields during the encoding time will cancel out in the final phase subtraction as given in Equation (3.6). However, this would make total scan time impractical for single breath-hold imaging.

Alternatively, the phase error can be corrected for in the subtracted image using the fact that the phase error can be fitted to a polynomial. In this approach, a quadratic polynomial is fitted to the final velocity images using the stationary material such as the chest wall as points of zero velocity. The phase error can then be calculated and subtracted from the image. This method has the advantage that phase errors due to eddy current and concomitant field can be removed at the same time. However, it is not always accurate as the fitting may be affected by the flow-related phase. Care also has to be taken when designing the correction algorithms, that the software is able to fit non-linear slopes as this can be a problem especially in oblique planes through the body.

Another correction method is to calculate the phase error directly from the gradient waveform and then subtract it from the final image. Firstly, the read-phase-slice gradient waveforms are transformed to x, y, z co-ordinate system using point-by-point multiplication by the orthogonal rotation matrix. Then, the phase correction coefficients can be calculated:

$$
\begin{aligned}
A &= \frac{\gamma}{2B_0}\int\left\{\left(G_x^2(t)+G_y^2(t)\right)_{venc}-\left(G_x^2(t)-G_y^2(t)\right)_{ref}\right\}dt \\
B &= \frac{\gamma}{8B_0}\int\left\{G_z^2(t)_{venc}-G_z^2(t)_{ref}\right\}dt \\
C &= -\frac{\gamma}{2B_0}\int\left\{\left(G_x(t)G_z(t)\right)_{venc}-\left(G_x(t)G_z(t)\right)_{ref}\right\}dt \\
D &= -\frac{\gamma}{2B_0}\int\left\{\left(G_y(t)G_z(t)\right)_{venc}-\left(G_y(t)G_z(t)\right)_{ref}\right\}dt
\end{aligned}
\tag{3.7}
$$

These integrals are evaluated for all the gradients over the period between the two velocity encodes. The calculated phase error can then be expressed in terms of the calculated coefficients:

$$\Delta\phi_C = Az^2 + B(x^2 + y^2) + Cxz + Dyz \tag{3.8}$$

3.4.4 Partial Volume Error

When a small structure is entirely contained within the slice thickness with other tissue of differing signal intensity then the resulting signal displayed on the image is a combination of these two intensities. This may cause the small structure to disappear. If the slice is the same thickness or thinner than the small structure, only that structures signal intensity is displayed on the image.

The phase of an image voxel is the phase of the complex average of signals within the voxel. In voxels straddling the edge of a vessel, the error depends on the relative magnitudes of static and flowing signals. It also depends on the flow profile since signal from slow flow near vessel walls may become saturated. Therefore, the type of sequence, relaxation time and repetition time all affect the error level.

In a voxel on the vessel edge, if static and moving signals have the same amplitude, partial volume error is not significant. However, if the static signal is negligible, the velocity represented by the voxel will be the mean velocity of the flowing material resulting in over-estimation of the true velocity. One method to address this problem is to outline the vessel by thresholding the magnitude image at about 50% of the flow signal. This method may be further refined by interpolated display and is accurate in cine flow imaging where static surroundings tend to become saturated. In general, the accuracy of flow measurement increases with the number of voxels in the cross-section of the vessel being imaged.

Some researchers have suggested the use of a combination of complex subtraction and phase subtraction to estimate the fraction of signal from moving spins in voxels on the vessel edges to correct for the measured phase shift [103, 104]. The applicability of this technique is limited by the need of some assumptions on the ratio of static and moving signal strengths and the range of velocity phase shifts. A possible solution to this problem is to use Fourier velocity imaging to separate the different motions in each voxel.

3.4.5 Flow variability

Phase variation between phase encoding steps will appear as position shift after Fourier transform. Varying flow in any direction would generate this kind of "accidental phase-encoding" effect in a velocity sensitive image. This ghosting effect is greatly reduced by using a velocity compensated reference image. This is accomplished by acquiring two opposing velocity-encoded phase images with velocity sensitivity equals to $+v_{max}/2$ and $-v_{max}/2$, which are then subtracted to get the final velocity image with velocity sensitivity v_{max} instead of the use of a reference image and a velocity-encoded image with sensitivity v_{max}. This effect occurs because ghosting and its related signal loss are reduced more when velocity sensitivity is reduced from v_{max} to $v_{max}/2$, rather than when velocity sensitivity is set from 0 to $v_{max}/2$.

In general, variations in flow during the long imaging time of conventional phase velocity mapping are assumed to be averaged out, although this assumption is debatable. Phase velocity mapping has been attempted without cardiac gating to obtain mean flow rates in the aorta but this may result in large random errors. It has been shown that flow variability with respiration is around 20% in the inferior and superior venae cavae. This effect might lead to flow measurement biased towards one end of the respiratory range.

3.4.6 Flow-related Signal Loss

The most significant factor that can affect the accuracy of flow measurement is flow-related signal loss. This normally results from a loss of phase coherence within a voxel and can eventually fail to detect the encoded phase of the flow signal above the random phase of the background noise. This loss of phase coherence arises from the acceleration and higher orders of motion present in complex flows, which is unavoidable even if a velocity-compensated imaging sequence is used. Nevertheless, partial signal loss on its own, when not accompanied by partial volume errors, does not greatly affect the accuracy of the phase contrast velocity measurement. An effective way to reduce signal loss is to use a symmetrical gradient waveform that nullifies phase shifts due to all odd-order derivatives of position and then to shorten the sequence as much as possible to reduce the effects of the

even-order derivatives [105]. This kind of signal loss is much less of a problem for the Fourier flow imaging method in which the Fourier transform is used to separate out constituent velocities.

3.4.7 Phase-encoded Motion Artefacts

In MR velocity mapping, phase-encoded motion artefacts appear as bright noise or repeating densities oriented in the phase direction. These artefacts may be seen from arterial pulsations, swallowing, breathing, peristalsis, and physical movement of a patient. Phase-encoded artefacts can be reduced by various techniques depending on their cause and location. Arterial pulsation artefacts can be reduced by spatial presaturation pulses prior to entry of the vessel into the slices. Spatial presaturation can also reduce some swallowing and breathing artefacts. Surface coil localization can reduce artefacts generated at a distance from the area of interest. Alternatively, pulse sequences can be shortened to reduce this artefact.

3.5 Conclusions

MR velocity imaging is a non-invasive and versatile modality that is well suited for imaging in vivo blood flow because the acquisition process does not affect the quantity being measured. The two main approaches of MR velocity imaging are time-of-flight and phase flow imaging methods, of which phase contrast velocity mapping is the most frequently used technique in both clinical and research settings. This technique allows the acquisition of comprehensive quantitative blood flow information, thus enabling detailed physiological flow studies to be performed.

With conventional phase contrast velocity mapping, the acquisition of three dimensional velocity data usually involves cardiac gating and averaging over several cardiac cycles to reduce artefacts. This could significantly prolong the acquisition time, rendering the method unsuitable for analysing short-term physiological flow changes. To this end, a number of rapid flow-imaging techniques have been developed in recent years. The most

common way to speed up acquisition is to combine a phase mapping approach with imaging methods such as echo-planar and spiral imaging. Typical imaging time for these techniques can be made as short as 50ms. In practice, MR velocity data is susceptible to a certain amount of noise. The source of error could be intrinsic to system hardware setup or caused by patient movements. Commonly encountered errors include cardiac and respiratory motion artefacts, phase wrap, errors due to partial volume effects, flow variability and other flow related signal loss. A number of methods have been developed to address such sources of error. Nevertheless, it is practically impossible to remove all noise in the acquisition process. It is therefore important to develop robust noise removal algorithms for improving the consistency of the MR velocity data. Before we move on to the technical details of our proposed vector field restoration technique, we shall first discuss the existing blood flow analysis and processing techniques in Chapter 4.

Chapter 4

Blood Flow Analysis and Processing Techniques

4.1 Introduction

In the previous chapter, we have discussed the basic physical principles of MR velocity imaging and outlined the potential sources of error that may be introduced in practical clinical applications. In recent years, significant improvements in both the temporal and spatial resolution have been made in MR velocity imaging techniques, thus making them important clinical tools in blood flow analysis and the assessment of flow related cardiovascular disease. Key clinical applications of MR velocity imaging techniques, for example, include the measurement of wall shear stress, which has been implicated as a localised factor of atherosclerosis. MR techniques have also been widely used to study the velocity profile of major blood vessels and the flow patterns in the cardiac chambers, thus allowing the interaction between blood flow and its surrounding structure to be explored. In this Chapter, we will outline common flow processing techniques for extracting the inherent haemodynamic indices of the velocity distribution, and their clinical applications.

As mentioned in the Introduction, one of the major emphases of the thesis is to perform comprehensive validation of flow field restoration, abstraction, and feature tracking techniques. This requires the generation of noise free reference data sets with known flow features. To this end, we have used computational fluid dynamics (CFD) in this thesis to simulate detailed LV flow patterns based on realistic in vivo anatomic geometries. Although the exact technical details of CFD with patient specific geometry fall out of the scope of this thesis, we will provide an overview of the basic principle of blood flow simulation with CFD, and discuss some of the technical caveats related to model reconstruction, mesh generation, and numerical simulation.

4.2 Blood Flow Analysis

4.2.1 Wall Shear Stress

As described in previous chapters, atherosclerosis can lead to myocardial infarction, strokes and aneurysms. As such, the genesis and progression of atherosclerosis have been studied extensively. Clinical studies have revealed that atherosclerosis primarily occurs in large and medium-sized arterial vessels and several arterial segments including the abdominal aorta. The carotid artery and the coronary arteries are particularly prone to atherosclerosis. Previous studies have also shown that certain regions may be more susceptible to the disease and that atheroma tends to form at bifurcations, branches and along the inner wall of curvatures [106]. The localisation of the disease has led to the hypothesis that haemodynamics play a role in the genesis or progression of atherosclerosis. In particular, wall shear stress (WSS) has been implicated as a localising factor. To this end, studies have been conducted to investigate the correlation between wall shear stress and the development of atherosclerosis.

Wall shear stress is the force per unit area that flowing blood exerts on arterial vessel walls. For a Newtonian fluid, whose viscosity is constant with a varying shearing force, wall shear stress τ_w can be calculated from the product of the fluid viscosity and the velocity gradient at the wall:

$$\tau_w = \mu \cdot \frac{\partial v}{\partial r_w} \tag{4.1}$$

where μ is the viscosity of the fluid and $\frac{\partial v}{\partial r_w}$ is the shear rate or the velocity gradient at the wall. Wall shear stress may act as a localising factor by influencing the morphology and function of the endothelial layer that lines the interior of arterial blood vessels [107, 108]. The shape of endothelial cells determines the cell turnover rate, the amount of cholesterol deposition within the arterial wall and the permeability to various proteins. Several studies have reported a correspondence between the areas of low wall shear stress and the locations of atheroma [109-111]. However, the precise correlation between wall shear stress and the locations of atheroma cannot be established due to several shortcomings in these studies. Firstly, the models were constructed from the mean anatomical structure and the results were correlated to the average postmortem histologic results, thereby limiting the investigation of the relation between geometry and shear stress in each individual. Secondly, over-simplified models with approximated haemodynamics conditions were used. Lastly, the upstream flow conditions of the arterial segment cannot be represented exactly in an in vitro model, thus further limiting the accuracy of the method.

To overcome these drawbacks, MR phase velocity mapping, which provides quantitative measurements of *in vivo* flow velocity, has been used to directly calculate the wall shear stress in various arteries [112-114]. Oshinski *et al.* have used MR phase velocity mapping to calculate wall shear stress in the suprarenal and infrarenal abdominal aorta, two sites with very different proclivities in the development of atherosclerosis [112]. Eight subjects were studied and the maximum, minimum and mean wall shear stress was calculated at the posterior and anterior walls of the suprarenal and infrarenal abdominal aorta. The values of the peak and mean wall shear stress over the cardiac cycle showed a wide variation among the subjects. However, a general trend was observed that the peak and mean wall shear stress values were higher in the suprarenal aorta than in the infrarenal aorta. As the infrarenal aorta is known to be more sceptical to atherosclerosis than the suprarenal aorta, these findings supported the hypothesis that low wall shear stress may be a localising factor for atherosclerosis and that high wall shear stress may be a deterrent to the formation of atheroma. In the same study, a wide variation in the mean values of wall shear stress was

also observed, from 10.4 dynes/cm^2 at the posterior wall of the suprarenal aorta to 4.7 dynes/cm^2 at the posterior wall of the infrarenal aorta, representing a 150% difference over a 70mm distance within the vessel. This result suggested that wall shear stress values might vary significantly in different regions in the vessel.

In a later study by Oyre *et al.*, the oscillating shear index (OSI) values at the anterior and posterior walls of suprarenal and infrarenal abdominal aorta were measured in addition to the wall shear stress values [115]. The oscillating shear index describes the degree of deviation of wall shear stress from the antegrade flow direction and it is defined as:

$$OSI = \frac{|A_{neg}|}{|A_{neg}| + |A_{pos}|} \tag{4.2}$$

where $|A_{pos}|$ and $|A_{neg}|$ are the absolute values of the integrals over time under the positive and negative parts of the WSS curve respectively. By convention, wall shear stress values are considered to be negative when flow is directed towards the heart. The results supported the theory that more pronounced atherosclerosis development was found in areas with low and oscillating wall shear stress. In a similar study of the abdominal aorta, the intimal thickness was measured blindly using histomorphometric techniques and correlated to wall shear-stress variables using linear-regression analysis [116]. Experiment results showed a linear relationship between the intimal thickness and the values of mean and peak wall shear stress. The findings suggested that low and oscillating wall shear stresses are localising factors for intimal thickening and hence the early development of atherosclerosis.

Although most early studies on wall shear stress were performed at the abdominal aorta, other arteries have also been investigated. Stokholm *et al.* performed a study on wall shear stress in the internal carotid artery using *in vivo* data [113]. In this study, velocity fields were acquired using a FID-Acquired-Echoes (FAcE) sequence while the wall shear rate was determined using a 3-dimentional paraboloid (3DP) fitting technique [117]. This technique allows highly accurate measurement of circumferential sub-pixel vessel wall position and wall shear stress by fitting the velocity profiles to a multiple sectored three-dimensional paraboloid model [117]. With this technique, velocity data from all sector layers at four specified radial positions were fitted to the 3DP model and wall shear rate

was then derived by differentiating the polynomial of the model at the vessel wall where velocity equals zero. Wall shear stress can subsequently be obtained by multiplying the value of wall shear rate by a fixed value of the viscosity of the blood. The results, which showed that low and oscillating wall shear stress was found in the parts of the carotid artery that are prone to atherosclerosis, further supporting the hypothesis that low and oscillating wall shear stress is associated with the development of atherosclerosis.

With the recent advances in 3D MR velocity acquisition techniques, methods that apply high-resolution three-dimensional phase contrast mapping for estimation of wall shear stress *in vivo* have been explored [118]. Wall shear stress derived from 3D velocity measurements were compared with that derived from 2D velocity measurements and a good agreement was found. The improved resolution and image quality of 3D velocity mapping enables the accurate estimation of wall shear stress patterns circumferentially and longitudinally in human arteries. Wu *et al.* used 3D MR velocity mapping to investigate wall shear rates *in vivo* in the common carotid, brachial, and superficial femoral arteries [114]. The mean, maximum, and minimum wall shear rate and an oscillatory shear index were measured for 20 volunteers by using the 3D paraboloid fitting technique [117]. The results were in good agreement with previous studies. It was concluded that a nonuniform distribution of wall shear rates throughout the arterial system.

4.2.2 Other Haemodynamic Parameters

The potential of MR velocity mapping in measuring haemodynamic parameters such as blood pressure, vascular compliance and shear stress has drawn a lot of research interests in recent years. Urchuk et al [64, 119, 120] approached the problem by considering the vascular compliance and vessel distension. The estimates of vascular compliance are obtained from a correlation of spatial and temporal velocity derivatives and that of vessel distension based on measurements of the velocity gradient in the direction of flow. The derived pressure waveform showed a good correlation with catheter pressure measurements taken in a porcine model [64].

Yang *et al.* [65] have taken a different approach by deriving flow pressure maps from the cine phase contrast velocity maps using the Navier-Stokes equations, which are recognised

as a complete description of simple fluid mechanics. Using this technique, altered pressure distribution has been demonstrated in patients with cardiovascular disease. Figure 4.1(a) shows the pressure field in an aortic aneurysm of a patient with Marfan's syndrome derived from the MR velocity measurements by using the Navier-Stokes equations. The pressure distribution was displayed using 1 mmHg pressure bands and overlapped on an anatomical image. Figure 4.1(b) illustrates the associated flow pattern within the area marked by the rectangle in Figure 4.1(a). The distortion to the normal pressure distribution has resulted in a high pressure area at the right lateral wall and a low pressure area near the left lateral wall. The high pressure area was believed to be introduced by the impact of the oblique flow jet whereas the low pressure area was associated with a vortex due to flow separation.

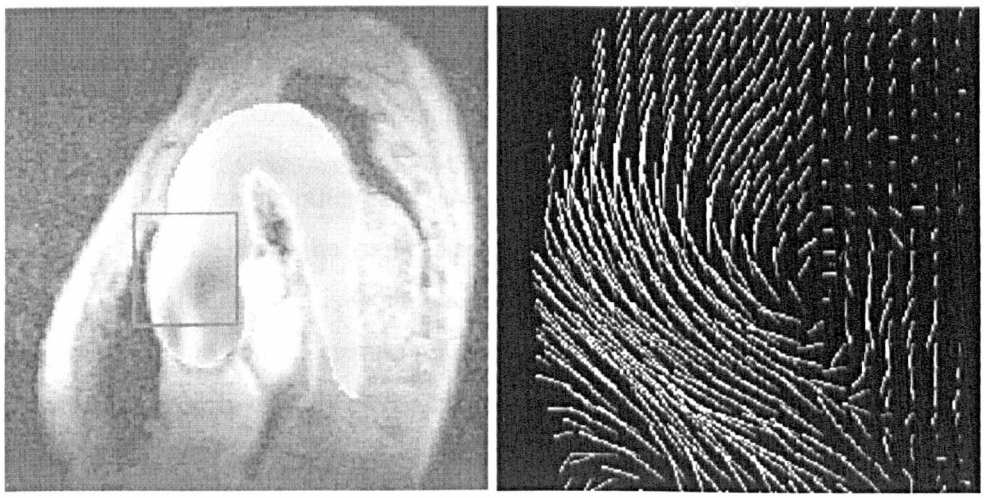

(a) **(b)**

Figure 4.1 (a) Pressure distribution in an aortic aneurysm calculated from the MR velocity measurements by using the Navier-Stokes equations for incompressible fluids. The pressure distribution was displayed using 1 mmHg pressure bands and overlapped on an anatomical image. (b) The associated velocity vector map of the bounded area in (a). [Yang GZ, *et al.*, *Computation of flow pressure fields from magnetic resonance velocity mapping.* Magn Reson Med, 1996. 36**(4): p. 520]**

4.2.3 Blood Flow Pattern Visualisation

Effective visualisation techniques are crucial in the analysis of blood flow patterns. Thus far, the most frequently used visualisation techniques in clinical research are vector mapping and streamlines display [121, 122], each having its own strength. Vector mapping techniques are typically employed in the study of instantaneous velocity distribution. Basically, a vector map, also called arrow map or vector arrow-map, is composed of the velocity vectors or short-duration particle paths displayed at on a uniform grid within the flow domain. It was first used for visualisation of ascending aorta flow in normal subjects [123] which revealed that the right-handed helical flows predominated in the upper aortic arch in late systole and end-systolic retrograde flow along inner wall curvatures were clearly displayed. This technique has also been applied to visualise flow in aortic aneurysms and grafts [124] and in dilated left ventricle [125].

Streamline technique, on the other hand, are mainly used to visualise the transition of blood flow patterns and it allows the rapid assessment of spatial and temporal varying flow patterns. In clinical settings, this technique can be applied to investigate the progression of atherosclerosis, as streamline separation and recirculation are known to be associated with the genesis of atherosclerosis. With the conventional streamline tracking techniques, one or more seed points are first identified within the blood vessel of interest and they are then tracked through the velocity field. One of the earliest studies combined the calculated streamlines with 3D MR angiograms and the results were then visualised in 3D [121]. By using this combined technique, the helical flow patterns in aneurysms, and the filling patterns of the common carotid artery and the carotid bulb were revealed. Nevertheless, early techniques may produce unrealistic streamlines that pass through the vessel walls or intraluminal sources and sinks of blood. Algorithms have been developed to correct these problems by pre-processing the velocity field to ensure that it obeys the divergence free constraints [126].

An alternative technique, called transient streamlines, uses texture synthesis for flow visualisation [127]. With this method, the streamlines generated are uniformly distributed and their appearances are similar to those generated with the conventional techniques. This technique has been applied to visualise the disturbed flow patterns in aortic aneurysm and dilated ventricle and the cavity filling patterns. Transient streamline technique has also been successfully applied to elucidate major directional changes of the blood, thus facilitating the investigation of the functional implications of the inter-cavity flow patterns. Figure 4.2 illustrates the flow patterns in the right atrium of a normal subject at different phases of the cardiac cycle using transient streamlines. It can be seen that the streams enter from the superior vena cava from above and inferior vena cava from below and these two opposing streams do not collide head on but are deflected to form a forward-rotating vortex.

The technique was used in a recent study on the redirection of flow through the heart by Kilner *et al.*[8]. In this study, it was proposed that asymmetries and curvatures of the looped heart have potential fluidic and dynamic advantages. The atrial filling patterns appear to be asymmetric, thereby allowing the momentum of the inflow stream to be redirected towards the atrio-ventricular valves. Whereas at the ventricular level, the flow stream change direction in such a way that recoil of the ventricle away from ejected blood enhances ventriculo-atrial coupling. Based on these observations, it was suggested that the heart is able to redirect blood through the heart with minimal dissipation of energy and dynamically enhanced reciprocation of atrial and ventricular function during exercise and that the efficiency of the heart involves coupled interactions between contractility, elasticity and change in momentum of all heart chambers. This interpretation was expected to provide further insight in clinical cases where the relations between forms, flow, mobility and timing of the heart was affected.

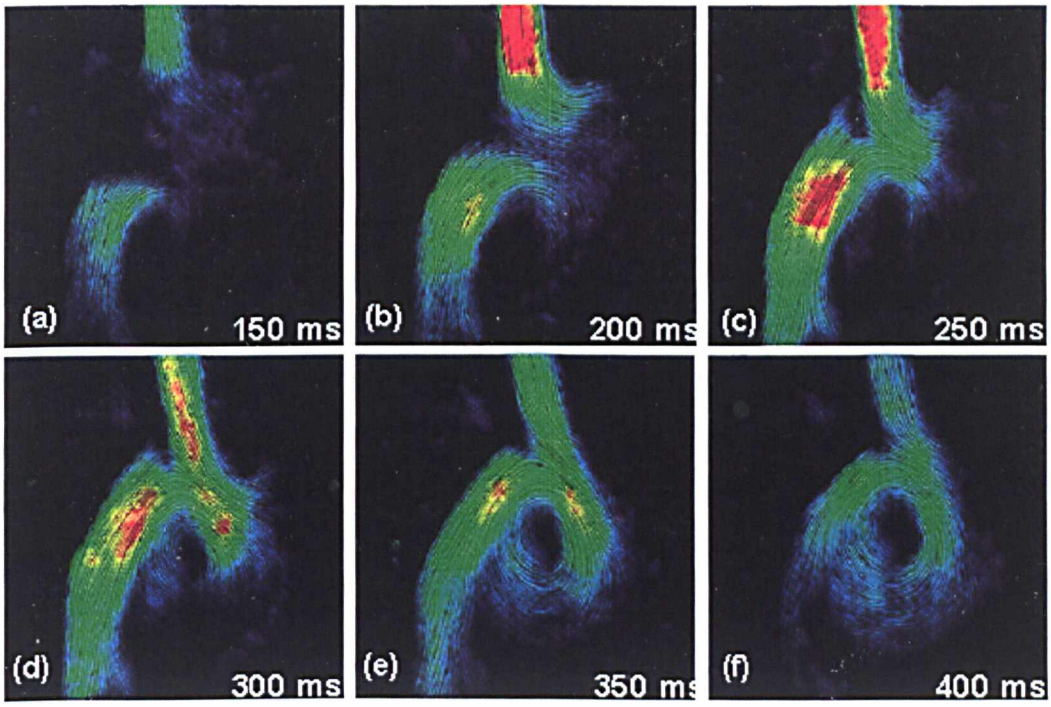

Figure 4.2 Visualisation of flow pattern in the right atrium of a normal subject at different phases of the cardiac cycle using transient streamlines. (a-c) In systole, the streams enter from the superior vena cava from above and inferior vena cava from below. (d-f) The two opposing streams do not collide head on but are deflected to form a forward-rotating vortex in diastole. [Yang GZ, *et al.*, *Transient streamlines: texture synthesis for in vivo flow visualisation.* Int J Card Imaging, 2000. 16(3)**: p. 175-84.]**

4.2.3.1 Flow Patterns in the Aorta and Great Vessels

The flow patterns in the aorta and its branches have been studied extensively with MR velocity imaging. Klipstein *et al.* described the blood flow patterns in the aorta with detailed velocity profiles [128]. A skewed velocity profile with higher velocities around the inside arch of the aorta was revealed. In diastole, flow was reversed along the posterior left wall of the ascending aorta while it continued forwards at the anterior right wall. This phenomenon was later quantified in a study by Bogren *et al.*[129].

In a later study [130], Bogren and Buonocore measured the antegrade and retrograde flow in the aorta and its major branches using cine MR velocity mapping in order to determine the haemodynamic significance of retrograde flow in arteries. Synchronous or isolated antegrade and retrograde flow was found in the entire aorta and in arteries supplying muscles. No retrograde flow was found in arteries supplying internal organs, such as the internal carotid artery. Based on these findings, it was suggested that the retrograde flow in the aorta and the extremity arteries contributes substantially to supplying diastolic perfusion of internal organs such as the heart, brain, and kidneys.

Flow patterns in the pulmonary artery have also been studied. Abnormal flow patterns with large retrograde flow have been reported in patients with pulmonary hypertension [131]. In a study of the flow patterns in the pulmonary arteries of patients with lung transplant [132], the flow profile in the pulmonary artery of the transplanted lung showed a wide forward flow during systole and most of diastole, whereas that of the native lung showed a narrow early systolic peak and a reverse flow in most of diastole. The volume of blood flow in transplanted lung was 2.8 times of that in native lung. It was suggested that the relative resistance in the native and transplanted lung contributed to the significant differences in volume and flow patterns between the native and transplanted lungs.

Blood flow in the superior and inferior vena cava were also measured [133]. Both normal subjects and patients with right-sided cardiac diseases were studied. In patients with tricuspid regurgitation, a reduced systolic peak and retrograde flow in the inferior vena cava were observed. In patients with pulmonary hypertension, pericardial constriction, and right ventricular dysplasia, reduced diastolic peak was seen, implicating reduced diastolic

compliance of the right ventricle. In patients with obstruction of the superior vena cava, absence of flow was confirmed, and retrograde flow was seen in the azygos vein.

A recent study has investigated the effect of aging and coronary artery disease on the aortic flow [134]. The flow patterns in the thoracic aorta of patients with coronary artery disease of variable age were compared with those in age-matched normal subjects. Flow patterns in mid to late systole and diastole were found to be irregular, implying that there was a wide range of flow directions which change frequently and smaller regions of organised antegrade flow in the ascending aorta. The extent and duration of these irregular flow patterns were found to increase with age. In patients with coronary artery disease, reduced regions of organised antegrade flow and increased irregular flow could be explained by a loss of elasticity in the aortic wall. Similar abnormalities in flow patterns were also found in the elderly group of normal subjects. These abnormal flow patterns may result in reduced blood flow to the coronary artery, which could lead to more severe consequences.

4.2.3.2 Quantitative Analysis

Vortical motion of the blood is an intriguing aspect of blood flow pattern that has long attracted attention [135]. These flow patterns have been reported in aneurismal aortas and the cardiac chambers. Visualisation techniques permit visual assessment of flow patterns but do not allow quantitative evaluation of salient flow features and their interaction with the surrounding structure. As such, quantitative methods for characterising flow patterns are needed.

Kim *et al.* investigated the left ventricular flow patterns in normal subjects using 3D MR velocity mapping [15]. The results showed that early diastolic mitral inflow was directed towards the apex and a large anterior vortex developed in the left ventricle shortly after the onset of the mid-diastolic semi-closure of the anterior mitral leaflet and reappeared during the final mitral valve closure. These findings demonstrated the coupling between the formation of vortex in the left ventricle and the mitral valve motion. In the same study, the velocity distributions at the mitral and aortic valves were also analysed. The velocity distribution in the aortic annulus was slightly skewed, with the highest velocities directed towards the septum. At the mitral valve, a uniform velocity profile was seen at the mitral

annulus whereas a skewed profile, with the highest velocities near the posterior leaflets, was found at the leaflets.

Yang *et al.* developed an automatic vortex detection method to allow extraction of vortical flow feature and the comparison of their propagation through the cardiac cycle [16]. Figure 4.3(b-d) illustrate the flow patterns in the left ventricle of a patient with dilated left ventricle visualised using vector map. The figures show that the early diastolic inflow was directed towards the posterior free wall and two vortices were formed beneath the posterior and anterior leaflets of the mitral valve. The positions of the vortices extracted by the automatic detection method are marked in the figures. By using the vortex detection method, it was found that there was a clear difference in the dynamics of the two vortices formed during diastole between normal subjects and patients with dilated left ventricles. However, the clinical significance and implication of the difference between normal and dilated left ventricles has yet to be fully established.

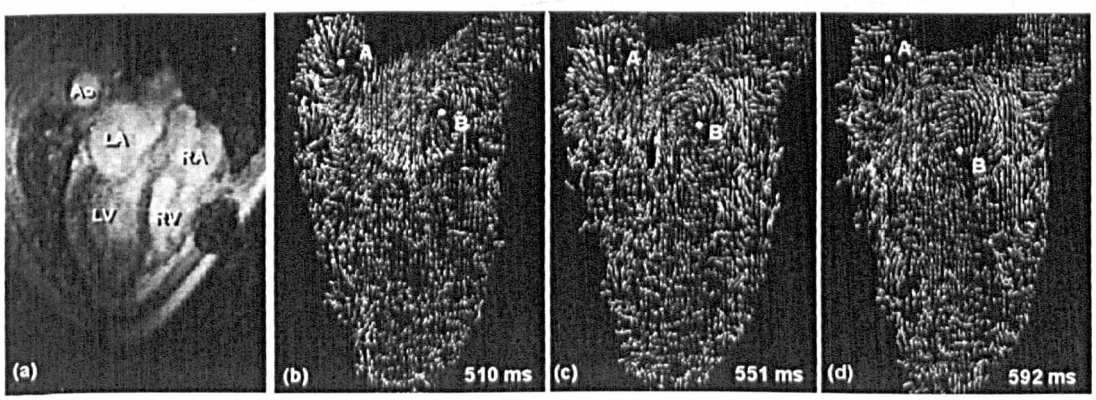

Figure 4.3 (a) A horizontal long axis MR image of a patient with dilated left ventricle. Ao: aorta, LA: left atrium, LV: left ventricle, RA: right atrium, RV: right ventricle. (b-d) Vector map visualisation of the flow patterns in the dilated left ventricle during diastole. The early diastolic inflow was directed towards the posterior free wall and two vortices were formed beneath the posterior and anterior leaflets of the mitral valve. The two detected vortices are marked in the figures. [Yang GZ, *et al.*, *Vortical flow feature recognition: a topological study of in vivo flow patterns using MR velocity mapping.* J Comput Assist Tomogr, 1998. 22(4): p. 577-86.]

Figure 4.4 shows the result from a patient with aortic aneurysm due to Marfan's syndrome. The anatomical image in Figure 4.4(a) depicts the symmetrically dilated aortic root and ascending aorta. The flow patterns as shown in Figure 4.4(b-d) show a central forward stream, slightly skewed to the right, with vortices developing on both sides of the flow. These vortices, which are in fact the cross section of an advancing vortex ring, lasted through systole and most of diastole as demonstrated in Figure 4.4(f). The trajectories of the two vortices are depicted in Figure 4.4(e), the amount of movement is not seen in a normal aorta.

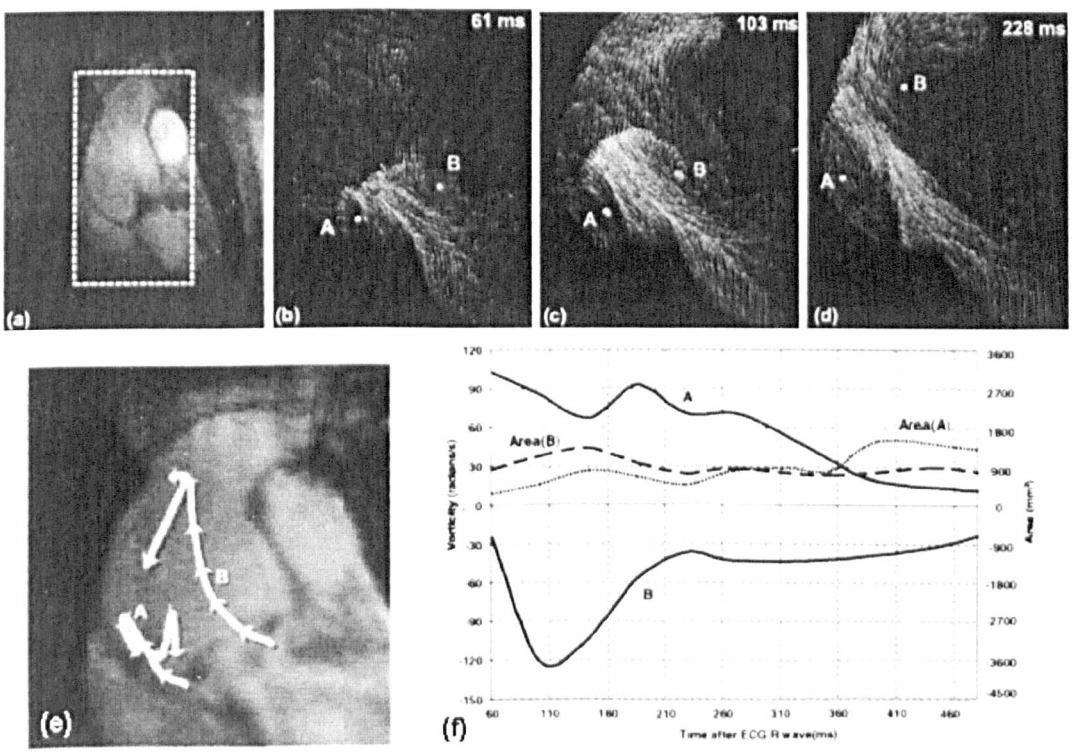

Figure 4.4 (a) An anatomical MR image depicting the aneurismal ascending aorta of a patient with Marfan's Syndrome. (b-d) Reconstructed flow patterns and the detected vortices (A & B) at different phases of the cardiac cycle. (e) The trajectories of the two detected vortices overlaid on the anatomical image. (f) The size and vorticity of the two vortices measured over the cardiac cycle. [Image Courtesy GZ Yang, Imperial College London, UK]

4.3 Blood Flow Simulation with CFD

As mentioned in the introduction, the validation of the proposed flow restoration and feature extraction techniques in this thesis will be carried out by using CFD simulated data sets. CFD is a method of determining a numerical solution to the governing equations of fluid flow whilst advancing the solution through space or time to obtain a numerical description of the complete flow field of interest [136]. The basic steps involved in applying CFD for flow simulations given a morphological shape definition are: (1) discretise the fluid domain into small cells to form a volume mesh or grid; (2) define the physical model, *i.e.* the set of equations to be solved; (3) define the boundary conditions; and (4) apply numerical methods to solve the equations. The physical laws that govern the motion of fluid within a complex geometer are highly complex. As such, it is not feasible to construct a physical model that can represent the entire flow domain as a single entity. It is necessary to partition the flow domain into smaller units in a process called meshing. After meshing, the set of equations governing the flow within each cell can be constructed. The governing equations of fluid flow used in CFD simulations are the Navier-Stokes equations. These equations form a system of coupled non-linear partial differential equations. In general, closed form analytical solutions do not exist, thus numerical methods are employed to solve these equations. To get a unique solution, the boundary conditions have to be defined prior to the numerical simulation process. In cardiac flow simulations, blood is modelled as an incompressible, unsteady flow. Coupled with an accurate morphological representation of the structure of the left ventricle, CFD technique can be employed to simulate time-dependent blood flow. With this technique, high spatial and temporal resolutions, usually much higher than those acquired by any medical modality, can be achieved. The prerequisite of success of CFD, however, is an accurate delineation of the geometrical boundaries of the dynamic structure. In the next section, we will review some of the key techniques that have been used for ventricular modelling.

4.3.1 Ventricular Modelling Techniques

4.3.1.1 Parameterisation Models

Early techniques for 3D ventricular modelling involved the fitting of simple geometric primitives such as ellipsoids and cylinders to the image data to generate a globally parameterised model [137]. These techniques are generally inadequate for capturing the morphology of the ventricle and have inspired the use of more complex primitives such as superquadric to obtained a more accurate model [138]. Superquadrics have been used to describe general shapes with a small number of parameters, thus making it possible to apply statistical analysis to classify the morphology of the ventricles. Another parameterisation scheme decomposes the object surface into sinusoidal basis functions, allowing a wide variety of smooth surfaces to be described with a small number of parameters [139]. Application specific parameters have also been used. One such technique incorporates functional parameters acquired with MR tagging to allow the representation of radial and longitudinal contraction, twisting and long-axis deformation [140].

Contrary to the global parameterisation techniques described above, local parameterisation techniques generally enable higher degrees of freedom, thus allowing more complex geometries to be represented. One existing technique applies B-spline to delineate cardiac boundaries in a set of cross-sectional images [141]. However, this approach requires a human observer to identify the points on the cardiac boundaries and is therefore not practical in clinical settings.

To overcome the shortcomings of both the global and local parameterisation models, hybrid models have been developed. A typical hybrid model is obtained by fitting a global model to the image data by using a small number of parameters and then deforming the global model by incorporating finer local variations. In this way, the overall shape of the left ventricle can be captured rapidly while further refinements may be performed when necessary to improve the accuracy of the model. In one study, a truncated ellipsoid was translated, rotated and scaled to fit the cardiac boundaries and the model was then deformed using B-spline curves to approximate the set of manually delineated contours [142].

A more sophisticated method used superquadrics with free-form deformation to model the LV surface [143]. This technique has been applied to characterise LV motion in an image sequence by fitting a model in the first time frame and then adjusting the free-form deformation in the following time frames. Similar techniques that combine global parameterisation with local deformation have been applied to delineate cardiac boundaries in the assessment of gated perfusion SPECT and promising results have been demonstrated [144, 145].

4.3.1.2 Active Contour Models

The active contour models, also called Snakes, were first introduced by Kass *et al.*[146]. They have been extensively used for the segmentation of biological shapes such as the cardiac chambers [147, 148]. Multiple active contour models have been used to model the 3D morphology given a set of cross-sectional images. This technique is generally formulated as an energy minimisation problem in which low gradient and high curvature correspond to high energy.

The model starts from an initial approximation of the contour, usually defined manually, and evolves automatically subject to certain constraints defined using the prior knowledge on the object geometry and topology. To reduce the amount of human involvement needed in defining the initial approximations, several techniques have been employed. One such technique utilises the fact that the object shape does not change drastically in consecutive time frames to reduce the number of manual delineation needed. With this technique, only the first time frame requires initial manual delineation, the subsequent frames uses the model obtained in the previous time frame as the initial approximation.

When applied to cardiac delineation, the active contour model can be problematic in areas with significant partial volume effects such as the region near the apex. This method is also error-prone in delineating objects with complex geometry such as the papillary muscles. As a result, heavy involvement of human interaction is required in practice to ensure the accuracy of this method.

Variations of the basic active contour model have been developed to improve the robustness and accuracy of the method. Cohen *et al.* introduced the balloon model in 1991, which extends the active contour model by using a sphere as the initial model and making it behaves like a balloon which is inflated by an additional force [149]. Unlike the original snake model, this deformable balloon model does not require the initial curve to be placed close to the solution. A finite element method for solving the balloon model in 2D and 3D images were also developed subsequently [150].

Bredno *et al.* further extended the active contour model to multi-dimensional image domain [151]. In this model, the object is represented by a set of simplex meshes and the iterative segmentation process is driven by a mechanical formulation of influences. Both the representation and the influences are valid for any dimension of the image domain. In [151], a 4D spatio-temporal model was applied to delineate a left ventricle from an MR sequence.

4.3.1.3 Statistical Shape Models

Statistical shape model is a powerful tool in capturing the variability of the anatomical structure over time and across different subjects. When used in delineating an object in an image, a statistical model, called the point distribution model (PDM), is first constructed from a training set of images with the object boundaries delineated manually, then the constructed model is allowed to deform iteratively to fit into an unseen occurrence of the object in a new image. The final model can subsequently be compared to the statistical model to ensure consistency. Two widely used statistical models for shape modelling are the Active Shape Model (ASM) [152, 153] and the Active Appearance Model (AAM) [154, 155]. The Active Shape Model represents a parametric deformable model where a point distribution model of the global shape variation from a training dataset is built. The AAM is similar to the ASM but it incorporates the statistics of the image intensity on top as well as the shape variation.

To construct a point distribution model, each labelled shape as described by a vector **X** is aligned to a common coordinate frame by applying rigid body transformation:

$$\mathbf{x} = \mathbf{S} \cdot \mathbf{R} \cdot \mathbf{X} + \mathbf{T} \tag{4.3}$$

where **S** denotes the scaling matrix, **R** the rotation matrix and **T** the translation matrix. Then, Principal Component Analysis (PCA) [156, 157] is applied to these aligned vectors to compute the modes of variations, *i.e.* transforming the axes in a multidimensional space, in such a way that each mode of variation is linearly independent of each other. This can be accomplished by first computing the covariance matrix of the aligned vectors

$$\mathbf{C} = \frac{1}{N}\sum_{i=1}^{N} \mathbf{dx}_i \cdot \mathbf{dx}_i^{\mathrm{T}} \tag{4.4}$$

where N is the number of vectors in the training set, $\mathbf{dx}_i$ is the deviation of vector $\mathbf{x}_i$ from the mean shape $\overline{\mathbf{x}}$ given by

$$\mathbf{dx}_i = \mathbf{x}_i - \overline{\mathbf{x}} \tag{4.5}$$

The modes of variation, given by the principle axes of the transformation, are described by the unit eigenvectors $\mathbf{p}_i$ of the matrix **C** such that

$$\begin{aligned} \mathbf{Cp}_i &= \lambda_i \mathbf{p}_i \\ \text{and } \mathbf{p}_i \cdot \mathbf{p}_i^{\mathrm{T}} &= 1 \end{aligned} \tag{4.6}$$

where λ_i is the ith eigenvalues of the covariance matrix **C** which represents the variance of the vectors in the ith dimension and the eigenvectors are arranged in such a way that $\lambda_i \geq \lambda_{i+1}$.

By applying PCA, the dimensionality of the sample space or the number of parameters required may be reduced by truncating the dimension with the least variance. The number of dimensions or parameters needed is determined by the total variance of the samples, where the total variance represented by t-dimension is

$$\lambda_T = \sum_{i=1}^{t} \lambda_i \tag{4.7}$$

It is usually sufficient to ensure that 98% of the variation is captured, *i.e.* $\lambda_T / \lambda_{All} \geq 0.98$. In this way, any instance **x** can be approximated by using the mean shape and a linear combination of its deviation as follow:

$$\mathbf{x} = \bar{\mathbf{x}} + \mathbf{P}_s \cdot \mathbf{b}_s \tag{4.8}$$

where $\mathbf{P}_s = (\mathbf{p}_1, \mathbf{p}_2, \ldots, \mathbf{p}_t)$ is the set of orthogonal modes of variations and $\mathbf{b}_s$ is a set of shape parameters. With the PDM as described in Equation (4.8), new shapes can be generated by varying the shape parameter $\mathbf{b}_s$ within suitable limits. The variation of the shape parameter can be restricted by ensuring that the Mahalanobis distance D_m is less than a predefined threshold

$$D_m^2 = \sum_{i=1}^{t} \left(\frac{b_i}{\lambda_i} \right)^2 \leq D_{\max}^2 \tag{4.9}$$

After the PDM is built, a functional is needed for evaluating the fit of current shape model to the unseen image. The original ASM used the intensity distribution or the gradient profiles normal to the shape boundary to determine the quality of the fitted model [152]. Several other similarity measures have been developed since then. One such method used the cross correlation coefficient between the measured and the mean profiles [158]. Cootes *et al.* proposed a non-linear representation of the appearance with improved robustness against lighting conditions in computer vision applications [159]. Using their method, both the orientation and the magnitude of the local gradient were evaluated at each pixel in the region of interest.

To overcome the problem of converging to local minima in the model matching process, multi-resolution strategy has been employed [160, 161]. This approach involves convoluting each image with Gaussian kernels of different scales in which the result from the coarse scale is used as the starting point of the subsequent finer resolutions. The potential of statistical shape models for 3D segmentation of anatomical structures from medical images have been demonstrated. Mitchell *et al.* generalised the concept of concatenating the shape vectors in spatio-temporal statistical shape and appearance models and extended it for volumetric data [162]. In this approach, a stack of planar contours was used to represent the PDM in 3D under the assumption that the underlying topology of the model was cylindrical or parabolic. Based on similar contour-based representation, several 3D PDMs have been implemented [163, 164]. These implementations have one major drawback that the topology of the derived model is constrained with the planes, thereby limiting the variations to the radial directions. As a result, the through-plane motion as well as non-radial components of the motion of the heart cannot be modelled. In view of this shortcoming, more generic representations have been proposed. One representation used spherical harmonic coefficient to build a parametric statistical shape model, in which the intensity information at the object boundary was represented as 1D profiles normal to the surface [165].

Based on the observation that the AAM tends to be less sensitive to local structure and boundary information whereas the ASM locates local boundaries well while disregarding the global shape, hybrid models that combine both models has been proposed. In a study by Mitchell *et al.*, a multistage hybrid model was proposed for the segmentation of the left and right ventricles in cardiac MR images [166]. In this method, both models were run in turn and the model parameters were combined after each turn and the process is repeated until convergence. In another study, the ASM was combined with the Active Contour Model for the segmentation of the left ventricle from echocardiography [167].

4.3.2 Patient Specific Flow Simulation with CFD

4.3.2.1 Navier-Stokes Equations

With a reliable morphological definition of the left ventricle and an appropriate setting of boundary conditions, it is possible to perform computational prediction of blood flow patterns. In fluid dynamics, the Navier-Stokes equations are a set of equations that describe the flow of fluid [168]. The equations are derived by considering the conservation of mass, momentum and energy for an infinitesimal control volume. For incompressible flow, the Navier-Stokes equations are given by [169]:

$$\frac{\partial u}{\partial x}+\frac{\partial v}{\partial y}+\frac{\partial w}{\partial y}=0 \tag{4.10}$$

for conservation of mass, and

$$\begin{aligned}
\rho\cdot\left(\frac{\partial u}{\partial t}+u\frac{\partial u}{\partial x}+v\frac{\partial u}{\partial y}+w\frac{\partial u}{\partial z}\right)&=-\frac{\partial P}{\partial x}+\eta\cdot\left(\frac{\partial^2 u}{\partial x^2}+\frac{\partial^2 u}{\partial y^2}+\frac{\partial^2 u}{\partial z^2}\right)+\rho\cdot F_x\\
\rho\cdot\left(\frac{\partial v}{\partial t}+u\frac{\partial v}{\partial x}+v\frac{\partial v}{\partial y}+w\frac{\partial v}{\partial z}\right)&=-\frac{\partial P}{\partial y}+\eta\cdot\left(\frac{\partial^2 v}{\partial x^2}+\frac{\partial^2 v}{\partial y^2}+\frac{\partial^2 v}{\partial z^2}\right)+\rho\cdot F_y\\
\rho\cdot\left(\frac{\partial w}{\partial t}+u\frac{\partial w}{\partial x}+v\frac{\partial w}{\partial y}+w\frac{\partial w}{\partial z}\right)&=-\frac{\partial P}{\partial z}+\eta\cdot\left(\frac{\partial^2 w}{\partial x^2}+\frac{\partial^2 w}{\partial y^2}+\frac{\partial^2 w}{\partial z^2}\right)+\rho\cdot F_z
\end{aligned} \tag{4.11}$$

for conservation of momentum, where u, v and w are the velocity components of the fluid, ρ the density of the fluid, P the pressure, η is the dynamic viscosity, and F_x, F_y and F_z the components of the body force, such as gravity, acting directly on the fluid. Equation (4.10) is often referred to as the equation of continuity.

4.3.2.2 Mesh Generation

As discussed earlier, meshing is a vital process in CFD flow simulation. The process of dividing the flow domain into a large number of cells, which are usually tetrahedral or hexahedral, is a challenging problem itself. This is because an interwoven set of conditions must be maintained in the process. First of all, every point within the flow domain must be included in one and only one cell. Secondly, neighbouring cells should have approximately the same size and thirdly, the shape of the cells should not vary extensively from a regular tetrahedron or hexahedron. For flow domains with a simple structure, a basic method called structured meshing may be used. On the other hand, flow domains with a complex structure require a more sophisticated technique called unstructured meshing.

Structured Meshing

There are many well-established methods of structured mesh generation in the literature [170-172]. In a typical structure mesh, the flow domain is typically divided into a large set of hexahedral cells arranged in a regular lattice. With this regular layout, neighbouring cells have similar size and orientation and the neighbours of each cell can be efficiently identified with a simple indexing scheme. Limited by its simplicity, this technique can only be applied to relatively simple topologies. Objects that have the same topologies as a hexahedron can be represented by one single lattice. On the other hand, for more complex topologies such as cylinders, spheres and bifurcation, a block-structured approach may be adopted to first divide the flow domain into a number of lattice structures and then further divide each lattice structures into a large set of hexahedral cells. Care must be taken when partitioning the entire domain into lattice structures to ensure that the number of cells on both sides of each interface is equal.

Unstructured Meshing

Contrary to structured meshing, unstructured meshing allows any number of elements to meet at a single node, *i.e.* the cells are arranged in an irregular mesh [173-175]. This irregular arrangement requires a separate list to store the connectivity information, thus adding extra complexity to the computation process. Nevertheless, the flexibility in cell

arrangement allows the modelling of more complex structures that could not be achieved with structured meshing.

In unstructured meshing, tetrahedral meshes are most commonly used. A large number of tetrahedral meshing techniques have been established over the years and they can be broadly categorised into three main classes: Octree [176, 177], Delaunay [178-180] and Advancing Front [181-184]. The Octree techniques involve recursively sub-dividing the cubes containing the geometric model until the desired resolution is reached. The Delaunay techniques refer to mesh generation methods that utilise the Delaunay criterion, which states that every circumcircle of any three points must be an empty circle. With the Advancing Front method, tetrahedrons are built progressively inward from the triangulated surface while an active front of the newly formed tetrahedrons is maintained.

4.3.2.3 Numerical Flow Simulation

With recent advances in CFD, it is now possible to simulate time-dependent 3D blood flow. Blood flow is generally considered to be incompressible, viscous and laminar. Except for very simple steady flow, exact solution for the Navier-Stokes equations do not exist. Numerical methods are required to solve the Navier-Stokes equations. Methods commonly used in CFD are finite difference method (FDM), finite volume method (FVM) and finite element method (FEM).

To obtain a unique solution in a CFD simulation, the boundary conditions have to be specified at all points on the outer surface of the fluid domain. In general, three types of boundary conditions are used, for flow inlet, outlet and impermeable walls. For flow inlet, Dirichlet conditions are used, in which the velocity at each boundary point is specified. For flow outlet, Neumann conditions, in which the derivative of the velocity is specified instead of its actual value, are applied such that the outflow velocity can be made to be dependent on the flow simulation. For impermeable walls, they are simply represented by setting the velocity of the fluid relative to the boundary to zero.

Finite Difference Method

Finite difference method (FDM) [185] is the simplest method used in CFD applications. This method requires that the domain, including the boundary of the physical problem, being covered by a grid or mesh. At each of the interior grid point the original Differential Equations are replaced by equivalent finite difference approximations. By substituting the partial derivative terms in the PDE with its equivalent finite difference approximations, a difference equation is obtained. The finite difference approximations are usually obtained by Taylor series expansion or polynomial fitting. In this substitution process, an error that is proportional to the size of the grid is introduced. This error can be reduced by making the grid size smaller to get an accurate solution within some specified tolerance. Although the FDM is simple to implement and computationally inexpensive, its applications are generally restricted to simple geometries.

Finite Volume Method

Finite volume method (FVM) is generally considered as the standard approach in commercial software and research world. The solution domain is divided into a finite number of control volumes (CV). Unlike the FDM, the FVM starts from the integral form of the conservation equations. In each CV, the solution at the centre is first computed and is then used to calculate the values at the CV surface by interpolation. The advantage of the finite volume method is that it can be easily formulated to allow for unstructured meshes. Hence, it is particularly suitable for complex geometries.

Finite Element Method

Finite element method (FEM) involves breaking up a solution domain into small regions known as finite elements. Similar to the FVM, an approximating function known as interpolation polynomial is selected to represent the variation of the dependent variable within each element. The equations are then multiplied with a weighting function to produce a set of algebraic equations, one equation for each element. The set of algebraic equations are then solved to get the approximate solution of the problem. Solutions are found for each region taking into account only the regions that are right next to the one

being solved. Therefore, the FEM formulation requires special care to ensure a conservative solution.

4.3.2.4 Immersed Boundary Method

The immersed boundary (IB) method is an innovative approach for simulating fluid-structure interaction given the information on geometry and contractile pattern [186]. This method is applicable to any modelling problem in which fluid flows interact with a flexible, elastic boundary such as the muscle fibres of the heart [187]. In essence, it is a "coupled system", in which the elastic boundary moves the fluid at the same time as the fluid pushes back against it and thus, the standard techniques of computational fluid dynamic are inadequate. This technique represents an alternative to blood flow simulation where the prescription of the cardiac wall motion is not required.

The principle of the immersed boundary method is to treat the elastic material as part of the fluid in which additional forces arising from the elastic stresses are applied. The fluid equations are solved on a regular cubic lattice, while the elastic material is tracked by following a set of pre-defined points. First, the elastic forces are computed from the spatial configuration of the pre-defined material points. Subsequently, the fluid velocities of the neighbouring fluid lattice points under the influence of the elastic forces are updated and the updated velocities are then interpolated to obtain the velocity at the elastic material points. Finally, the elastic material points are moved at the calculated velocity.

4.4 Towards Subject Specific Ventricular Blood Flow Simulation

The success of CFD techniques in flow modelling has greatly advanced research into physiological blood flow modelling. Studies have been performed to investigate ventricular blood flow using CFD. Most of the early studies that apply CFD in cardiac blood flow simulation used simplified heart models [188-191]. As these models represent huge simplifications of the geometry of the heart, the practicality was limited to qualitative

analysis. Nevertheless, similar techniques can be combined with more realistic model to allow quantitative analysis. Attempts have been made to improve the ventricular flow simulation by deriving a ventricular model from real anatomical data. In one such study, a realistic model of a canine left ventricle was constructed from a cast using a coordinate measuring device [11]. With this model, it was found that complex vortices were formed in the diastolic phase and these complex vortices could account for experimentally observed turbulent blood flow fluctuations in the aorta.

With the recent improvement in the spatial and temporal resolutions of medical imaging techniques, subject specific ventricular modelling and blood flow simulation were made possible [192-194]. Various techniques for constructing realistic anatomical geometry of the heart from medical images were developed and they have been discussed in the previous sections. The derived ventricular models can be combined with flow simulation techniques to allow subject-specific flow simulation and analysis. One of the early patient specific flow simulation study was performed by Jones *et al.*, where the LV models were constructed from tagged MR images [192]. Using tagged images, twisting motion of the left ventricle may be captured, thereby improving the accuracy of the subsequent flow simulation. Another patient specific flow modelling study also employed MR images to obtain anatomical information of the LV [193]. In this study, the simulation involved the construction of a geometric model of the LV and imposition of flux conditions at orifices that corresponds to the mitral and aortic valves. The flow structure and qualitative characteristics derived from their model agreed well with *in vivo* clinical experiments. However, some quantitative discrepancies were found between the CFD and MRI flow velocities. These discrepancies were believed to be caused by the limitations of the MR dataset in the valve region, heart rate differences in the anatomical and velocity acquisitions, and certain conditions that were not simulated.

In a clinical investigation performed by Merrifield [195], the flow fields in the left ventricle of a patient who had a history of myocardial infarction measured with MR velocity imaging and simulated using CFD techniques were compared. Their results showed that the overall topology and some key flow features such as the formation of a vortex in diastole were similar in both flow fields. However, discrepancies were also displayed in the inflow direction and the formation of a vortex near the outflow tract.

Despite the advances in ventricular modelling, the prescription of proper flow boundary conditions remains one of the major challenges towards accurate subject specific flow simulation [196]. In most ventricular flow simulation studies, the aortic and mitral valves are not modelled explicitly but are typically simplified as an inflow or outflow boundary that opens and closes at specific times. It has been demonstrated that the predicted flow was highly sensitive to the prescribed boundary conditions. To further improve the robustness of existing subject specific CFD simulation techniques, Long *et al.* have developed a technique for improving the prescription of inflow boundary conditions [197].

4.5 Conclusions

Blood flow patterns *in vivo* are complex, and abnormal flow patterns have been implicated in various cardiovascular diseases such as atherosclerosis and aortic aneurysm. With the availability of detailed *in vivo* blood flow information acquired by MR velocity imaging techniques, comprehensive studies in exploring the relation between blood flow and cardiovascular disease are possible. In this chapter, key clinical applications of blood flow analysis have been discussed.

Atherosclerosis, being the leading cause of death in the developed world, has been studied extensively. Methods have been developed to derive wall shear stress from velocity data. Most studies have confirmed the hypothesis that wall shear stress is a localising factor in atherosclerosis. To elucidate the complex flow patterns *in vivo*, various visualisation techniques have been developed over the years. These techniques provide convenient ways to interpret the flow patterns and have greatly improved our understanding of the transition and underlying structure of blood flow.

The flow patterns in the aorta and the great vessels that are prone to atherosclerosis are an active area of research. Abnormal flow patterns have been reported in the great vessels of patients with atherosclerotic coronary artery diseases. It was suggested that these disturbed flow patterns could be both the causes and consequences of cardiovascular disease. To further characterise the difference between normal and disturbed flow patterns, methods for quantifying the flow features are necessary. The idea of extracting salient flow features

such as vortices and tracking its evolution over the cardiac cycle has been proposed. By using this approach, significant differences in the vortical flow patterns between normal and dilated ventricle were reported. This study has demonstrated the potential of quantitative flow pattern analysis in exploring the interaction between blood flow and its surrounding structure in health and disease.

Like any feature extraction techniques, the reliability of the method is highly dependent on the quality of the underlying data. As discussed in Chapter 3, there are many different factors that can introduce artefact to the MR velocity data. The prerequisite of flow pattern analysis is therefore the development of a robust flow restoration method that can facilitate the subsequent feature extraction process. In this thesis, we have developed an analysis framework that consists of three main components: flow field restoration, flow field abstraction and feature extraction and vortex tracking. Each of these components will be described in detail in the next three chapters. With the proposed framework, it is possible to extract and quantify vortical flow patterns in a systematic way, thus making it easier to characterise abnormal flow patterns and perform inter- and intra-subjects comparison.

Chapter 5

Flow Field Restoration

5.1 Introduction

To enable a systematic study and quantitative analysis of the flow patterns, several techniques for extracting salient topological features depicted by phase contrast MR velocity mapping techniques have been developed in recent years. The success of these techniques, however, depends greatly on the quality of the MR images. Flow velocity images acquired with MR velocity-mapping are subject to a certain amount of noise that is intrinsic to system hardware setup and specific to patient movement in relation to imaging sequence designs. In practice, the signal-to-noise ratio (SNR) is frequently compromised in order to increase the speed of the image acquisition. To alleviate this problem, it is desirable to enhance the overall quality of the velocity data prior to analytical assessment of blood flow patterns.

Restoration and denoising of vector-valued image has drawn a lot of interest in recent years due to its general applicability to a wide variety of applications [198-200], which include colour image restoration [201-203], regularization of orientation [204] and tensor fields[205-208]. Majority of the existing methods are based on functional minimisations

via a variational approach[209-211], and Total Variation (TV) based method is one of the most commonly used technique [212-214]. The choice of TV norm as the function to be minimised is due to the fact that it does not penalise discontinuities, thus edges and other topological features in the image can be preserved. TV-based restoration methods have been demonstrated to be effective and superior to linear filtering methods for scalar images [215], and several researchers have extended TV norm to vector-valued image [201, 211]. In particular, Chan and Shen [211] have extended the definition of TV-norm for the restoration of non-flat image features that do not reside on Euclidean space. Examples of commonly encountered non-flat image features include vector distribution from flow images and chromaticity features from colour images. Coulon *et al.* [216]has applied this method to restore the principal diffusion direction (PDD) of Diffusion Tensor Magnetic Resonance (DT-MR) images.

The restoration method in this study is formulated as a constrained optimisation problem that restores the original images by minimising the total variation (TV) energy of the normalised velocity field subject to a constraint that depends on the noise level. It has been shown that the effectiveness of this restoration method greatly depends on the choice of a regularization parameter [211], which is often conveniently fixed or determined empirically in practice. This renders a major difficulty to the practical application of the technique as the restored image may converge to different results depending on the parameter settings. To avoid having to fix this parameter, we propose to use the First Order Lagrangian Method to derive the optimal value of this parameter while solving the minimisation problem.

5.2 Total Variation (TV) Based Restoration

Image restoration method based on the total variation (TV) norm was first introduced by Rudin *et al.* [215]. TV norms are essentially L_1 norms of the gradients. Using TV norms in image restoration problem allows discontinuities to be preserved while spurious oscillations are removed. Rudin *et al.* have formulated the image restoration problem as a constrained minimisation problem. The image restoration problem is given by

$$u_0(x,y) = u(x,y) + n(x,y) \tag{5.1}$$

where $u(x,y)$ denotes the original noise-free image, $u_0(x,y)$ denotes the noisy image with additive noise $n(x,y)$. By assuming that the noise is Gaussian distributed and that the variance of the noise σ^2 is known, the constrained minimisation problem can be written as

$$\text{minimise} \quad \int_\Omega \sqrt{u_x^2 + u_y^2} \tag{5.2}$$

$$\text{subject to} \quad \frac{1}{|\Omega|}\int_\Omega (u - u_0)^2 = \sigma^2 \tag{5.3}$$

where Ω denotes the image domain and $|\Omega|$ the size of the image domain.

This optimisation problem can be resolved by solving the corresponding Tikhonov regularised unconstrained problem [217], which can be written in one of the following forms:

$$\begin{aligned} &\min \int_\Omega (u - u_0)^2 + \gamma \int_\Omega \sqrt{u_x^2 + u_y^2} \\ &\min \lambda \int_\Omega (u - u_0)^2 + \int_\Omega \sqrt{u_x^2 + u_y^2} \end{aligned} \tag{5.4}$$

where λ is a regularization parameter known as the Lagrange Multiplier of the constrained optimisation problem, γ is a positive regularization parameter and is inversely proportional to λ. This approach can be viewed as a penalty approach for the constrained optimisation problem, in which the first term is to restrict the distance between the final image and the initial noisy image and the second term is the smoothness term. Several computational algorithms [213, 214] have been proposed to solve this unconstrained problem and in most cases, the value of the regularisation parameter is conveniently fixed. Alternatively, the constrained problem can be resolved by applying the First Order Lagrangian method [218], which finds both the minimal solution and the associated Lagrange Multiplier for the constrained optimisation problem.

Although the initial TV based restoration scheme was designed for the restoration of scalar images, the technique was later extended to cover vector-valued images and non-flat image features. Chan and Shen [211] have presented a systematic way for constructing the TV energy of non-flat image features. For a feature distribution $f \in (\Omega \rightarrow M)$ where Ω denotes the image domain and M represents the feature manifold, the TV norm is defined as

$$E^{TV}(f) = \int_{\Omega} e(f;\alpha) \tag{5.5}$$

where $e(f;\alpha)$ denotes the energy at pixel α which is defined as

$$e(f;\alpha) = \sqrt{\left\|\partial_x f(\alpha)\right\|^2 + \left\|\partial_y f(\alpha)\right\|^2} \tag{5.6}$$

Then, the fitted TV energy can be written as

$$E^{TV}(f;\lambda) = \int_{\Omega} e(f;\alpha) + \frac{\lambda}{2}\int_{\Omega} d^2(f_0, f) \tag{5.7}$$

where the first term regularises the restoration solution and the second term is the fitting constraint, λ is the Lagrange multiplier and d denotes the metric on M that measures the distance of the path that link any two points g and h in M.

Minimising the fitted TV energy is analogous to minimising the Tikhonov regularised unconstrained problem given in Equation (5.4). Typically, the Euler-Lagrange equation is employed to solve the unconstrained minimisation problem.

5.2.1 First Order Lagrangian Method

As discussed earlier, a constrained optimisation problem can be solved by solving its unconstrained counterpart. Alternatively, it can also be tackled directly. Consider a constrained optimisation problem with m constraints:

$$\begin{aligned} &\text{minimise } f(\mathbf{x}) \\ &\text{subject to } h_i(\mathbf{x}) = 0, \quad \mathrm{i} = 1, \ldots, \mathrm{m} \end{aligned} \tag{5.8}$$

where $\mathbf{x}$ is an n-vector, $f(\mathbf{x})$ is the function to be minimised and $h_i(\mathbf{x})$ are the equality constraints of the problem. For a minimum to exist, the gradient of the function $f(\mathbf{x})$ must equal to 0 at the minimal solution $\mathbf{x}^*$, *i.e.*

$$\nabla f(\mathbf{x}^*) = 0 \tag{5.9}$$

The constraints, being constant at the minimal solution, should have zero gradients:

$$\nabla h_i(\mathbf{x}^*) = 0, \qquad \forall i \tag{5.10}$$

Subsequently, by assuming that the gradients of the function and constraints are linearly independent, we have

$$\nabla f(\mathbf{x}^*) + \sum_{i=1}^{m} \lambda_i \nabla h_i(\mathbf{x}^*) = 0 \tag{5.11}$$

where $\lambda_1, \ldots, \lambda_m$ are scalar constants. Based on this derivation, the Lagrange Multiplier theorem states that the necessary condition for optimality is that for a given minimal solution $\mathbf{x}^*$, there exist scalars $\lambda_1, \ldots, \lambda_m$ such that they satisfy the necessary condition given in Equation (5.11), in which λ_i are referred to as the Lagrange multipliers of the constrained problem and are sometimes represented as a vector $\boldsymbol{\lambda} = [\lambda_1, \ldots, \lambda_m]$, called the Lagrange multiplier vector.

The necessary condition given in Equation (5.11), together with the set of constraints $h_i(\mathbf{x})=0$ can be viewed as a system of (n+m) nonlinear equations with (n+m) unknowns – the vectors $\mathbf{x}$ and $\boldsymbol{\lambda}$. This system of nonlinear equations is referred to as the Lagrangian system. It is sometimes more convenient to write Equation (5.11) in terms of the Lagrangian function $L(\mathbf{x}, \boldsymbol{\lambda})$ defined as

$$L(\mathbf{x},\lambda) = f(\mathbf{x}) + \sum_{i=1}^{m} \lambda_i h_i(\mathbf{x}) \tag{5.12}$$

Thus, the necessary condition given in Equation (5.11) can be rewritten compactly in the following form

$$\begin{cases} \nabla_x L(\mathbf{x}^*,\lambda^*) = 0 \\ \nabla_\lambda L(\mathbf{x}^*,\lambda^*) = 0 \end{cases} \tag{5.13}$$

where the vectors $\mathbf{x}^*$ and λ^* are the optimal solutions of the Lagrangian system.

A general class of methods, called the Lagrangian methods, for solving the Lagrangian system [218] is given by

$$\begin{aligned} \mathbf{x}^{k+1} &= G(\mathbf{x}^k,\lambda^k) \\ \lambda^{k+1} &= H(\mathbf{x}^k,\lambda^k) \end{aligned} \tag{5.14}$$

where G and H are continuously differentiable functions. The iterations defined in (5.14) can only converge at fixed points $(\mathbf{x}^*,\lambda^*)$ satisfying

$$\begin{aligned} \mathbf{x}^* &= G(\mathbf{x}^*,\lambda^*) \\ \lambda^* &= H(\mathbf{x}^*,\lambda^*) \end{aligned} \tag{5.15}$$

The simplest of all Lagrange Methods, called the First Order Method, is given by:

$$\begin{aligned} \mathbf{x}^{k+1} &= \mathbf{x}^k - \delta_s \nabla_x L(\mathbf{x}^k,\lambda^k) \\ \lambda^{k+1} &= \lambda^k + \delta_s \nabla_\lambda L(\mathbf{x}^k,\lambda^k) \end{aligned} \tag{5.16}$$

where δ_s is a positive scalar step-size and $L(\cdot)$ is the associated Lagrangian function. The convergence of this method can be proved using the Ostrowski's theorem, which states that if $(\mathbf{x}^*,\lambda^*)$ is a fixed point of the iterations defined in (5.14), and all eigenvalues of the matrix

$$\mathbf{R}^* = \begin{pmatrix} \nabla_x G(\mathbf{x}^*, \lambda^*) & \nabla_x H(\mathbf{x}^*, \lambda^*) \\ \nabla_\lambda G(\mathbf{x}^*, \lambda^*) & \nabla_\lambda H(\mathbf{x}^*, \lambda^*) \end{pmatrix} \tag{5.17}$$

lie strictly within the unit circle of the complex plane, then $(\mathbf{x}^*, \lambda^*)$ is a point of attraction of the iterations and that if the generated sequence $\{(\mathbf{x}^k, \lambda^k)\}$ converges to $(\mathbf{x}^*, \lambda^*)$, then the rate of convergence is at least linear. A pair $(\mathbf{x}^*, \lambda^*)$ is said to be a point of attraction if there exists an open set S such that if $(\mathbf{x}^0, \lambda^0) \in S$, then the sequence $\{(\mathbf{x}^k, \lambda^k)\}$ generated by the iterations also belongs to S and converges to $(\mathbf{x}^*, \lambda^*)$.

To show that the iterations given in Equation (5.16) converge for sufficiently small value of δ_s, consider its associated matrix $\mathbf{R}^*$

$$\begin{aligned} \mathbf{R}^* &= \begin{pmatrix} \nabla_x G(\mathbf{x}^*, \lambda^*) & \nabla_x H(\mathbf{x}^*, \lambda^*) \\ \nabla_\lambda G(\mathbf{x}^*, \lambda^*) & \nabla_\lambda H(\mathbf{x}^*, \lambda^*) \end{pmatrix} \\ &= \begin{pmatrix} \mathbf{I}_n - \delta_s \nabla^2_{xx} L(\mathbf{x}^*, \lambda^*) & \delta_s \nabla h(\mathbf{x}^*)' \\ -\delta_s \nabla h(\mathbf{x}^*) & \mathbf{I}_m \end{pmatrix} \\ &= \mathbf{I}_{n+m} - \delta_s \mathbf{B} \end{aligned} \tag{5.18}$$

where $$\mathbf{B} = \begin{pmatrix} \nabla^2_{xx} L(\mathbf{x}^*, \lambda^*) & -\alpha \nabla h(\mathbf{x}^*)' \\ \alpha \nabla h(\mathbf{x}^*) & \mathbf{0} \end{pmatrix} \tag{5.19}$$

It can be shown that the real part of each eigenvalues of $\mathbf{B}$ is strictly positive and that for sufficiently small value of δ_s, $\mathbf{R}^*$ satisfy the condition stated in the Ostrowski's theorem and it follows that $(\mathbf{x}^*, \lambda^*)$ is a point of attraction of the iterations given in Equation (5.16). Thus, the iterations in Equation (5.16) will converge with a small value of δ_s at a linear rate.

5.3 TV Base Flow Field Restoration

In this study, the restoration scheme is formulated as a constrained optimisation problem that minimise the TV energy of the direction field of the flow images. The definition of TV-norm for direction field proposed by Chan *et al.* [211] was adopted and a new numerical scheme based on the First Order Lagrangian Method is developed for solving the constrained optimisation problem.

Let $\mathbf{u}^0$ denote the directional field of the noisy velocity images, $\mathbf{u}$ represent the desired direction field that we want to restore and that $\mathbf{u}^0 = \mathbf{u} + \mathbf{n}$, where $\mathbf{n}$ is the additive noise. Assuming the variance of the noise $\mathbf{n}$ is σ^2 and the value of which is known, the restoration of the direction field of a velocity field can be formulated as a constrained optimisation problem by minimizing the following term

$$E^{TV}(\mathbf{u}) = \int_{\Omega} e(\mathbf{u};\alpha) \tag{5.20}$$

subject to the equality constraint:

$$h(\mathbf{u}) = \frac{1}{2}\left(\int_{\Omega} (\mathbf{u} - \mathbf{u}_0)^2 - |\Omega|\sigma^2 \right) = 0 \tag{5.21}$$

where E^{TV} denotes the total variation energy of the whole image, $e(\mathbf{u};\alpha)$ denotes the energy at pixel α, Ω denotes the image domain and $|\Omega|$ the size of the image domain.

5.3.1 Numerical Scheme

Based on the First Order Method, a numerical scheme is derived for solving the constrained optimisation problem. The definition of the TV energy for direction (*i.e.* unit vector that lives on unit sphere S^2) and the numerical scheme of our proposed method can be defined as follows.

Let **v** denotes the velocity vector defined in $\mathbf{R}^3$ and **u** denotes the corresponding normalised vector defined in $\mathbf{S}^2$. The velocity vector **v** is mapped to the unit vector **u** by a mapping f: $\mathbf{R}^3 \rightarrow \mathbf{S}^2$ defined as:

$$\mathbf{u} = \mathbf{f}(\mathbf{v}) = \frac{\mathbf{v}}{|\mathbf{v}|} \tag{5.22}$$

Note that the mapping defined in Equation (5.22) is valid for both 2D and 3D vectors as we can consider a 2D vector as a 3D vector with the z-component set to zero. Therefore, the following formulation applies to both 2D and 3D vector fields.

The strength function $e(\mathbf{u};\alpha)$ at voxel α can be defined as:

$$e(\mathbf{u};\alpha) = \left[\sum_{\beta \in N\alpha} d_l^2(\mathbf{u}_\beta, \mathbf{u}_\alpha) \right]^{\frac{1}{2}} \tag{5.23}$$

where N_α denotes the neighbourhood of voxel α, d_l denotes the embedded Euclidean distance in $\mathbf{S}^2$ and is given by:

$$d_l(\mathbf{f},\mathbf{g}) = \|\mathbf{f} - \mathbf{g}\|_{R^3} \; \forall \mathbf{f},\mathbf{g} \in S^2 \tag{5.24}$$

The total variation (TV) energy of the direction field is then:

$$E^{TV} = \sum_{\alpha \in \Omega} \left[\sum_{\beta \in N\alpha} d_l^2(\mathbf{u}_\beta, \mathbf{u}_\alpha) \right]^{\frac{1}{2}} \tag{5.25}$$

Therefore, the constrained optimisation problem becomes:

$$\min E^{TV} = \sum_{\alpha}\left[\sum_{\beta\in N\alpha} d_l^2(\mathbf{u}_\beta,\mathbf{u}_\alpha)\right]^{\frac{1}{2}} \tag{5.26}$$

subject to:

$$\frac{1}{2}\left[\sum_{\alpha\in\Omega} d_l^2(\mathbf{u}_\alpha,\mathbf{u}_\alpha^0)-|\Omega|\sigma^2\right]=0 \tag{5.27}$$

The corresponding Lagrangian function, referred to as the unconstrained TV energy, is:

$$L(\mathbf{u};\lambda)=\sum_{\alpha\in\Omega}\left[\sum_{\beta\in N\alpha} d_l^2(\mathbf{u}_\beta,\mathbf{u}_\alpha)\right]^{\frac{1}{2}}+\frac{\lambda}{2}\left[\sum_{\alpha\in\Omega} d_l^2(\mathbf{u}_\alpha,\mathbf{u}_\alpha^0)-|\Omega|\sigma^2\right] \tag{5.28}$$

Note that at the optimal solution, $L(\mathbf{u};\lambda)$ is the same as the constrained TV energy E^{TV} because at the minimal point, the second term of the equation equals to zero when the constraint is met.

To compute the gradient of $L(\mathbf{u};\lambda)$ w.r.t. $\mathbf{u}$ at $\mathbf{u}_\alpha$, we first consider the first term on the right hand side of Equation (5.28)

$$\begin{aligned}
&\frac{\partial}{\partial\mathbf{u}_\alpha}\sum_{\alpha\in\Omega}\left[\sum_{\beta\in N\alpha} d_l^2(\mathbf{u}_\beta,\mathbf{u}_\alpha)\right]^{\frac{1}{2}}\\
&=\frac{\partial}{\partial\mathbf{u}_\alpha}\left[\sum_{\beta\in N\alpha} d_l^2(\mathbf{u}_\beta,\mathbf{u}_\alpha)\right]^{\frac{1}{2}}+\sum_{\beta\in N_\alpha}\left(\frac{\partial}{\partial\mathbf{u}_\alpha}\left[\sum_{\alpha\in N\beta} d_l^2(\mathbf{u}_\alpha,\mathbf{u}_\beta)\right]^{\frac{1}{2}}\right)\\
&=\frac{1}{2}\frac{1}{e(\mathbf{u};\alpha)}\frac{\partial}{\partial\mathbf{u}_\alpha}\left[\sum_{\beta\in N\alpha} d_l^2(\mathbf{u}_\beta,\mathbf{u}_\alpha)\right]+\sum_{\beta\in N_\alpha}\left(\frac{1}{2}\frac{1}{e(\mathbf{u};\beta)}\frac{\partial}{\partial\mathbf{u}_\alpha}\left[\sum_{\alpha\in N\beta} d_l^2(\mathbf{u}_\alpha,\mathbf{u}_\beta)\right]\right)\\
&=\sum_{\beta\in N_\alpha}\left(\frac{1}{2}\left(\frac{1}{e(\mathbf{u};\alpha)}+\frac{1}{e(\mathbf{u};\beta)}\right)\frac{\partial}{\partial\mathbf{u}_\alpha}\left[\sum_{\alpha\in N\beta} d_l^2(\mathbf{u}_\alpha,\mathbf{u}_\beta)\right]\right)
\end{aligned} \tag{5.29}$$

Accordingly, the gradient of the second term on the right hand side of Equation (5.28) can be derived as follow:

$$\frac{\partial}{\partial \mathbf{u}_\alpha}\left(\frac{\lambda}{2}\left[\sum_{\alpha\in\Omega} d_l^2(\mathbf{u}_\alpha,\mathbf{u}_\alpha^0)-|\Omega|\sigma^2\right]\right)=\frac{\lambda}{2}\frac{\partial}{\partial \mathbf{u}_\alpha}d_l^2(\mathbf{u}_\alpha,\mathbf{u}_\alpha^0) \tag{5.30}$$

By combining Equations (5.29) and (5.30), the gradient of $L(\mathbf{u};\lambda)$ w.r.t. $\mathbf{u}$ at $\mathbf{u}_\alpha$ is given by

$$\begin{aligned}\frac{\partial L}{\partial \mathbf{u}_\alpha} = &\sum_{\beta\in N\alpha}\left[\frac{\partial}{\partial \mathbf{u}_\alpha}d_l^2(\mathbf{u}_\beta,\mathbf{u}_\alpha)\right]\left(\frac{1}{2}\left[\frac{1}{e(\mathbf{u};\alpha)}+\frac{1}{e(\mathbf{u};\beta)}\right]\right)\\ &+\frac{\lambda}{2}\left(\frac{\partial}{\partial \mathbf{u}_\alpha}d_l^2(\mathbf{u}_\alpha,\mathbf{u}_\alpha^0)\right)\end{aligned} \tag{5.31}$$

In order to compute the gradient of any given function G(**u**) on $\mathbf{S}^2$, the gradient of G(**u**) on $\mathbf{R}^3$ is first calculated and then projected onto the plane orthogonal to **u**, *i.e.*,

$$\frac{\partial}{\partial \mathbf{u}}G(\mathbf{u})=\Pi_{\mathbf{u}}\, grad_{\mathbf{R}^3}G(\mathbf{u}) \tag{5.32}$$

where $\Pi_{\mathbf{u}}$ denotes projection to the plane orthogonal to **u**. For any vectors **f** and **g**, the projection of **g** onto the plane orthogonal to **f** can be computed by

$$\Pi_{\mathbf{f}}\,\mathbf{g}=\mathbf{g}-\left(\frac{\mathbf{f}\cdot\mathbf{g}}{|\mathbf{f}|^2}\right)\mathbf{f} \tag{5.33}$$

In the case when **f** is unit vectors, this can be simplified to

$$\Pi_{\mathbf{f}}\,\mathbf{g} = \mathbf{g} - (\mathbf{f}\cdot\mathbf{g})\mathbf{f} \tag{5.34}$$

Hence, the gradient terms in Equation (5.31) can be rewritten as follow

$$\frac{\partial}{\partial \mathbf{u}_\alpha} d_l^2(\mathbf{u}_\beta, \mathbf{u}_\alpha) = \Pi_{\mathbf{u}_\alpha} grad\left(\left[\mathbf{u}_\beta - \mathbf{u}_\alpha\right]^2\right) = -2\,\Pi_{\mathbf{u}_\alpha}(\mathbf{u}_\beta) \tag{5.35}$$

Therefore, the gradient of $L(\mathbf{u};\lambda)$ w.r.t. $\mathbf{u}$ at $\mathbf{u}_\alpha$ can be simplified to

$$\frac{\partial L}{\partial \mathbf{u}_\alpha} = -\sum_{\beta\in N\alpha} \Pi_{\mathbf{u}_\alpha}(\mathbf{u}_\beta)\left(\frac{1}{e(\mathbf{u};\alpha)} + \frac{1}{e(\mathbf{u};\beta)}\right) - \lambda\,\Pi_{\mathbf{u}_\alpha}(\mathbf{u}_\alpha^0) \tag{5.36}$$

The gradient of $L(\mathbf{u};\lambda)$ w.r.t. λ can be derived easily and is given by

$$\frac{\partial L}{\partial \lambda} = \frac{1}{2}\left[\sum_{\alpha\in\Omega} d_l^2(\mathbf{u}_\alpha, \mathbf{u}_\alpha^0) - |\Omega|\sigma^2\right] \tag{5.37}$$

Based on the above equations, the discrete form of the First Order Lagrangian method can be written as follows:

$$\begin{cases} \mathbf{u}_\alpha^{n+1} = \mathbf{u}_\alpha^n + \delta_s \cdot \Pi_{\mathbf{u}_\alpha}\left[\sum_{\beta\in N\alpha} wt_\alpha^\beta \mathbf{u}_\beta + \lambda^n \mathbf{u}_\alpha^0\right] \\ \lambda^{n+1} = \lambda^n + \delta_s \cdot \frac{1}{2}\left[\sum_{\alpha\in\Omega} d_l^2(\mathbf{u}_\alpha^n, \mathbf{u}_\alpha^0) - |\Omega|\sigma^2\right] \end{cases} \tag{5.38}$$

$$where \quad wt_\alpha^\beta = \left(\frac{1}{e(\mathbf{u};\alpha)} + \frac{1}{e(\mathbf{u};\beta)}\right)$$

To ensure that $\mathbf{u}_\alpha^{n+1}$ remains on S^2, $\mathbf{u}_\alpha^{n+1}$ is normalised at the end of each step.

In theory, the iterative algorithm is considered to have converged when the constraint is met, *i.e.* when the constrained and unconstrained energy terms converged to the same value. In practice, this can be ensured by terminating the iterative process when the differences in both the constrained and unconstrained energy terms between the current and previous iterations and that between the two energy terms are smaller than a predefined threshold. After the direction field is restored, the final velocity field is obtained by multiplying the unit vectors with the corresponding original magnitudes.

5.3.2 Validations

In order to provide a detailed analysis of the performance of the proposed restoration method, a set of 3D CFD data simulating flow in a normal left ventricle and a set of MR flow images were used for validation. To illustrate the effect of restoration, the winding index method for vortex detection was applied to the original and restored MR flow images.

5.3.2.1 CFD Simulated Data

The CFD flow simulation was based on a LV structure reconstructed from MR images of the entire LV of a normal subject [197]. A volume mesh that described the internal structure of the flow domain was generated so that the flow domain can be divided into a large set of hexahedral volumetric cells, which were then partitioned into 24 blocks. This mesh generation scheme gives a final model that contains 54,230 nodes and 41,000 cells. To enable CFD simulation, a higher temporal resolution than that acquired by MR images is required. This is achieved by applying cubic spline interpolations to generate 60 meshes from the 20 meshes generated from the MR images over the cardiac cycle. With the final LV model constructed, the blood flow was simulated by solving the Navier-Stokes equations for 3D unsteady laminar flow with prescribed wall motions using CFX4 (AEA technology), a finite-volume based CFD solver. The simulation was repeated until a periodic solution was reached and the result obtained in the following cycle was used.

A set of 2D flow data was then extracted from the 3D data at a particular time frame and Gaussian noise was added to the velocity distribution and the corresponding noise variance

in the direction field was then calculated from the noisy velocity data to assess the accuracy of the proposed technique.

5.3.2.2 MR Velocity Mapping Data

Twelve MR flow velocity data sets acquired from five patients with sequential examination following myocardial infarction with consent were selected from seventeen data sets for evaluating the proposed flow restoration method. The five discarded datasets were too noisy to be used. All images were acquired using a Picker Edge whole body MR scanner operating at 1.5T. Cine phase contrast velocity mapping was performed using a Field Even Echo Rephasing (FEER) sequence with a flip angle of 30° and a TE of 4.4ms. The sequence is ECG-gated and velocity encoding was performed on all 3 velocity-axes with a velocity sensitivity (VENC) of 200cm/s. The slice thickness was 10mm and the in-plane pixel size is 2mm by 3.125mm, with a field of view of 30-40cm. Selected frames acquired during diastole from the 12 datasets were used for validation. The datasets have a temporal resolution of 40ms-50ms and the diastolic phase is covered in about 5-10 frames.

5.3.2.3 Winding Index Method

Winding index method is a traditionally used vortex detection method. Winding index is the total accumulated directional change for a vector field along a closed path that encloses the point of interest. It can be computed using the equation:

$$C_{index} = \frac{1}{2\pi}\sum_{i=1}^{N}\psi(\theta_{i+1} - \theta_i) \tag{5.39}$$

where N is the number of velocity vectors along the path, θ_i is the angle formed by a vector v_i and the x-axis and $\psi(\cdot)$ is a phase-wrapping operator that confines the angular difference between adjacent vectors within the range $(-\pi, \pi)$. If the selected closed path encloses a single critical point, the value of C_{index} will be 1.

After a critical point is extracted by calculating the index, it can be classified by using the phase portrait theory. This is accomplished by examining the eigenvalues of the

characteristic matrix $\vec{A}$ of each critical point. A critical point is classified as a vortex if the imaginary parts of the eigenvalues of $\vec{A}$ are large. Further details on using phase portrait theory on classifying critical points are provided in the next chapter.

5.4 Results

5.4.1 CFD Simulated Data

To analyse the sensitivity of the regularization parameter, the existing variational method with various fixed lambda values was used to restore the noisy synthetic data with results as shown in Figure 5.1. It is found that when the value of lambda is set to be the optimal value, the restoration result is at its best and comparable to that of our newly proposed method. As expected, when the value of lambda is too small, the image is over-smoothed; whereas when the value of lambda is too big, the image is under-smoothed. The result clearly demonstrates the advantage of the proposed method in converging automatically to the optimal solution without explicitly presetting the regularization parameter.

To verify that the value of regularization parameter found by the proposed method corresponds to the optimal value, experiments with a range of lambda values were carried out and the RMS error of the results are compared. In Figure 5.2, the optimal value of lambda found empirically coincides with the value obtained by the First Order method, justifying the robustness of the proposed technique.

To assess the convergence behaviour of the proposed technique, the constrained and unconstrained energy terms and the value of lambda recorded at each step are plotted in Figure 5.3 It is found that both energy terms converge to the same value as expected and the value of lambda converges in a similar behaviour. The rate of convergence depends on the choice of step size, which is typically of the order of 0.01. The algorithm converged after approximately 1500 iterations.

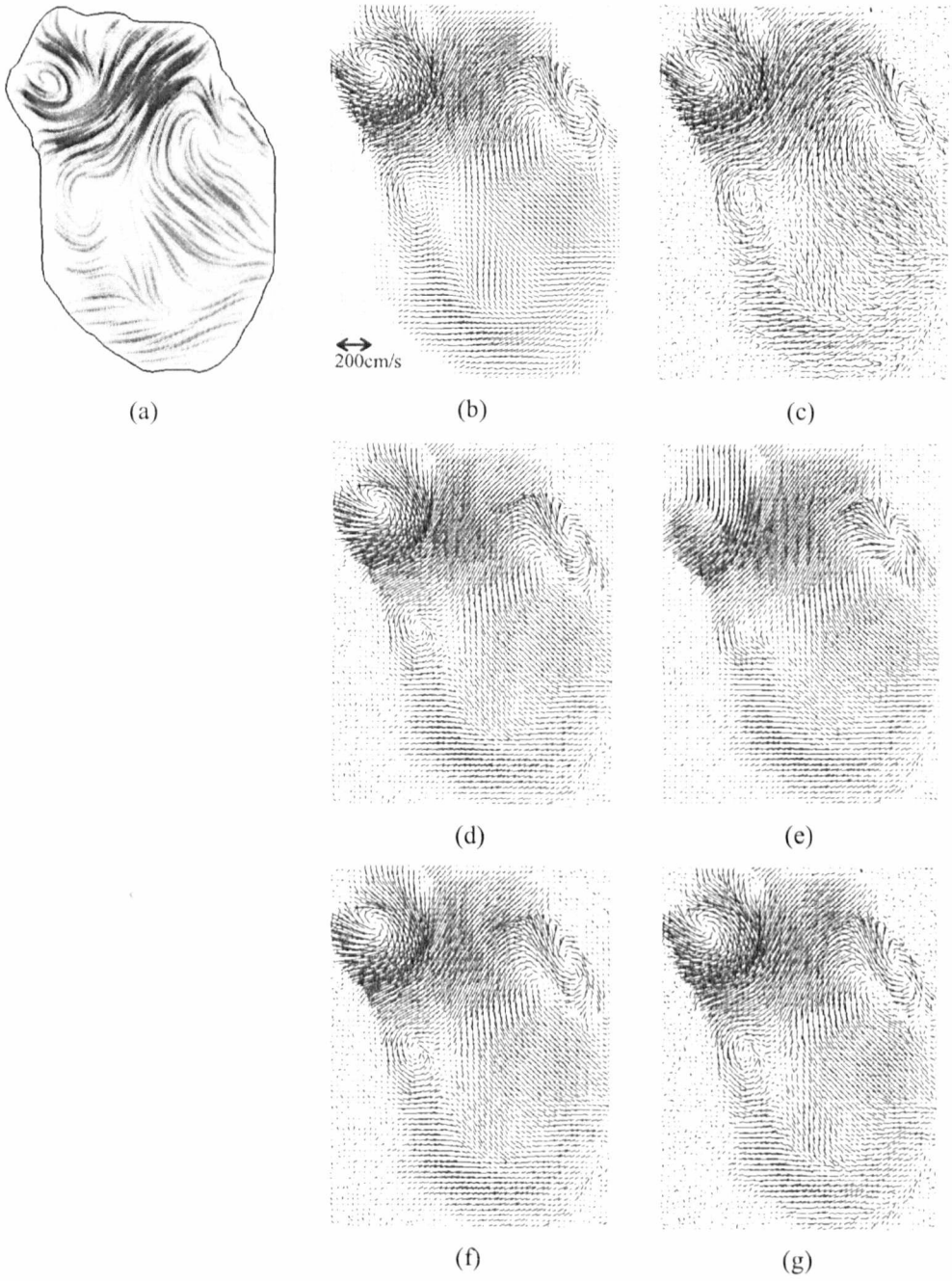

Figure 5.1 A comparison of the restored images selected from the 2D CFD dataset, which simulates flow in a normal left ventricle, with streamline flow visualisation (a), with arrow plots of the original velocity field (b), with additive noise (c), restored with First Order Method (d), restored with lambda fixed at 1.0 (over-smoothed) (e), restored with lambda fixed at 3.5 (optimal) (f), and restored with lambda fixed at 20.0 (under-smoothed) (g).

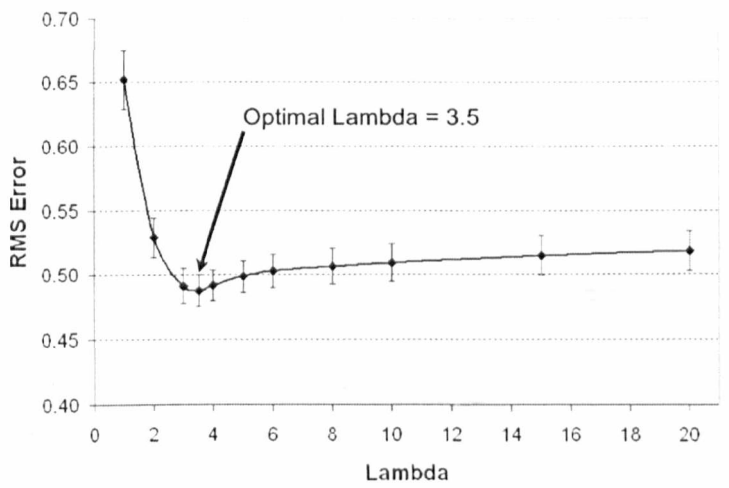

Figure 5.2 A plot of the average RMS error against the value of fixed lambda of the restoration method for the 2D CFD dataset as shown in Figure 5.1. The optimal value of lambda found automatically by the First Order Method for this dataset is 3.5, which coincides with the value determined empirically as shown in this graph.

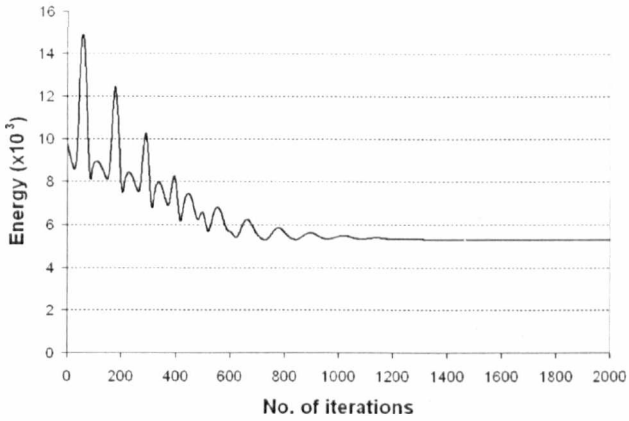

(a)

(b)

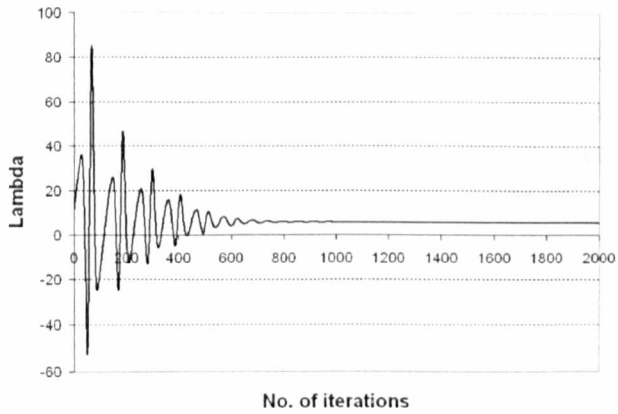

(c)

Figure 5.3 Convergence behaviour of the constrained (a) and unconstrained (b) energy terms and the value of lambda (c) of the restoration process of the 2D CFD data shown in Figure 5.1. (Note the difference in the scales of the two energy terms.)

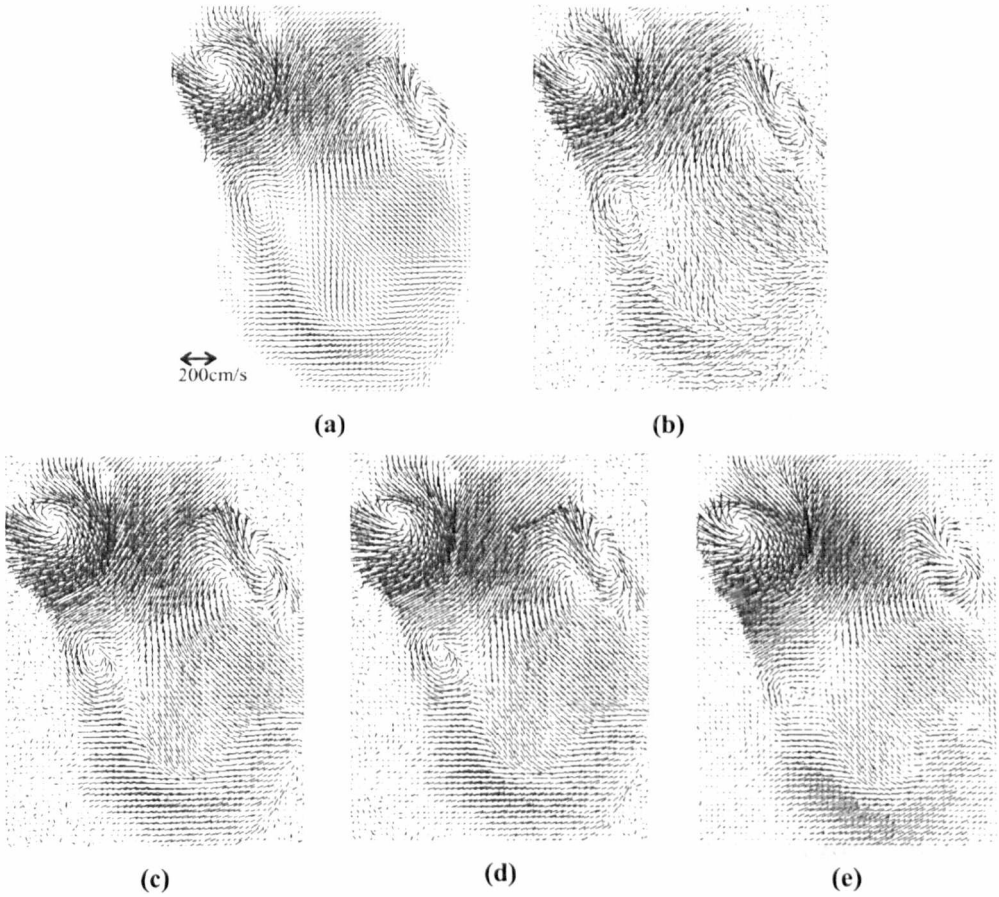

Figure 5.4 A comparison of the restored images selected from the 2D CFD dataset, which simulates flow in a normal left ventricle, with arrow plots of the original velocity field (a), restored with estimated noise variance = 0.10 (b), restored with estimated noise variance = 0.30 (actual value) (c) and restored with estimated noise variance = 0.50 (d).

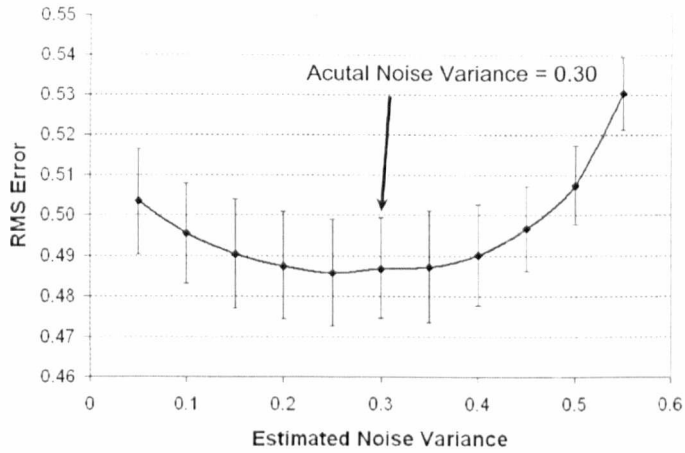

Figure 5.5 A plot of the average RMS error of the 2D CFD dataset against the estimated noise variance. The actual noise variance is 0.30.

To analyse the sensitivity of the restoration method to the estimated noise variance, experiments with a range of variance were carried out and the results were compared with that of using the known value. Figure 5.4 demonstrates the restoration results with different estimated noise variance. It is apparent that the restoration process is not sensitive to the estimated noise level within the range of $\pm 50\%$ of the actual value. As a reference, Figure 5.5 illustrates the RMS errors of the restoration results at various estimated noise variance, further justifying the immunity of the restoration result to the selection of σ .

Although the main framework of this study is described for 2D velocity mappings, the restoration method can be readily applied to restore 3D flow data. To evaluate the effectiveness of the proposed method on 3D flow data, the 3D CFD dataset simulating flow in a normal left ventricle was used. The visualised streamline plot of the simulated flow at a selected time frame during diastole is illustrated in Figure 5.6(a), which depicts the formation of a vortex ring in the left ventricle. The proposed method and the existing variational method with various fixed λ values were applied to restore the noisy flow pattern. It is evident from Figure 5.6 that a similar trend to that of 2D flow data can be observed. That is, when the value of lambda is set to be smaller than the optimal value, the image is over-smoothed; when the value of lambda is too big, the image is under-smoothed.

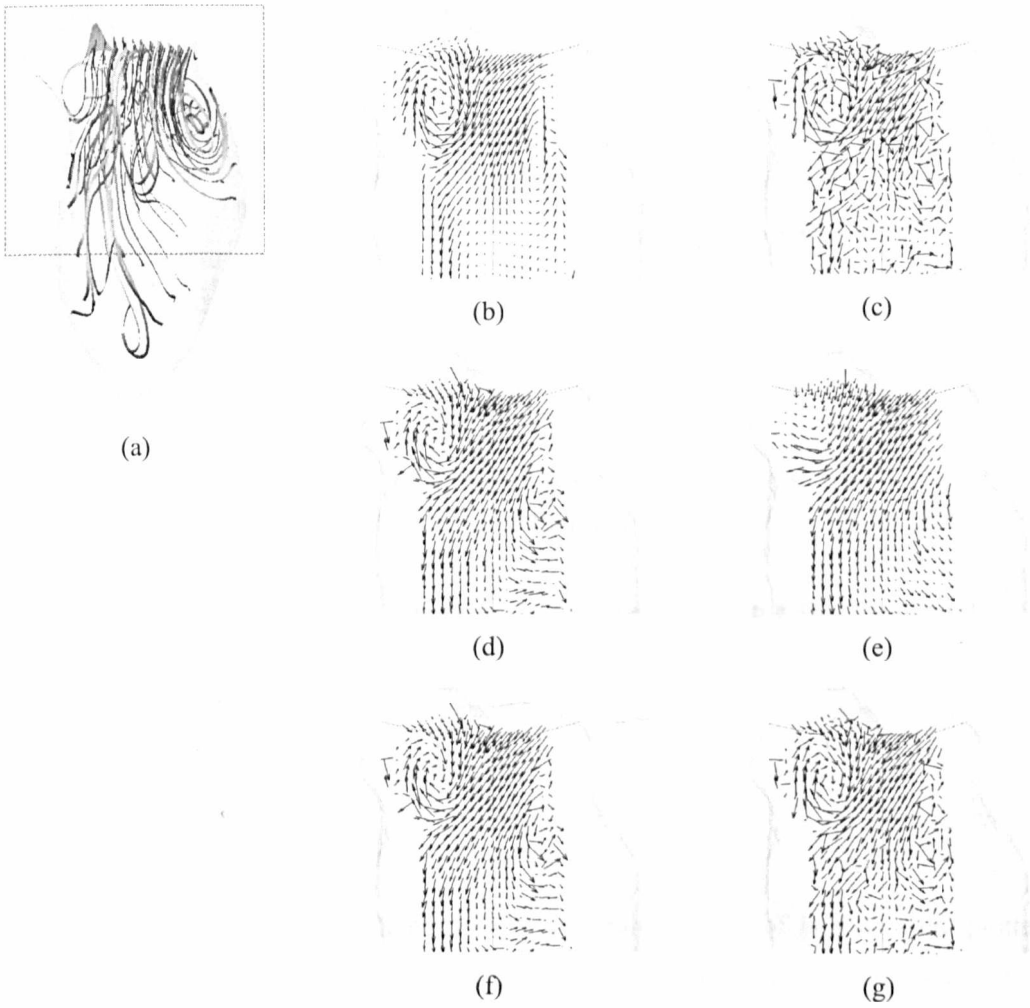

Figure 5.6 A comparison of the restored images selected from the 3D dataset, which simulates blood flow in the left ventricle during diastole, with streamline flow visualisation (a) and arrow plots of the original velocity field (b), with additive noise (noise variance = 0.15) (c), restored with First Order method (d), restored with lambda fixed at 1.5 (over-smoothed) (e), restored with lambda fixed at 3.5 (optimal) (f), and restored with lambda fixed at 7.0 (under-smoothed) (g).

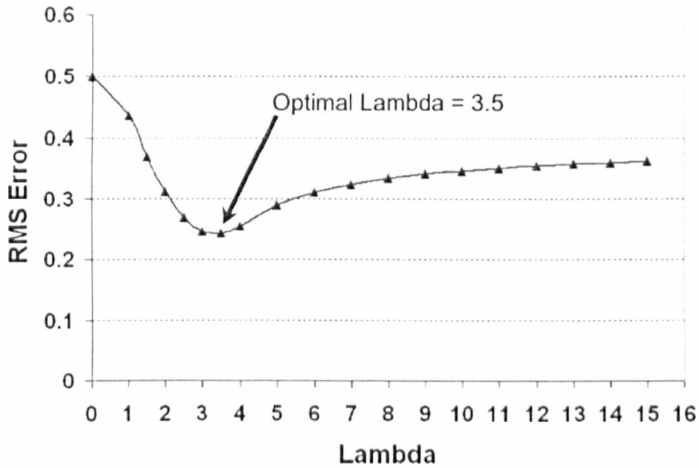

Figure 5.7 Plots of the RMS error against the value of lambda for the 3D CFD dataset.

The corresponding RMS error of the results at various values of lambda were plotted in Figure 5.7 and the optimal value of lambda found empirically also coincides with the value obtained by the First Order method. In order to assess the convergence behaviour of the energy terms and lambda, the values of the constrained and unconstrained energy and lambda were plotted against the number of iterations as depicted in Figure 5.8. The graphs show that all three values converged after about 5000 iterations in a similar behaviour and the two energy terms converged to the same value as expected.

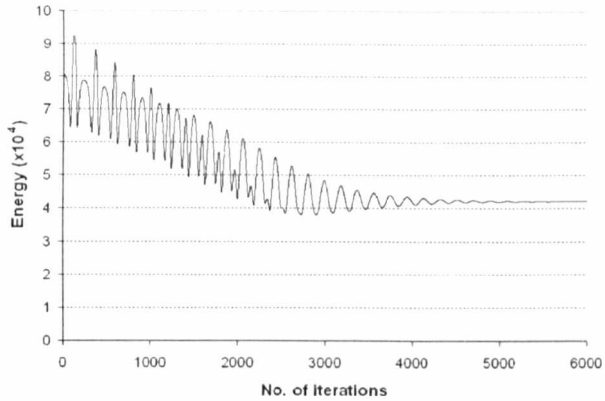

(a)

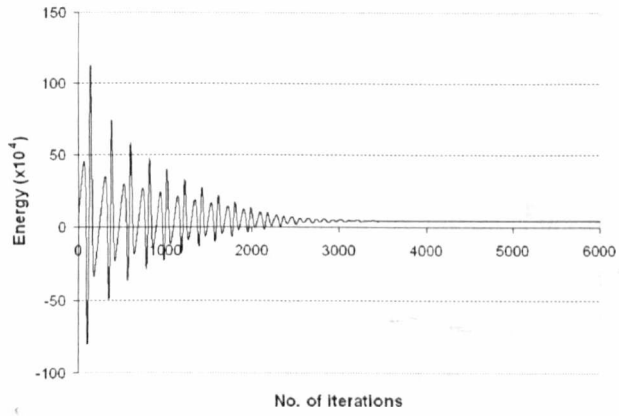

(b)

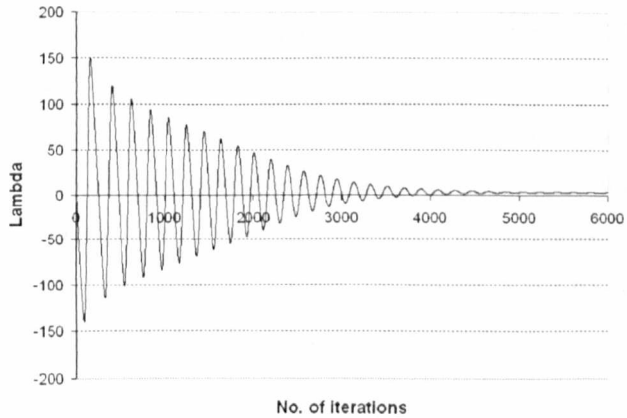

(c)

Figure 5.8 Convergence behaviour of the constrained (a) and unconstrained (b) energy terms and the value of lambda (c) of the restoration process of the 3D simulated data as shown in Figure 5.6. (Note the difference in the scales of the two energy terms.)

5.4.2 MR Velocity Mapping Data

After validating our method by using the synthetic dataset, the proposed method was applied to MR flow velocity data acquired from six patients with sequential examination following myocardial infarction. The noise level in this case was estimated from a static region of interest in the image, and was approximated by calculating the variance of noise in terms of direction when the noise vectors extracted from the static region were added to a flow field with a constant velocity that equals to the average of the selected region of interest.

A sample MR image depicting the four main chambers of the heart and the flow pattern reconstructed from the velocity data are shown in Figure 5.9(a-b). The flow patterns obtained using the proposed method with the estimated noise acquired as described above is given in Figure 5.9(c), which clearly show that the consistency of the flow pattern was greatly improved with the main features well preserved after restoration. To study the effect of the choice of lambda and the value of estimated noise on restoration, experiments with a range of fixed lambda value and estimated noise variance were carried out. The results with fixed lambda values are shown in Figure 5.9(d-f). As expected, the restored pattern with fixed lambda equals to the optimal value is comparable to that with the proposed method. When the value of lambda is too small, the result image is over-smoothed; when the value of lambda is larger then optimum, the image is under-smoothed. When the value of estimated noise was varied in the range of +/-50% of the calculated value, the restoration results were only slightly affected as shown in Figure 5.9(g-h), thus, justifying the robustness of the proposed method with unknown noise level.

To demonstrate the importance of the restoration step, the traditionally used winding index method was applied to extract vortices from the original images from the twelve datasets and the corresponding restored images. A sequence of flow images depicting the two main vortices identified by the winding index method with and without the restoration step are shown in Figure 5.10. It is obvious from the results that vortices are more readily detected if the original flow image is pre-processed by using the restoration method.

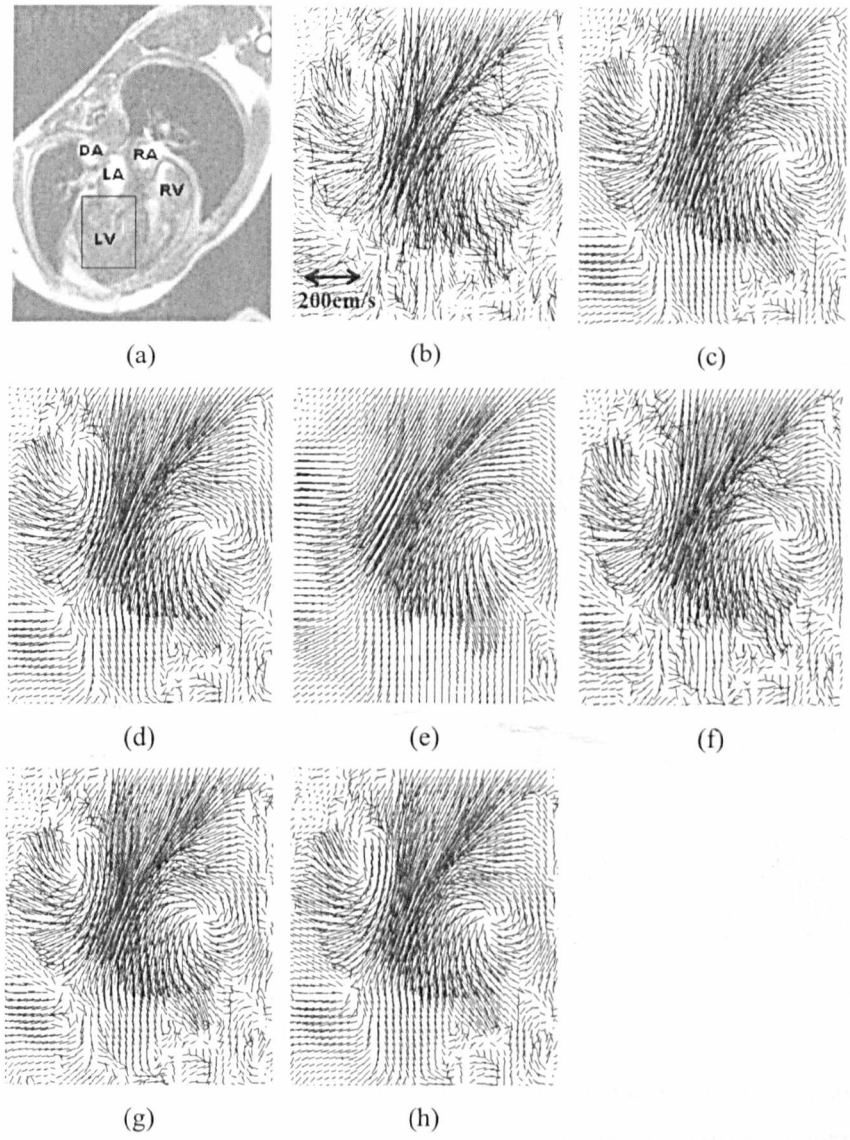

Figure 5.9 (a) A horizontal long axis (HLA) MR image of the left ventricle with the four main chambers and the descending aorta are labelled (DA: descending aorta; LA: left atrium; LV: left ventricle; RA: right atrium; RV: right ventricle). (b) The flow pattern in the left ventricle (the region marked in Figure (a) at the onset of diastole) consists of 1728 vectors. (c-h) The restored flow patterns using the proposed method with calculated noise variance = 0.1(c), with fixed lambda= 5 (optimal) (d), with fixed lambda = 1 (e), with fixed lambda = 20 (f), with fixed noise variance = 0.05 (g) and with fixed noise variance = 0.15 (h).

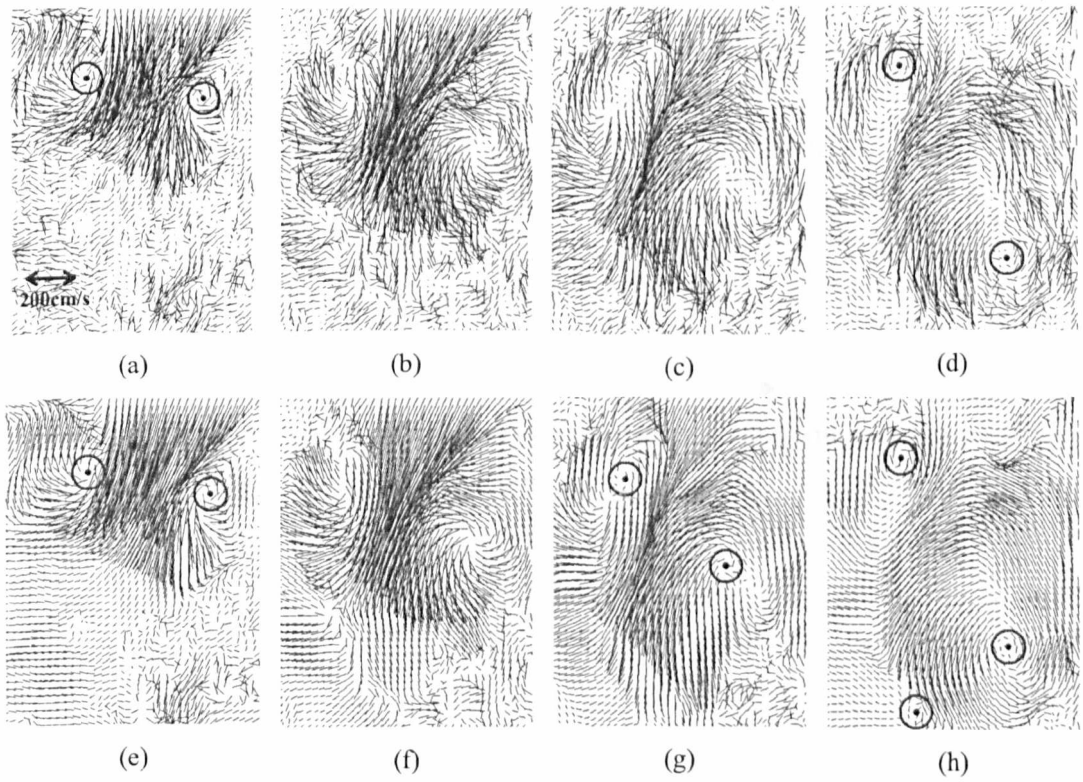

Figure 5.10 The flow patterns and the extracted vortices at various stages of the diastolic phase of the cardiac cycle from one of the patients studied. All extracted vortices are marked with a circle. (a-d) The depicted vortices were extracted by using the traditional winding index method. (e-h) The flow patterns were first restored followed by vortex extraction with the winding index method.

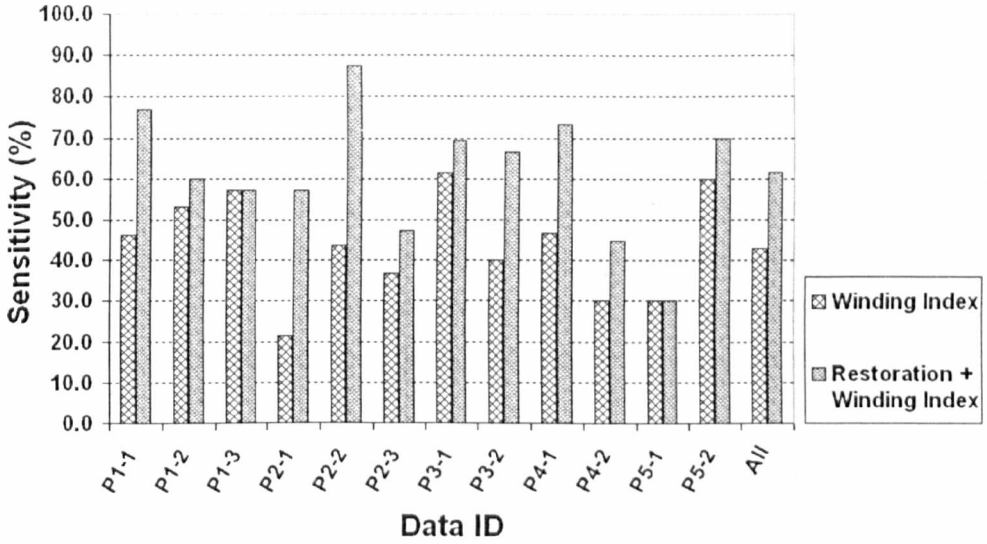

Figure 5.11 The sensitivities of the winding index method with and without a restoration step of the MR data.

To analyse the sensitivity of the winding index method with and without a restoration step, the number of vortices correctly identified by this method performed prior to and after restoration were recorded and compared against the number of vortices spotted visually. The sensitivities, defined as the number of vortices correctly identified divided by the number of vortices spotted visually, of the two combinations are given in Figure 5.11. It is evident from the chart that with restoration, the winding index method has performed consistently better than the others across all twelve datasets, achieving an average sensitivity of over 60%, much higher than that of the winding index method.

5.5 Discussions and Conclusion

In this chapter, we have proposed a new numerical scheme for the restoration of flow field. We have demonstrated that the First Order Lagrangian based restoration method is effective in restoring velocity field and that the choice of the regularization term greatly affects the restoration result. Fixing the regularisation parameter renders a major difficulty to the practical application of the technique as the restored image may converge to different results depending on the parameter settings. With the proposed method, this problem is avoided as the optimal value of this parameter is derived automatically without explicit or empirically defined stopping criteria, thus greatly enhancing its practical value.

It has been shown that the optimum performance of the proposed method relies on the correct identification of the noise level of the image. Because in most restoration applications, the exact value of σ is unknown, an estimated value has to be used instead. For MR velocity mapping, the variance of noise can be estimated from the variance of signal in a region where the velocity is expected to be zero, which typically can be located at the chest wall of the images. It has been demonstrated in this study that the performance of the restoration and vortex detection process is not greatly affected by the value of σ, thus justifying the robustness of the proposed restoration method for practical applications. It is expected that the proposed restoration method is equally applicable to flow field with varying local noise variance such as those encountered in parallel imaging.

It is worth noting that the proposed restoration scheme has the advantage that it allows extra constraints to be incorporated. With additional constraints, we expect that the consistency of the velocity data can be further improved. One of the possible constraints is the zero divergence constraint based on the law of mass conservation for incompressible fluid. This, however, is only applicable to volumetric data and is not suitable for 2D MR images. Limited by the prolonged acquisition time, 3D cine MR velocity imaging is still not widely used in routine clinical examinations. Nevertheless, with the recent advances in echo planar and spiral flow imaging techniques combined with selective volume excitation and *k-t* space interpolation, 3D cine velocity measurement will become clinically applicable in the near future. The proposed restoration method can then be served as a vital pre-processing tool for systematic study of the velocity data.

In conclusion, we have described a new numerical method for the restoration of flow field. The use of the First Order Lagrangian method proves to be effective in improving the consistency of the MR velocity data. The convergence behaviour and accuracy of the method evaluated with both simulated and patient data demonstrated the practical value of the proposed method.

Chapter 6

Flow Feature Extraction

6.1 Introduction

Although blood flow patterns have been investigated by both computational modelling [11, 191], invasive and non-invasive imaging techniques [15, 16], their evolution and connection with cardiovascular diseases has yet to be explored. Previous research has shown that in order to achieve a comprehensive and integrated description of flow in health and disease, it is necessary to characterise and model both normal and abnormal flows and their effects. This permits the establishment of links between blood flow patterns and the localised genesis and development of cardiovascular disease.

With the introduction of MR phase contrast velocity mapping, detailed quantitative analysis of flow patterns is made possible. For MR velocity imaging, direct visualisation or quantification of vector fields is of limited clinical uses, especially for inter-subject or serial comparisons of changes of flow patterns due to the progression of disease or in response to therapeutic measures. To achieve a comprehensive assessment of MR flow data, it is necessary to generate a compact topological description of the complex flow patterns such that dynamic indices associated with salient flow features can be measured and compared.

To accommodate the diversity of flow patterns in relation to morphological and functional changes, the approach of detecting salient topological features prior to analytical assessment of dynamical indices of the fluid has been regarded as an important way forward [16]. To this end, critical points associated with salient flow features have to be extracted such that the remaining flow field and its geometry and topology can be compactly described. The practicality of these feature extraction techniques, however, relies greatly on the quality of the MR images. As pointed out in the previous chapter, flow velocity images acquired with MR phase contrast velocity mapping are subject to a certain amount of noise that is intrinsic to system hardware setup and specific to patient movement in relation to imaging sequence designs. To alleviate this problem, a restoration method was developed for improving the overall quality of MR flow velocity images.

The purpose of this Chapter is to provide a compact representation of the entire flow field by using a clustering algorithm to partition the dense vector field after restoration. Unlike the conventional approaches, we propose to use local linear expansion for the representation of a cluster of 2D vectors. With this representation, the neighbourhood of a critical point can be compactly described, thus greatly reduces the amount of information needed to describe complex flow fields while preserving intrinsic flow details. Another advantage of using this representation is that given a cluster, the approximation of the original vectors can be easily deduced from the analytical description of the vector fields. We demonstrate in this Chapter that with the proposed flow abstraction technique, critical points can be more easily and accurately extracted by subsequent processing steps. After the critical points are extracted, phase portrait theory can be applied to separate them into attracting/repelling focuses, attracting/repelling nodes and planar vortex [219, 220]. Comparison to the traditional approach of vortex detection with winding index [16, 221] is also provided, demonstrating the much-improved sensitivity of the proposed technique.

6.1.1 Flow Field Abstraction

Both in MR and in CFD, the flow data to be analysed is typically of large size and high complexity. To facilitate quantitative comparison, there is a need for generating an abstract representation of the flow field. Helman and Hesselink [222] introduced the idea of simplifying a vector field by visualising its topology. Their methods involve the extraction and classification of critical points of vector fields and the computation of streamlines

emanating from saddle points. These streamlines separate the vector field into disjoint regions, thus providing a simplified view of the topology of the vector field.

Since then, there has been extensive research in compressing or simplifying a complex flow field in the fluid dynamic community, mainly for visualisation purposes [223-227]. Two different approaches involving topology simplification and topology preserving have been developed. With the topology simplification approach, a flow field is compressed by simplifying the topology. This approach is particularly useful for flow data containing turbulent flows with complex topology. The topology preserving approach aims to compress a flow field while preserving the critical points and is generally suited for smaller dataset with less complex flows.

6.1.1.1 Topology simplification

Topology simplification methods usually involve the removal or merging of minor critical points. De Leeuw *et al.* [224] used a filtering mechanism to prune minor critical points. The filtering criterion is based on an area metric that measures the influence region of a critical point. Tricoche *et al.*[223] proposed another method, where simplification is achieved by merging critical points within a prescribed radius into higher order critical points. This method has the advantage that the simplified result can be easily visualised by using existing visualisation techniques.

6.1.1.2 Topology preserving compression

Most of the topologically preserving compression methods are based on hierarchical clustering. They can generally be divided into two categories: a top-down strategy and a bottom-up strategy. In both cases, a hierarchical tree is generated to represent the vector field. Heckel *et al.* [225] used a top-down approach where a discrete vector field is segmented into a disjoint set of clusters. Initially, it starts with a single cluster containing all the vector data and then at each step, the cluster with the highest associated error is split into two clusters. The bisection plane is selected using principal component analysis, and the error measure depends on the differences in the streamlines generated in the original field and the simplified field.

Telea *et al.* [226] used a bottom-up clustering approach. Initially every cell, each containing a single vector, belongs to its own cluster. The clusters are then recursively merged using a cost function until there is only one cluster left. The cost function is based a composition of the direction and magnitude error and the position error. Lodha *et al.* [227] used the same clustering approach as Telea *et al.* but with a different error metric to preserve topology of the vector field. In their approach, the topology of the vector field needs to be pre-computed and two additional error measures are used, involving either the local node importance error or the global Earth Mover Distance (EMD) error. The node importance error is added especially for the preservation of topology. Topology preservation is achieved by assigning a high value of "node importance" to critical points and their neighbours, a low value to all other nodes such that the cost of merging a critical point with a non-critical point is high and hence not preferred. The EMD [228, 229] is a measure of the global topology, which is defined as the cost for moving a set of critical points from one vector field to another.

More recently, Garcke *et al.* [230] have proposed a continuous clustering method based on the Cahn-Hilliard model for the simplification of vector fields. This technique is effectively a bottom-up method in which a multi-scale vector field representation is built by merging neighbouring cells in a continuous manner. Generally speaking, all these methods use a single vector to represent a cluster and are well suited for visualisation purposes, however, given a set of such clusters, it is difficult to recover the original vector field.

6.1.2 Vortex Detection

Vortex is a complex flow feature and the analysis of vortices plays an important role in the study of fluid dynamics. In aerodynamics, vortices can produce undesirable effects such as reduced lifting on wings and hence it is a vital feature to be considered in aeroplane design [231]. In oceanography, the evolution of vortices also plays an important role in ocean circulation. In medicine, vortical motion is known to exist in the diastolic phase of the cardiac cycle and its evolution over different phases of the cardiac cycle can provide important insight into the health status of the heart. It has been suggested that vortices in the left ventricle may help avoiding left atrial stasis and facilitating the closure of the mitral valve.

Detecting vortex in fluid flow is a difficult task because there is no unified definition of a vortex, which is usually identified by its swirling flow pattern. A wide range of methods has been developed. Some methods based on physical quantities such as pressure and velocity gradient at fixed sample points of the flow domain. As for detecting vortices in velocity vector field, most methods are based on the concept of critical points. Critical points are points at which the velocities vanish. They can be characterised into attracting/repelling focuses, attracting/repelling nodes and planar vortex by using phase portrait theory [219, 220]. Alternative methods that based on the analysis of winding angle or curvature of streamline, and the global topology of the flow patterns are also available.

Winding index method, also called the winding angle method, is commonly employed for detecting vortices in 2D flow [221]. The winding angle is defined as the total directional changes along a closed path surrounding a point and it should equals $\pm 2\pi$ if it the path encloses a critical point. In which case, the corresponding winding index should equal ± 1. This method has been combined with phase portrait theory for detecting vortical flow patterns in MR velocity data [16].

Sadarjoen *et al.* [232] approached the problem by identifying circular path or streamlines in velocity field. Two methods were proposed. The first method is based on the concept of winding-angle in the selection of streamlines that belong to a vortex by ensuring that the selected streamlines have a winding-angle of a multiple of 2π, and that the starting and final point of the streamline are relatively close. Afterwards, these selected streamlines are clustered such that those belonging to the same vortex are grouped together. The second method is known as the curvature centre method, which detects 2D vortices by finding the centre of curvature of the streamline through the sample points within a box-shaped window. If the window contains a vortex, the centre points would be clustered near a point, otherwise, the centre points would be scattered. This method works well on circular vortices but fails to locate elliptical vortices.

Alternatively, Brandt *et al.* proposed a 3D template matching strategy to detect vortex [233]. Idealised vortex patterns were first defined and a similarly measure is used to compare a vector field with the idealised patterns. The similarity measure is computed by convolving oriented templates of a 3D vortex core pattern with velocity data. Isosurfaces

are then derived by thresholding the similarity data. This method has been applied to detect a vortex ring inside an *in vivo* left ventricle depicted in 3D MR velocity data.

6.2 Flow Feature Extraction Based on Abstraction and Phase Portrait

6.2.1 Flow Field Abstraction

For the work reported in this thesis, the original flow field is partitioned into a set of flow regions, each containing a cluster of vectors. A crucial factor to a good abstraction algorithm is the choice of the representation for a cluster of vectors. In our study, local linear expansion of the velocity vectors is employed to represent a cluster of 2D vectors. This representation is effectively the same as using two planes with limited scopes, one for each velocity component, to locally represent the cluster of vectors. The choice of using planes to represent a flow field is particularly suitable for regions near critical points, and thus this abstraction technique intrinsically preserves critical points and provides a good foundation for the identification of critical points.

To partition the flow field, we apply a hierarchical clustering algorithm to merge individual flow vectors into clusters through an iterative process. The planes are fitted automatically by using a least squares fitting method and the fitting error, $E(C)$, for each cluster C is defined as the total squared distance between the data points and the plane. Subsequently, the cost of merging two clusters, C_1 and C_2, to form a new cluster C_{new} is defined as:

$$MergeCost(C_1, C_2) = E(C_{new}) - [E(C_1) + E(C_2)] \tag{6.1}$$

Initially, each vector forms its own cluster and the neighbouring vectors are used to approximate the local linear expansion of this cluster. Subsequently, the associated cost of merging a pair of clusters is calculated and stored in a pool for each pair of neighbouring

clusters. After the initialisation step, the following steps are repeated until all clusters are merged to form one single cluster that contains the entire flow field. Firstly, the pair of clusters with the smallest merging cost in the pool is selected and merged to form a new cluster. Then, the cost of merging the newly formed cluster with its neighbours is calculated and inserted into the pool. By repeatedly merging clusters, a hierarchical tree is constructed in the process, as illustrated in Figure 6.1. In this figure, each node represents a cluster and its children represent its sub-clusters. Once the hierarchical tree is constructed, abstract flow field at various compression ratios can then be obtained from this tree efficiently.

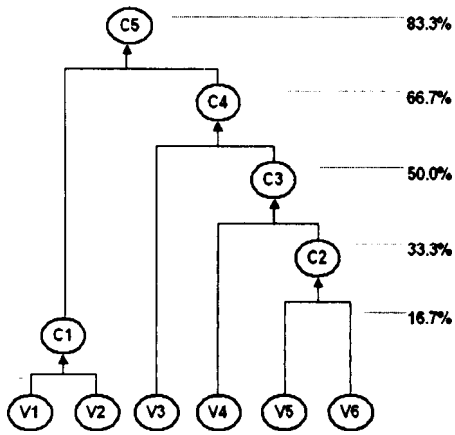

Figure 6.1 A diagram illustrating how a hierarchical tree is built from six initial vectors. The corresponding abstraction ratio is shown on the right.

With the proposed cluster representation, either one or none critical point can be extracted from each cluster, hence the number of critical points that can be extracted from an abstract flow field varies with the compression ratio (*i.e.* the number of clusters needed to represent the entire flow field). At low compression ratios, the critical points extracted directly from all clusters would clutter together around the actual location of all real critical points and therefore further processing is needed to determine the actual number of critical points and their corresponding location. Details of the post-processing algorithm are given in the following section. At high compression ratios, some or all critical points may be merged and disappeared. In other words, the choice of compression ratio affects the accuracy of

our vortex detection algorithm. In this study, the optimal compression ratio is obtained by increasing the compression ratio from a fixed ratio until the extracted critical points do not clutter together.

6.2.2 Vortex Detection based on Phase Portrait

The detection of vortices and other salient flow features in vector fields can be accomplished by using phase portrait theory [234, 235], which is a useful tool for analysing the qualitative behaviour of non-linear dynamical systems . If we express the velocity components of a velocity vector as a pair of coupled first-order equations as below:

$$\begin{cases} u = P(x, y) \\ v = Q(x, y) \end{cases} \tag{6.2}$$

where $P(x, y)$ and $Q(x, y)$ are continuously differentiable functions and x and y are the coordinates in the (x, y) plane, the solution to this system of equations may be plotted in the (x, y) plane, known as phase plane, and the collection of trajectories of the system, known as the phase portrait, describes the flow pattern of the velocity field. In this system, critical points are points at which the magnitude of the vector vanishes, that is, when velocity is zero. By assuming that in the region of a critical point the equations $P(x,y)$ and $Q(x,y)$ are linearisable, they can be expressed in matrix form

$$\begin{bmatrix} u \\ v \end{bmatrix} = \begin{bmatrix} a_{11} & a_{12} \\ a_{21} & a_{22} \end{bmatrix} \begin{bmatrix} x - x_0 \\ y - y_0 \end{bmatrix} = A(\bar{x} - \bar{x}_0) \tag{6.3}$$

where A is the Jacobian matrix of the critical point defined as:

$$\left[\frac{\partial(u,v)}{\partial(x,y)}\right]_{x_0,y_0} = \begin{bmatrix} \frac{\partial u}{\partial x} & \frac{\partial u}{\partial y} \\ \frac{\partial v}{\partial x} & \frac{\partial v}{\partial y} \end{bmatrix}_{x_0,y_0} \tag{6.4}$$

The two eigenvalues, λ_1 and λ_2, of matrix A govern the qualitative behaviour of the system and can be used to classify the critical point. If both λ_1 and λ_2 are real and have equal sign, the portrait describes an attracting node or a repelling node. If λ_1 and λ_2 are real and are of opposite sign, the portrait describes a saddle point. If λ_1 and λ_2 are complex, the portrait describes a centre if λ_1 and λ_2 are pure imaginary, or a repelling or attracting focus otherwise. The classification of critical points is given in Figure 6.2.

With the proposed local linear expansion representation, the location (x_0, y_0) of the critical point in a cluster can be computed at sub-pixel accuracy by solving the following set of equations:

$$\begin{cases} u_{x_0,y_0} = A_1 x_0 + B_1 y_0 + C_1 = 0 \\ v_{x_0,y_0} = A_2 x_0 + B_2 y_0 + C_2 = 0 \end{cases} \tag{6.5}$$

where u and v are the velocity components, x and y are the coordinates of the velocity vector and A, B and C are constants. After the critical points are extracted, phase portrait theory described above can be applied to separate them into attracting/repelling focuses, attracting/repelling nodes, planar vortex, or saddle by solving for the eigenvalues of the Jacobian matrix. For vortices, the associated eigenvalues will have large imaginary values.

The traditionally adopted method of winding index is sensitive to image noise as one single noisy vector can cause the method to fail. With the proposed flow field abstraction method, this problem is naturally avoided as each vortex is derived from the velocity planes, which are, in turn, derived from a cluster of velocity vectors.

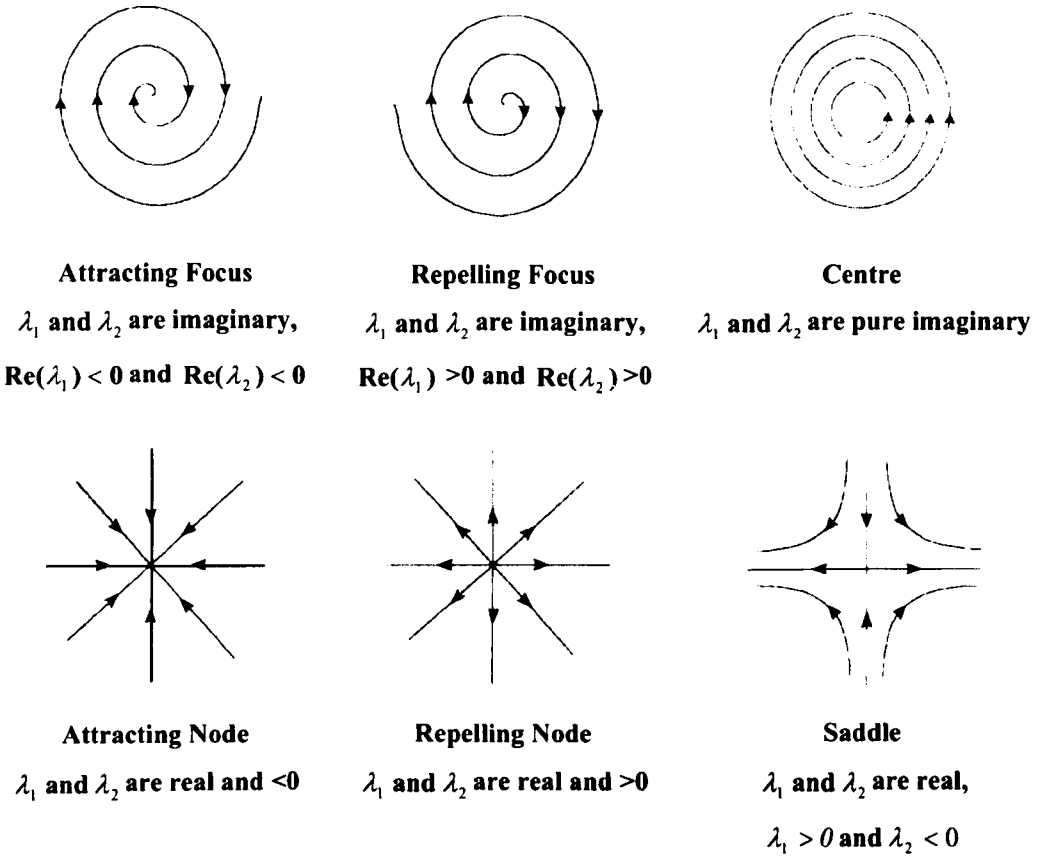

Figure 6.2 Classification criteria of critical points. λ_1 and λ_2 are the eigenvalues of the characteristic matrix A as defined in Equation 6.3. Re(·) denotes the real part of eigenvalues and Im(·) denotes the imaginary parts.

6.2.2.1 Voting

With the proposed abstraction method, the neighbourhood of a vortex maybe partitioned into two or more clusters, each containing one vortex. In this case, two or more vortices referring to the same vortex would be identified in the region where there should be only one vortex. To resolve this issue, post-processing is needed to select the best candidate from a group of potential vortices.

A simulated velocity field depicting a vortex as shown in Figure 6.3(a) was used to illustrate this idea. First, the proposed abstraction algorithm was applied to generate an abstract flow field at 99% compression level, *i.e.* the entire flow field was partitioned into 3 clusters. The dense vector field reconstructed form this abstract flow field overlaid on the corresponding cluster map depicting the cluster boundary was shown in Figure 6.3(b). Then phase portrait method was employed to extract vortices from the three clusters and the extracted vortices were shown in Figure 6.3(c). It is obvious that there should be only one vortex in the flow field but three vortices, which were cluttered together, were found using the proposed method.

A simple voting algorithm is adopted to select the best candidate from a group of cluttered vortices in this study. First, the mean position (x_{mean}, y_{mean}) of all vortices in the same group G is calculated using the size of the cluster as a weighting factor. It is defined as:

$$(x_{mean}, y_{mean}) = \left(\frac{1}{\sum_{V_i \in G} |C_{V_i}|} \sum_{V_i \in G} x_{v_i} * |C_{V_i}|, \frac{1}{\sum_{V_i \in G} |C_{V_i}|} \sum_{V_i \in G} y_{v_i} * |C_{V_i}| \right) \tag{6.6}$$

where C_V denotes the cluster from which vortex V is derived, $|C_v|$ denotes the size of the cluster and x_v and y_v denote the x and y coordinate of vortex V. After the mean position is computed, all vortices in the group are compared to the mean value and the one with position nearest to the mean is selected with the rest discarded.

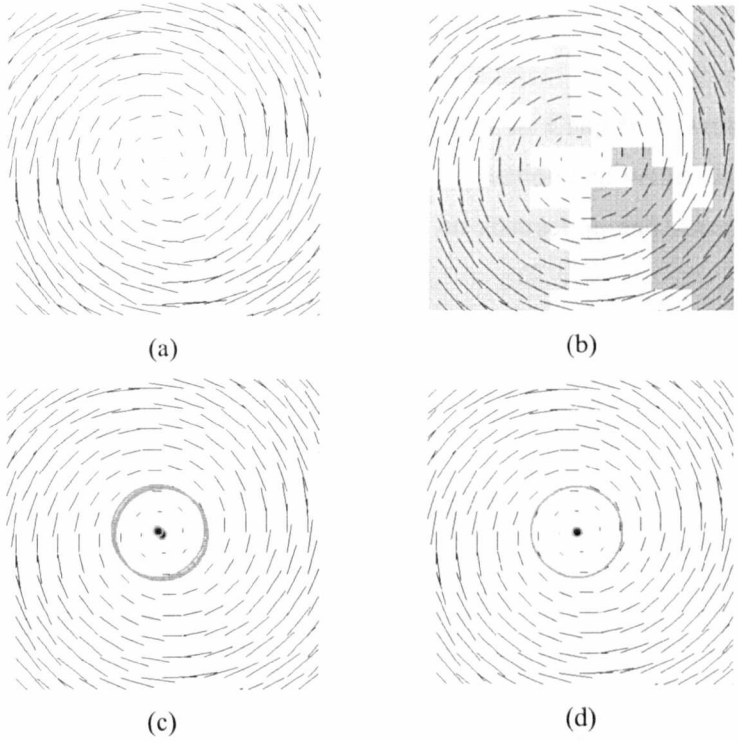

Figure 6.3 A simulated vortical flow pattern illustrating the effect of vortex voting. (a) Dense vector field of the region containing one vortex. (b-d) The vector field reconstructed from the abstract flow field at 99% compression level (3 clusters) overlaid on the corresponding cluster map delineating the cluster boundary. (c) The three vortices (marked with circles) derived from the three clusters by applying phase portrait method. (d) The selected vortex (marked with circle) after voting.

6.2.3 Validations

6.2.3.1 CFD Simulated Data

The set of 2D CFD data simulating flow in the left ventricle as described in Chapter 5 was used to validate the abstraction and vortex detection method. The effect of restoration on the proposed abstraction and vortex detection method was studied.

6.2.3.2 MR Velocity Mapping Data

The twelve sets of MR flow velocity data described in Chapter 5 were used here for evaluating the effectiveness of the proposed flow abstraction and vortex detection method. The effect of restoration on the proposed method on abstraction and vortex detection was also studied by using the MR flow data.

6.3 Results

6.3.1 CFD Simulated Data

The 2D CFD flow data was used to analyse the performance of our proposed flow abstraction algorithm. A number of abstract flow fields at various compression ratios were generated for each flow field and the abstract flow fields were then used to reconstruct the original flow field. The reconstructed flow fields were compared to the original uncompressed flow fields as shown in Figure 6.4. It is evident that with the proposed local linear representation, the flow pattern and the salient flow features were well preserved in the abstract flow field even at a very high compression ratio, typically up to 90% and in the sample shown in Figure 6.4, up to 98%. As a reference, the cluster map delineating the cluster boundaries of the abstract flow field at 98% compression ratio was provided in Figure 6.4(f). The results show clear evidence that with a suitable representation, a complex flow field can be accurately represented in a much more compact way. For reference purposes, the corresponding RMS errors of the velocity vector field (normalised with V_{enc}) at different compression ratios were provided in Figure 6.5.

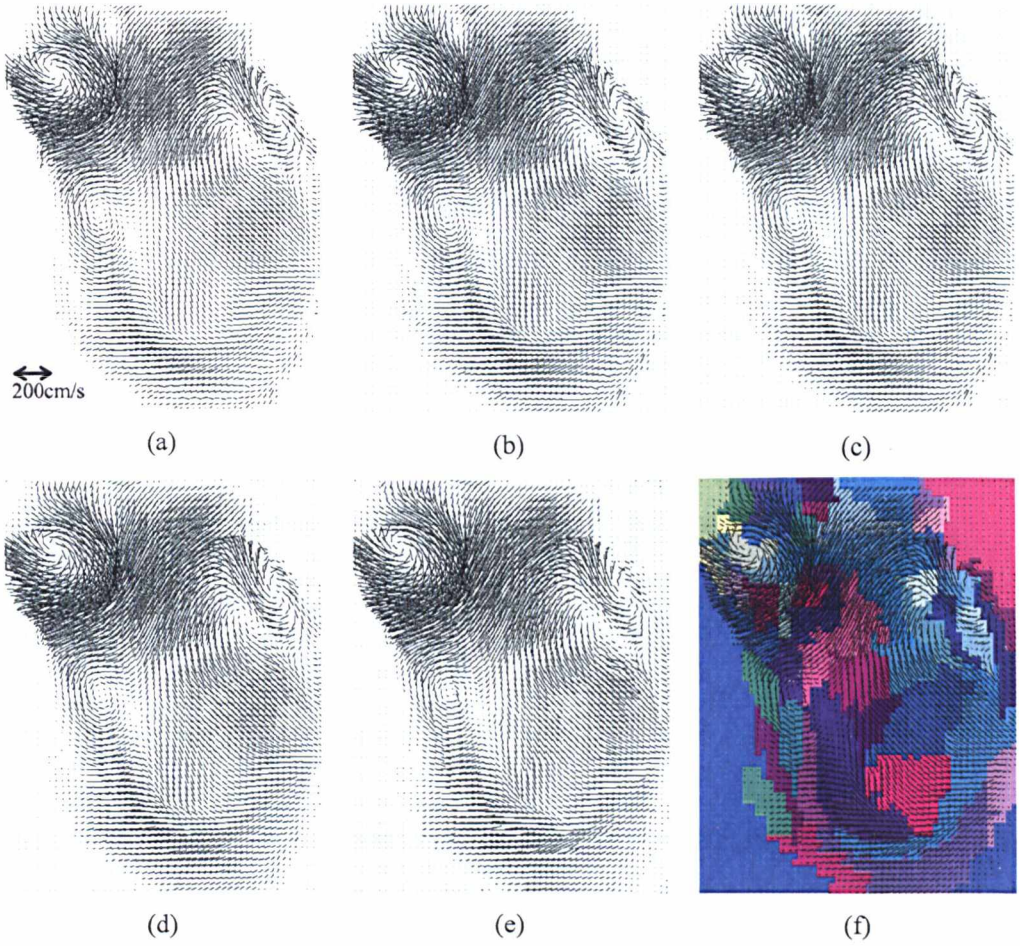

Figure 6.4 Flow abstraction results. (a) The original flow pattern, consisting 3536 vectors, in the left ventricle of the 2D CFD dataset. (b-e) Dense vector fields reconstructed from the abstract flow fields at 75%(b), 85%(c), 95%(d) and 98%(e) compression. (f) The cluster map delineating the cluster distribution at 98% compression level (71 clusters).

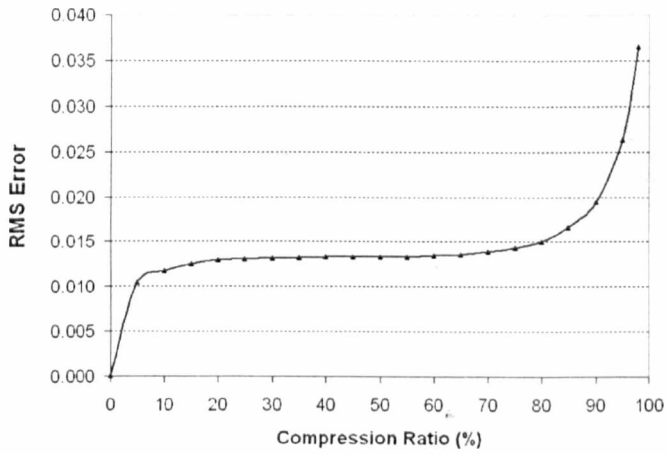

Figure 6.5 The RMS error in the velocity field (normalised with V_{enc}) of the abstract flow fields at various compression ratios of the simulated flow field shown in Figure 6.4.

To analyse the performance of combining the restoration and abstraction method, the same set of experiments was repeated with the 2D CFD flow data restored using our proposed method described in Chapter 5. A number of abstract flow fields at various compression ratios were generated for each restored flow field and the abstract flow fields were then used to reconstruct the original flow field. The reconstructed flow fields were compared to the original noise-free flow fields as shown in Figure 6.6. The results again show that the flow pattern and the salient flow features were well preserved in the abstract flow field even at a very high compression ratio. For reference purposes, the RMS errors of the directional field and velocity vector field (normalised with V_{enc}) at different compression levels were provided in Figure 6.7.

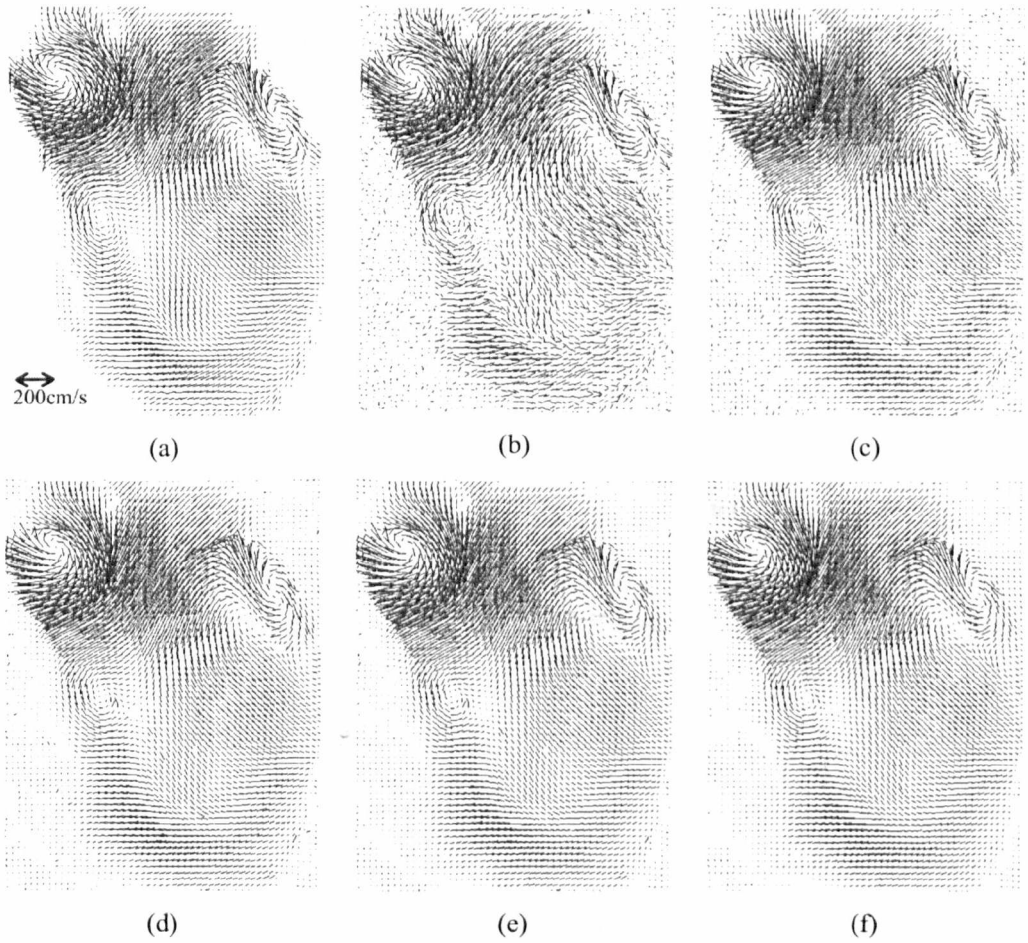

Figure 6.6 Flow patterns demonstrating the effect of restoration and abstraction on a noisy dataset. (a) The original flow pattern in the left ventricle of the 2D CFD dataset. (b) The noisy flow field. (c) The restored flow field. (d-f) Dense vector fields reconstructed from the restored abstract flow fields at 75% (d), 85% (e) and 95% (f) compression.

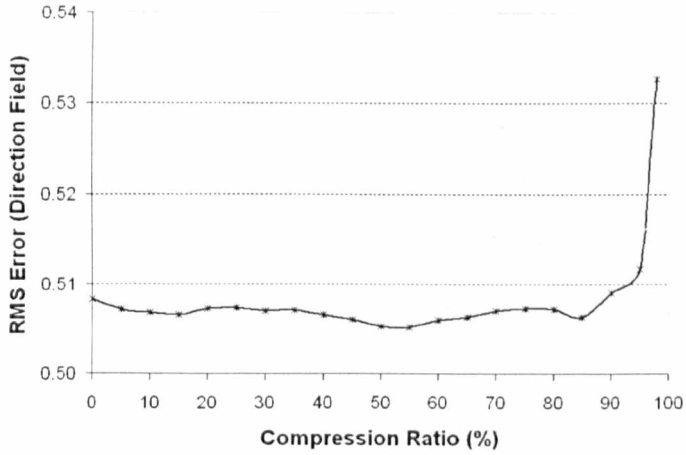

(a)

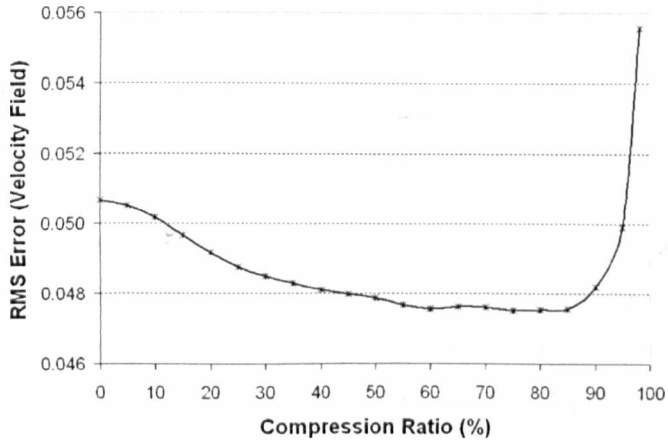

(b)

Figure 6.7 The corresponding RMS error in the directional field (a) and the velocity vector field with velocity normalised with V_{enc} (b) of the abstract flow fields depicted in Figure 6.6.

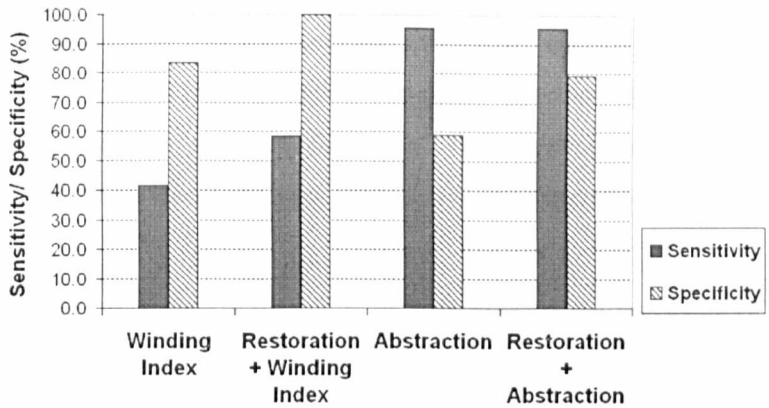

Figure 6.8 The overall sensitivity and specificity of the Winding Index method and the proposed vortex detection method with and without a restoration step of the 2D CFD dataset. The abstraction method achieved a much higher sensitivity than the winding index method both with and without the restoration step.

To validate the new vortex detection method and demonstrate the importance of the restoration step, the proposed method and the winding index method were applied to the noisy images and the corresponding restored images and the number of vortices correctly and falsely identified by these two methods were recorded and compared against the number of vortices spotted visually. The sensitivity and specificity measures used here are slight variants of the ones commonly used and are defined as follows:

$$Sensitivity = \frac{No.\ of\ Vortices\ Correctly\ Identified}{No.\ of\ Vortices\ Spotted\ Visually} \times 100\%$$

$$Specificity = \frac{No.\ of\ Vortices\ Correctly\ Identified}{Total\ no.\ of\ Vortices\ Identified\ \ (Correct + False\ ones)} \times 100\% \qquad (6.7)$$

The sensitivities and specificities of different combinations of pre-processing are compared in Figure 6.8. It is evident that the proposed abstraction method achieved a much higher sensitivity than the winding index method. The result also showed that with the restoration step, both the sensitivity and specificity of the winding index method improved significantly, whereas for the abstraction method, only the specificity was further improved.

To assess the sensitivity of the vortex detection framework on the value of the estimated noise variance and lambda for the restoration process, the proposed vortex detection method was applied to flow fields restored with different values of estimated noise variance and lambda. The sensitivity and specificity versus estimated noise variance were plotted in Figure 6.9, which shows that within a range of $\pm 50\%$ of the actual noise variance, the sensitivity maintains a high value of nearly 90% and reaches its maximum when the actual noise variance is used, whereas the specificity increases with the estimated noise variance, indicating the possible side effect of over-smoothing. The sensitivity and specificity versus lambda were given in Figure 6.10, which shows that the sensitivity reaches its maximum when the value of lambda equals to the optimal value found by the proposed method and drops as the value of lambda deviate from the optimal value.

Finally, to evaluate the effect of compression ratio in the abstraction process on the vortex detection framework, experiments were carried out with various fixed compression levels and the corresponding sensitivity and specificity of the proposed vortex detection method were recorded and plotted in Figure 6.11. It has been shown that the sensitivity remains consistent at a value of nearly 90% with increasing compression rate, giving strong evident that the vortex detection result does not vary with the compression rate. On the other hand, the specificity improves gradually with compression ratio, indicating that at low compression level, the effect of noise is more significant and introduces a higher false identification rate with lower specificity.

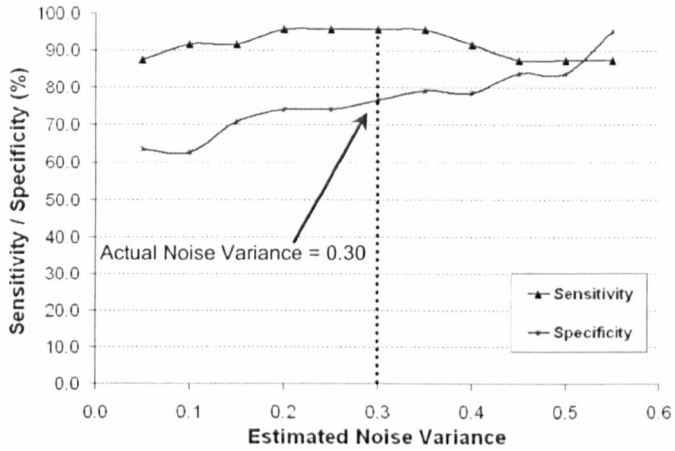

Figure 6.9 The overall sensitivity and specificity of the proposed vortex detection method with varying estimated noise variance in the restoration step for the 2D CFD dataset. The actual noise variance was 0.30.

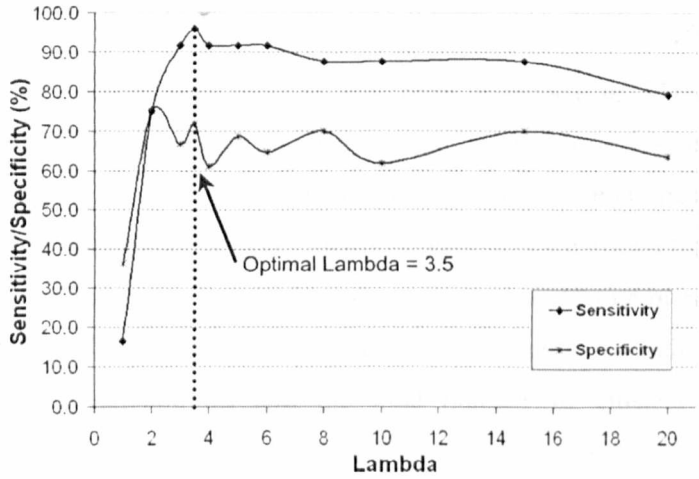

Figure 6.10 The overall sensitivity and specificity of the proposed vortex detection method with varying lambda in the restoration step for the 2D CFD dataset. The optimal lambda was 3.5.

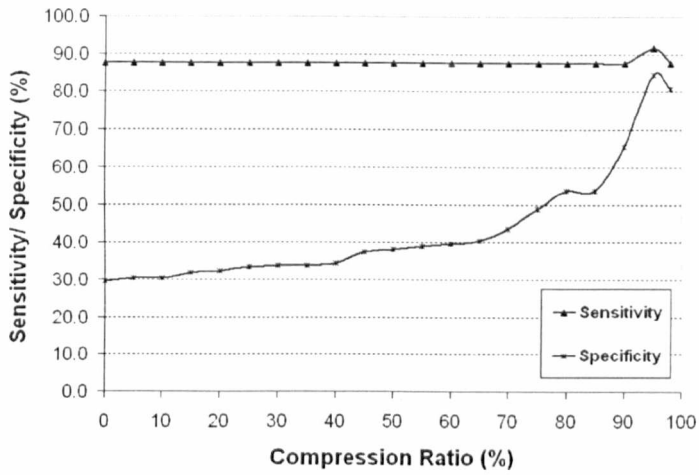

Figure 6.11 The overall sensitivity and specificity of the proposed vortex detection method with varying compression level in the abstraction step for the 2D CFD dataset. The optimal compression level ranges from 90% to 98% for this dataset.

6.3.2 3D Extension

The proposed flow abstraction method has been extended to 3D and an effective visualisation method was especially designed to display the clustering results [236]. The essence of this visualisation method is to selectively display streamlines using correlation information of streamlines and clusters. Firstly, streamlines are grown from equally spaced points throughout the image and each streamline passes through one or several clusters. A streamline "correlation" matrix $C_{cluster}$ is then built by computing the ratio between common clusters occupied by streamlines and the total number of clusters panned by each streamline:

$$C_{cluster}(e,v) = \frac{\tau(e,v)}{\gamma(e)} \tag{6.8}$$

where $\tau(e,v)$ is the number of clusters occupied by both streamlines e and v and $\gamma(e)$ is the total number of clusters occupied by streamline e.

After the correlation matrix is created, the total "correlation" $T_{cluster}(e)$ of each streamline is computed:

$$T_{cluster}(e) = \sum_{v \in E, v \neq e} C_{cluster}(e, v) \tag{6.9}$$

where E denotes the set of all streamlines. By setting a threshold on the value of total correlation, the most representative streamlines can then be selected. Users can interactively choose the threshold value in the process. Figure 6.12 shows the visualised results of a 3D CFD dataset.

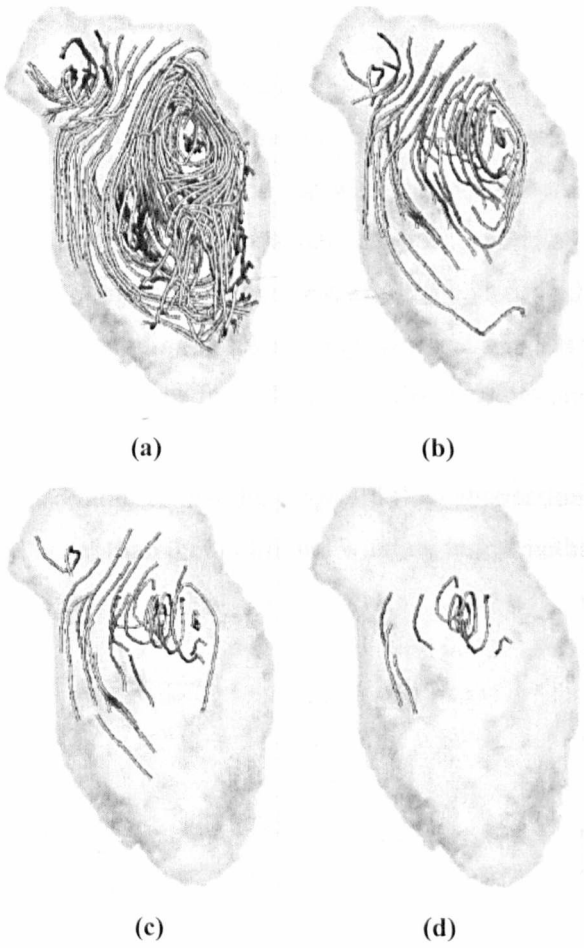

Figure 6.12 A 3D simulated flow data visualised using a combined flow abstraction and selective visualisation method with various total correlation threshold values. (a) All streamlines are shown. (b) Max $T_{cluster}(e) = 20$. (c) Max $T_{cluster}(e) = 10$. (d) Max $T_{cluster}(e) = 5$.

6.3.3 MR Velocity Mapping Data

A sample MR image depicting the four main chambers of the heart and the flow pattern reconstructed from the velocity data are shown in Figure 6.13(a-b). To illustrate the effect of restoration and abstraction, the flow patterns obtained after restoration and that followed by abstraction are also given in Figure 6.13(c-d), which clearly show that the consistency of the flow pattern was greatly improved with the main features well preserved after restoration and abstraction. For reference purposes, a cluster map superimposed on the velocity vectors is also included to depict the boundary of clusters. The average processing time for the entire restoration and abstraction process for a typical MR flow image, such as the one shown in Figure 6.13, is approximately 28 seconds on a PC with a Pentium III 1GHz processor with 256M RAM.

To validate the new vortex detection method and demonstrate the importance of the restoration step, the proposed method and the winding index method were applied to the original images from the twelve datasets and the corresponding restored images. A sequence of flow images depicting the two main vortices identified by the proposed flow abstraction method and the winding index method with and without the restoration step are shown in Figure 6.14. It is obvious from the results that vortices are more readily detected if the original flow image is pre-processed by using the restoration method. The results shown in Figure 6.14 also indicate that the proposed flow abstraction method, together with restoration, performed better than the traditional winding index method.

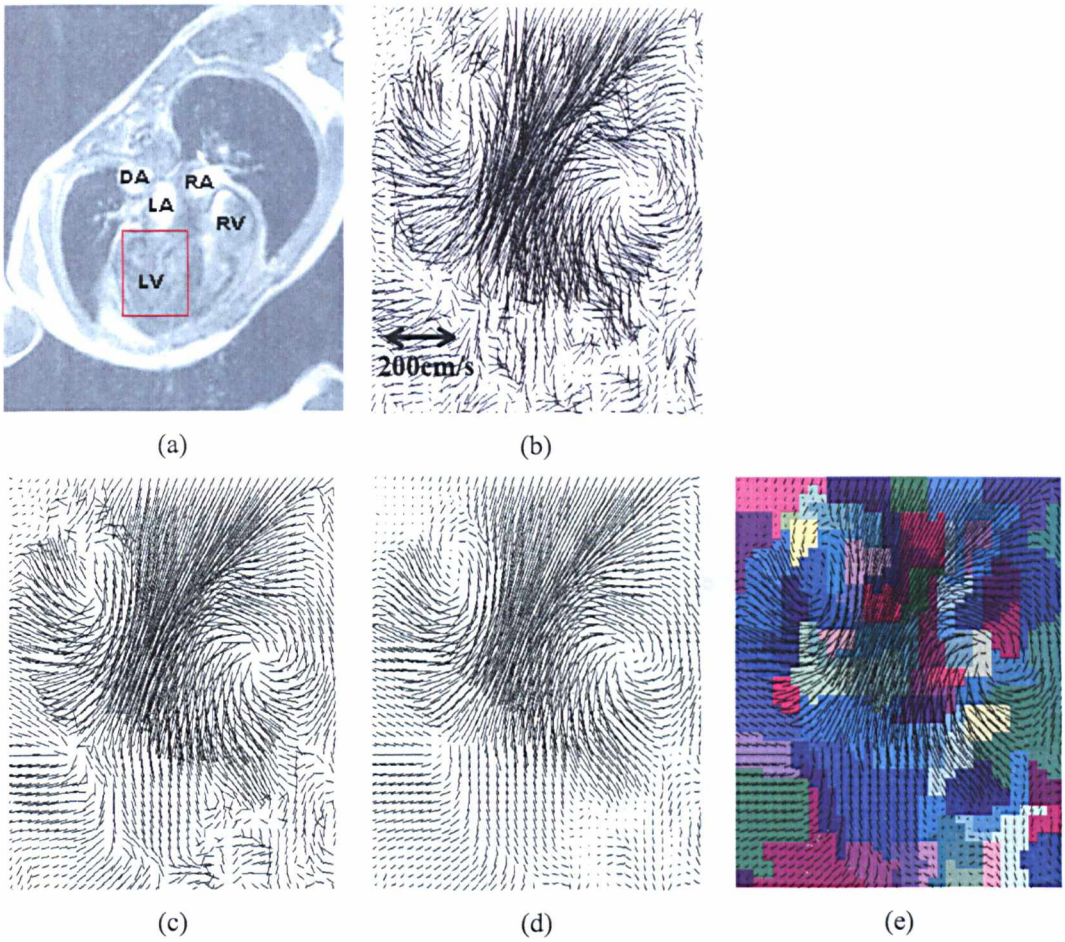

Figure 6.13 (a) A horizontal long axis (HLA) MR image of the left ventricle with the four main chambers and the descending aorta are labelled (DA: descending aorta; LA: left atrium; LV: left ventricle; RA: right atrium; RV: right ventricle). (b) The flow pattern in the left ventricle (the region marked in Figure (a) at the onset of diastole) consists of 1584 vectors. (c) The restored flow pattern. (d-e) Dense vector fields reconstructed from the abstracted flow fields at 95% compression level (79 clusters) and the corresponding cluster map delineating the boundary of clusters.

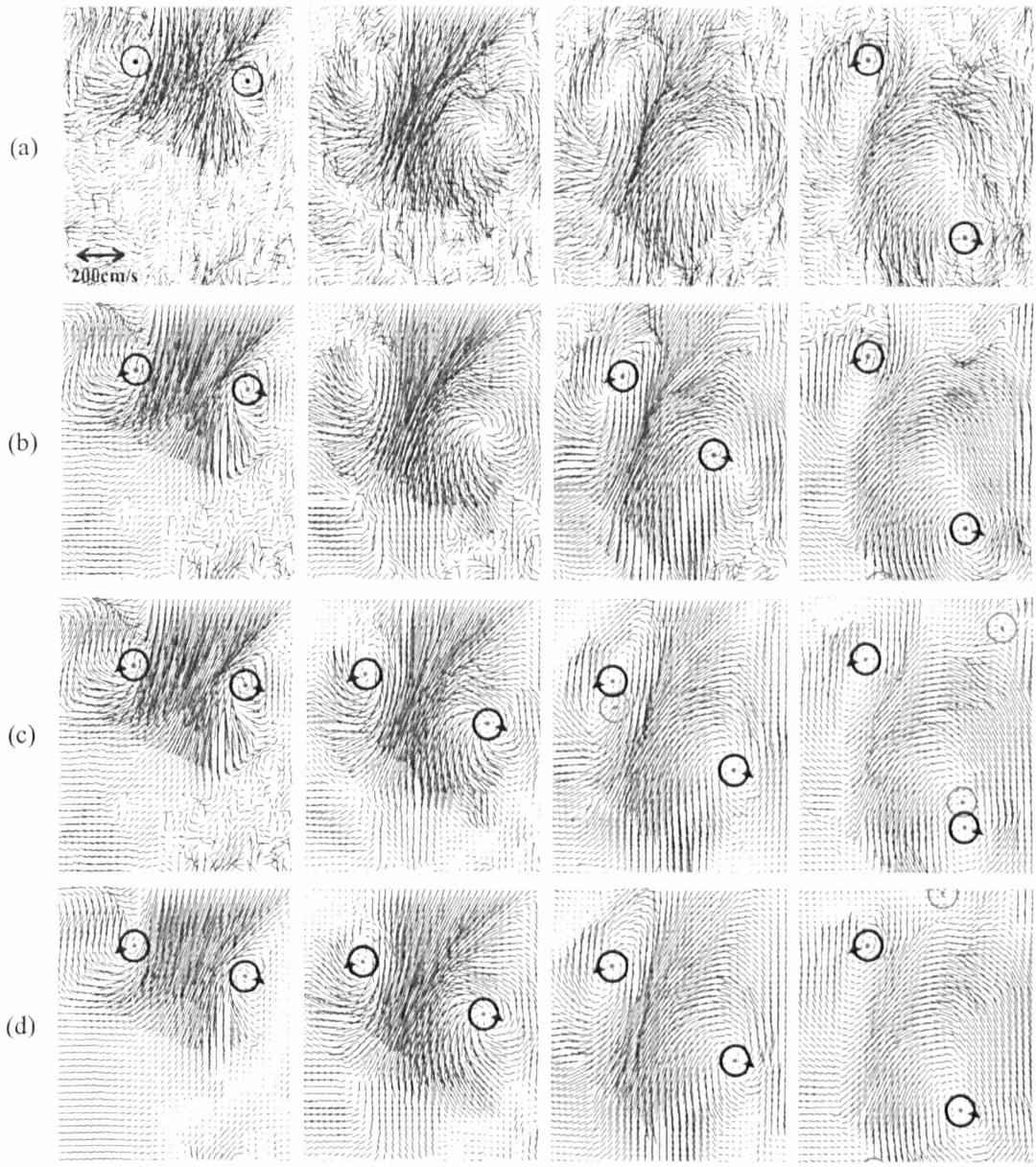

Figure 6.14 The flow patterns and the extracted vortices at various stages of the diastolic phase of the cardiac cycle from one of the patients studied. All extracted vortices, including minor and misclassified vortices, are marked with circles where the major vortices are highlighted with an arrow to indicate its rotational direction. (a) The depicted vortices were extracted by using the traditional winding index method. (b) The flow patterns were first restored followed by vortex extraction with the winding index method. (c)-(d) The flow patterns were reconstructed from the abstract flow field at 95% to 98% compression using the flow abstraction method with and without the preceding restoration step, followed by the new vortex detection algorithm. The results shown in (b) and (d) are restored using the proposed First Order method with 500 iterations.

To analyse the sensitivity of the two vortex detection methods, the number of vortices correctly identified by these two methods performed prior to and after restoration were recorded and compared against the number of vortices spotted visually. The sensitivities, measured against the number of vortices spotted visually, of the four combinations are given in Figure 6.15. It is evident from the chart that the method of combining restoration and abstraction has performed consistently better than the others across all twelve datasets, achieving an average sensitivity of nearly 90%, much higher than that of the winding index method.

Although the proposed vortex detection method has achieved a much higher sensitivity than the traditional method of using winding index, some unwanted vortices, either minor vortices or false identification, are identified along with the major vortices as shown in Figure 6.14(d). This problem can be rectified by applying a tracking algorithm to track the two main vortices. To achieve this, the two main vortices were first identified manually in the time frame where they first appear, then a tracking algorithm which locates the nearest neighbour with the same rotating direction in the next time frame were applied to track the two main vortices through the image sequence. In this way, the two main vortices can be located and all the unwanted vortices can be filtered out. A tracking algorithm based on relaxation labelling is introduced in the next chapter.

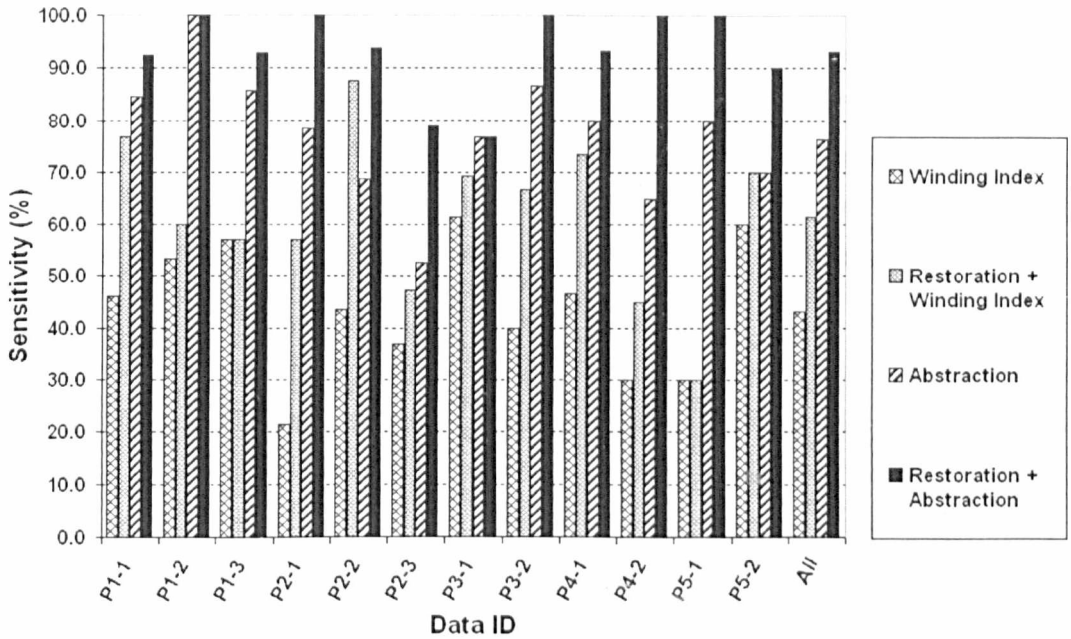

Figure 6.15 The sensitivities of the proposed vortex detection method and the winding index method with and without the restoration step for the twelve MR flow image data sets studied. The method of combining restoration and abstraction has performed consistently better than the others across all twelve datasets, achieving an average sensitivity of 93.1%, much higher than that of the winding index method.

6.4 Discussions and Conclusion

In this Chapter, we have shown that the proposed flow abstraction method together with the vortex detection algorithm is effective in detecting vortical flow features with much improved sensitivity than that of the winding index method. It was shown that the proposed method achieved the best result when combined with the restoration approach described in Chapter 5. The sensitivity of the proposed vortex detection technique on the estimated noise variance and lambda was compared, and the results showed that sensitivity depended more on the value of lambda than estimated noise variance. This justifies the robustness of combining restoration with flow field abstraction and vortex detection.

It was also shown that the proposed method achieved a high sensitivity irrespective of the compression ratio chosen in the abstraction step, indicating that the choice of compression ratio does not affect the apparent accuracy of our method and hence can be conveniently fixed. It must be noted that this can potentially be coupled with a decreased specificity in that some unwanted vortices might be wrongly identified. This, however, does not pose a major problem to our study as these vortices can be filtered out by applying the tracking algorithm as will be described in the next chapter. In conclusion, we have described a new framework for the restoration, abstraction, and extraction of flow features. The method allows accurate quantification of dynamic indices associated with salient features so that inter- and intra-subject comparisons can be easily performed. The use of the First Order Lagrangian method proves to be effective in improving the consistency of the MR velocity data and the proposed flow abstraction technique greatly reduces the amount of data required to encode the velocity distribution, which permits an analytical representation of the flow field from which critical points associated with salient flow features can be accurately extracted.

Chapter 7

Vortex Tracking

7.1 Introduction

In the previous Chapter, we have shown that vortical motion in diastole is a salient flow feature and its evolution over time can provide important insight into the health status of the heart. Previous study has shown that there are significant differences in flow pattern topology between normal subjects and patients with dilated ventricle [16]. The difference is manifested not only in general flow pattern such as the formation and propagation of vortices, but also in its dynamics over the cardiac cycle. To allow for a detailed study on the evolution of vortices, it is desirable to track salient flow features to examine its temporal characteristics.

Tracking techniques for time resolved image sequences have found a wide range of applications, particularly in the field of computer vision. Common applications include motion tracking in video stream, contour tracking in image sequence and cloud tracking in meteorological satellite images. To accommodate the wide variety of problems associated with different applications, a number of techniques have been developed. They include Hopfield neural network [237], image warping, condensation algorithm [238] and

correlation relaxation labelling [239]. Most of the techniques available require a large training dataset and are, therefore, not suitable to this study because the image sequence typically contains 10 or less time frames.

For tracking vortices over time, the simplest method is the nearest neighbour approach which identifies the nearest vortex with the same rotation direction in the next time frame. This method is based on the assumption that vortices do not move drastically between consecutive time frames. The technique is simple to implement but has a major drawback that it fails to work when there is a missing vortex in any of the time frames, usually due to image noise.

Reinders *et al.* [240] has proposed a feature-based tracking algorithm for tracking time-resolved 2D vortices. First, a number of features of the vortex are extracted and then these features are used in the tracking algorithm. The selected features are the position, size and rotational direction of the vortices. Each feature is associated with a set of attributes that helps to further define the correspondence between them. Subsequently, a correspondence function is defined for each attribute, which measures the similarity between a candidate and the prediction. The correspondence between two features can be defined as the weighted sum of all the correspondence values of its attributes. By computing the correspondence value of a candidate feature and a prediction, one can define whether or not there is a match. In a later study by the same authors [241], the tracking method was applied to first construct 3D vortex tube by tracking vortices in a stack of 2D planes and then to track the 3D vortex in a time-resolved data sequence. However, this method has only been validated using simulated data, which is free from image noise, and its practicality in real-life flow data is limited because the problem of missing vortices in noisy dataset was not addressed.

To overcome the drawback of the existing vortex tracking methods, a probabilistic relaxation technique can be used. In this chapter, we shall describe a vortex tracking algorithm that is formulated as a relaxation labelling problem in which each vortex is assigned a label, namely "connected" or "not connected". Relaxation labelling is a formal method of expressing low-level contextual information and applying them to extract high-level image features such as edges, lines and segments [242]. It is an effective technique for incorporating contextual information and has been applied to many areas of image

analysis and computer vision. In image analysis applications, the basic elements of the relaxation labelling method are a set of objects such as pixels or line segments in the context of vision and a set of labels for the objects. The labelling schemes are normally probabilistic in that for each object, probabilities are assigned to each and every label in the set initially basing on the estimated likelihood of the label being the correct one for the given object. Subsequently, a probabilistic approach is used to adjust the probabilities iteratively by taking into account the probabilities associated with neighbouring objects.

7.2 Relaxation Techniques

7.2.1 Technical background

The first practical use of relaxation technique was the computation of stresses in braced frameworks. Nowadays, relaxation technique has found a much wider range of applications. In the field of image analysis and computer vision, this technique has been used for interpreting high-level objects using low-level contextual information. Typically, the identification of a high-level object is based on a set of measurements that are related to the object itself. This object-specific information is usually not sufficient for unambiguous interpretation of the object and therefore, the inter-relationship among objects within the same image domain may be used to reduce the ambiguity. In essence, each object can be considered as a source of contextual information for interpreting other objects. A relaxation process therefore incorporates this contextual information and iteratively updates the object labels so that a consistent interpretation can be obtained without violating the constraints imposed.

There are many types of relaxation techniques available and the two most common ones are probabilistic relaxation, also called relaxation labelling, and stochastic relaxation. Probabilistic relaxation process is essentially a labelling process, hence the name relaxation labelling. A relaxation labelling problem consists of a set of objects, a set of possible labels for each object and a set of neighbourhood relationship specifying the constraints among the objects. A solution to such a problem is in effect a consistent assignment of labels to

the set of objects without violating the constraints. The classical algorithm and the probabilistic framework shall be discussed in more details in Section 7.2.2.

Stochastic relaxation technique, also referred to as simulated annealing, is a statistical mechanics technique that has been introduced to solve complex optimisation problem. During the relaxation process, a random element is introduced into the iterative scheme to prevent the result from being trapped in local minima. With simulated annealing, the value of the random element is made to depend on a 'temperature'. As the temperature increases, larger disturbances are input to the system, when it is reduced, the process converges and the optimal result is reached. German *et al.* [243] have shown that simulated annealing can be employed in image restoration problem with low signal-to-noise ratios. With this approach, the pixel grey levels and the orientation of edges are mapped to the states of molecules in a lattice-like physical system, which are then updated using the simulated annealing algorithm until the result converged. However, this technique falls out of scope of this thesis and will not be discussed further.

7.2.2 Relaxation Labelling Algorithm

The initial work in relaxation labelling was done by Waltz [244], in which the problem of line drawing interpretation for a set of polyhedra was studied. An unambiguous interpretation of the line segments was derived by sequentially filtering out inconsistent connected label pairs. Rosenfeld [245] popularised Waltz's approach by demonstrating that the method could be carried out in parallel and subsequently implemented as a network of processors, each associated with one object. Since then, relaxation labelling method has drawn a considerable amount of interests.

The basic elements in a labelling problem are: 1) a set of objects, 2) a set of labels for each object, 3) connectivity relation of the objects and 4) a set of constraints defined over labels at pairs of connected objected. The solution to such a problem comes in two forms, either only a single label is assigned to an object, or a set of labels, each with a probability of belonging to an object, can be associated with an object. The former is referred to as a discrete relaxation labelling whereas the later one is a continuous one. In a discrete formulation, the constraints are represented as a logical compatibility function, *i.e.* each

pair of labels is either entirely compatible or incompatible. The continuous relaxation scheme, on the other hand, allows greater flexibility in the constraints by replacing the logical compatibility values with real value that express the relative preferences of compatibility. This feature has increased the general applicability of the continuous relaxation framework. Our discussion will focus on the continuous framework.

To describe the relaxation labelling process, we first introduce the essential notations. We denote:

$$\begin{aligned} &\textit{Set of objects } \mathbf{O} : \{o_1, o_2, \ldots\ldots, o_N\} \\ &\textit{Set of labels } \mathbf{L} : \{\lambda_1, \lambda_2, \ldots\ldots, \lambda_M\} \\ &\textit{Connectivity } \mathbf{\Omega} : \{\Omega_1, \Omega_2, \ldots\ldots, \Omega_N\} \end{aligned} \tag{7.1}$$

where N is the number of objects, M the number of labels, and Ω_i denotes the connectivity relation of the object o_i, *i.e.* the set of neighbour of o_i. The goal of the relaxation labelling process is to assign labels θ_i to objects o_i for all i using measurements X_i taken from the objects o_i. The constraints are represented as a set of compatibility functions that give the support for labelling o_i with λ_l from labelling o_i with λ_k:

$$C(\theta_i = \lambda_l, \theta_j = \lambda_k) \tag{7.2}$$

In general, the value of all the compatibility functions ranges from -1 to 1, with negative value representing inconsistency, 0 representing no connection and positive value representing consistency. Specifically, in the discrete formulation, this value will be either 1 or 0. The label assignment of λ_l to object o_i, denoted as $P(\theta_i = \lambda_l)$, is defined as the likelihood of such assignment. The assignment value has to fulfil the requirements:

$$\begin{aligned} &0 \le P(\theta_i = \lambda_l) \le 1 \quad \forall i, l \\ &\sum_{l=1}^{M} P(\theta_i = \lambda_l) = 1 \quad \forall i \end{aligned} \tag{7.3}$$

Subsequently, the support function for assigning λ_l to object o_i can be formulated. As this support function would be iteratively updated in the relaxation process, we denote the support function in the Sth iteration as $Q^S(\theta_i = \lambda_l)$, which can be computed as:

$$Q^S(\theta_i = \lambda_l) = \sum_{j \in \Omega_i} \sum_{k=1}^{M} C\big((\theta_i = \lambda_l), (\theta_j = \lambda_k)\big) \cdot P^S(\theta_j = \lambda_k) \tag{7.4}$$

Based on the intuition that the current label assignment should be adjusted according to the relative support given by its neighbours, the updating formula of the assignment value $P(\theta_i = \lambda_l)$ proposed by Rosenfeld [245] can be written as follow:

$$P^{S+1^*}(\theta_i = \lambda_l) = P^S(\theta_i = \lambda_l) \cdot Q^S(\theta_i = \lambda_l) \tag{7.5}$$

To ensure that the requirement of $\sum_{l=1}^{M} P(\theta_i : \lambda_l) = 1$ is fulfilled at all time, the values are normalised after each iteration:

$$P^{S+1}(\theta_i = \lambda_l) = \frac{P^{S+1^*}(\theta_i = \lambda_l)}{\sum_{k=1}^{N} P^{S+1^*}(\theta_i = \lambda_k)} \tag{7.6}$$

The updating scheme given in Equations (7.5) and (7.6) is termed the non-linear relaxation scheme. Its linear counterpart, also proposed by Rosenfeld [245], aimed to find label assignments such that

$$P(\theta_i = \lambda_l) = Q(\theta_i = \lambda_l) \qquad \forall i, l \tag{7.7}$$

This linear approach suffers from a major pitfall that it may reach a unique solution that is independent of any measurements X_i. A remedy to this problem is to incorporate the measurements in the relaxation process by means of initial probabilities, which are defined as

$$P^0(\theta_i = \lambda_l) = P(\theta_i = \lambda_l | X_i) \qquad \forall i, l \tag{7.8}$$

where $P(\theta_i = \lambda_l | X_i)$ denotes the a posteriori probabilities of assigning label λ_l to object o_i given the measurement X_i.

7.2.3 Compatibility and Support Functions

The choice of compatibility and support functions plays a crucial role in the design of a relaxation labelling process. Several researchers have attempted to define and interpret the functions using various theories. Zucker *et al.* [246] suggested that the compatibility coefficients should be rewritten such that they convey the meaning of conditional probabilities by expressing $C((\theta_i = \lambda_l),(\theta_j = \lambda_k))$ in the form of conditional probability $P((\theta_i = \lambda_l)|(\theta_j = \lambda_k))$. Using this representation, it is required that:

$$\begin{aligned} & P((\theta_i = \lambda_l)|(\theta_j = \lambda_k)) > 0 \\ \text{and} \quad & \sum_{l=1}^{M} P((\theta_i = \lambda_l)|(\theta_j = \lambda_k)) \end{aligned} \tag{7.9}$$

The aim of using this expression is to provide better control over the relaxation process and facilitate interpretation. It doe not cause any fundamental change in the formulation discussed above. Zucker *et al.* have also argued that the geometric averaging should be used instead of arithmetic averaging in Equation (7.4). The modified support function takes the form:

$$Q^S(\theta_i = \lambda_l) = \prod_{j \in \Omega,} \sum_{k=1}^{M} P((\theta_i = \lambda_l) \,|\, (\theta_j = \lambda_k)) \cdot P^S(\theta_j = \lambda_k) \tag{7.10}$$

Peleg [247] suggested the first theoretically correct interpretation of relaxation labelling in 1980. In his theory, the labels have an unknown probability distribution and various

statistical independence assumptions are used in developing the algorithm. He suggested that the compatibility coefficient should be expressed in the form

$$C(\theta_i = \lambda_l, \theta_j = \lambda_k) = \frac{P(\theta_i = \lambda_l, \theta_j = \lambda_k)}{P(\theta_i = \lambda_l)P(\theta_j = \lambda_k)} \tag{7.11}$$

For the case where only object o_j have influence over o_i, he made the conditional independence assumption that:

$$P(P_i^S, P_j^S | \theta_i = \lambda_l, \theta_j = \lambda_k) = P(P_i^S | \theta_i = \lambda_l) P(P_j^S | \theta_j = \lambda_k) \tag{7.12}$$

where P_i^s denotes the probability distribution of the labels for object o_i given probability distribution at iteration *S-1* for all objects that have influence over o_i. Based on this assumption, it can be derived that

$$P(\theta_i = \lambda_l | P_i^S, P_j^S) = \frac{P(\theta_i = \lambda_l | P_i^S) \sum_{k=1}^{M} P(\theta_j = \lambda_k | P_j^S) C(\theta_i = \lambda_l, \theta_j = \lambda_k)}{\sum_{m=1}^{M} P(\theta_i = \lambda_m | P_i^S) \sum_{k=1}^{M} P(\theta_j = \lambda_k | P_j^S) C(\theta_i = \lambda_l, \theta_j = \lambda_k)} \tag{7.13}$$

Equation (7.13) was then generalised to the case where more than one object have influence on object o_i by taking the average of all the pairwise influences:

$$P(\theta_i = \lambda_l | P_i^S, \ldots, P_N^S) = \sum_{j=1}^{N} a_{ij} P(\theta_i = \lambda_l | P_i^S, P_j^S) \tag{7.14}$$

where $\sum_{j=1}^{N} a_{ij} = 1$ for all object o_i.

Contrary to the approach proposed by Peleg, Kittler *et al.* [248] suggested that both the compatibility and support functions should be derived using statistical decision theory. To

perform labelling using their theory, it is necessary to first compute the a posteriori class probabilities:

$$P(\theta_0 = \lambda_l | X_0, \ldots, X_\mu) \tag{7.15}$$

where $o_1, \ldots, o_\mu$ belongs to the contextual conveying neighbourhood of o_0, and X_i denotes the set of measurements associated to object o_i. Subsequently, the assignment of labels can be performed in such a way that label θ_i is assigned to object o_i only if the following condition is satisfied

$$P(\theta_0 = \lambda_l | X_0, \ldots, X_\mu) = \underset{k}{MaxOf}\{P(\theta_0 = \lambda_k | X_0, \ldots, X_\mu)\} \tag{7.16}$$

By assuming conditional statistical independence between observations X_i, we have

$$P(X_0, \ldots, X_\mu | \theta_0, \ldots, \theta_\mu) = \prod_{j=1}^{\mu} P(X_j | \theta_j) \tag{7.17}$$

and the following can be derived:

$$P(\theta_0 = \lambda_l | X_0, \ldots, X_\mu) = \frac{P(\theta_0 = \lambda_l | X_0) \sum_{\theta_1} \ldots \sum_{\theta_\mu} \left\{ \prod_{j=1}^{\mu} \frac{P(\theta_j | X_j)}{P(\theta_j)} P(\theta_1, \ldots, \theta_\mu | \theta_0 = \lambda_l) \right\}}{\sum_{k=1}^{M} P(\theta_0 = \lambda_k | X_0) \sum_{\theta_1} \ldots \sum_{\theta_\mu} \left\{ \prod_{j=1}^{\mu} \frac{P(\theta_j | X_j)}{P(\theta_j)} P(\theta_1, \ldots, \theta_\mu | \theta_0 = \lambda_l) \right\}} \tag{7.18}$$

It can be seen from Equation (7.18) that the contextual label probability $P(\theta_0 = \lambda_l | X_0, \ldots, X_\mu)$ can be computed from the initial label probabilities $P(\theta_l | \lambda_l)$ at o_0 and its neighbours and the knowledge represented by the a priori probabilities

$P(\theta_1,\ldots,\theta_\mu|\theta_0 = \lambda_l)$. From this equation, the support function provided for λ_l at o_0 can be derived in the form

$$Q^S(\theta_0 = \lambda_l) = \sum_{\theta_1}\cdots\sum_{\theta_\mu}\left\{\prod_{j=1}^{\mu}\frac{P^S(\theta_j)}{P(\theta_j)}P(\theta_1,\ldots,\theta_\mu|\theta_0 = \lambda_l)\right\} \tag{7.19}$$

The computational complexity of Equation (7.19) could be exponential. It is therefore necessary to reduce its complexity to make it practical. One such method complied an exhaustive list of all possible configurations of labels in the contextual neighbourhood and stored the list in a "dictionary" [249, 250]. This strategy could greatly reduce the computational complexity in applications where the contextual neighbourhood is relatively small.

7.2.4 Optimisation Approach

The heuristic nature of the updating scheme given in (7.6) makes it difficult to establish the convergence properties. This has motivated the development of an alternative scheme using optimisation approach. Faugeras *et al.* [251] formulated the labelling problem as an optimisation problem, in which a new objective function was introduced. The objective function comprises of two components, a criterion of consistency and a measure of ambiguity, where consistency is defined as the difference between the current probability $P(\theta_i = \lambda_l)$ and the total support $Q(\theta_i = \lambda_l)$ and ambiguity is a measure of the distance between the current probabilities of all labels for each object and that of a unique label assignment. This objective function is then minimised subject to the constraints:

$$\begin{aligned} &\sum_{l=1}^{M} P(\theta_i = \lambda_l) = 1 \qquad \forall i \\ &0 \le P(\theta_i = \lambda_l) \le 1 \quad \forall i,l \end{aligned} \tag{7.20}$$

Combining ambiguity and consistency measures in the objective function has a major drawback that both measures tend to follow opposite directions. A simplified objective function was also proposed [252], and it takes the form

$$F = \sum_{i=1}^{N}\sum_{l=1}^{M} P(\theta_i = \lambda_l)Q(\theta_i = \lambda_l) \tag{7.21}$$

The definition of F, which is usually referred to as the average local consistency, was widely adopted by many researchers [252-255]. Using this formulation, the updating scheme defined in Equation (7.6) can be viewed as an algorithm optimising the objective function.

7.3 Relaxation Labelling for Vortex Tracking

In this study, the objective is to track the vortices in patients with dilated left ventricles. The tracking problem is treated as a labelling problem and a probabilistic relaxation scheme is used.

7.3.1 Relaxation Labelling for Tracking

To formulate a tracking problem as a labelling problem, an object is first selected from the set of N objects as the starting point of tracking. Each object may be assigned as "connected" or "not connected" to the selected object o^*. We denote

$$\begin{aligned} &\text{Set of Objects } \mathbf{O}: \{o_1, o_2, \ldots\ldots, o_{N-1}, o^*\} \\ &\text{Set of Labels } \mathbf{L}: \{C: \text{Connected},\ NC: \text{Not Connected}\} \end{aligned} \tag{7.22}$$

Each object is associated with two probabilities:

$$\{P(\theta_i = C), P(\theta_i = NC)\} \tag{7.23}$$

where $P(\theta_i = \lambda_l)$ denotes the probability of object o_i having label λ_l and $\sum_{l \in \mathbf{L}} P(\theta_i = \lambda_l) = 1$. A set of measurements taken from the objects and the contextual information are used for defining the initial label probabilities and the compatibility function.

Subsequently, a probabilistic relaxation scheme is used to update the label probabilities until convergence. The classical probabilistic updating scheme is given as

$$P^{S+1}(\theta_i = \lambda_l) = \frac{P^S(\theta_i = \lambda_l) Q^S(\theta_i = \lambda_l)}{\sum_{k \in \mathbf{L}} P^S(\theta_i = \lambda_k) Q^S(\theta_i = \lambda_k)} \tag{7.24}$$

and $$Q^S(\theta_i = \lambda_l) = \sum_{j \in \mathbf{O}_i} wt_{ij} \sum_{k \in \mathbf{L}} C\big((\theta_i = \lambda_l), (\theta_j = \lambda_k)\big) \cdot P^S(\theta_j = \lambda_k)$$

where wt_{ij} is a weighted factor representing the influence of object o_j on object o_i.

One undesirable property of the probabilistic relaxation scheme defined in Equation (7.24) is that after an initial improvement in a small number of iterations, the scheme collapses and produces an answer that can be erroneous. In order to determine when the iteration has converged. Several consistency measures have been suggested, and the simplest is that

$$\forall i, l \;\; P^s(\theta_i = \lambda_l) = Q^s(\theta_i = \lambda_l) \tag{7.25}$$

Alternatively, the iterative scheme in Equation (7.24) can be considered to have converged when the following condition is met

$$P^{S+1}(\theta_i = \lambda_l) - P^S(\theta_i = \lambda_l) < P_{threshold} \qquad \forall i, l \tag{7.26}$$

where $P_{threshold}$ is a predefined threshold, typically of the order of 10^{-3}.

7.3.2 Compatibility Functions and Initial Probabilities

The set of objects is defined as the set of all extracted vortices in all time frames and we want to label each object as connected or not connected to a selected object V^*. We have:

$$\begin{aligned} &\text{Set of Objects } \mathbf{O}: \{V_1, V_2, \ldots\ldots, V_{N-1}, V^*\} \\ &\text{Set of Labels } \mathbf{L}: \{C: \text{Connected},\ NC: \text{Not Connected}\} \end{aligned} \tag{7.27}$$

$$\begin{aligned} &N = \text{No. of vortices} = \sum_{m=1}^{F} N_m \\ \text{where} \quad &N_m = \text{No. of vortices in frame m} \\ &F = \text{No. of frames in the sequence} \end{aligned}$$

The selected measurements associated with each vortex are the vorticity, the position and the occurrence time frame in the sequence. We have for each vortex

$$\textit{Measurements } \mathbf{X}_i = \{vorticity(V_i), pos(V_i), frame(V_i)\} \tag{7.28}$$

The initial probabilities of each label assignment are defined using the given measurements. We first consider the probabilities of labelling a vortex V_i with "connected". Obviously, if vortex V_i is the selected starting vortex, the probability will be 1. Otherwise, if vortex V_i appears on the same time frame as V^*, the probability is zero given the known fact that there is only one tracked vortex in each time frame. The probability is also zero if V_i and V^* have different rotation direction, *i.e.* opposite sign of vorticity. For all other cases, the initial probabilities shall be dependent on the distance between V_i and V^* and the difference in vorticity of V_i and V^* such that a smaller distance and vorticity difference gives a higher probability. This is based on the assumption that both the location and strength of a vortex does not change drastically relative to other minor vortices between

time frames. Based on the requirement that the sum of probabilities of all possible labelling for each vortex has to be 1, the initial probabilities of labelling a vortex with "not-connected" can be simply calculated from that of labelling with "connected". To summarise, the initial probabilities for labelling a vortex can be written as follow:

$$P^0(V_i, C) = \begin{cases} 1, & \text{if } V_i = V^* \\ 0, & \text{if } V_i \neq V^* \ \& \ frame(V_i) = frame(V^*) \\ 0, & \text{if } sign(vorticity(V_i)) \neq sign(vorticity(V^*)) \\ (1 - d_{curl}(V_i, V^*)) \times (1 - d_{dist}(V_i, V^*)), & \text{otherwise} \end{cases} \quad (7.29)$$

$$P^0(V_i, NC) = 1 - P^0(V_i, C)$$

where

$d_{vorticity}(V_i, V_j) = abs(vorticity(V_i) - vorticity(V_j)) / abs(MaxVorticity)$

$d_{dist}(V_i, V_j) = dist(V_i, V_j) / MaxDist$

$MaxVorticity = MaxOf\{vorticity(V_i): sign(vorticity(V_i)) = sign(vorticity(V^*)\}$

$MaxDist$ = maximum distance between any two vortices

Subsequently, the contextual information is expressed as compatibility functions $C((V_i : \lambda_l), (V_j : \lambda_k))$, which measure how compactable it would be to label V_i with λ_l and V_j with λ_k. Given the fact that only one vortex in each time frame may be tracked, we can derive that the compatibility of any two vortices to be labelled as connected is zero if they appear on the same time frame, or is dependent on their relative position and vorticity otherwise. For other labelling compatibilities, a neutral value is assigned. The compatibility functions can be defined as follows:

$$\begin{aligned} C((V_i : C), (V_j : C)) &= \begin{cases} 0, & \text{if } frame(V_i) = frame(V_j) \\ (1 - d_{curl}(V_i, V_j)) \times (1 - d_{dist}(V_i, V_j)), & \text{otherwise} \end{cases} \\ C((V_i : C), (V_j : NC)) &= 0.5 \\ C((V_i : NC), (V_j : C)) &= 0.5 \\ C((V_i : NC), (V_j : NC)) &= 0.5 \end{aligned} \quad (7.30)$$

As the influence of the vortices on others decrease with time, we define the relative importance between nodes basing on this property:

$$a_{ij} = \begin{cases} 0, & \text{if } i = j \\ 1, & \text{if } abs(frame(V_i) - frame(V_j)) <= 1 \\ 1/2^{abs(frame(Vi) - frame(vj))}, & \text{otherwise} \end{cases} \tag{7.31}$$

With the contextual support from other objects and the relative importance between nodes defined, the support function can now be derived as:

$$Q^S(Vi, l_l) = \sum_{j=1}^{N} a_{ij} \sum_{k=1}^{L} C_{ij}((V_i, l_l), (V_j, l_k)) P^S(V_j, l_k) \tag{7.32}$$

Subsequently, the probability updating schemed can be written as

$$P^{S+1}(V_i, l_l) = \frac{P^S(V_i, l_l) \cdot Q^S(V_i, l_l)}{\sum_{k=1}^{M} P^S(V_i, l_k) \cdot Q^S(V_i, l_k)} \tag{7.33}$$

Note that at the end of each step, the probabilities have to be normalised to ensure that the total probability of all label assignments for each object equals 1. When the iterative scheme converges according to the criteria set out in Equation (7.26), we have for each object (or vortex) the probabilities of two possible labels, which add up to be 1. For each vortex, the label with the larger probability is assigned to it and thus we can determine whether it is connected to the selected vortex.

7.4 Results

The proposed tracking algorithm was applied twice to each of the 12 MR image sequences to track the anterior and posterior vortices. The vortices in the 12 image sequences were extracted using the proposed restoration and vortex detection methods described in the previous chapters. The proposed tracking method achieved an overall accuracy of over 95%, *i.e.* an error rate of less than 5%. Table 7-1 summarised the tracking results.

	(a)	(b)	(c)	(d)	(e) =(b)-(c)	(f) =(d)+(e)	(g)=(f)/(a) x 100%
DateSet	**No. of Vortices Extracted**	**No. of Vortices in the Sequence**	**Correctly Identified**	**Falsely Included**	**Missed Vortices**	**Total Error Count**	**Error Rate (%)**
P1-1A	23	6	6	1	0	1	4.35
P1-1P	23	6	6	0	0	0	0.00
P1-2A	30	9	6	2	3	5	16.67
P1-2P	30	6	6	2	0	2	6.67
P1-3A	22	6	6	1	0	1	4.55
P1-3P	22	7	7	0	0	0	0.00
P2-1A	21	7	7	0	0	0	0.00
P2-1P	21	7	6	2	1	3	14.29
P2-2A	29	7	7	0	0	0	0.00
P2-2P	29	8	8	3	0	3	10.34
P2-3A	22	8	7	2	1	3	13.64
P2-3P	22	7	7	0	0	0	0.00
P3-1A	17	8	8	0	0	0	0.00
P3-1P	17	2	2	0	0	0	0.00
P3-2A	26	8	7	0	1	1	3.85
P3-2P	26	7	7	0	0	0	0.00
P4-1A	24	8	8	0	0	0	0.00
P4-1P	24	6	5	0	1	1	4.17
P4-2A	37	10	10	0	0	0	0.00
P4-2P	37	10	10	0	0	0	0.00
P5-1A	16	5	4	1	1	2	12.5
P5-1P	16	5	5	0	0	0	0.00
P5-2A	19	5	3	0	2	2	10.53
P5-2P	19	4	4	1	0	1	5.26
All	**572**	**162**	**152**	**15**	**10**	**25**	4.37

Table 7-1 Results of applying the proposed tracking algorithm to track the posterior (P) and anterior (A) vortices in 12 image sequences.

To assess the convergence behaviour of the proposed relaxation algorithm, the probabilities of labelling the vortices with "Connected (C)" are recorded and plotted against the number of iterations. The probabilities of all vortices in all datasets converged to either 0 or 1 in between 100 to 7000 iterations in a manner similar to a typical probabilistic relaxation labelling algorithm. The typical convergence behaviour of the "connected" probabilities is depicted in Figure 7.1, which is taken from dataset "P1-3P" in Table 7-1. It can be seen that a significant improvement was achieved initially and then the rate of convergence becomes very slow towards the end.

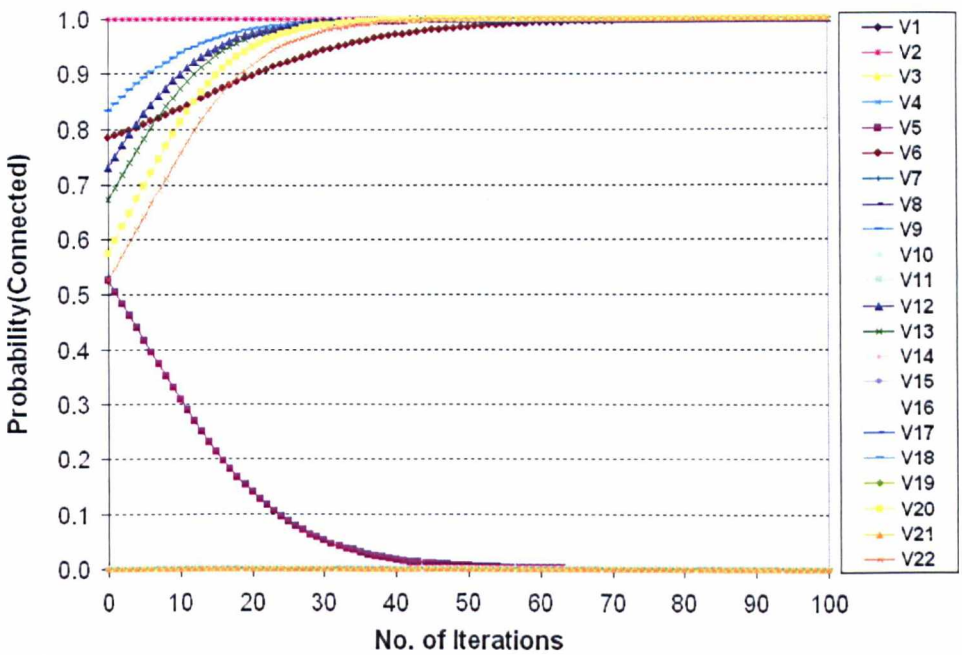

Figure 7.1 Probabilities of labelling the set of 22 vortices with "Connected (C)" in dataset P1-3P listed in Table 7-1. All probabilities converged to 0 or 1 in 100 iterations.

To allow inter- and intra-patient comparison, the trajectories of the tracked vortices were overlaid on the MR anatomical images and the corresponding vorticities were plotted against the time after ECG R-wave. The results of two patients studied are shown in Figure 7.2 and Figure 7.3, which demonstrate significant difference in the vortical flow patterns acquired in three sequential examinations, from 2 weeks to 3 months, following myocardial infarction.

In the first patient studied, the vortical flow patterns acquired in the three examinations did not vary significantly. It can be seen in Figure 7.2(a-c) that the trajectories of the two main vortices at 2 weeks, 1 month and 3 months following myocardial infarction demonstrated a similar movement and location. The corresponding vorticity as shown in Figure 7.2(d) also demonstrated a similar trend in the three examinations.

In contrast to the first patient, the vortical flow patterns of another patient demonstrated significant differences in the three examinations. Figure 7.3(a-c) depict the trajectories of this patient at 2 weeks, 1 month and 3 months following myocardial infarction respectively. The direction of the movement of the anterior vortex (A) does not change in Figure 7.3(a), whereas those in Figure 7.3(b) and Figure 7.3(c) seem to deviate a lot more from the initial movements. The corresponding vorticity of the vortices measured in the three examinations were given in Figure 7.3(d). It can be seen that the variations in vorticity through the diastolic phase were significantly different in the three examinations.

A significant difference between the vortical flow patterns of the two patients can be found by comparing the trajectories of the vortices. It can be seen that the posterior vortex in the first patients depicted in Figure 7.2(a-c) demonstrated a larger movement compared to that of the second patient depicted in Figure 7.3(a-c). The anterior vortex (A), on the other hand, seems to be more restrained in the first patient than in the second patient. By comparing the vorticity plots, one could easily find that the maximum strength of the vortex in the second patient (Figure 7.3(d)) is higher than that in the first patient (Figure 7.2(d)).

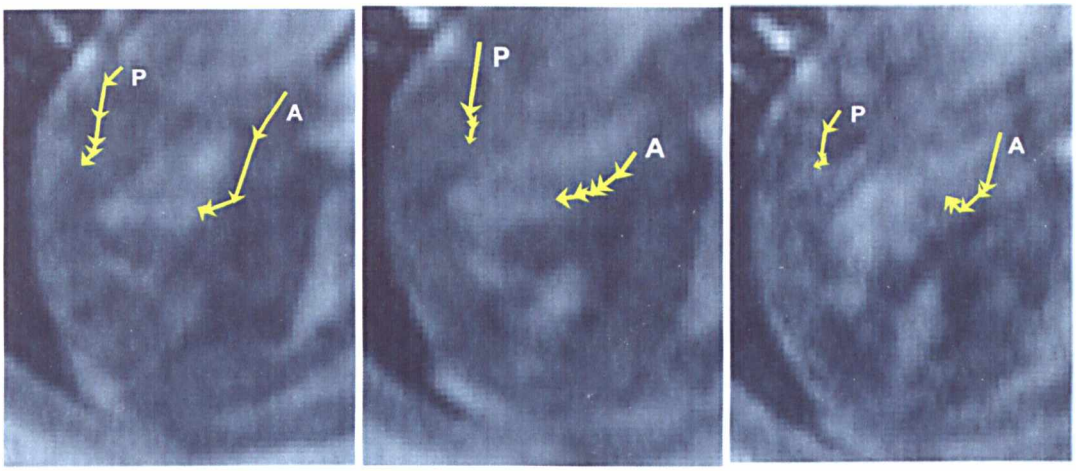

(a) (b) (c)

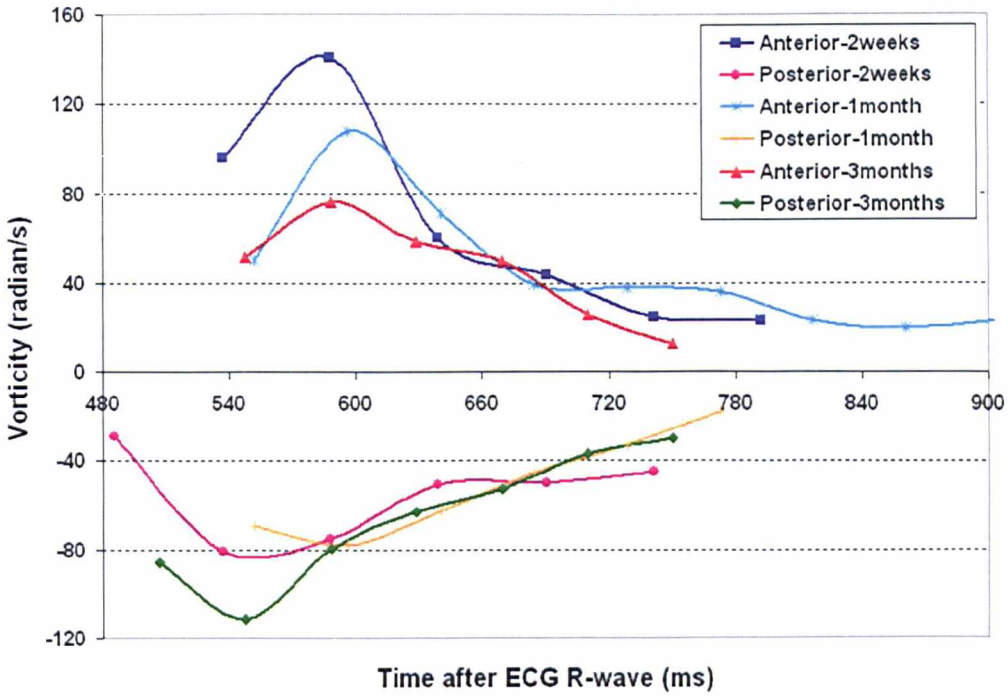

(d)

Figure 7.2 (a-c) Trajectories of the posterior (P) and anterior (A) vortices in the left ventricle of a patient with a history of myocardial infarction. The vortices were extracted from velocity images acquired at 2weeks (a), 1 month (b) and 3months (c) following myocardial infarction. (d) The corresponding vorticity of the vortices depicted in (a-c).

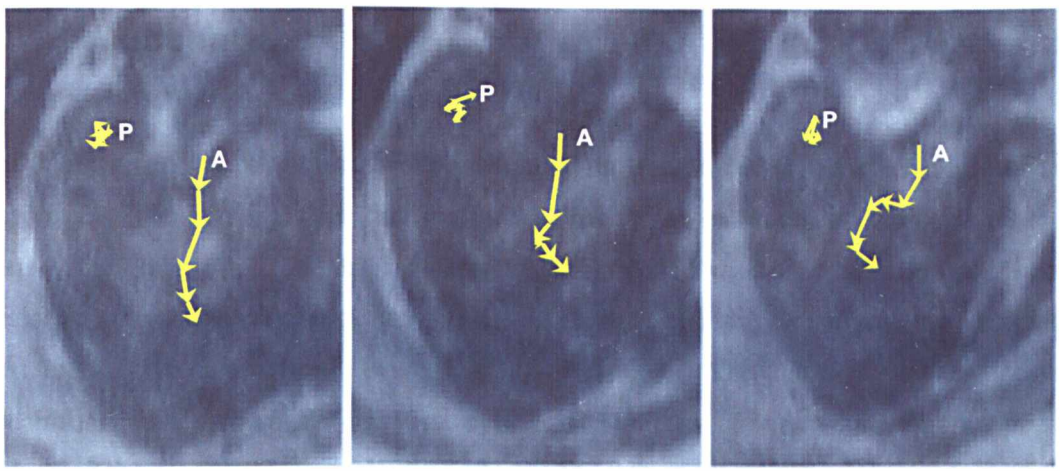

(a) (b) (c)

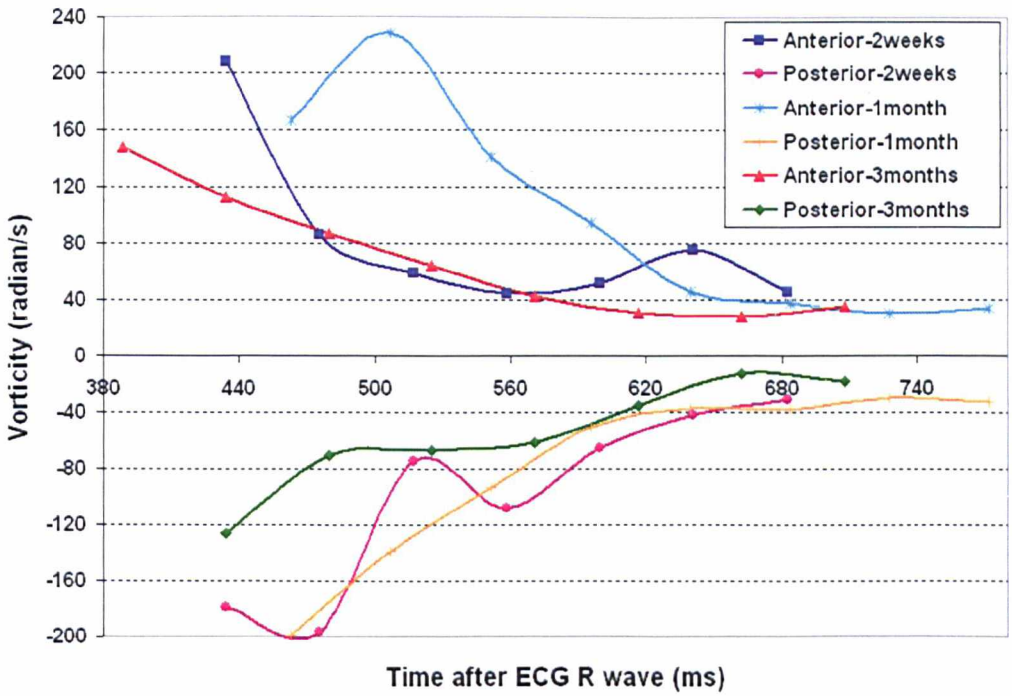

(d)

Figure 7.3 (a-c) Trajectories of the posterior (P) and anterior (A) vortices in the left ventricle of a patient with a history of myocardial infarction. The vortices were extracted from velocity images acquired at 2weeks (a), 1 month (b) and 3months (c) following myocardial infarction. (d) The corresponding vorticity of the vortices depicted in (a-c).

7.5 Conclusions

In this chapter, we have described a tracking algorithm based on the relaxation labelling approach. The tracking algorithm performed well on the patient sequences with an error rate of less than 5%. The proposed algorithm, combined with the restoration and vortex detection method introduced in the previous chapters, offers a practical framework for the extraction and comparison of vortical flow features. The method enables accurate quantification of vortical flow patterns and facilitates inter- and intra-subjects comparison. By using the proposed technique, the vortical flow patterns in the left ventricles for patients with sequential examinations following myocardial infarction were compared. The general similarities and differences are manifested in the vortex trajectories and temporal changes in vorticity, which are caused by a coupled effect of ventricular contractility, morphology, and function.

Chapter 8

Conclusions

Cardiovascular disease is the leading cause of death in the developed world, and extensive clinical studies have been conducted to investigate the causes and consequences of the disease. This is mainly attributed to atherosclerosis which leads to narrowing or obstruction of one or more of the coronary arteries. This may subsequently result in myocardial infarction, which could be fatal. Following myocardial infarction, a natural process called myocardial remodelling may occur. The remodelling process typically involves topological changes characterised by the dilation of one or both ventricles and functional changes such as reduced contractility. This process can also be associated with non-ischaemic heart disease such as dilated cardiomyopathy and heart failure. It is generally believed that the topological changes of the ventricle and the associated functional impact can be reflected in the blood flow patterns.

8.1 Blood Flow Patterns and Cardiovascular Disease

With the introduction of MR velocity imaging techniques, comprehensive multi-dimensional flow distribution can now be measured. MR phase contrast velocity mapping

is a versatile technique that is well suited for the study of in vivo flow patterns. With this technique, abnormal flow patterns in the cardiac chambers and major blood vessels have been analysed in great detail. The aortic flow, in particular, is one of the most extensively studied flow distributions. Existing studies have shown that abnormal flow patterns can be caused by a loss of elasticity in the vessel wall, which is one of the consequences of atherosclerosis and aging. Disturbed flow patterns have also been observed in the left ventricle of patients who have undergone myocardial remodelling. It has been demonstrated that the morphology and dynamics of the ventricular structure can have a significant influence on the resultant flow patterns. However, whether the disturbed flow would in turn affect the remodelling process remains an intriguing question to be explored.

8.2 Flow Patterns Analysis using MR Velocity Imaging

To elucidate the connections between blood flow patterns and cardiovascular disease, we have adopted the approach of detecting salient topological features prior to analytical assessment of dynamical indices of the flow patterns. The primary focus of this study is on vortical flow features during diastole. We have developed a framework that consists of three main components: flow restoration, feature extraction and tracking. The proposed framework is applied to the analysis of flow patterns in the left ventricle using MR velocity mapping.

8.2.1 Flow Field Restoration

As discussed in Chapter 3, MR velocity imaging techniques are subject to a number of errors that are intrinsic to hardware setup, pulse sequence design and patients movement. Although attempts have been made to minimise these errors in the image acquisition process, it is practically impossible to remove all image noises. As such, the acquired MR velocity data has to be post-processed to improve the consistency of the data prior to further analysis.

In this thesis, the velocity restoration method is formulated as a constrained optimisation problem, and a numerical scheme is developed based on First Order Lagrangian method. We have demonstrated that the proposed restoration method is effective in restoring velocity field. The main advantage of the proposed method is that it converges to the optimal solution without explicit or empirically defined stopping criteria, thus greatly enhancing its practical value. Nevertheless, the optimum performance of the proposed method relies on the correct identification of the noise behaviour of the image. As the precise amount of noise in the MR velocity images is not known, estimated values calculated from the velocity images are used. The variance of noise in the MR velocity image can be estimated by calculating the variance of signal in a region where the velocity is expected to be zero, which typically can be located at the chest wall of the images. The proposed restoration scheme has the advantage that it allows extra constraints to be incorporated. With additional constraints, we expect that the consistency of the velocity data can be further improved.

Although the proposed restoration algorithm is primarily developed for 2D MR velocity data, it is equally applicable to 3D velocity data. To demonstrate this feature, the result of applying the proposed method to a 3D dataset is also presented in Chapter 5. Currently, 3D cine MR velocity imaging is still not widely used in routine clinical examinations due to the prolonged acquisition time. However, with the recent advances in echo planar and spiral flow imaging techniques combined with selective volume excitation and *k-t* space interpolation, it is expected that 3D cine velocity measurement will become clinically applicable in the near future. The proposed restoration method can be served as a valuable pre-processing tool for a systematic study of the velocity data.

8.2.2 Flow Feature Extraction

To accommodate the diversity of flow patterns in relation to morphological and functional changes, we have advocated the approach of detecting salient topological features prior to analytical assessment of dynamical indices of the fluid. To this end, critical points associated with salient flow features have to be extracted such that the remaining flow field and its geometry and topology can be compactly described. We have described in Chapter 6 a flow abstraction and vortex extraction method for the extraction of vortical flow features.

The flow abstraction algorithm proposed is a hierarchical clustering algorithm that partitions a velocity flow field into different clusters. Each cluster is represented by the local linear expansion of its velocity components. With this representation, the neighbourhood of a critical point can be compactly described, thus greatly reducing the amount of information required to describe the complex flow fields while preserving the intrinsic flow details. Another advantage of using this representation is that given a cluster, the approximation of the original vectors can be easily deduced from the analytical description of the vector fields. After an abstract flow field is generated by using the proposed flow abstraction algorithm, critical points, including vortices, can be more reliably extracted and classified by using the phase portrait theory.

We have shown that the proposed flow abstraction method together with the vortex detection algorithm is effective in extracting vortices with much improved sensitivity than that of the traditional winding index approach. We have further demonstrated that for noisy data such as MR velocity mapping the sensitivity is further improved by pre-processing the noisy data by using the proposed restoration method. However, the improved sensitivity could be coupled with a decreased specificity. This, however, does not pose a major problem to our study as these vortices could be filtered out by applying the tracking algorithm described.

8.2.3 Vortex Tracking

As discussed in Chapter 7, the vortex detection results can be improved by using a tracking algorithm to prune out the unwanted vortices. We have described in Chapter 7 an effective vortex tracking method based on the relaxation labelling approach. The parameters and constraints of the tracking algorithm are designed by using the data associated with the vortices specific to our application. By using the proposed framework, the evolution of the two major vortices in the left ventricle is tracked throughout diastole. The results have shown distinctive trends across different serial examination of the subjects. We have shown that the changes in flow patterns in early examinations can be significantly different across patients. This could be caused by the difference in the initial myocardial injury and the extent of subsequent remodelling. Further study involving a large patient population is required to further validate this hypothesis. The computational framework developed in this thesis should greatly facilitate such future studies.

8.3 Conclusions and Future Work

In conclusion, this thesis presents a new framework for the restoration, extraction and tracking of flow features. The method allows the accurate tracking and quantification of dynamic indices associated with salient features so that inter- and intra-subject comparisons can be more easily made. The use of the First Order Lagrangian method proves to be effective in improving the consistency of the MR velocity data and the proposed flow abstraction technique greatly reduces the amount of data required to encode the velocity distribution, which permits an analytical representation of the flow field from which critical points associated with salient flow features can be accurately extracted. The tracking algorithm adds a final touch to the proposed framework by improving the vortex detection results through tracking. The convergence behaviour and accuracy of the method demonstrate the practical value of the proposed framework.

It is worth noting that although the reliability of the proposed framework is demonstrated, it is necessary to analyse the reproducibility of the method to make it clinically useful. To carry out this analysis, however, will require a large set of flow data acquired from both normal subjects and patients. This is not performed in this study due to limited velocity data acquired.

Limited by the prolonged acquisition time of three dimensional time-resolved (4D) velocity images, the analysis of blood flow patterns using the proposed framework is mainly restricted to the use of 2D MR velocity data in this thesis. Volumetric velocity data covering the entire volume of the ventricle will allow a more comprehensive and realistic description of the flow patterns. To this end, research into fast imaging techniques for the acquisition of 4D velocity data is necessary. At present, spiral and EPI imaging have been successfully combined with zonal selective imaging to speedup the acquisition process and reduce the breath-hold time. Alternative methods for reducing scanning time have also been investigated. One potential solution would be to reduce the amount of k-space encoding data required by exploiting the information content of the k-space data. This idea could be achieved by using a scheme that is similar to the generalised series reconstruction technique for dynamic imaging, in which a time-resolved image sequence of high-resolution is

reconstructed from a single high-resolution reference image and a sequence of low-resolution images.

With the continuous improvements in MR velocity imaging techniques and hardware equipment, 3D cine velocity measurement is expected to be more widely available in the near future. To address the increasing volume and dimensionality of the acquired velocity data, further improvement to the image processing techniques are essential in enhancing the practical value of the proposed framework. As demonstrated in this thesis, the underlying principles of the proposed restoration and flow abstraction method can be applied directly to 3D velocity data. However, this abstraction scheme presents a major problem for visualisation because flow surrounding the vortices may occlude them from the observer if the traditional way of displaying the flow patterns with streamline is used. Therefore, more sophisticated visualisation methods are needed for visualising the 3D flow patterns and displaying the vortices effectively. One possible solution to this problem is to build on top of the flow abstraction algorithm to use selective visualisation of the streamlines such that salient flow features can be displayed clearly. The proposed abstraction algorithm can serve as a natural aid for this purpose. For three-dimension velocity field, however, identifying a vortex ring could be a more complicated issue. An effective way for the extraction and quantification of 3D vortices from the abstraction result is desired. Similarly, significant modifications to the constraints and parameters of the tracking algorithm would be required to allow the tracking of 3D vortex. Another potential enhancement to the proposed framework is to perform coupled modelling of myocardial dynamics and ventricular flow. By analysing the simultaneous changes in ventricular morphology with the flow patterns, the fluid-structure interaction can be investigated. It is expected that further insight can be gained with the morphology incorporated, as the disturbed flow patterns in diseased heart are believed to be introduced by the change in ventricular morphology.

The idea of evaluating the fluid-structure interaction in the left ventricle has been explored by using computational flow models. Extensive research has been performed to extract the ventricular topology from medical images and to evaluate the influence of the prescribed flow boundary conditions in ventricular flow simulation. It has been shown that with a realistic model of the ventricular structure and flow boundary conditions, subject specific flow simulations can be achieved by using CFD techniques. These techniques have been

applied to predict the effect of myocardial dysfunction on flow patterns. Not only do they allow the measurements of haemodynamic parameters that cannot be obtained from in vivo data, they also provide velocity measurements with a much higher temporal and spatial resolution. These techniques are continuously being improved to enable realistic flow prediction and they can be combined with the flow feature extraction framework proposed in this thesis to enable detailed analysis on the correlation among flow patterns, other haemodynamics parameters and myocardial function in healthy and diseased heart. Ultimately, the combined efforts in subject specific flow simulations, medical image acquisition and flow image analysis techniques could help to establish the connection between blood flow and cardiovascular disease. The work presented in this thesis combines pattern recognition, image processing, flow modelling and simulation. It is an interdisciplinary effort made possible by the unique facilities at the Royal Society/Wolfson Foundation Medical Image Computing Laboratory at Imperial College London.

References

1. Petersen S, Peto V and Rayner M, *2004 Coronary heart disease statistics*. 2004, London, UK: British Heart Foundation.

2. Anderson R and Becker A, *Cardiac Anatomy: an integrated text and colour atlas*. 1980, London: Gower Medical.

3. Torrent-Guasp F, Zarco P, Lunkenheimer P, *et al.*, *Estructura Y Mecaniica Del Corazon (English Translation of Chapter 2: Macroscopical Structure of the Heart)*. 1987, Barcelona: GRASS Ediciones.

4. Torrent-Guasp F, Buckberg GD, Clemente C, *et al.*, *The structure and function of the helical heart and its buttress wrapping. I. The normal macroscopic structure of the heart.* Semin Thorac Cardiovasc Surg, **2001**. 13(4): p. 301-19.

5. Jouk PS, Usson Y, Michalowicz G, *et al.*, *Mapping of the orientation of myocardial cells by means of polarized light and confocal scanning laser microscopy.* Microsc Res Tech, **1995**. 30(6): p. 480-90.

6. LeGrice IJ, Smaill BH, Chai LZ, *et al.*, *Laminar structure of the heart: ventricular myocyte arrangement and connective tissue architecture in the dog.* Am J Physiol, **1995**. 269(2 Pt 2): p. H571-82.

7. Sunthareswarana R, *Cardiovascular system*. 1998, London: Mosby.

8. Kilner PJ, Yang GZ, Wilkes AJ, *et al.*, *Asymmetric redirection of flow through the heart.* Nature, **2000**. 404(6779): p. 759-61.

9. Silverman PR, Ten Cate FJ, Serruys PW, *et al.*, *Abnormal diastolic flow patterns in hypertrophic cardiomyopathy: evaluation by simultaneous Doppler echocardiography, cineangiography, and hemodynamics.* J Am Soc Echocardiogr, **1989**. 2(5): p. 346-9.

10. Kvitting JP, Ebbers T, Wigstrom L, *et al.*, *Flow patterns in the aortic root and the aorta studied with time-resolved, 3-dimensional, phase-contrast magnetic resonance imaging: implications for aortic valve-sparing surgery.* J Thorac Cardiovasc Surg, **2004**. 127(6): p. 1602-7.

11. Taylor TW and Yamaguchi T, *Flow patterns in three-dimensional left ventricular systolic and diastolic flows determined from computational fluid dynamics.* Biorheology, **1995**. 32(1): p. 61-71.

12. Berthier B, Bouzerar R and Legallais C, *Blood flow patterns in an anatomically realistic coronary vessel: influence of three different reconstruction methods.* J Biomech, **2002**. 35(10): p. 1347-56.

13. Saloner D, *Cardiovascular flow patterns: what should we make of them?* Int J Card Imaging, **1999**. 15(2): p. 97-8.

14. Yang GZ, *Exploring in vivo blood flow dynamics.* IEEE Eng Med Biol Mag, **1998**. 17(3): p. 64-72, 104.

15. Kim WY, Walker PG, Pedersen EM, *et al.*, *Left ventricular blood flow patterns in normal subjects: a quantitative analysis by three-dimensional magnetic resonance velocity mapping.* J Am Coll Cardiol, **1995**. 26(1): p. 224-38.

16. Yang GZ, Mohiaddin RH, Kilner PJ, *et al.*, *Vortical flow feature recognition: a topological study of in vivo flow patterns using MR velocity mapping.* J Comput Assist Tomogr, **1998**. 22(4): p. 577-86.

17. Klabunde RE, *Cardiovascular Physiology Concepts.* 2004: Lippincott Williams & Wilkins.

18. Brauwald E, Zipes D and Libby P, *Heart disease: a textbook of cardiovascular medicine.* 6 ed. 2001, Philadelphia: Saunders.

19. Gersh B and Rahimtoola S, *Acute Myocardial Infarction.* 2 ed, ed. B. Gersh and S. Rahimtoola. 1997, New York; London: Chapman & Hall.

20. White HD, Cross DB, Elliott JM, *et al.*, *Long-term prognostic importance of patency of the infarct-related coronary artery after thrombolytic therapy for acute myocardial infarction.* Circulation, **1994**. 89(1): p. 61-7.

21. Pfeffer MA and Braunwald E, *Ventricular remodeling after myocardial infarction. Experimental observations and clinical implications.* Circulation, **1990**. 81(4): p. 1161-72.

22. Braunwald E and Pfeffer MA, *Ventricular enlargement and remodeling following acute myocardial infarction: mechanisms and management.* Am J Cardiol, **1991**. 68(14): p. 1D-6D.

23. Pfeffer MA and Braunwald E, *Ventricular enlargement following infarction is a modifiable process.* Am J Cardiol, **1991**. 68(14): p. 127D-31D.

24. McKay RG, Pfeffer MA, Pasternak RC, *et al.*, *Left ventricular remodeling after myocardial infarction: a corollary to infarct expansion.* Circulation, **1986**. 74(4): p. 693-702.

25. Webb S, *The physics of medical imaging.* 2nd ed. 2001, Bristol: Institute of Physics. 656.

26. Klingenbeck-Regn K, Flohr T, Ohnesorge B, *et al.*, *Strategies for cardiac CT imaging.* Int J Cardiovasc Imaging, **2002**. 18(2): p. 143-51.

27. Wang S, Detrano RC, Secci A, *et al.*, *Detection of coronary calcification with electron-beam computed tomography: evaluation of interexamination reproducibility and comparison of three image-acquisition protocols.* Am Heart J, **1996**. 132(3): p. 550-8.

28. Redberg RF and Shaw LJ, *A review of electron beam computed tomography: implications for coronary artery disease screening.* Prev Cardiol, **2002**. 5(2): p. 71-8.

29. Guy C, *An introduction to the principles of medical imaging.* 2000, London: Imperial College Press.

30. Pennell D, Underwood R, Costa D, *et al.*, *Thallium Myocardial Perfusion Tomography in Clinical Cardiology.* 1993, New York: Springer-Verlag.

31. van den Hoff J, Burchert W, Wolpers HG, *et al.*, *A kinetic model for cardiac PET with [1-carbon-11]-acetate.* J Nucl Med, **1996**. 37(3): p. 521-9.

32. Mathie RT, *Blood flow measurement in man.* 1982: Tunbridge Wells : Castle House.

33. Sciacca R, Akinboboye O, Chou R, *et al.*, *Measurement of myocardial blood flow with PET using 1-11C-acetate.* J Nucl Med, **2001**. 42: p. 63-70.

34. Herrero P, Markham J and Bergmann SR, *Quantitation of myocardial blood flow with H2 15O and positron emission tomography: assessment and error analysis of a mathematical approach.* J Comput Assist Tomogr, **1989**. 13(5): p. 862-73.

35. Kaulitz R, Luhmer I and Kallfelz HC, *Pulsed Doppler echocardiographic assessment of patterns of venous flow after the modified Fontan operation: potential clinical implications.* Cardiol Young, **1998**. 8(1): p. 54-62.

36. Ayabakan C and Ozkutlu S, *Normal patterns of flow in the superior cava, hepatic and pulmonary veins as measured using Doppler echocardiography during childhood.* Cardiol Young, **2003**. 13(2): p. 143-51.

37. DeGroff CG, Orlando W and Shandas R, *Insights into the effect of aortic compliance on Doppler diastolic flow patterns seen in coarctation of the aorta: a numeric study.* J Am Soc Echocardiogr, **2003**. 16(2): p. 162-9.

38. Wei K, Jayaweera AR, Firoozan S, *et al.*, *Quantification of myocardial blood flow with ultrasound-induced destruction of microbubbles administered as a constant venous infusion.* Circulation, **1998**. 97(5): p. 473-83.

39. Gorg C, Riera-Knorrenschild J and Dietrich J, *Pictorial review: Colour Doppler ultrasound flow patterns in the portal venous system.* Br J Radiol, **2002**. 75(899): p. 919-29.

40. Mehta TS, Raza S and Baum JK, *Use of Doppler ultrasound in the evaluation of breast carcinoma.* Semin Ultrasound CT MR, **2000**. 21(4): p. 297-307.

41. Blomley MJ and Eckersley RJ, *Functional ultrasound methods in oncological imaging.* Eur J Cancer, **2002**. 38(16): p. 2108-15.

42. Valentin L, *Use of colour and spectral Doppler ultrasound examination in gynaecology.* Eur J Ultrasound, **1997**. 6(3): p. 143-63.

43. Peshock R, *Normal Cardiac Anatomy, Orientation and Function*, in *Cardiovascular Magnetic Resonance*, D. Pennell and W. Manning, Editors. 2002, Churchill Livingstone: Philadelphia, Pennsylvania, USA. p. 75-96.

44. Balaban RS, *The Physics of Image Generation by Magnetic Resonance*, in *Cardiovascular Magnetic Resonance*, D. Pennell and W. Manning, Editors. 2002, Churchill Livingstone: Philadelphia, Pennsylvania, USA. p. 3-17.

45. Haacke M, Brown R, Thompson M, *et al.*, *Magnetic Resonance Imaging: Physical Principles and Sequence Design.* 1999: John Wiley & Sons Inc. 944.

46. Bellenger NG and Pennell DJ, *Assessment of Cardiac Function*, in *Cardiovascular Magnetic Resonance*, D. Pennell and W. Manning, Editors. 2002, Churchill Livingstone: Philadelphia, Pennsylvania, USA. p. 99-111.

47. Rehr RB, Malloy CR, Filipchuk NG, *et al.*, *Left ventricular volumes measured by MR imaging.* Radiology, **1985**. 156(3): p. 717-9.

48. Lincoff AM and Topol EJ, *Illusion of reperfusion. Does anyone achieve optimal reperfusion during acute myocardial infarction?* Circulation, **1993**. 88(3): p. 1361-74.

49. Kim RJ, Chen EL, Lima JA, *et al.*, *Myocardial Gd-DTPA kinetics determine MRI contrast enhancement and reflect the extent and severity of myocardial injury after acute reperfused infarction.* Circulation, **1996**. 94(12): p. 3318-26.

50. Schaefer S, Malloy CR, Katz J, *et al.*, *Gadolinium-DTPA-enhanced nuclear magnetic resonance imaging of reperfused myocardium: identification of the myocardial bed at risk.* J Am Coll Cardiol, **1988**. 12(4): p. 1064-72.

51. Kim RJ, Fieno DS, Parrish TB, *et al.*, *Relationship of MRI delayed contrast enhancement to irreversible injury, infarct age, and contractile function.* Circulation, **1999**. 100(19): p. 1992-2002.

52. Lima JA, Judd RM, Bazille A, *et al.*, *Regional heterogeneity of human myocardial infarcts demonstrated by contrast-enhanced MRI. Potential mechanisms.* Circulation, **1995**. 92(5): p. 1117-25.

53. Wu KC, Zerhouni EA, Judd RM, *et al.*, *Prognostic significance of microvascular obstruction by magnetic resonance imaging in patients with acute myocardial infarction.* Circulation, **1998**. 97(8): p. 765-72.

54. Croisille P, Moore CC, Judd RM, *et al.*, *Differentiation of viable and nonviable myocardium by the use of three-dimensional tagged MRI in 2-day-old reperfused canine infarcts.* Circulation, **1999**. 99(2): p. 284-91.

55. Shapiro EP, Rogers WJ, Beyar R, *et al.*, *Determination of left ventricular mass by magnetic resonance imaging in hearts deformed by acute infarction.* Circulation, **1989**. 79(3): p. 706-11.

56. Singer JR, *NMR diffusion and flow measurement and an introduction to spin phase graphing.* Journal of Physics E: Scientific Instruments, **1978**. 11(4): p. 281.

57. Axel L, Shimakawa A and MacFall J, *A time-of-flight method of measuring flow velocity by magnetic resonance imaging.* Magn Reson Imaging, **1986**. 4(3): p. 199-205.

58. Mohiaddin RH, Kilner PJ, Rees S, *et al.*, *Magnetic resonance volume flow and jet velocity mapping in aortic coarctation.* J Am Coll Cardiol, **1993**. 22(5): p. 1515-21.

59. Paz R, Mohiaddin RH and Longmore DB, *Magnetic resonance assessment of the pulmonary arterial trunk anatomy, flow, pulsatility and distensibility.* Eur Heart J, **1993**. 14(11): p. 1524-30.

60. Aurigemma G, Reichek N, Schiebler M, *et al.*, *Evaluation of mitral regurgitation by cine magnetic resonance imaging.* Am J Cardiol, **1990**. 66(5): p. 621-5.

61. Kilner PJ, Manzara CC, Mohiaddin RH, *et al.*, *Magnetic resonance jet velocity mapping in mitral and aortic valve stenosis.* Circulation, **1993**. 87(4): p. 1239-48.

62. Kozerke S, Schwitter J, Pedersen EM, *et al.*, *Aortic and mitral regurgitation: quantification using moving slice velocity mapping.* J Magn Reson Imaging, **2001**. 14(2): p. 106-12.

63. Urchuk SN and Plewes DB, *A velocity correlation method for measuring vascular compliance using MR imaging.* J Magn Reson Imaging, **1995**. 5(6): p. 628-34.

64. Urchuk SN, Fremes SE and Plewes DB, *In vivo validation of MR pulse pressure measurement in an aortic flow model: preliminary results.* Magn Reson Med, **1997**. 38(2): p. 215-23.

65. Yang GZ, Kilner PJ, Wood NB, *et al.*, *Computation of flow pressure fields from magnetic resonance velocity mapping.* Magn Reson Med, **1996**. 36(4): p. 520-6.

66. Thompson RB and McVeigh ER, *Fast measurement of intracardiac pressure differences with 2D breath-hold phase-contrast MRI.* Magn Reson Med, **2003**. 49(6): p. 1056-66.

67. Singer JR, *Blood-flow rates by nuclear magnetic resonance measurements.* Science, **1959**. 130: p. 1652-3.

68. Singer JR and Crooks LE, *Nuclear magnetic resonance blood flow measurements in the human brain.* Science, **1983**. 221(4611): p. 654-6.

69. Axel L, *Blood flow effects in magnetic resonance imaging.* AJR Am J Roentgenol, **1984**. 143(6): p. 1157-66.

70. Feinberg DA, Crooks L, Hoenninger J, 3rd, *et al.*, *Pulsatile blood velocity in human arteries displayed by magnetic resonance imaging.* Radiology, **1984**. 153(1): p. 177-80.

71. Shimizu K, Matsuda T, Sakurai T, *et al.*, *Visualization of moving fluid: quantitative analysis of blood flow velocity using MR imaging.* Radiology, **1986**. 159(1): p. 195-9.

72. Edelman RR, Mattle HP, Kleefield J, *et al.*, *Quantification of blood flow with dynamic MR imaging and presaturation bolus tracking.* Radiology, **1989**. 171(2): p. 551-6.

73. Moran PR, *A flow velocity zeugmatographic interlace for NMR imaging in humans.* Magn Reson Imaging, **1982**. 1(4): p. 197-203.

74. Bryant DJ, Payne JA, Firmin DN, *et al.*, *Measurement of flow with NMR imaging using a gradient pulse and phase difference technique.* J Comput Assist Tomogr, **1984**. 8(4): p. 588-93.

75. van Dijk P, *Direct cardiac NMR imaging of heart wall and blood flow velocity.* J Comput Assist Tomogr, **1984**. 8(3): p. 429-36.

76. Nayler GL, Firmin DN and Longmore DB, *Blood flow imaging by cine magnetic resonance.* J Comput Assist Tomogr, **1986**. 10(5): p. 715-22.

77. Redpath TW, Norris DG, Jones RA, *et al.*, *A new method of NMR flow imaging.* Phys Med Biol, **1984**. 29(7): p. 891-5.

78. Frahm J, Haase A and Matthaei D, *Rapid NMR imaging of dynamic processes using the FLASH technique.* Magn Reson Med, **1986**. 3(2): p. 321-7.

79. Atkinson DJ and Edelman RR, *Cineangiography of the heart in a single breath hold with a segmented turboFLASH sequence.* Radiology, **1991**. 178(2): p. 357-60.

80. Wang SJ, Nishimura DG and Macovski A, *Multiple-readout selective inversion recovery angiography.* Magn Reson Med, **1991**. 17(1): p. 244-51.

81. Firmin D, Kilner P, Keegan J, *et al. The development of a subsecond flow velocity mapping technique.* In Proc. 9th SMRM Annual Meeting. 1990. p. 848.

82. Keegan J, Gatehouse PD, Taylor AM, *et al.*, *Coronary artery imaging in a 0.5-Tesla scanner: implementation of real-time, navigator echo-controlled segmented k-space FLASH and interleaved-spiral sequences.* Magn Reson Med, **1999**. 41(2): p. 392-9.

83. Mansfield P and Pykett I, *Biological and medical imaging by NMR.* J Magn Reson, **1978**. 29(2): p. 355-73.

84. Chapman B, Turner R, Ordidge RJ, *et al.*, *Real-time movie imaging from a single cardiac cycle by NMR.* Magn Reson Med, **1987**. 5(3): p. 246-54.

85. Howseman AM, Stehling MK, Chapman B, *et al.*, *Improvements in snap-shot nuclear magnetic resonance imaging.* Br J Radiol, **1988**. 61(729): p. 822-8.

86. van Uijen CM, den Boef JH and Verschuren FJ, *Fast Fourier imaging.* Magn Reson Med, **1985**. 2(3): p. 203-17.

87. Haacke EM, Bearden FH, Clayton JR, *et al.*, *Reduction of MR imaging time by the hybrid fast-scan technique.* Radiology, **1986**. 158(2): p. 521-9.

88. Feinberg DA and Oshio K, *Phase errors in multi-shot echo planar imaging.* Magn Reson Med, **1994**. 32(4): p. 535-9.

89. Gatehouse P, Hughes R and Firmin D. *The effect of different gradient axis delays on oblique echo planar imaging.* In Proc. 4th SMR. 1996. p. 1841.

90. Ljunggren S, *A simple graphical representation of Fourier based imaging methods.* J Magn Reson, **1983**. 54(2): p. 338-43.

91. Glover GH and Pauly JM, *Projection reconstruction techniques for reduction of motion effects in MRI.* Magn Reson Med, **1992**. 28(2): p. 275-89.

92. Glover GH and Lee AT, *Motion artifacts in fMRI: comparison of 2DFT with PR and spiral scan methods.* Magn Reson Med, **1995**. 33(5): p. 624-35.

93. Mueller E, Laub G, Grauman R, *et al. RACE - Real time ACquisition and Evaluation of pulsatile blood flow on a whole body MRI unit.* In Proc. 7th SMRM Annual Meeting. 1988. p. 729.

94. Yang GZ, Gatehouse P, Mohiaddin RH, *et al. Zonal echo-planar flow imaging with respiratory monitoring.* In Proc. 5th ISMRM Annual Meeting. 1997. p. 1885.

95. Yang GZ, Gatehouse PD, Keegan J, *et al., Three-dimensional coronary MR angiography using zonal echo planar imaging.* Magn Reson Med, **1998**. 39(5): p. 833-42.

96. Keegan J, Firmin D, Gatehouse P, *et al., The application of breath hold phase velocity mapping techniques to the measurement of coronary artery blood flow velocity: phantom data and initial in vivo results.* Magn Reson Med, **1994**. 31(5): p. 526-36.

97. Keegan J, Gatehouse P, Yang GZ, *et al., Interleaved spiral cine coronary artery velocity mapping.* Magn Reson Med, **2000**. 43(6): p. 787-92.

98. Conturo TE and Smith GD, *Signal-to-noise in phase angle reconstruction: dynamic range extension using phase reference offsets.* Magn Reson Med, **1990**. 15(3): p. 420-37.

99. Buonocore MH, *Blood flow measurement using variable velocity encoding in the RR interval.* Magn Reson Med, **1993**. 29(6): p. 790-5.

100. Yang GZ, Burger P, Kilner PJ, *et al., Dynamic range extension of cine velocity measurements using motion-registered spatiotemporal phase unwrapping.* J Magn Reson Imaging, **1996**. 6(3): p. 495-502.

101. Bittoun J, Bourroul E, Jolivet O, *et al., High-precision MR velocity mapping by 3D-Fourier phase encoding with a small number of encoding steps.* Magn Reson Med, **1993**. 29(5): p. 674-80.

102. Bernstein MA, Zhou XJ, Polzin JA, *et al., Concomitant gradient terms in phase contrast MR: analysis and correction.* Magn Reson Med, **1998**. 39(2): p. 300-8.

103. Polzin JA, Alley MT, Korosec FR, *et al.*, *A complex-difference phase-contrast technique for measurement of volume flow rates.* J Magn Reson Imaging, **1995**. 5(2): p. 129-37.

104. Tang C, Blatter DD and Parker DL, *Correction of partial-volume effects in phase-contrast flow measurements.* J Magn Reson Imaging, **1995**. 5(2): p. 175-80.

105. Firmin DN, Nayler GL, Kilner PJ, *et al.*, *The application of phase shifts in NMR for flow measurement.* Magn Reson Med, **1990**. 14(2): p. 230-41.

106. Glagov S, Rowley DA and Kohut RI, *Atherosclerosis of human aorta and its coronary and renal arteries. A consideration of some hemodynamic factors which may be related to the marked differences in atherosclerotic involvement of the coronary and renal arteries.* Arch Pathol, **1961**. 72: p. 558-71.

107. Glagov S, Zarins C, Giddens DP, *et al.*, *Hemodynamics and atherosclerosis. Insights and perspectives gained from studies of human arteries.* Arch Pathol Lab Med, **1988**. 112(10): p. 1018-31.

108. Nerem RM, Levesque MJ and Cornhill JF, *Vascular endothelial morphology as an indicator of the pattern of blood flow.* J Biomech Eng, **1981**. 103(3): p. 172-6.

109. Ku DN, Giddens DP, Zarins CK, *et al.*, *Pulsatile flow and atherosclerosis in the human carotid bifurcation. Positive correlation between plaque location and low oscillating shear stress.* Arteriosclerosis, **1985**. 5(3): p. 293-302.

110. Sabbah HN, Khaja F, Brymer JF, *et al.*, *Blood velocity in the right coronary artery: relation to the distribution of atherosclerotic lesions.* Am J Cardiol, **1984**. 53(8): p. 1008-12.

111. Moore JE, Jr., Ku DN, Zarins CK, *et al.*, *Pulsatile flow visualization in the abdominal aorta under differing physiologic conditions: implications for increased susceptibility to atherosclerosis.* J Biomech Eng, **1992**. 114(3): p. 391-7.

112. Oshinski JN, Ku DN, Mukundan S, Jr., *et al.*, *Determination of wall shear stress in the aorta with the use of MR phase velocity mapping.* J Magn Reson Imaging, **1995**. 5(6): p. 640-7.

113. Stokholm R, Oyre S, Ringgaard S, *et al.*, *Determination of Wall Shear Rate in the Human Carotid Artery by Magnetic Resonance Techniques.* European Journal of Vascular and Endovascular Surgery, **2000**. 20(5): p. 427-33.

114. Wu SP, Ringgaard S, Oyre S, *et al.*, *Wall shear rates differ between the normal carotid, femoral, and brachial arteries: an in vivo MRI study.* J Magn Reson Imaging, **2004**. 19(2): p. 188-93.

115. Oyre S, Pedersen EM, Ringgaard S, *et al.*, *In vivo wall shear stress measured by magnetic resonance velocity mapping in the normal human abdominal aorta.* Eur J Vasc Endovasc Surg, **1997**. 13(3): p. 263-71.

116. Pedersen EM, Oyre S, Agerbaek M, *et al.*, *Distribution of early atherosclerotic lesions in the human abdominal aorta correlates with wall shear stresses measured in vivo.* Eur J Vasc Endovasc Surg, **1999**. 18(4): p. 328-33.

117. Oyre S, Ringgaard S, Kozerke S, *et al.*, *Quantitation of circumferential subpixel vessel wall position and wall shear stress by multiple sectored three-dimensional paraboloid modeling of velocity encoded cine MR.* Magn Reson Med, **1998**. 40(5): p. 645-55.

118. Wu SP, Ringgaard S and Pedersen EM, *Three-dimensional phase contrast velocity mapping acquisition improves wall shear stress estimation in vivo.* Magn Reson Imaging, **2004**. 22(3): p. 345-51.

119. Urchuk SN and Plewes DB, *MR measurements of pulsatile pressure gradients.* J Magn Reson Imaging, **1994**. 4(6): p. 829-36.

120. Urchuk SN and Plewes DB, *MR measurement of time-dependent blood pressure variations.* J Magn Reson Imaging, **1995**. 5(6): p. 621-7.

121. Napel S, Lee DH, Frayne R, *et al.*, *Visualizing three-dimensional flow with simulated streamlines and three-dimensional phase-contrast MR imaging.* J Magn Reson Imaging, **1992**. 2(2): p. 143-53.

122. Buonocore MH, *Visualizing blood flow patterns using streamlines, arrows, and particle paths.* Magn Reson Med, **1998**. 40(2): p. 210-26.

123. Kilner PJ, Yang GZ, Mohiaddin RH, *et al.*, *Helical and retrograde secondary flow patterns in the aortic arch studied by three-directional magnetic resonance velocity mapping.* Circulation, **1993**. 88(5 Pt 1): p. 2235-47.

124. Bogren HG, Mohiaddin RH, Yang GZ, *et al.*, *Magnetic resonance velocity vector mapping of blood flow in thoracic aortic aneurysms and grafts.* J Thorac Cardiovasc Surg, **1995**. 110(3): p. 704-14.

125. Mohiaddin RH, *Flow patterns in the dilated ischemic left ventricle studied by MR imaging with velocity vector mapping.* J Magn Reson Imaging, **1995**. 5(5): p. 493-8.

126. Buonocore MH, *Algorithms for improving calculated streamlines in 3-D phase contrast angiography.* Magn Reson Med, **1994**. 31(1): p. 22-30.

127. Yang GZ, Kilner PJ, Mohiaddin RH, *et al.*, *Transient streamlines: texture synthesis for in vivo flow visualisation.* Int J Card Imaging, **2000**. 16(3): p. 175-84.

128. Klipstein RH, Firmin DN, Underwood SR, *et al.*, *Blood flow patterns in the human aorta studied by magnetic resonance.* Br Heart J, **1987**. 58(4): p. 316-23.

129. Bogren HG, Klipstein RH, Firmin DN, *et al.*, *Quantitation of antegrade and retrograde blood flow in the human aorta by magnetic resonance velocity mapping.* Am Heart J, **1989**. 117(6): p. 1214-22.

130. Bogren HG and Buonocore MH, *Blood flow measurements in the aorta and major arteries with MR velocity mapping.* J Magn Reson Imaging, **1994**. 4(2): p. 119-30.

131. Kondo C, Caputo GR, Masui T, *et al.*, *Pulmonary hypertension: pulmonary flow quantification and flow profile analysis with velocity-encoded cine MR imaging.* Radiology, **1992**. 183(3): p. 751-8.

132. Mohiaddin RH, Paz R, Theodoropoulos S, *et al.*, *Magnetic resonance characterization of pulmonary arterial blood flow after single lung transplantation.* J Thorac Cardiovasc Surg, **1991**. 101(6): p. 1016-23.

133. Mohiaddin RH, Wann SL, Underwood R, *et al.*, *Vena caval flow: assessment with cine MR velocity mapping.* Radiology, **1990**. 177(2): p. 537-41.

134. Bogren HG, Buonocore MH and Valente RJ, *Four-dimensional magnetic resonance velocity mapping of blood flow patterns in the aorta in patients with atherosclerotic coronary artery disease compared to age-matched normal subjects.* J Magn Reson Imaging, **2004**. 19(4): p. 417-27.

135. Bellhouse BJ and Bellhouse FH, *Fluid mechanics of the mitral valve.* Nature, **1969**. 224(219): p. 615-6.

136. Ferziger J and Peric M, *Computational methods for fluid dynamics.* 3rd ed. 2002, Berlin, London: Springer. 423.

137. Cauvin JC, Boire JY, Zanca M, *et al.*, *3D modeling in myocardial 201TL SPECT.* Comput Med Imaging Graph, **1993**. 17(4-5): p. 345-50.

138. Chen CW, Luo J, Parker KJ, *et al.*, *CT volumetric data-based left ventricle motion estimation: an integrated approach.* Comput Med Imaging Graph, **1995**. 19(1): p. 85-100.

139. Staib LH and Duncan JS, *Model-based deformable surface finding for medical images.* Medical Imaging, IEEE Transactions on, **1996**. 15(5): p. 720-31.

140. Park J, Metaxas D, Young AA, *et al.*, *Deformable models with parameter functions for cardiac motion analysis from tagged MRI data.* Medical Imaging, IEEE Transactions on, **1996**. 15(3): p. 278-89.

141. Kuwahara M and Eiho S, *3-D heart image reconstructed from MRI data.* Comput Med Imaging Graph, **1991**. 15(4): p. 241-6.

142. Gustavsson T, Pascher R and Caidahl K, *Model based dynamic 3D reconstruction and display of the left ventricle from 2D cross-sectional echocardiograms.* Comput Med Imaging Graph, **1993**. 17(4-5): p. 273-8.

143. Bardinet E, Cohen LD and Ayache N, *Tracking and motion analysis of the left ventricle with deformable superquadrics.* Medical Image Analysis, **1996**. 1(2): p. 129-49.

144. Germano G, Kavanagh PB, Chen J, *et al.*, *Operator-less processing of myocardial perfusion SPECT studies.* J Nucl Med, **1995**. 36(11): p. 2127-32.

145. Germano G, Kavanagh PB and Berman DS, *An automatic approach to the analysis, quantitation and review of perfusion and function from myocardial perfusion SPECT images.* Int J Card Imaging, **1997**. 13(4): p. 337-46.

146. Kass M, Witkin A and Terzopoulos D, *Snakes: Active contour models.* Int. J. Comput. Vis., **1988**. 1(4): p. 321-31.

147. Pardo J, Cabello D and Heras J, *A Snake for Model-Based Segmentation of Biomedical Images.* Pattern Recognition Letters, **1997**. 18(14): p. 1529-38.

148. Ranganath S, *Contour extraction from cardiac MRI studies using snakes.* Medical Imaging, IEEE Transactions on, **1995**. 14(2): p. 328-38.

149. Cohen LD, *On active contour models and balloons.* CVGIP: Image Understanding, **1991**. 53(2): p. 211-8.

150. Cohen LD and Cohen I, *Finite-element methods for active contour models and balloons for 2-D and 3-D images.* Pattern Analysis and Machine Intelligence, IEEE Transactions on, **1993**. 15(11): p. 1131-47.

151. Bredno J, Lehmann TM and Spitzer K, *A general discrete contour model in two, three, and four dimensions for topology-adaptive multichannel segmentation.* Pattern Analysis and Machine Intelligence, IEEE Transactions on, **2003**. 25(5): p. 550-63.

152. Cootes TF, Hill A, Taylor CJ, *et al.*, *Use of active shape models for locating structures in medical images.* Image and Vision Computing, **1994**. 12(6): p. 355-65.

153. Cootes TF, Taylor CJ, Cooper DH, *et al.*, *Active Shape Models-Their Training and Application.* Computer Vision and Image Understanding, **1995**. 61(1): p. 38-59.

154. Cootes TF, Edwards GJ and Taylor CJ. *Active Appearance Models.* In Proc. 5th European Conference on Computer Vision. 1998. Freiburg, Germany: Springer-Verlag.

155. Cootes TF, Edwards GJ and Taylor CJ, *Active appearance models.* Pattern Analysis and Machine Intelligence, IEEE Transactions on, **2001**. 23(6): p. 681-5.

156. Berthold M and Hand DJ, *Intelligent data analysis : an introduction.* 2nd ed. 2002, Berlin ; London: Springer.

157. Brandt S, *Statistical and Computational Methods in Data Analysis.* 1983, Amsterdam: North Holland.

158. Behiels G, Maes F, Vandermeulen D, *et al.*, *Evaluation of image features and search strategies for segmentation of bone structures in radiographs using Active Shape Models.* Medical Image Analysis, **2002**. 6(1): p. 47-62.

159. Cootes TF and Taylor CJ. *On representing edge structure for model matching.* In Proc. Computer Vision and Pattern Recognition, 2001. CVPR 2001. Proceedings of the 2001 IEEE Computer Society Conference on. 2001. p. I-1114-I-9 vol.1.

160. Cootes TF, Taylor CJ and Lanitis A. *Multi-resolution search with active shape models*. In Proc. Pattern Recognition, 1994. Vol. 1 - Conference A: Computer Vision & Image Processing., Proceedings of the 12th IAPR International Conference on. 1994. p. 610-2 vol.1.

161. Mahmoodi S, Sharif BS and Chester EG. *Contour detection using multi-scale active shape models*. In Proc. Image Processing, 1997. Proceedings., International Conference on. 1997. p. 708-11 vol.2.

162. Mitchell SC, Bosch JG, Lelieveldt BPF, *et al.*, *3-D active appearance models: segmentation of cardiac MR and ultrasound images*. Medical Imaging, IEEE Transactions on, **2002**. 21(9): p. 1167-78.

163. Li B and Reinhardt JM. *Automatic generation of object shape models and their application to tomographic image segmentation*. In Proc. Medical Imaging 2001: Image Processing. 2001. San Diego, CA, USA: SPIE. p. 311-22.

164. Dickens MM, Gleason SS and Sari-Sarraf H. *Volumetric segmentation via 3D active shape models*. In Proc. Image Analysis and Interpretation, 2002. Proceedings. Fifth IEEE Southwest Symposium on. 2002. p. 248-52.

165. Kelemen A, Szekely G and Gerig G, *Elastic model-based segmentation of 3-D neuroradiological data sets*. Medical Imaging, IEEE Transactions on, **1999**. 18(10): p. 828-39.

166. Mitchell SC, Lelieveldt BPF, van der Geest RJ, *et al.*, *Multistage hybrid active appearance model matching: segmentation of left and right ventricles in cardiac MR images*. Medical Imaging, IEEE Transactions on, **2001**. 20(5): p. 415-23.

167. Hamarneh G and Gustavsson T. *Combining snakes and active shape models for segmenting the human left ventricle in echocardiographic images*. In Proc. Computers in Cardiology 2000. 2000. p. 115-8.

168. Fung YC, *Biodynamics Circulation*. 1984, New York: Springer-Verlag.

169. Panton R, *Incompressible flow*. 2nd ed. 1996, New York ; Chichester: Wiley.

170. Thompson J, Warsi Z and Masin C, *Numerical Grid Generation: Foundations and Applications*. 1985, Amsterdam: North-Holland.

171. Thompson J, *A survey of composite grid generation for general three-dimensional regions*, in *Numerical methods for engine-airframe integration*, S. Murthy and G. Paynter, Editors. 1986, AIAA: New York.

172. Thompson J, *Grid Generation*, in *Handbook of Numerical Heat Transfer*, W. Minkowycz, et al., Editors. 1988, Wiley: New York; Chichester.

173. Baker T, *Developments and trends in three-dimensional mesh generation*. Appl. Numer. Methods, **1989**. 5: p. 275-309.

174. George P, *Automatic mesh generation : application to finite element methods*. 1991, Chichester: Wiley.

175. Thacker W, *A brief review of techniques for generating irregular computational grids.* Int. J. Numer. Methods Eng., **1980**. 15: p. 1335-41.

176. Yerry M and Shephard M, *Three-Dimensional Mesh Generation by Modified Octree Technique.* Int. J. Numer. Methods Eng., **1984**. 20: p. 1965-90.

177. Shephard M and Georges M, *Three-Dimensional Mesh Generation by Finite Octree Technique.* Int. J. Numer. Methods Eng., **1991**. 32: p. 709-49.

178. Watson D, *Computing the Delaunay Tesselation with Application to Voronoi Polytopes.* The Computer Journal, **1981**. 24(2): p. 167-72.

179. Baker T, *Automatic Mesh Generation for Complex Three-Dimensional Regions Using a Constrained Delaunay Triangulation.* Engineering with Computers, **1989**. 5: p. 161-75.

180. Weatherill N and Hassan O, *Efficient Three-dimensional Delaunay Triangulation with Automatic Point Creation and Imposed Boundary Constraints.* Int. J. Numer. Methods Eng., **1994**. 37: p. 2005-39.

181. Lohner R and Parikh P, *Three dimensional grid generation by the advancing-front method.* Int'l J. Numer. Methods Fluids, **1988**. 8: p. 1135-49.

182. Lo S, *Volume Discretization into Tetrahedra-I. Verification and Orientation of Boundary Surfaces.* Computers and Structures, **1991**. 39(5): p. 493-500.

183. Lo S, *Volume Discretization into Tetrahedra - II. 3D Triangulation by Advancing Front Approach.* Computers and Structures, **1991**. 39(5): p. 501-11.

184. Lohner R, *Progress in Grid Generation via the Advancing Front Technique.* Engineering with Computers, **1996**. 12: p. 186-210.

185. Smith C, *Numerical Solution of Partial Differential Equations: Finite Difference Methods.* 3rd ed. 1985, Oxford: Oxford University Press.

186. Peskin CS, *Numerical analysis of blood flow in the heart.* J Comput Phys, **1977**. 25: p. 220-52.

187. Lemmon JD and Yoganathan AP, *Three-dimensional computational model of left heart diastolic function with fluid-structure interaction.* J Biomech Eng, **2000**. 122(2): p. 109-17.

188. Gonzalez E and Schoephoerster RT, *A simulation of three-dimensional systolic flow dynamics in a spherical ventricle: effects of abnormal wall motion.* Ann Biomed Eng, **1996**. 24(1): p. 48-57.

189. Taylor TW, Okino H and Yamaguchi T, *Three-dimensional analysis of left ventricular ejection using computational fluid dynamics.* J Biomech Eng, **1994**. 116(1): p. 127-30.

190. Schoephoerster RT, Silva CL and Ray G, *Evaluation of left ventricular function based on simulated systolic flow dynamics computed from regional wall motion.* J Biomech, **1994**. 27(2): p. 125-36.

191. Baccani B, Domenichini F, Pedrizzetti G, *et al.*, *Fluid dynamics of the left ventricular filling in dilated cardiomyopathy.* J Biomech, **2002**. 35(5): p. 665-71.

192. Jones TN and Metaxas DN. *Patient-specific Analysis of Left Ventricular Blood Flow.* In Proc. Medical Image Computing and Computer-Assisted Intervention. 1998. Cambridge, MA, USA: Springer. p. 156-66.

193. Saber NR, Gosman AD, Wood NB, *et al.*, *Computational flow modeling of the left ventricle based on in vivo MRI data: initial experience.* Ann Biomed Eng, **2001**. 29(4): p. 275-83.

194. Saber NR, Wood NB, Gosman AD, *et al.*, *Progress towards patient-specific computational flow modeling of the left heart via combination of magnetic resonance imaging with computational fluid dynamics.* Ann Biomed Eng, **2003**. 31(1): p. 42-52.

195. Merrifield R, Long Q, Xu XY, *et al. Combined CFD/MRI Analysis of Left Ventricular Flow.* In Proc. Medical Imaging and Augmented Reality. 2004. Beijing, China: Springer-Verlag. p. 229-36.

196. Hunter PJ, Pullan AJ and Smaill BH, *Modeling total heart function.* Annu Rev Biomed Eng, **2003**. 5: p. 147-77.

197. Long Q, Merrifield R, Yang GZ, *et al.*, *The influence of inflow boundary conditions on intra left ventricle flow predictions.* J Biomech Eng, **2003**. 125(6): p. 922-7.

198. Trahanias PE and Venetsanopoulos AN, *Vector directional filters-a new class of multichannel image processing filters.* Image Processing, IEEE Transactions on, **1993**. 2(4): p. 528-34.

199. Karakos DG and Trahanias PE, *Generalized multichannel image-filtering structures.* Image Processing, IEEE Transactions on, **1997**. 6(7): p. 1038-45.

200. Tschumperle D and Deriche R. *Vector-valued image regularization with PDE's: a common framework for different applications.* In Proc. Computer Vision and Pattern Recognition, 2003. Proceedings. 2003 IEEE Computer Society Conference on. 2003. p. I-651-I-6 vol.1.

201. Blomgren P and Chan TF, *Color TV: total variation methods for restoration of vector valued images.* IEEE Trans. Image Processing, **1998**. 7(3): p. 304-09.

202. Sapiro G and Ringach DL, *Anisotropic diffusion of multivalued images with applications to color filtering.* IEEE Trans. Image Processing, **1996**. 5(11): p. 1582-6.

203. Trahanias PE, Karakos D and Venetsanopoulos AN, *Directional processing of color images: theory and experimental results.* Image Processing, IEEE Transactions on, **1996**. 5(6): p. 868-80.

204. Perona P, *Orientation diffusions.* IEEE Trans Image Processing, **1998**. 7(8): p. 457-67.

205. Vemuri BC, Chen Y, Rao M, *et al. Fiber tract mapping from diffusion tensor MRI.* In Proc. Variational and Level Set Methods in Computer Vision, 2001. Proceedings. IEEE Workshop on. 2001. p. 81-8.

206. Wang Z, Vemuri BC, Chen Y, *et al. A constrained variational principle for direct estimation and smoothing of the diffusion tensor field from DWI.* In Proc. IPMI. 2003. Ambleside, UK. p. 660-71.

207. Coulon O, Alexander DC and Arridge SR, *Diffusion tensor magnetic resonance image regularization.* Medical Image Analysis, **2004**. 8: p. 47-67.

208. Tschumperle D and Deriche R. *Diffusion tensor regularization with constraints preservation.* In Proc. Computer Vision and Pattern Recognition, 2001. CVPR 2001. Proceedings of the 2001 IEEE Computer Society Conference on. 2001. p. I-948-I-53 vol.1.

209. Tschumperle D and Deriche R. *Variational frameworks for dt-mri estimation, regularization and visualization.* In Proc. Computer Vision, 2003. Proceedings. Ninth IEEE International Conference on. 2003. p. 116-21.

210. Krissian K. *A new variational image restoration applied to 3D angiographies.* In Proc. Variational and Level Set Methods in Computer Vision, 2001. Proceedings. IEEE Workshop on. 2001. p. 65-72.

211. Chan T and Shen J, *Variational restoration of non-flat image features: models and algorithms.* SIAM Journal on Applied Mathematics, **2000**. 61(4): p. 1338-61.

212. Chan T, Kang SH and Shen J, *Total variation denoising and enhancement of color images based on the CB and HSV color representation.* J. Visual Comm. Image Rep., **2001**. 12(4): p. 422-35.

213. Li Y and Santosa F, *A computational algorithm for minimizing total variation in image restoration.* IEEE Trans. Image Processing, **1996**. 5(6): p. 987-95.

214. Vogel CR and Oman ME, *Iterative methods for total variation denoising.* SIAM Journal on Scientific Computing, **1996**. 17(1): p. 227-38.

215. Rudin LI, Osher S and Fatemi E, *Nonlinear total variation based noise removal algorithms.* Physica D: Nonlinear Phenomena, **1992**. 60(1-4): p. 259-68.

216. Coulon O, Alexander DC and Arridge SR, *Tensor field regularisation for DT-MR images*, in *Proc. MIUA*. 2001: Birmingham, UK.

217. Tikhonov AN and Arsenin VY, *Solutions of ill-posed problems.* 1977: John Wiley.

218. Bertsekas DP, *Nonlinear programming.* 1995, Belmont, Massachusetts: Athena Scientific.

219. Helman J and Hesselink L, *Representation and display of vector field topology in fluid flow data sets.* Computer, **1989**. 22(8): p. 27-36.

220. Chong MS, Perry AE and Cantwell BJ, *A general classification of three dimensional flow fields.* Physics of Fluids A, **1990**. 2(5): p. 765-77.

221. Ford RM, Strickland RN and Thomas BA, *Image models for 2-D flow visualization and compression.* CVGIP: Graphical Model and Image Processing, **1994**. 56(1): p. 75-93.

222. Helman JL and Hesselink L, *Visualizing vector field topology in fluid flows.* Computer Graphics and Applications, IEEE, **1991**. 11(3): p. 36-46.

223. Tricoche X, Scheuermann G and Hagen H. *A topology simplification method for 2D vector fields.* In Proc. Visualization 2000. 2000. p. 359-66, 576.

224. De Leeuw W and Van Liere R. *Collapsing flow topology using area metrics.* In Proc. Visualization '99. Proceedings. 1999. p. 349-542.

225. Heckel B, Weber G, Hamann B, *et al. Construction of vector field hierarchies.* In Proc. Visualization '99. Proceedings. 1999. p. 19-505.

226. Telea A and Van Wijk JJ. *Simplified representation of vector fields.* In Proc. Visualization '99. 1999. p. 35-507.

227. Lodha SK, Renteria JC and Roskin KM. *Topology preserving compression of 2D vector fields.* In Proc. Visualization 2000. Proceedings. 2000. p. 343-50, 574.

228. Lavin Y, Batra R and Hesselink L. *Feature comparisons of vector fields using Earth mover's distance.* In Proc. Visualization '98. Proceedings. 1998. p. 103-9, 524.

229. Batra R and Hesselink L. *Feature comparisons of 3-D vector fields using earth mover's distance.* In Proc. Visualization '99. Proceedings. 1999. p. 105-14.

230. Garcke H, Preußer T, Rumpf M, *et al.*, *A phase field model for continuous clustering on vector fields.* IEEE Trans. Visualization and Computer Graphics, **2001**. 7(3): p. 230-41.

231. Kenwright D and Haimes R. *Vortex identification-applications in aerodynamics: a case study.* In Proc. Visualization '97., Proceedings. 1997. p. 413-6, 566.

232. Sadarjoen IA and Post FH, *Geometric methods for vortex detection*, in *VisSym'99.* 1999, Springer Verlag: Vienna, Austria. p. 53-62.

233. Brandt E, Ebbers T, Wigstrom L, *et al. Automatic detection of vortical flow patterns from three-dimensional phase contrast MRI.* In Proc. 9th ISMRM meeting, Proceedings. 2001. Glasgow, Scotland, UK. p. 1838.

234. Rao R and Jain R. *Analysing oriented textures through phase portraits.* In Proc. Proc. 10th Int. Conf. Patt. Rec. 1990. p. 336-40.

235. Shu C-F, Jain R and Quek F. *A linear algorithm for computing the phase portraits of oriented textures*. In Proc. Computer Vision and Pattern Recognition, 1991. IEEE Computer Society Conference on. 1991. p. 352-7.

236. Carmo BS, Ng YHP, Prugel-Bennett A, *et al. A data clustering and streamline reduction method for 3D MR flow vector field simulation*. In Proc. 7th International Conference on Medical Image Computing and Computer Assisted Intervention (MICCAI). 2004. Rennes, France: Springer-Verlag. p. 451-8.

237. Cote S and Tatnall RL, *The Hopfield neural network as a tool for feature tracking and recognition from satellite sensor images*. Int'l Journal of Remote Sensing, **1997**. 18(4): p. 871-85.

238. Isard M and Blake A, *CONDENSATION-Conditional Density Propagation for Visual Tracking*. International Journal of Computer Vision, **1998**. 29(1): p. 5-28.

239. Wu QX, McNeill SJ and Pairman D, *Correlation and relaxation labelling: an experimental investigation on fast algorithms*. Int'l Journal of Remote Sensing, **1997**. 18(3): p. 651-62.

240. Reinders F, Post FH and Spoelder HJW. *Attribute-based feature tracking*. In Proc. Data Visualization '99. 1999. Vienna, Austria: Springer Verlag. p. 63-72.

241. Reinders F, Sadarjoen A, Vrolijk B, *et al.*, *Vortex tracking and visualisation in a flow past a tapered cylinder*. Computer Graphics Forum, **2002**. 21(4): p. 675–82.

242. Kittler J and Illingworth J, *Relaxation labelling algorithms -- a review*. Image and Vision Computing, **1985**. 3(4): p. 206-16.

243. Geman S and Geman D, *Stochastic relaxation, Gibbs distributions and Bayesian restoration of images*. IEEE Trans on Pattern Analysis and Machine Intelligence, **1984**. PAMI-6(6): p. 721-41.

244. Waltz DL, *Understanding line drawings of scenes with shadows*, in *The Psychology of Computer Vision*, P. H. Winston, Editor. 1975, McGraw-Hill: New York.

245. Rosenfeld A, Hummel RA and Zucker SW, *Scene labelling by relaxation operations*. Systems, Man and Cybernetics, IEEE Transactions on, **1976**. SMC-6(6): p. 420-33.

246. Zucker SW and Mohammed JL, *Analysis of probabilistic relaxation labeling processes*. Proceedings of the 1978 Conference on Pattern Recognition and Image Processing, **1978**: p. 307-12.

247. Peleg S, *A new probabilistic relaxation scheme*. IEEE Trans on Pattern Analysis and Machine Intelligence, **1980**. PAMI-2(4): p. 362-9.

248. Kittler J and Föglein J, *On compatibility and support functions in probabilistic relaxation*. Computer Vision, Graphics, and Image Processing, **1986**. 34: p. 257-67.

249. Hancock ER and Kittler J, *Discrete relaxation.* Pattern Recognition, **1990**. 23(7): p. 711-33.

250. Hancock ER and Kittler J, *Edge-labeling using dictionary-based relaxation.* Pattern Analysis and Machine Intelligence, IEEE Transactions on, **1990**. 12(2): p. 165-81.

251. Faugeras OD and Berthod M, *Improving consistency and reducing ambiguity in stochastic labeling: an optimization approach.* IEEE Transactions on Pattern Analysis and Machine Intelligence, **1981**. PAMI-3(4): p. 412-24.

252. Berthod M and Faugeras O. *Using context in the global recognition of a set of objects: an optimization approach.* In Proc. Information Processing 80. Proceedings of the IFIP Congress 80. 1980. p. 695-8.

253. Faugeras OD, *Decomposition and decentralization techniques in relaxation labeling.* Computer Graphics and Image Processing, **1981**. 16(4): p. 341-55.

254. Lloyd S, *An optimization approach to relaxation labelling algorithms.* Image and Vision Computing, **1983**. 1(2): p. 85-91.

255. Hummel RA, *On the foundations of relaxation labelling processes.* IEEE Trans on Pattern Analysis and Machine Intelligence, **1983**. 5(3): p. 267-87.